HAL
open science

Molecular modeling of the genesis of the active phase of a supported catalyst

Amit Sahu

To cite this version:

Amit Sahu. Molecular modeling of the genesis of the active phase of a supported catalyst. Catalysis. Université de Lyon, 2021. English. NNT : 2021LYSEN037 . tel-03434989

HAL Id: tel-03434989

https://theses.hal.science/tel-03434989v1

Submitted on 18 Nov 2021

HAL is a multi-disciplinary open access archive for the deposit and dissemination of scientific research documents, whether they are published or not. The documents may come from teaching and research institutions in France or abroad, or from public or private research centers.

L'archive ouverte pluridisciplinaire **HAL**, est destinée au dépôt et à la diffusion de documents scientifiques de niveau recherche, publiés ou non, émanant des établissements d'enseignement et de recherche français ou étrangers, des laboratoires publics ou privés.

Numéro National de Thèse : 2021LYSEN037

THESE DE DOCTORAT DE L'UNIVERSITE DE LYON

opérée par

l'Ecole Normale Supérieure de Lyon

Ecole Doctorale N°206
Ecole Doctorale de Chimie (Chimie, Procédés, Environnment)

Discipline : Chimie

Soutenue publiquement le 27/09/2021, par :

Amit SAHU

Molecular modeling of the genesis of the active phase of a supported catalyst

Modélisation moléculaire de la genèse de la phase active d'un catalyseur supporté

Devant le jury composé de :

Monica Calatayud, Professeure des universités, Sorbonne Université	Rapporteure
Jean-François Paul, Professeur des universités, Université de Lille 1	Rapporteur
Valerie Briois, Directrice de Recherche, Synchrotron SOLEIL	Examinatrice
Victor Mougel, Professeur Assistant, ETH Zürich (Suisse)	Examinateur
Pascal Raybaud, Chercheur EPIC H.D.R., IFP Energies nouvelles	Directeur de thèse
Stephan Steinmann, Chargé de Recherche CNRS, ENS de Lyon	Co-Encadrant

Acknowledgments

First and foremost, I would like to thank my thesis director Pascal Raybaud for providing me the opportunity to perform research under his guidance. His expertise was immensely valuable in the progress of the project. His consistent support, discussions, and encouragement for attending the conferences have been exceptional. Every conversation with him inspires me to observe the problem from a different angle and improves my understanding. I want to thank my co-supervisor, Stephan N. Steinmann, for his valuable advice, ideas on various calculations, insightful feedback, and enriching scientific discussions. His mastery over the methodological part has been exceptionally helpful in enhancing my knowledge. I am grateful to both of my supervisors for reviewing the thesis and their valuable corrections. Particularly to Pascal, who has also done the proofreading for this thesis. It won't be an exaggeration if I say I was fortunate enough to find such amazing supervisors.

I would also like to thank Luc Nougier, Director of the Catalysis, Biocatalysis, and Separation Direction, Mathieu Digne and Magalie Roy-Auberger, my Department Chiefs (Catalysis by sulfides). Marie-Claude Beaufils, Executive Assistant, for taking care of my administrative work, IFPEN and ENS-Lyon for providing me funding and facilities to work. I thank the providers of all the high-performance computational resources we have used in this thesis: CINES, IDRIS, ENER440. Apart from that, I would also like to thank IACS for selecting me for Young Scientists Travel Support Prize, though I could not use it due to COVID.

Furthermore, this work wouldn't have been possible without various discussions and an excellent scientific environment with Jérôme Rey, Céline Chizallet, Manuel Corral Valero, Christèle Legens, and Charlie Blons. Specifically, to Jérôme for his help with IRC analysis and determining TS for complex cases.

Discussion on several occasions as internal meetings (or coffee breaks) with Pierre-Louis, Virgile, Antoine, Etienne, Soundar, and Sourav on various experimental aspects of the MoS_3 phase and Carine, David, Tangui, Masoud, Thomas, Adrian, Adrian on theoretical aspects have been constructive.

I thank Laureline for being a great office mate for the first two years and accompanying me whenever I changed the office. She and Nathalie have helped me a lot during the beginning of my PhD with many paperwork. PhD is not a short race; it is like running a marathon, so support is needed from all aspects of life. I am fortunate to have amazing friends and colleagues as Elsy, Sharmin, Adrian, Adrien, Thomas, Gabriel, Aleksandra, Giulia, Flor, Catarina, Julien, Hanane, Corentin, Anand, Danish, Anvesh, and all other IFPEN and ENS Lyon PhD students. They have supported me or helped me in various stages of my three-year journey and created a pleasant ambiance for work.

I would also like to thank my flatmate Frederic Scheffler for being very welcoming when I first arrived in France. He made my transition to the country smooth. He accommodated me as one of his family members. He, Jeanne, and Corentin have provided emotional strength and moral support, and thanks to my rabbit for being with me during the confinement.

Thanks to Prof. Monica Calatayud and Prof. Jean-François Paul for reviewing the thesis and providing their valuable feedback. I also would like to thank Victor Mougel and Valerie Briois for accepting the invitation to be the thesis examiners.

Last but not least, I cannot thank my friends and family back in India enough, who have always been supportive and encouraging. It would not have been possible for me to be here without their help and guidance. I am grateful to them for their invaluable contribution to my life.

« This work is part of the project IDEXLYON funded by the French National Research Agency (ANR-16-IDEX-0005), the Commissariat-General for Investment (CGI) and awarded of M€ 25 (for 4 years) by the French Government within the framework of the Investissements d'Avenir program ("Investment for the Future") »

Abstract

The genesis of industrially used MoS_2 based catalysts involves a crucial activation step where the sulfo-reduction of a Mo-oxide precursor occurs on the γ–alumina support. However, the complex mechanisms and various trisulfides or oxysulfides intermediates are still poorly rationalized at the molecular scale. This thesis investigates key mechanisms and intermediates involved in the transformation of γ–alumina supported Mo-oxide oligomers into Mo-sulfided ones by means of state-of-the-art density functional theory (DFT) simulation.

In the first part, we determine the sulfidation mechanisms and free energy profiles of the transformation of (100) γ–alumina supported Mo_3O_9 oligomers (cyclic and chain conformers) into Mo_3S_9. We unveil the activation energies for various O/S exchanges under H_2S as a function of O sites of $Mo_3O_xS_y$ intermediates. The structural and spectroscopic features of these intermediates are compared to available experimental data. We quantify the reduction paths of $Mo_3O_3S_6$ oxysulfides and Mo_3S_9 trisulfides oligomers into Mo_3S_6 disulfides under H_2. We analyze the effects of the cluster's nuclearity as well as reconstruction.

In the second part, we focus on the non-supported MoS_3 intermediate involved in the activation process. We simulate the energetic, structural, and spectroscopic features of 0D-, 1D- and 2D-MoS_3 polymorphs and revisit the interpretation of their IR spectrum. The growth energy evolution and the computed IR spectra suggest the coexistence of various polymorphs (chain or triangular) as a function of their size. Molecular dynamics reveals how small triangular oligomers reconstruct into MoS_3 patches resembling embryos of the 2D 1T'-MoS_2 phase. We propose plausible transformation paths from one polymorph to another. We finally discuss the possible role of the support on the stabilization of chain and triangular conformers.

This thesis provides an atomic-scale understanding of the Mo sulfides activation crucial for optimizing the resulting catalytic properties.

Résumé

La genèse des catalyseurs industriels de type MoS_2 implique une étape d'activation cruciale durant laquelle la sulfo-réduction d'un précurseur Mo-oxide intervient sur le support γ–alumine. Cependant, les mécanismes complexes et multiples intermédiaires (trisulfures et oxysulfures) demeurent encore mal compris à l'échelle moléculaire. Cette thèse examine les mécanismes-clés et les intermédiaires impliqués dans la transformation d'oligomères Mo-oxides supportés sur γ–alumines en oligomères Mo-sulfurés en employant la simulation quantique dans le formalisme de la théorie de la fonctionnelle de la densité (DFT).

Dans la première partie, nous déterminons les mécanismes de sulfuration et les profils d'énergie libre du processus de transformation des oligomères Mo_3O_9 (cycliques ou chaines) supportés sur la surface (100) d'alumine–γ en Mo_3S_9. Nous quantifions les énergies d'activation pour divers échanges O/S en présence d'H_2S pour différents sites O des intermédiaires $Mo_3O_xS_y$. Les caractéristiques structurales et spectroscopiques de ces intermédiaires sont comparées aux données expérimentales disponibles. Nous quantifions les voies réactionnelles de réduction des oligomères oxysulfures $Mo_3O_3S_6$ et trisulfures Mo_3S_9 en disulfures Mo_3S_6 en présence d'H_2. Nous analysons les effets de la nucléarité des oligomères et de leur reconstruction.

Dans la seconde partie, nous nous focalisons sur les intermédiaires MoS_3 impliqués dans le processus d'activation. Nous simulons les propriétés énergétiques, structurales et spectroscopiques des polymorphes of 0D-, 1D- et 2D-MoS_3 et revisitons l'interprétation de leur spectre infrarouge. L'évolution de la croissance énergétique et des spectres infrarouges calculés suggère la coexistence de divers polymorphes (de type chaine ou triangle) en fonction de leur taille. Les dynamiques moléculaires révèlent que de petits oligomères triangulaires se reconfigurent en feuillets MoS_3 semblables à des embryons de la phase 2D 1T'-MoS_2. Nous proposons une hypothèse sur la manière dont ces polymorphes se transforment. Finalement, nous discutons le possible rôle du support sur la stabilisation des conformères de type chaine ou triangle.

Cette thèse propose une compréhension à l'échelle atomique de l'activation des sulfides Mo, cruciale pour l'optimisationdes propriétés catalytiques finales.

“We think there is color, we think there is sweet, we think there is bitter, but in reality, there are atoms and a void.”

- *Democritus*

“The atoms or elementary particles themselves are not real; they form a world of potentialities or possibilities rather than one of things or facts”

- *Werner Heisenberg*

"The fundamental laws necessary for the mathematical treatment of a large part of physics and the whole of chemistry are thus completely known, and the difficulty lies only in the fact that application of these laws leads to equations that are too complex to be solved."

- *Paul Dirac*

“One is almost tempted to say... at last I can almost see a bond. But that will never be, for a bond does not really exist at all: it is a most convenient fiction which, as we have seen, is convenient both to experimental and theoretical chemists. “

- *Charles Alfed Coulson*

“Each new insight into how the atoms in their interactions express themselves in structure and transformations, not only of inanimate matter, but particularly also of the living matter, provides a thrill.”

- *Henry Taube*

"To my Mom and Dad, who took me to the School…"

ACKNOWLEDGMENTS I

ABSTRACT IV

RESUME VI

CHAPTER 1: INTRODUCTION 1

CHAPTER 2: BIBLIOGRAPHY 9

2.1. APPLICATIONS OF MoS_2/MoS_3 BASED NANOMATERIALS 10
2.1.1. New energy applications *10*
2.1.2. Hydrodesulfurization *13*
2.1.3. Catalyst preparation and activation *16*
2.1.4. The challenging MoS_3 Phase *24*
2.2. DFT STUDIES OF ALUMINA SUPPORT AND ALUMINA SUPPORTED MO-OXIDES AND MO-SULFIDES 29
2.2.5. Alumina surfaces *30*
2.2.6. Description of Mo-oxide on the support *34*
2.2.7. Sulfidation of Mo-oxide *35*
2.2.8. Alumina supported MoS_2 ..... *36*
2.3. CONCLUSIONS AND STRATEGY OF THE THESIS 38

CHAPTER 3: METHODS AND COMPUTATIONAL DETAILS 43

3.1. DENSITY FUNCTIONAL THEORY 43
3.1.1. Hohenberg and Kohn theorems *45*
3.1.2. Kohn-Sham DFT *46*
3.1.3. Exchange-Correlation functional *49*
3.1.4. Dispersion Corrections *51*
3.1.5. Solving KS-equations self-consistently *52*
3.1.6. Plane-wave basis set *53*
3.1.7. Projector augmented wave method *54*
3.1.8. Ab initio molecular dynamics (AIMD) *56*
3.2. SIMULATION OF SPECTROSCOPIC PROPERTIES 57
3.2.9. Vibrational analysis within harmonic approximations *57*
3.2.10. Core level shift and binding energies *61*
3.3. APPROACH TO FIND MINIMUM ENERGY PATHS AND SADDLE POINTS 63
3.3.11. The NEB method *65*
3.3.12. CI-NEB method *66*
3.3.13. The Dimer method *67*
3.3.14. Intrinsic Reaction coordinate (IRC) *69*
3.4. CONCLUSIONS 70

CHAPTER 4: GENESIS OF MOS_2 FROM MO-OXIDE PRECURSORS ON γ-ALUMINA 73

4.1. INTRODUCTION 73
4.2. METHODS 77
4.3. RESULTS 81
4.3.1. Oxides precursors interaction with γ-alumina *81*
4.3.2. Oxygen/Sulfur exchange Mo-oxides on alumina *85*
4.3.3. Mechanism and kinetics of O/S exchange from MoO_3 to MoS_3 (step I and II) *91*
4.3.4. Transformation of Mo_3S_9 trisulfides into Mo_3S_6 disulfides (step IV) *99*
4.3.5. Reduction of oxysulfides to disulfides by H_2 (step III) *102*
4.4. DISCUSSION 105
4.4.6. Sulfidation from Mo_3O_9 to $Mo_3O_3S_6$ (step I) *105*
4.4.7. Competition between sulfidation from $Mo_3O_3S_6$ to Mo_3S_9 (step II) and reduction from $Mo_3O_3S_6$ to Mo_3S_6 (step III) *107*
4.4.8. Chain to triangular cluster reconstruction *108*
4.4.9. Mobility and growth of intermediates *111*
4.4.10. Size effects *112*
4.5. CONCLUSIONS 114

CHAPTER 5: AMORPHOUS MoS_3: SIZE-DEPENDENT STRUCTURAL PROPERTIES, SPECTROSCOPIC, AND ENERGETIC ANALYSIS 117

5.1. INTRODUCTION 117
5.2. METHODS 119
5.3. STRUCTURE ANALYSIS 121
5.3.1. 0D- and 1D-model of triangular oligomers (TO) 121
5.3.2. 0D and 1D-Chains: Open-ring (OR), wave-like (WL), linear (L), and helical (HL) 124
5.3.3. MoS_3 patches with 1T'-MoS_2 like structure 127
5.3.4. Energetics analysis 132
5.4. SPECTROSCOPIC ANALYSIS 135
5.4.5. Comparison of the simulation of $[Mo_3S_{13}]^0$, $[Mo_3S_{13}]^{2-}$ and $[Mo_3S_9]^0$ clusters with the reference $[Mo_3S_{13}^{2-}]$ compounds 135
5.4.6. IR spectrum of TO polymorphs 137
5.4.7. IR spectrum of chain-like (OR, R, and WL) polymorphs 139
5.5. DISCUSSION 141
5.6. CONCLUSIONS 145

CHAPTER 6: CONCLUSIONS AND PERSPECTIVES 149

6.1. SULFO-REDUCTION OF MO-OXIDES ON SUPPORTED ALUMINA 149
6.2. MoS_3 PHASE: TRIANGULAR, CHAIN, RING, OR HYBRID? 152
6.3. IMPACT OF THE SUPPORT 153
6.4. OPEN QUESTIONS AND PERSPECTIVES 153

REFERENCES 158

APPENDIX A - THERMOCHEMISTRY 172

APPENDIX B - COMPLEMENTARY ANALYSIS ON MO-OXIDES 175

B1. GAS-PHASE ANALYSIS 175
B1.1 Geometry analysis 175
B1.2 Sulfidation in the gas phase 175
B1.3 Thermodynamics of gas-phase sulfidation 176
B2. ALUMINA SUPPORTED Mo_3O_9 AND ITS SULFIDATION 176
B2.1 Vacancy creation on supported Mo_3O_9 176
B2.2 Cyclic-Mo_3O_9 sulfidation 177
B2.3 Chain1-Mo_3O_9 sulfidation through path-1 177
B2.4 Chain-1-Mo_3O_9 through path-2 178
B2.5 Most relevant-Mo_3O_9 to Mo_3S_9 sulfidation path 178
B2.6 Chain-2-Mo_3O_9 sulfidation 178
B3. THERMODYNAMICS OF SULFIDATION OF SUPPORTED Mo_3O_9 178
B4. KINETICS OF SULFIDATION OF SUPPORTED Mo_3O_9 180
B4.1 Electronic energy plot for various O/S exchange of supported chain-1-Mo_3O_9 180
B4.2 Electronic energy plot for O/S exchange supported cyclic Mo_3O_9 181
B4.3 Energetic span analysis for the kinetics of cyclic-Mo_3O_9 O/S exchange 184
B4.4 Electronic energy plots for removing oxygen from $Mo_3O_3S_6$(step-III) 184
B4.5 Electronic energy plots for removing sulfur from Mo_3S_9 (step-IV) 185
B5. O/S EXCHANGE ON SUPPORTED Mo_1O_3 (MONOMER) 186
B5.1 Terminal oxygen site 186
B5.2 Interfacial oxygen site 187
B6. FREQUENCY ANALYSIS 188

APPENDIX C - COMPLEMENTARY ANALYSIS ON VARIOUS ASPECTS OF MoS_3 POLYMORPHS 192

C1. STRUCTURAL ANALYSIS 192
C2. SPECTROSCOPIC ANALYSIS 197

APPENDIX D - HYDRODESULFURIZATION OF DIBENZOTHIOPHENE ON COMOS EDGE 203

Chapter 1: Introduction

Due to global warming and climate change issues, there is an urgent need to find alternative ways to make energy cleaner and efficient than ever before. The effects are alarming and would be disastrous for the forthcoming generation.

There are several reasons for that, the increasing concentration of greenhouse gases being one of them. Fossil fuels cannot be entirely removed from prospective scenarios because the perpetual population growth causes an immense increase in world energy demand and inherent intensive energy consumption by developed countries. Moreover, as the living standard in developing countries continues to improve, the rise in energy consumption is intensifying. The increase in energy consumption gives an additional burden to satisfy the growing energy demand by other energy sources and reduce fossil fuel dependency.

The most significant contributors to this growing energy demand are the developing countries. For the most part, they are still dependent on coal, even though the renewable energy sector in China, and to some extent in India as well, is growing faster than ever before. The energy balance needs to be maintained promptly [1].

This stability can be maintained by including more renewable and green energy contributions to fulfill the world's energy demand while maintaining the environmental equilibrium. On the one hand, to satisfy the world's growing energy demand, we need new and efficient energy sources. On the other hand, taking care of the ecological balance is the most crucial challenge humanity has ever faced. Immediate actions need to be taken in this direction; otherwise, the alarming rate of increasing global temperature and the abrupt change in climate conditions can have a detrimental effect on humanity's survival.

Two possible strategies exist to address this issue. The first one is to find out renewable energy resources and making them more efficient, economical, and user-friendly. The second one is to reduce the carbon footprints in existing energy resources, including the

use of fossil fuels in a better and more efficient way. However, the critical challenges in the field of renewables are energy storage and efficiency.

Many attempts have been made to improve the energy efficiency of chemical processes thanks to a wide range of catalysts and energy storage capacity by innovative storage materials. Reducing the carbon footprints in exiting technology, energy consumption, and production would require global cooperation among all power sectors, from the producer to the consumer. Several promising efforts are being made to counter the issues mentioned above.

Despite the relatively rapid change in the power sector, the world's power-related CO_2 emissions are rising uninterruptedly because of already locked-in emissions in existing systems. Thus, the extensive lifespan and efficiency of these existing bodies cause more trouble to change them. For example, a coal-fired power plant's average life span is forty years, and it is accountable for 30% of global energy-related CO_2 emissions today (international agency report) [2]. Therefore, there is a desperate need to improve the existing systems. The world's energy demand was increased by about 2.9% in 2018; it is the fastest growth since 2010 and is driven mainly by China and India [3]. Despite a historical Covid-19 crisis resulting in a drop in energy demand by 2% in 2020, these observations remain constant for 2021 [4]. More than forty countries have agreed to reach NetZero, a new initiative of the EU climate foundation, by 2050 [5]. Meaning that these countries will try to achieve an ambitious net balance between total CO_2 emissions produced and emissions captured from the atmosphere.

Though many assuring efforts are being made, we cannot get away from oil. Oil remains a significant contributor to world energy mixture, and it contributes to world energy consumption by about 35%. In 2018, the world's oil production was 98 million barrels per day [2], which approximately consumes about 2.3×10^5 tons of catalyst per year. The use of such a vast amount of oil requires stringent constraints from higher administrative authorities on oil specifications in order to reduce the adverse effects of burning oil. These constraints have several scales to remove harmful carcinogenic elements from crude oil. Usually, the limitations are based on concentrations of CO, NO_x, SO_x, particulates, and other impurities. According to European Union's standards, the sulfur content of diesel

should not exceed more than ten ppm [6]. The environmental regulations are getting incrementally stringent due to the alarming rate of climate change. It makes the task of refining the crude oil more challenging. Oil refineries used the hydrodesulfurization (HDS) process to refine the crude oil to reach such specifications.

The residual content of heteroelements such as S and N, cetane number, smoke point, and density are the various specifications that should be respected as directed by authorities. Different chemical conversions are used to meet these specifications. Hydrotreatment (HDT) is performed in order to meet some of them. Therefore, HDT is an essential process in petroleum refining. In particular, it is a process to remove heteroatom species, carcinogenic metals to make cleaner fuels. The catalysts used in the HDS/HDT process are usually heterogeneous catalysts, commonly made of bimetallic sulfided nanomaterials such as NiWS, CoMoS, or NiMoS. The majority of them are supported on alumina.

Several parameters need to be considered at various catalyst life cycle stages to generate an optimal catalytic active phase. Some of them are the effect of support, the interaction of active phase precursors with support during the impregnation steps, the impact of the sulfo-reductive conditions during activation and reaction, and the active phase dispersion [7]. Conventionally, Mo-content to catalyst reaction is about 10% by weight, and Mo to promoter ratio is about 0.3 (Ni-Co/Mo). The reactions occur at the interface of MoS_2-nanoparticles and the fluid phase [7].

According to Sabatier's principle [8], an efficient and optimal catalyst should appropriately balance adsorption and desorption steps. High barriers in adsorption steps and very low barriers in the desorption step are generally considered inadequate. Catalyst interactions with reaction components should indeed be optimal. A weak interaction would not give enough time to allow the chemical substances to react, and a strong interaction would poison the catalyst's reactivity [9].

In heterogeneous catalysis, the Sabatier principle implies that when the catalytic activity of the various elements is plotted across the periodic table for the desired reaction, it gives rise to a "volcano plot." The peak of this volcano curve shows the most reactive catalyst.

Both the left and the right-hand side elements across the peak are not optimal catalysts due to too strong or weak intermediates' adsorption.

The most commonly best-known sulfided bimetallic catalysts are CoMoS, NiMoS, NiWS, and trimetallic CoMoWS, NiMoWS. These are the catalysts that come very close to the top of the volcano curves [10]. The catalytic activities of combining two elements Co/Ni with Mo/W, were higher than those of catalysts taken individually. This phenomenon is known as the synergetic effect when combining two components shows higher efficiency than the individual sum of its constituents.

Much research has been undertaken to understand this effect on Co(Ni)MoS systems. Certain complexities are involved in this process, starting from the preparation, the genesis of the active phase, the interaction of the precursors with support, the role of this support, the generated intermediate species, and the active sites, etc.

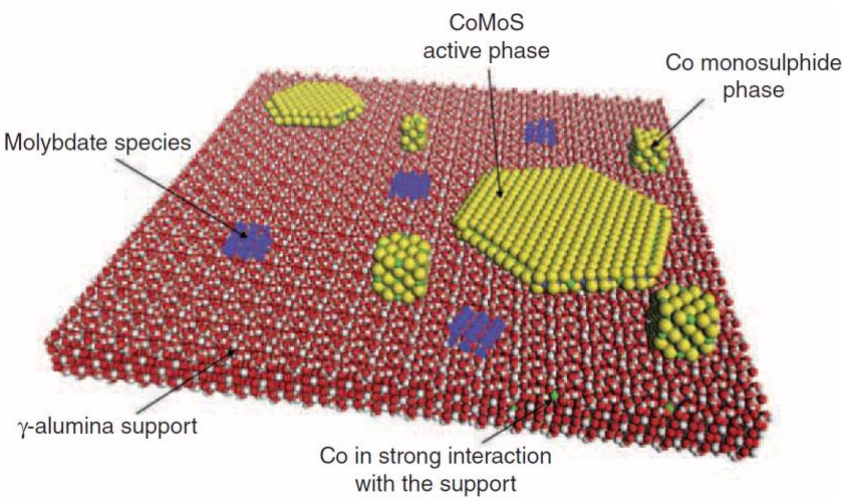

Figure 1-1: Schematic representation of MoS_2 based catalyst promoted by Co supported on gamma-alumina. Various possible species during the genesis of the active phase have been shown. Color code: Al-red, O-red, H-white, S-yellow, Mo-blue, Co-green (taken from reference [7]).

Figure **1-1** shows a schematic overview of an alumina-supported CoMoS catalyst. It highlights some key features such as the layered structure of MoS_2, the active phase, the

promoter Co, some of the remaining Mo-oxide species on alumina, and the strongly interacted single atom Co with alumina.

The nature of the active sites, the chemical role and the allocation of Co/Ni promoters, the exact morphology of the active phase, and reaction conditions are the main intricacies faced. They result directly from the various steps involved in the genesis of the supported active phase.

At the industrial and laboratory scales, one of the most widely used protocols of the preparation of heterogeneous supported catalysts involves three main steps: the impregnation in a water solvent firstly, the drying/calcination secondly and the activation (reduction, sulfidation) thirdly[7, 11, 12]. Among these, the activation step is still highly challenging because it is the last step before the catalyst is placed in reaction conditions. Providing an atomic-scale description and rationalization of the precursor's evolution from its dried phase to the sulfided active phase on support would allow more accurate control of this crucial step. This is particularly true for HDT catalysts, where it is empirically invoked that the metal-support interactions between an γ–alumina support and various molybdenum, tungsten, cobalt, or nickel oxide precursors play a crucial role in driving the formations of mixed oxide phases ($Co(Ni)Al_2O_4$, or $AlMo_6$)[13] which might be detrimental to the shape of the wished Co(Ni)Mo(W)S phase during activation.

The support itself has a substantial impact on the sulfided active phase's morphology, a dispersion that directly affects the activity of the catalyst. At a macroscopic scale, the mechanical strength of support will decide on the shape and size of the catalyst's pellets. At a mesoscopic scale, the porosity of the catalyst affects the diffusion of oxide precursors during the impregnation of the active phase and the diffusion of the reactants. At an atomistic scale, the sites and acid-base properties of the surface sites of the support influence the anchoring (nucleation) and growth of the active phase.

During the impregnation process, the Molybdenum oxidic precursor disperses on the alumina support. After drying or calcination, these highly distributed Mo-oxide species must undergo a sulfidation process to obtain the active phase. The most commonly used

sources for sulfidation are H_2S (and hydrocarbon feedstock in industrial conditions) at ~350°C and H_2, providing a reducing environment either in gas-phase or liquid phase conditions.

Regarding the sulforeduction of molybdenum oxide precursor, numerous experimental analyses (XPS, RAMAN, EXAFS, and TPS) described in Chapter 2 have been used in order to understand the activation steps better and revealed two main intricate pathways involving Mo-oxysulfide (MoO_xS_y) intermediates and/or MoS_3 intermediate before the formation of the targeted MoS_2 phase. Thus, better control of the genesis pathways leading selectively to MoS_2 could give rise to the suitable design of the catalyst.

These pathways may depend on various preparation conditions such as the hydration state of the oxide precursor, sulfo-reductive conditions such as temperature, pressure, or even the presence of organic/inorganic additives. However, the precise nature of oxide species, the propensity of oxide species towards sulfidation, the role of various anchoring sites of alumina, the detailed mechanistic pathway, and the intermediates involved in the activation process remains challenging to elucidate at a molecular or even atomic scale. Hence, we will attempt to address the several issues that might arise during the HDS catalyst's activation step using density functional theory (DFT) calculations.

A systematic DFT study is indeed required to quench the quest for a more accurate atomistic scale description of the activation step of the genesis of the active phase. There already exists a reliable atomistic model of γ-alumina [14, 15] and its interaction with oxide precursors [16, 17]. However, a theoretical study based on quantum simulation on the genesis of an active MoS_2 phase on γ-alumina starting from oxide precursors does not exist, to the best of our knowledge.

This thesis is organized into six chapters (including this general introduction). The second chapter will provide a concise but relevant literature review on the broad context and the current understanding of the preparation and activation of the HDS catalyst. It pinpoints the existing knowledge and the still open questions on Mo-oxide to Mo-sulfide transformation on support involving the key MoS_3-intermediate-phase. The third chapter

will present the Kohn-Sham density functional theory methods used for our theoretical investigations and the relevant chosen computational parameters. The fourth chapter will describe the results we have obtained on the Mo-oxides' structural thermodynamic and kinetics aspects. The oxide interaction with support, lability of O/S exchange, and transformation from MoS_3 phase to disulfide phase will also be underlined. Following the insights from the previous chapter, the structural investigation of the MoS_3 polymorphs is extensively explored in chapter five. We will also unveil insights into the dynamic evolution of the amorphous MoS_3 towards a more condensed and crystallized structure by ab-initio molecular dynamics. In particular, this part of the DFT study will shed more light on the amorphous MoS_3 phase, which is substantially essential not only in the context of HDS but also for emerging new energy applications. In the sixth chapter, we will propose some perspectives where this work can be continued in the future.

Chapter 2: Bibliography

A considerable amount of research has been done to understand the intrinsic nature of the catalyst and its activity in hydrodesulfurization (HDS) [7]. However, during the last decade, MoS_2/MoS_3 based nanomaterials have renewed massive attention from the scientific community due to their versatile properties, making them helpful for a variety of applications as catalysts for different electrochemical and photochemical processes (hydrogen evolution reaction (HER), CO_2 reduction), biomass conversion, or as photodetectors and biosensors... There are also various new emerging applications of MoS_3, such as materials for energy, a cathode for Li-S or K-S batteries, supercapacitor, or material for capturing elemental Hg from industrial waste, and bio-sensors. [18–28]

Molybdenum disulfide (MoS_2) is a layered material consisting of S-Mo-S layers exhibiting structural similarities to graphene. However, the bulk MoS_2 can occur in four different crystalline structures: 1H-single layer primitive cells with AA stacking and hexagonal arrangement, 2H- double-layer primitive cell with ABAB stacking and hexagonal arrangement, 1T-single layer primitive cell with AA stacking tetragonal arrangement, and 3R triple-layer primitive cell with ABCABC stacking and rhombohedral arrangement (Figure **2-1**)[29, 30]. Nanolayers of MoS_2-phase are of the most interest for HDS catalytic applications and can be seen as a monolayer of finite size (about 3-4 nm), the edges of which depend on the influence of HDS conditions [31–33]. MoS_2 based nanomaterials exhibit reasonably well-defined structures, unlike amorphous *a*-MoS_3 based nanomaterials. Structural understanding about the MoS_3 phase and types of S species present in the system remains limited [34–42]. A better knowledge of the local structure of *a*-MoS_3 would enable us to improve the rationalization of its catalytic properties.

In what follows, we will first highlight the role of MoS_2/MoS_3 based nanomaterials in new energy applications. Then we will briefly discuss the HDS process, the nature of the catalyst in detail, followed by the preparation of this catalyst. We report the current state of atomistic scale comprehension of various aspects of the HDS process such as nature of support, precursors and involved intermediates, active phase. Finally, we point out the existing gaps in our understanding of the activation process of HDS catalyst, justifying our DFT approach to fill some of these gaps and lay out the plan of the thesis.

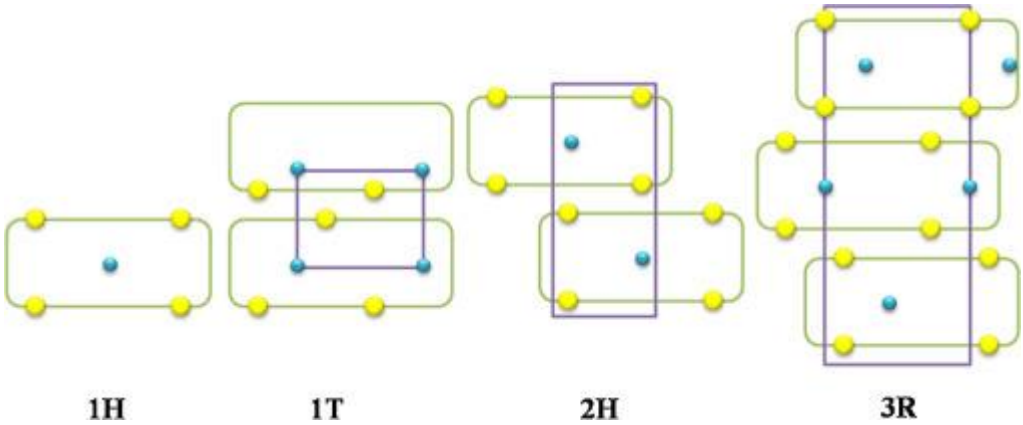

Figure 2-1: Schemes of commonly existing MoS_2 polytypes (extracted from ref [29])

2.1. Applications of MoS_2/MoS_3 based nanomaterials

2.1.1. New energy applications

Low cost, excellent chemical stability, and high activity towards hydrogen evolution reaction (HER) make materials more attractive than noble metals such as Pt. Although, the first study on molybdenum sulfide for HER was reported by Tributsch and Bennett in 1977[43], the momentum was gained during the past decade. The progress is plodded due to low activity of bulk-MoS_2 and deficiency of available active sites. Due to technological advancement, MoS_x (MoS_3 and MoS_2) nanostructures (not bulk) have shown more significant catalytic activity by increasing the number of active sites and reducing hydrogen interaction energy.

In 2005, Nørskov and co-workers computationally predicted that the edge sites (under coordinated S atoms) of MoS_2 would be catalytically more active than others for HER by estimating the bond energies and exchange current for HER[44, 45]. Jaramillo's further experiments on nanoclusters of MoS_2 supported by Au(111)validated this prediction[46]. The electrochemical hydrogen generation has a linear dependence on the edge length of MoS_2 nanoclusters. After identifying the active sites, many investigations have been performed to improve the intrinsic activity edge sites. The coverages of S atoms on MoS_2 edges affect the absorptions of atomic H and the binding energy of H_2 significantly,

depending on the size of MoS_2 nano-sheets. The lowest adsorption energy of atomic hydrogen on crystalline MoS_2 was observed on 50% S coverage on edge sites.

Several efforts have been made to improve the catalytic activity of MoS_2, which includes phase engineering, defect generation, and heteroatom doping such as Pt, Ni, Rh, Pd, and Ag[18, 19, 47–51]. Doping with these heteroatoms can enhance the intrinsic activity of the catalyst by reducing the binding energy of adsorbed hydrogen. Furthermore, this results in higher hydrogen coverage and lower value ΔG_H[18], where ΔG_H is the Gibbs free energy of adsorbed hydrogen on the catalytic surface which should be zero for the ideal catalytic surface.

However, MoS_2 exhibits various polymorphs with different atomic configurations, such as 2H-MoS_2 and 1T-MoS_2; these are the most extensively investigated polymorphs. 1T-MoS_2 has high atomic conductivity (metallic phase) compared to 2H-MoS_2 (semiconductor), giving rise to better HER activity compared to 2H. But, the metastable nature of the 1T phase makes the experimental synthesis very complicated. Besides synthesizing the 1T phase, a number of authors attempted to engineer the 2H phase by doping of heteroatoms on the basal plane of MoS_2. Doping will perturb the nearest neighbor interaction and basal plane structure, causing the change in adsorption energy of H with the active sites. Pt doping on MoS_2 nano-sheets is also identified as an enhancer for HER activity[26]. Enhancing the diffusion of hydrogen and conductivity of MoS_2 has a positive effect on catalytic activity on HER.

Apart from crystalline MoS_2, $MoS_{3 \text{ or } (2+x)}$ also attracted researchers' attention to simple preparation conditions such as electrodeposition, thermal decomposition, and wet synthesis[52]. Apart from the complicated synthesis process, its complex amorphous structure makes it more challenging to identify the active sites than in MoS_2. The structural complexity is still in the debate in the literature (Triangular vs. Chain will be discussed later section). In the recent past, it has been confirmed that S atoms present in the *a*-MoS_x act as an active catalyst site by the operando Raman spectroscopic technique. Also, the linear dependence of HER's turnover frequency (TOFs) on the percentage of higher energies S species presents in the catalyst by XPS, which indicates S_2^{2-} as an active site of the catalyst. The possible structural changes might occur on MoS_3 during HER. The

optimal level of S-vacancy and staining on MoS_2 nanosheets also enhance the HER activity of the catalyst[53].

The pH effect on the HER activity of anodically electrodeposited *a*-MoS_x films was investigated by Escalera et al. [19]. Enhancement in HER activity was observed in the pH range of 4-6; however, the activity slows down if pH increases beyond eight, which confirms slight acidic mediums help to improve activity, but an alkaline environment is detrimental for catalytic activity. The significant structural changes occur due to cleavage of $S_2^{2-}{}_{br}$ and the reduction of $S_2^{2-}{}_{term}$, and Raman spectra confirm the partial oxidation of Mo.

Cyclic voltammetry reveals that HER performance increases in the pH range of 3-5 while the structure is more stable. Furthermore, oxysulfide species are more active in this range rather than pure sulfide[19]. In addition to that, the cleavage of S_2^{2-} also creates more unsaturated S sites, which also enlarge the HER activity[19]. Several investigations [46, 53–56] reveal that unsaturated sulfur atoms on molybdenum sulfide play an essential role in catalytic activity. These unsaturated S atoms on the edge of MoS_2 adsorb the H atom with a small amount of free energy. Moreover, MoS_3 exhibits more catalytic activity than the bulk-MoS_2 in the presence of many defects and unsaturated sites available in *a*-MoS_3, which gives rise to high hydrogen coverage at low adsorption energy cost [19, 53].

It is observed that MoS_x can also be used for CO reduction to CH_4 (known as CO methanation). It was reported that activated H and SH groups are necessary to cleave the C-O bond and successively hydrogenation process. The presence of more S^{2-} bridging species would enhance the activity of HER as well as CO methanation [25, 57]. Furthermore, it has been reported that TiO_2 supported MoS_3 also shows efficient catalytic activity for photocatalytic water splitting along with CO_2 reduction simultaneously [25].

Last but not least, *a*-MoS_3 has some unique advantages due to its amorphous nature compared to crystalline MoS_2[58]. *a*-MoS_3 shows a very high specific capacity and excellent rate capability due to its unique molecular structure, which leads to improved Lithium-ion battery performance[20]. MoS_3 also outperforms all the existing MoS_2 based electrodes.[21] Explanations of the hypotheses were linked by 1D-chain like the structure

of MoS_3, which are bridged by sulfides and disulfides ligands and has lower diffusion barrier for Na ions. [28]

2.1.2. Hydrodesulfurization

In today's scenario, refineries worldwide are struggling to comply with the ever more stringent conditions to produce cleaner fuels, which is indispensable to reduce pollution effects. Hydrotreatment (HDT) is an essential industrial catalytic process used in oil refineries to eliminate heteroatomic species such as nitrogen and sulfur atoms by hydrodenitrogenation (HDN) and hydrodesulfurization (HDS). More rigorous constraints by environmental authorities make the refining processes more challenging. In order to meet these stringent regulations, a large part of research is devoted to improving the efficiency of the HDT process, either by enhancing the catalytic activity of the existing catalyst by tweaking or designing or synthesizing a new, more efficient catalyst.

2.1.2.1. Hydrodesulfurization Process

Hydrodesulfurisation is a catalytic chemical process to remove sulfur from crude oil to meet the required specifications of reaching less than ten ppm S in gasoline and diesel. Abundant sulfur-containing fuels not only have an unpleasant odor, but also combustion products of these oils are irritating, corrosive, and cause the emission of SO_x, which plays an essential role in acid rain. Long-term exposure to combustion products (diesel particulates) of high sulfur content fuel could result in adverse health issues such as cardiovascular diseases, cancer, elevated blood pressure, etc. [59]. Sulfur occurs in three different forms in crude oil: free sulfur (elemental sulfur), hydrogen sulfide (H_2S), and organic sulfur compounds (thiophene and dibenzothiophene derivatives). Organic sulfur (in particular alkyl-dibenzothiophene) is the most critical to remove sulfur because these molecular compounds are the most refractory ones[7].

The typical reaction that occurs during the HDS process involves severe temperature and pressure conditions, represented as in :

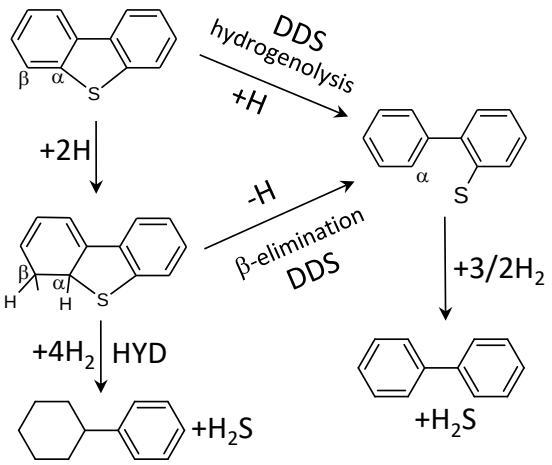

Figure 2-2: HDS of DBT via direct desulfurization pathway and hydrogenating pathway [60].

The feedstock is a complex mixture of hydrocarbons containing various heteroatoms such as sulfur, nitrogen, metals. These hydrocarbons consist predominantly of 5 or 6 membered aromatic ring structures such as thiophene, dibenzothiophene... Sulfur is an enormously prolific heteroatom in the feedstock and may vary 0.1% to 5% depending on the crude origin. Some of the most abundant sulfur-containing organosulfur compounds are thiols, thiophenes, sulfides, and disulfides.

Many of these organosulfur compounds are very stable and extremely difficult to remove. The organosulfur compounds are primarily consisting of alkyl-substitutes thiophenes and (di)benzothiophenes. Several detailed mechanistic pathways have been reported, including DFT approaches [61–64], but they broadly agree on some fundamental reaction steps that are present throughout the spectrum: chemisorption of an organosulfur compound on the active site, dissociative adsorption of hydrogen on the active phase near the organosulfur compound, and hydrogenolysis of C-S bond [7, 61–64]. Although this is not the core objective of the present thesis, we also investigated by DFT calculations some relevant mechanisms for the C-S bond scissions of DBT compounds catalyzed by MoS_2 based catalyst [60]. The reader interested in this aspect may refer to Appendix-D.

2.1.2.2. Nature of the supported catalyst

Conventionally, HDS catalysts are transition metal dichalcogenides, mainly group VI metal sulfides, supported by thermally stable pours materials with the larger surface area

such as alumina[65], TiO_2-anatase[66], silica[67], or silica-alumina[66], and promoted by Co, Ni, [11]. A molecular view of this active phase obtained by simulation is reported in ref[68] (Figure **2-3**).

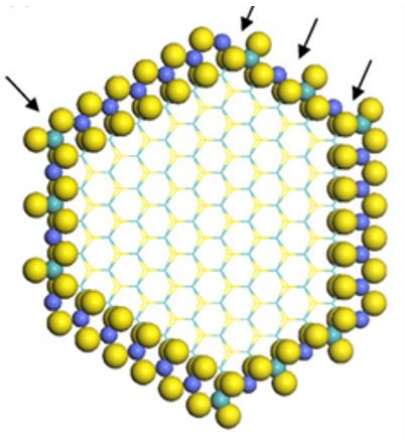

Figure 2-3: Molecular model of an equilibrium morphology of CoMoS phase with mixed Mo-Co sites on Mo-edge [68]. Ball color code: blue-Mo, yellow-S, and green-Co.

The active phase of the catalyst is dispersed on supports which are industrially γ-alumina or amorphous silica-alumina. Every part of the HDS catalyst has its own fundamental role to play in the final catalytic activity. The support effect is also one of them, and it greatly helps for the dispersion MoS_2 phase. γ-alumina and silica-alumina are the most widely used support for the HDT/HDS process due to their thermal and mechanical stabilities and tunable porous properties [69, 70].

Among alternative supports, TiO_2 supported MoS_2 (non-promoted) catalysts are 4 to 5 folds more effective than γ-alumina even at the same coverage of Mo on the surface[71, 72]. Many authors have tried to solve this puzzle and suggested several effects for the more significant activity of the catalyst: impact of geometry [73], orientation [74], Ti self-promotion, and electronic effects [75][76]. TEM images indicate the small size of MoS_2 slabs on TiO_2 and low stacking compared to other supports[66]. Further DFT study revealed that the epitaxial interaction of MoS_2 nanoparticles with TiO_2 surface favors the dispersion and changes the morphology of the MoS_2 nanoparticles[77].

However, the impact of the promoter is subject to support. For example, cobalt and nickel promotion enhances the activity of γ-alumina supported MoS_2 catalyst enormously (by several orders of magnitude), whereas for TiO_2 supported MoS_2[66], this effect is more moderate[69, 70]. Several reasons are invoked: the Ni sulfidation before Mo drives the formation of Ni_2S_3, causing lower promotion on NiMoS phase[78]. In contrast, the positive effect of the promotor on the activity of γ-alumina supported MoS_2 is primarily due to less pre-sulfidation of Ni. Moreover, DFT calculations have also shown that the strong interaction of MoS_2 nano-particles with the TiO_2 surfaces through the MoS_2 edge may prevent the addition of Co or Ni at these edges, which negatively impact the formation of the mixed Co(Ni)MoS phase.

A typical molecular view of alumina support CoMoS on alumina support has been represented in Figure **1-1**. The structure of the active phase is not unique and may vary according to Co coverage. Apart from the CoMoS phase, other species such as Co_9S_8 are also known to exist but remain poorly active. Mostly the CoMoS phase is responsible for catalytic activity.

However, the MoS_2 active phase is not always perfectly sulfided, and it remains a certain amount (10-20%) of Mo^{5+} or Mo^{6+} present in oxysulfides or even oxides which were identified by XPS [79]. This residual refractory phase may be detrimental for the final HDS activity, and it may result from the whole preparation/synthesis/activation process of the catalyst described in what follows.

2.1.3. Catalyst preparation and activation

Conventional preparation of the catalyst involves three main steps: impregnation of the support with oxide precursors in water solvent followed by thermal treatment such as drying (120-150 °C) or calcination if required (300-500 °C) is performed (Figure **2-4**). Finally, catalytic activation by a sulfo-reductive process at 350°C[80]. Nowadays, organic and inorganic additives are used to change the chemical properties or increase metal solubility[81, 82].

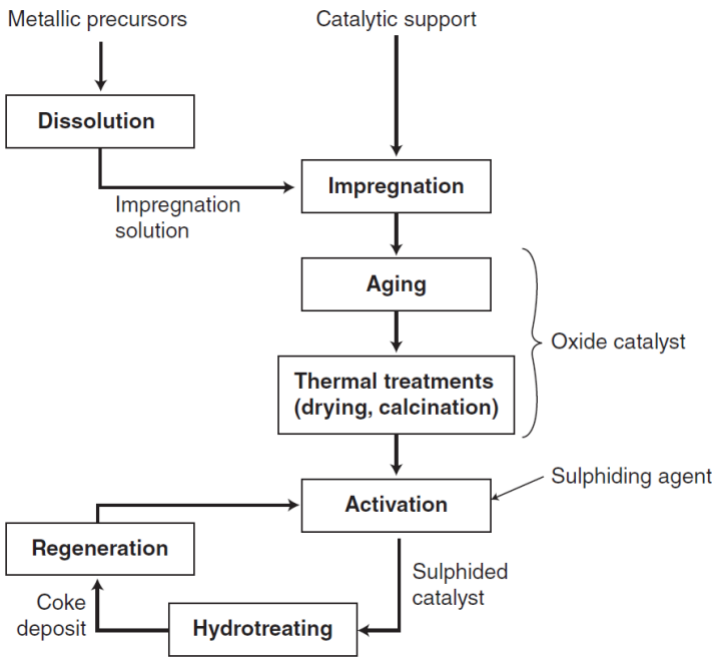

Figure 2-4: Illustrative representation of HDS catalyst preparation and involved different intermediate steps [80].

2.1.3.1. Impregnation

Usually, polyanions are used as oxide precursors for HDS catalysts. Four main types of polyoxometalates structures used in various applications are Keggin, Anderson, Strandberg, and Dawson structures [83, 84]. These structures differ in terms of molecular structure, acid-base properties, redox properties, thermodynamic stability with each other. In HDS catalyst, Keggin type heteropolyanions (HPA) and their derivatives are used predominantly. The transformation from Keggin to Anderson-type HPA might also take place. It is shown that this could impact the dispersion of Mo during incipient wetness impregnation at high Mo loading on γ–alumina [85]. A significant range of pH stability is expected from HPA due to change in pH during the impregnation process. The use of pre-reduced HPAs has been proven to be more beneficial for retaining the structural stability up to the formation of the dried oxide phase. Moreover, pre-reduction also helps to increase the loading of Mo [86–88].

Impregnation usually proceeds by dissolving the molecular oxide precursors in an aqueous solution to be added to the support (generally gamma-alumina or silica-alumina)

in an acidic environment. Routinely used impregnation methods are dry impregnation (also known as incipient wetness impregnation) and excess impregnation. In dry impregnation, the support's pore volume is filled with active phase precursors solution, which requires an almost equal volume of impregnation solution as pore volume of the support. In excess impregnation (equilibrium adsorption), the support is immersed in the volume of impregnation solution, which requires a large amount of solution-phase than the support's pore volume.[7]

2.1.3.2. The chemical process involved during impregnation

Ammonium heptamolybdate $(NH_4)_6Mo_7O_{24}$ is the most extensively studied precursor used in the literature for oxide precursors of HDS catalyst. Earlier studies performed on the impregnation of ammonium heptamolybdate on γ–alumina support considered adsorption only as a well-known interaction phenomenon [89]. However, Mo occurs as polymeric species at low pH, but in the acidic pH range, it exists monomeric species of (MoO_4^{2-})[90]. Thus, later, more complex phenomena [91, 92] described in what follows were described during impregnation of ammonium-heptamolybdate. Based on NMR and IR-RAMAN studies, the formation of heteropolyanion formation was verified [93, 94].

Usually, heptamolybdate ($Mo_7O_{24}^{6-}$) anion is stable in an acidic medium with a typical pH value range is 2-5. The zero-point charge (ZCP) of alumina support is around pH 8-9. If the pH of the solution increases beyond 5, heptamolybdate tends to depolymerize into monomeric species according to the following scheme:

2-1

$$Mo_7O_{24}^{6\,-} + 8HO^- \rightarrow 7MoO_4^{2\,-} + 4H_2O$$

This solution interacts with support, and acid-base reactions take place, which usually occurs between acid-base sites (hydroxyl group) of support and impregnated solution. As a consequence of this reaction, the pH value increases until it reaches the Zero Charge Point (ZCP) of support. According to the literature, several possible interaction modes of the molybdate species with the surface depend on the Mo concentration (Figure **2-5**).

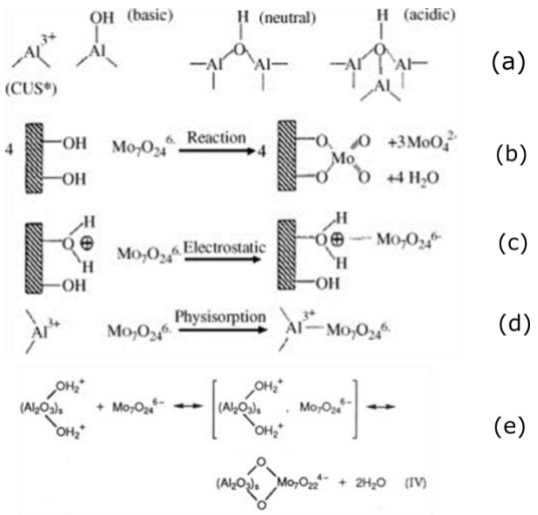

Figure 2-5: Various proposed chemical reactions of heptamolybdates (a-d)[95] and e [96]

The formation of monomeric MoO_4^{2-} and Al-OH_2^+ species have been confirmed by Raman spectroscopy; they have the characteristic band around 920 cm^{-1}; however, this holds true only for lower loading of dispersing Mo atom (< 2 Mo atom/nm^2) because higher loading Mo atoms causes neutralization of all basic hydroxyls by impregnation solution due to optimal presence of protons. This effect does not allow acid-base reaction, which restricts the pH causing no decomposition of heptamolybdate. This has been verified by Raman spectroscopy which revealed an intense peak at 940 cm^{-1}. Several adsorption modes are invoked for the heptamolybdates: purely electrostatic (reaction c in Figure **2-5**) if the hydroxyl groups of alumina are protonated, or chemical interaction with the Al sites (reaction d and e in Figure **2-5**). Moreover, a further increase in Mo deposition causes partial dissolution of support due to a more acidic environment. Dissolved Al^{3+} ions in impregnation solution react directly with the heptamolybdates as shown here:

2-2

$$6Mo_7O_{24}^{6}{}^{-} + 7Al_3^+ + 24H_2O \rightarrow 7Al(OH)_6Mo_6O_{18}^{3}{}^{-} + 6H^+$$

This is again confirmed by the characteristic Raman band around 950 cm^{-1}. Maturation is the consequent step closely related to impregnation. It involves the diffusion of solute into pore size volume of support and is typically performed in an enclosed environment and the excess presence of a solvent.

2.1.3.3. Thermal Treatment (Drying and Calcination)

Drying is performed to remove the excess solvent from the system; usually, the temperature is set close to the solvent's boiling point (~100°C for aqueous solution). The quality of the active phase could be damaged by inadequately applied drying due to various complexities involved in this process, such as temperature gradient created by evaporation of solvent and heat transfer by conduction and radiation. Removing the solution with this process gives potential risk to the inhomogeneous distribution of molecular species and might start precipitating if it reaches the required saturation limit.

The use of a chelating agent (organic molecules) has been proposed to overcome this issue[97]. Calcination is further thermal treatment after drying but is not mandatory if the catalyst is already activated. Calcination requires high thermal treatment (~350°C) to obtain a calcined oxide catalyst. Calcination is crucial because it removes unenviable ions which might be present after drying. However, If the use of organic additive is involved, calcination should be avoided due to the potential risk of additive decomposition, nullifying the effect of additives. It also plays a crucial role in forming a dispersed oxide phase which significantly differs from the drying step because at high temperature. It breaks down the molecular clusters and creates a highly dispersed phase with a strong interaction with the support, which might be detrimental for the activation step and the resulting catalytic activity.

Sarrazin et al. have performed an FTIR spectroscopy on low Mo surface coverage up to 2 Mo atom-nm^{-2} after calcination. This study indicates that the "basic," higher frequencies 3795 and 3770 cm^{-1}, hydroxyl groups present on γ-alumina are involved in the interaction with molybdate species, whereas the "neutral" and "acidic" ones with intermediate frequencies (3730 cm^{-1} and 3695 cm^{-1}) are not [96]. We will come back to a more detailed analysis of these alumina surface hydroxyls in section-2.1.4.

2.1.3.4. Activation

The activation step is the key and final step towards the genesis of the final HDT catalyst. It will also be at the core of the present thesis work. Once the catalyst is impregnated, dried, and calcinated (if required), activation is performed by placing the catalyst in the sulfo-reductive environment at a high temperature (~350 °C). The gas-phase sulfidic environment typically requires a 15% H_2S/H_2 mixture; however, dimethyl disulfide (DMDS) is also used as a precursor for in-situ H_2S generation in a liquid phase sulfidation environment. H_2S is used as a sulfur source in laboratory conditions (gas phase sulfidation); however, DMDS, CS_2, or excessive sulfur-containing feedstock (liquid phase sulfidation) are being used for industrial sulfidation. It has been reported that the sulfidation process (transition temperature), particularly in the presence of Co or Ni promoter precursors, might be influenced by the nature of the sulfiding agent (either liquid or gaseous) [98, 99]. Nevertheless, we will not address this question, and here, we focus on the possible activation mechanisms invoked so far.

Whether it is a gas phase sulfidation or liquid, the layered MoS_2 phase has always been formed. The large polyoxomolybdate precursors are thus sulfided and transformed into MoS_2-slabs decorated by Ni/Co. The average change in the size of the active phase under sulfidation conditions has been identified by TEM. The highest number of particles were observed, around 200 °C, based on the geometrical model of Kasztelan [33]. It indicates early-stage sulfide particles or nucleation before they start to agglomerate and form a layered structure. However, due to a lack of complete sulfidation, Al-O-Mo anchoring points would still exist. Some studies suggest that these very anchoring sites would lead to high active phase dispersion [77, 100, 101]. Moreover, the morphology of the final MoS_2 phase (triangle vs. hexagonal) is dependent on the sulfiding condition [32] and on the strength of the metal-support interaction [80].

This process involves all the intermediates steps required from Molybdenum oxide species to MoS_2 on support. To get a highly dispersed, fully sulfided, and optimally promoted MoS_2 catalyst, an appropriate sulfidation condition is needed. In the literature, it is proposed from experimental analyses (XPS [79, 102, 103], RAMAN [104], EXAFS [105, 106], TPS [107]) that the activation steps may go through two main intricate pathways: the first one involves oxysulfide (MoO_xS_y) intermediates and the second one, a "MoS_3"

intermediate phase. Thus, the better control of the genesis pathway leading selectively to the MoS_2 or MoS_3 phases could have some appealing applications in this area.

Firstly, Mo-O to Mo-S exchange, which takes place by the protonation of the Mo-O bond, results in the weakening of the Mo-O and S-H bond. The driving force for this reaction is the genesis of water as an exchange product. Secondly, redox reaction involves reducing Mo_{VI} to $Mo_{V\ or\ IV}$ and the oxidization of sulfide ligands during thermal decomposition. XPS spectra are the firm evidence of this reaction step. It was speculated that $Mo{=}O_t$ are the most labile species for S exchange (Figure **2-6**).

$$2S^{2-} \longrightarrow S_2^{2-} + 2e^-$$

$$2Mo^{6+} + 2e^- \longrightarrow 2Mo^{5+}$$

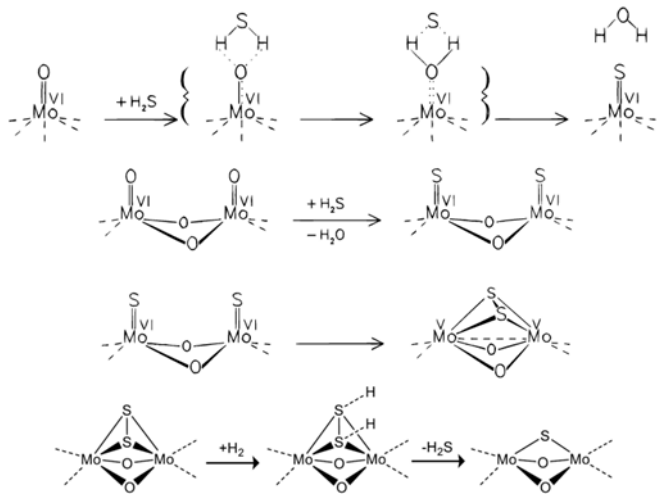

Figure 2-6: Schematically proposed mechanism for sulfidation of Mo-oxides [27].

The Temperature-dependent IR emission spectrum of sulfidation of crystalline MoO_3 shows that around 100-200 °C, the peak of bridging oxo-species Mo-O-Mo disappears, and a new peak is assigned to the top oxo-species $Mo{=}O_t$ appears. This indicates the Mo-O-Mo to Mo=O transformation occurs first as a precursor of Mo=S formation (Figure **2-6** giving partially sulfided oxide, also known as oxysulfides). Then, on Mo-oxysulfides, the $Mo{=}O_t$ species disappear more rapidly than Mo-O-Mo species (Figure **2-7**). After increasing the temperature further (200-400 °C), many significant changes occur as they differentiate to form oxysulfide below 200°C. Most of Mo_{VI} and Mo_V converted into Mo_{IV}, S_2^{2-} contribution eventually disappeared and formed MoS_2.

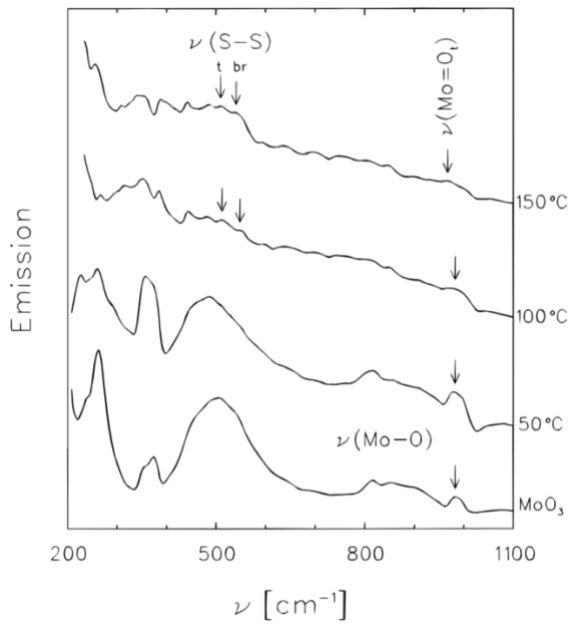

Figure 2-7: Temperature-dependent IR emission spectrum of sulfidation of crystalline MoO_3. $Mo=O_t$ peak around 970 cm^{-1} slowly disappears as temperature increases [27].

Other studies suggest that a MoS_3 amorphous phase would also be a relevant intermediate during the activation step of the HDS catalyst. S/Mo ratio is observed around nearly 3 [7, 104, 108]. Earlier it was invoked that this MoS_3 phase could be the mixture of poorly crystalline MoS_2 and sulfur[109]. But later, Diemann proved the existence of MoS_3 by X-ray radial distribution functions; it was not a mixture of poorly crystalline MoS_2 and Sulfur [110]. The formation of the MoS_3 phase is subject to exposed catalyst on sulfidation conditions. At a slightly low temperature (around 146 °C), the MoS_3 phase formed; however, it is still dependent on the reaction mixture (H_2/H_2S ratio). At 347 °C, only the characteristics of MoS_2 were observed irrespective of the reaction mixture[104].

The formation of both oxysulfide and MoS_3 intermediates during the sulfidation process has recently been confirmed by quick-XAS combined with chemometric analysis on alumina support[99, 106]. We will come back to a more detailed analysis of XAS studies in comparison with our DFT studies in chapter 4.

However, we cannot exclude that these different possible pathways may depend on various experimental conditions such as hydration state of precursor temperature, pressure, and sulfur-reductive environment and might also depend on the precursors. It also can be affected by the presence of organic and inorganic additives [105].

2.1.4. The challenging MoS_3 Phase

As discussed before, the MoS_3 phase requires to pay more and more attention because of its versatile properties valuable for various mature and emerging applications. Despite a very diverse range of use, many challenging questions remain open on the structural and electronic properties of MoS_3 due to its amorphous nature (Figure **2-8** a). Also, researchers recently tried to use MoS_3 as a precursor for HDS catalyst to produce highly dispersed MoS_2 phase on γ-alumina to improve the resulting activity of the catalyst[111]. Many experimental studies [36, 40, 41, 112–115] and very few theoretical ones [38, 39] have been undertaken better understand the electronic and physicochemical properties of the MoS_3 phase. However, the atomic scale's information available in the literature is still scarce or ambiguous. There is still an ongoing debate on the precise structural building blocks (triangular or chain) of *a*-MoS_3 depending on the characterization techniques used.

Many of these exciting properties of *a*-MoS_3 are supposed to originate from its intriguing amorphous 1D- or 2D-nano-structure, where Mo atoms are interconnected by various types of sulfur atoms such as S^{2-} and S_2^{2-} species. These versatile species are suspected to improve the reactivity towards the different key reactants involved in the targeted applications: diffusion of cations in battery materials[21, 28], activation of H_2 in HER[19, 53, 56, 116, 117], and HDS reaction[27], and specific interaction with Hg.[24]

Nevertheless, despite these wide ranges of potential applications of MoS_3, challenging questions remain open regarding its structural, electronic, and spectroscopic features. Indeed, the amorphous nature of MoS_3 makes it difficult to precisely identify the type and local structure of these active sulfur sites in order to rationalize their reactivity better.

Since the early 70' several experimental studies have been devoted to the *a*-MoS_3 phase.[34, 36, 37, 40–42, 110, 112–115, 118–122] However, the atomistic picture of *a*-MoS_3 remains uncertain. In particular, there is historical and still vivid debate on the nature of the structural building block, either Mo_3 triangular (Figure **2-8** a)[39, 40, 123] or Mo chain-like (Figure **2-8** d-e),[34, 41, 42, 120] and the oxidation states of Mo atoms, which also depends on the characterization techniques used.

Earlier studies based on radial distribution function (RDF), extended X-ray absorption spectroscopy (EXAFS), magnetic susceptibility, and X-ray photoelectron spectroscopy (XPS) proposed a chain-like model along with the Mo oxidation state five.[34, 41] EXAFS data suggested that two types of Mo-Mo bonds would be present in *a*-MoS_3: one short bond at 2.74 Å and one long at 3.14 Å (Figure **2-8** f).[41, 118] So, every metal atom would be involved in a Mo-Mo pair generating alternatively short Mo-Mo bond and longer Mo-Mo bond connecting each dimer. However, many subsequent EXAFS studies identified only one small Mo-Mo bond at 2.75-2.77 Å.[35, 120–122]

Based on an extensive EXAFS study, Cramer et al. proposed two possible models, a chain-like and cyclic Mo_3 model with two possible oxidation states $Mo^{5+}(S^{2-})_2(S_2^{2-})_{1/2}$ and $Mo^{4+}(S^{2-})(S_2^{2-})$ respectively, admitting that EXAFS cannot distinguish them.[35] By combining low angle X-ray diffraction (XRD) and theoretical models, Chien et al. preferentially suggested a Mo^{5+} chain-like model with two Mo-Mo bonds: one short at 2.80 Å and a very long one at 3.40 Å.[34] Such a chain like the model was inspired by other potentially existing crystalline transition metal trisulfides where metal atom connected with three sulfur atoms along the chain with molecular formula $M^{V}(S^{2-})_2(S_2^{2-})_{1/2}$. However, these linear structures are challenging to recover nowadays in the crystallographic database (ICSD or Pearson). For TiS_3, such a linear structure has been invoked in the presence of Strontium [124]. For many MS_3 materials (M=Ti, Zr, Hf, Nb, Ta), a 2D-layered structure was proposed, such as NbS_3 [125, 126]. However, for MoS_3, such a well-defined structure has never been resolved.

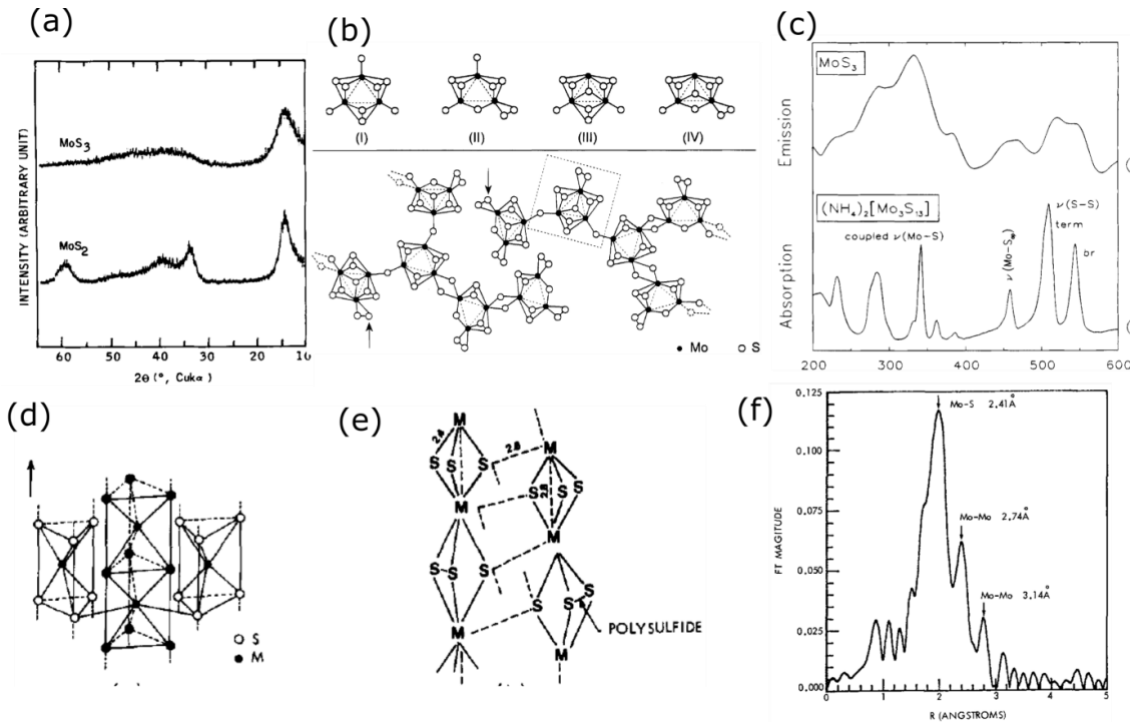

Figure 2-8: (a) XRD shows the amorphous nature of the MoS_3 phase [36]. (b) Weber's proposed triangular clusters and oligomers [40]. (c) IR spectrum and peak assignment from the reference compound $(NH_4)_2[Mo_3S_{13}]$ [40]. (d-e) Liang's chain-like model [41] (f) EXAFS spectrum, which indicates two different Mo-Mo bond lengths [41].

A combined neutron diffraction study and reverse Monte Carlo simulation method study by Hibble et al.[38] contradicted the previous studies by proposing a chain-like model of $Mo^{4+}(S^{2-})(S_2^{2-})$ with only one short Mo-Mo distance (Figure **2-9** b and c). This result was consistent with earlier XPS emission and absorption studies analyzing the nature of the covalent nature of chemical bonding in MoS_3 and concluding that Mo with the formal oxidation state of +4 was more plausible.[127]

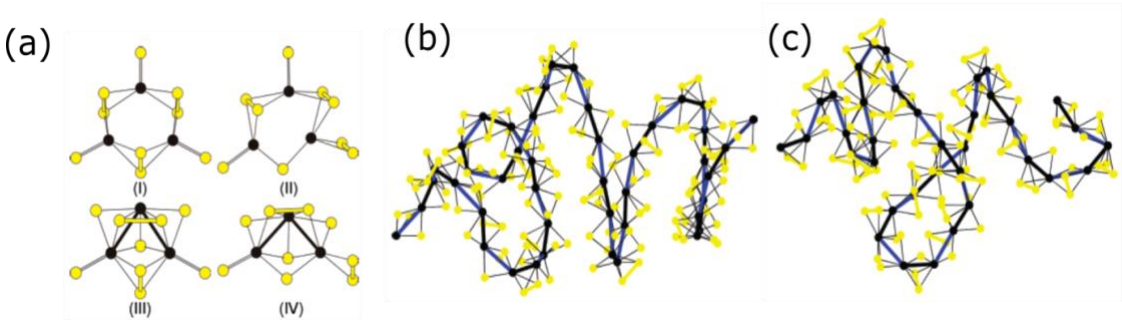

Figure 2-9: (a) Jiao's four optimized structures by DFT calculations [39] (b-c) Hibble's distorted chain-like structures by reverse Monte Carlo study based on neutron diffraction data [38].

IR and Raman investigations on *a*-MoS_3 and poorly crystalline MoS_2 provided other exciting insights into the features of the MoS_3 phase.[36] The characteristic peak at 522 cm^{-1} was assigned to S-S stretching present in MoS_3. Based on XPS and IR analyses, Weber et al. proposed a triangular model inspired by Mo_3 clusters also argued that Mo has a +4 formal oxidation state and identified the presence of various S species such as S^{2-} and S_2^{2-} ligands. By IR analysis, the prominent observed bands at 545, 520, and 470 cm^{-1} were assigned to $(S\text{-}S)_{br}$, $(S\text{-}S)_{t,}$ and $(Mo\text{-}S)_{ap}$ based on an $(NH_4^+)_2[Mo_3S_{13}^{2-}]$ reference compound (Figure **2-8** c). The interpretation of these peaks must be taken with care due to charge and over-stoichiometry of $[Mo_3S_{13}]^{2-,}$ as we will discuss in our DFT study (Figure **2-8** c and Figure **2-10** a).[40]

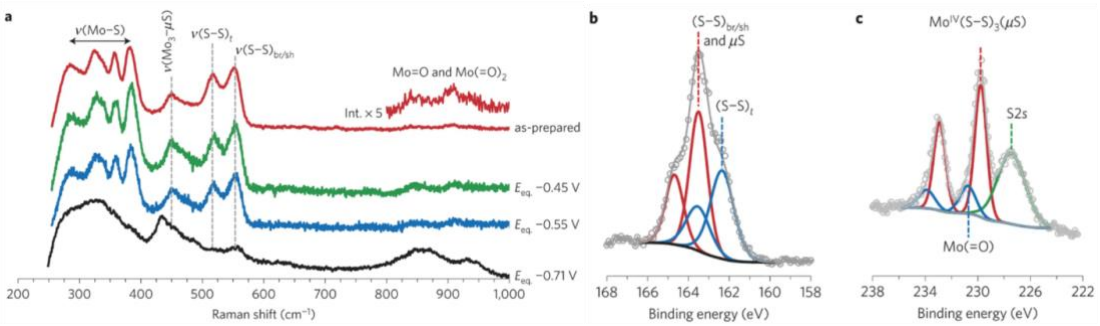

Figure 2-10: (a) Raman spectrum of *a*-MoS3 phase at different equilibrium potential (b-c) core-level XPS spectra of *a*-MoS3 [128].

Within the context of HER, Tran et al.[128] provided recently for the first time high-resolution HAADF-STEM images of the MoS_3 structures highly dispersed on carbon

materials. This analysis suggested that there would be an oligomeric arrangement of triangular Mo_3 cluster units in a one-dimensional quasi-linear or branched-chain (Figure **2-11**).[128]

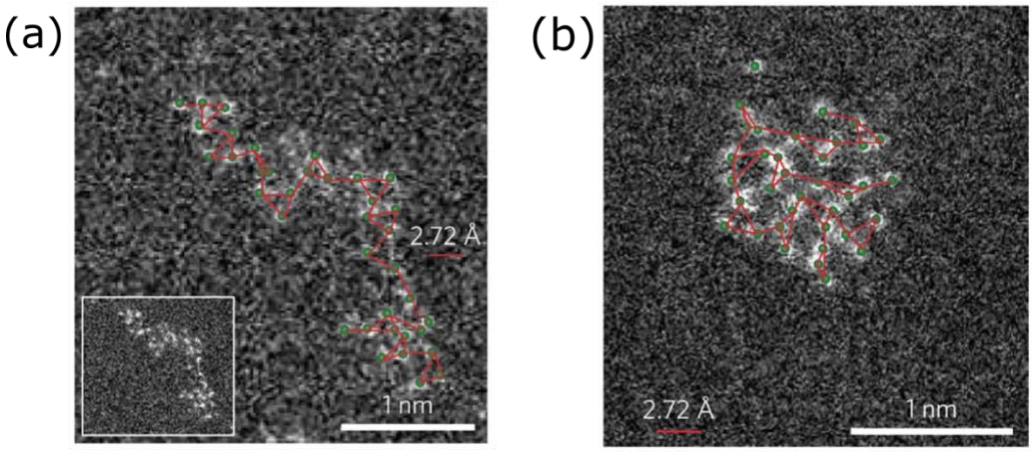

Figure 2-11: High-resolution HAADF-STEM analysis: (a-b) Triangular units [Mo3] seem to appear along with folded chain configuration [128].

Most experimental investigations which attempted to rationalize their observation refer either to the linear or triangular building blocks without clear justification. At the same time, there exist very few theoretical studies devoted to structural resolution, and most of the existing ones also assumed one type of structure. Considering quantum simulation dedicated to the MoS_3 structure, Jiao et al.[39] simulated four possible triangular Mo_3S_9 structures as empirically proposed earlier by Weber et al.[40]

It was found in particular that the most stable structures significantly reconstruct from the initial structure proposed by Weber et al., while the corresponding formal oxidation state of Mo shifts from +4 to +4.67 (Figure **2-9** a). In the lowest energy structures, short and long Mo-Mo distances are close to EXAFS data. However, due to the strong distortion of the clusters, it is difficult to compare the calculated vibrational frequencies with the experimental IR spectrum.[39] Other quantum simulations investigating the reactivity of the MoS_3 phase assumed a Mo_3 triangular model without clear justification of it.[129, 130]

A recent DFT study has explored the stability of Mo within these structures and those existing for alkaline earth trisulfides (SrS_3 and BaS_3) [131]. They found that the best compatible structure would be for the BaS_3-type (Space group: P-421 m, No.113) and SrS_3-type (Space group: B2ab, No.41) structures. Based on various electronic properties, it was concluded that MoS_3 has a metallic character compared to MoS_2 semiconductors [131]. However, due to the amorphous nature of the observed phases in the related topics of the present PhD work, it doesn't seem very easy to imagine that these crystalline phases are formed. Moreover, the nature of the S-species present in these phases (S_3 trimers) do not correspond to those observed by IR-RAMAN spectroscopies.

Within the quantum simulation context, we noticed several studies investigating the reactivity of simplified MoS_3 models for HER (hydrogen activation). Baloglou and co-workers have explored several molecular models of charged Mo_3S_X clusters ($7 \leq x \leq 13$) containing various hydrogen atoms[130]. Based on the charge, stoichiometry of hydrogen and sulfur atoms, H_yMo_3Sx clusters prefer to be in triangular or chain form. Li et al. investigate the active site for the hydrogen adsorption and desorption on Mo_3S_X triangular cluster without clarifying this choice [129].

As a consequence, there is an evident lack of accurate atomic-scale insights into the structural and spectroscopic properties of the *a*-MoS_3 phase—moreover, its further transformation into the MoS_2 phase (the genesis of the active phase).

2.2. DFT studies of alumina support and alumina supported Mo-oxides and Mo-sulfides

The support has a crucial role in the HDS process in all significant aspects of catalysis, from the preparation steps to the reacting conditions. The effect of support varies among various scales, and it may impact the activity, selectivity, and stability. Numerous experimental observations revealed the role of the support on the activity: the activity on titania-supported MoS_2 is four-fold higher than on γ–alumina supported MoS_2, or the effect of promoters (Co/Ni) on the catalytic activity is weaker on titania than on γ–alumina [66, 69]. These intriguing results have led to various hypotheses to explain the outcomes.

Several theoretical studies were carried out to understand the phenomenon at the atomistic scale, including promotors' effect [77, 101, 132, 133].

At the atomistic level, the physicochemical properties of the surface of the support sites affect the preparation and genesis of the active phase of the catalyst. The acidic-basic sites interact with the active phase and impact the active phase dispersion on the support. Alumina (Al_2O_3) exists in several structural polymorphs; many of them are metastable states of alumina [65]. These metastable states are formed during the dehydration of boehmite into α-alumina. Among them, γ-alumina is particularly interesting. In the HDS process, the most extensively used support is γ-alumina due to its impressive stability, tunable pore sizes, high surface area. It is essential to control the chemical surface state to optimize the impregnation and resulting dispersion of the active phase on the support. As we have illustrated in section 2.1.2.3, thorough extensive experimental research has been done so far to understand the atomistic nature of γ-alumina and its interaction with the active phase of the catalyst [7] at the various stages: from the preparation to the working conditions. To better rationalize this, we recalled in what follows some detailed atomistic description of the support under these conditions nowadays, which may be helpful for our work.

2.2.5. Alumina surfaces

One of the first experimental studies to understand the nature of γ-alumina was performed by Lippens and de-Boer by XRD, and the structure of γ-alumina was proposed to be a defective spinel[134]. Later, many experimental studies were carried out, such as vibrational spectroscopy, X-ray diffraction, and transition electron microscopy. However, the scarcity of atomistic description leads to ambiguous interpretation of γ-alumina bulk and surface. Moreover, theoretical studies have not observed any evidence supporting the spinel or defective spinel structure proposed earlier in the literature[135, 136]. In particular, Krokidis et al. simulated a step-by-step mechanism of the formation of γ-alumina from its boehmite precursor (Figure **2-12**). This process involves four essential steps: hydrogen transfer followed by water extraction, boehmite structural collapse, and finally aluminum diffusion from octahedral to the tetrahedral position leading to a non-defective spinel bulk model of γ-alumina still open to discussion nowadays [137]. 25-30% aluminum is usually present at tetrahedral sites in γ-alumina model, some of which occupy non-spinal sites. A broad range of properties and parameters has been in

reasonably good agreement with experimental ones or this model, such as cell volume, bulk modulus, percentage of migrated Al atoms from octahedral to tetrahedral position, and simulated XRD pattern. This particular work was the foundation for developing the first surface models [14, 15] or, more recently to edge models of alumina [138].

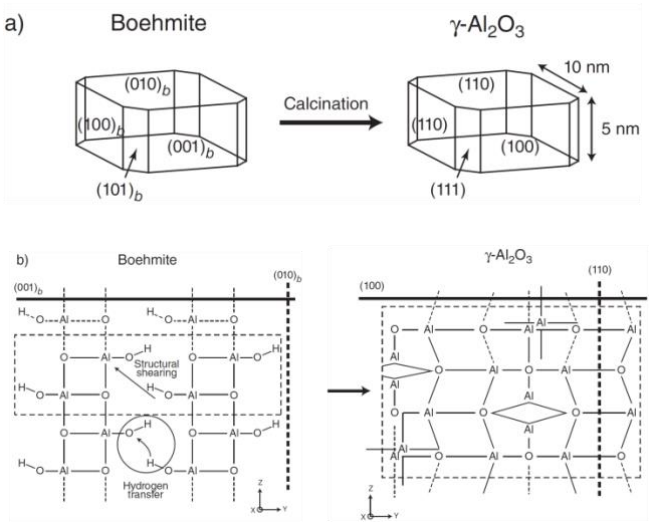

Figure 2-12: a) Topotactic transformation from boehmite to γ-alumina nano-crystallites. b) Atomistic scale bulk structure of boehmite and γ-alumina.[7]

An ideal way to prepare the γ-alumina is from aluminum salts precipitated in an aqueous solution, inducing boehmite formation. Further calcination of boehmite powder about 700K results into γ-alumina. Furthermore, the morphology of nanocrystals of γ-alumina will be dependent on the synthesis protocol. If the topotactic transformation of boehmite to γ-alumina is followed (Figure **2-12**), the γ-alumina morphology can be deduced from boehmite directly[139]. Rhombohedral [140] is the most common existing morphology for boehmite in addition to diamond, hexagonal or ellipsoid shapes [141]. Furthermore, in the case of rhombohedral (010) basal surface is the most predominant one. So as per topotactic transformation, the alumina surface would remain predominant in γ-alumina also. However, according to pseudomorphism rules, (010) and (100) surfaces in boehmite would give rise to the same surface in γ-alumina named as (110). It was theoretically predicted and supported by some experimental evidence such as neutron diffraction analysis and electron microscopy that in γ-alumina (110) surface is predominant with ~74% of total surface area. However, (100) and (111) surfaces may contribute ~16% and ~10% to the entire surface area, respectively[139].

Following the work of Krokidis et al. for γ-alumina bulk model, Digne et al. have constructed the (100), (110), and (111) surface models of γ-alumina by cleavage and relaxation[14, 15]. Digne also considers the effect of temperature on hydroxyl groups present on the surfaces. On (100) surface, unsaturated octahedral Alv and tetrahedral Al_{IV} ions are present. However, (110) surface shows Al_{IV} comes from either unsaturated octahedral or tetrahedral inherited from the bulk, and Al_{III} unsaturated tetrahedral resulting in higher surface energy for (110) than (100) Figure **2-13**.

As the degree of hydration increases, the adsorption energy difference decreases slightly for the (100) surface; however, the change in water adsorption energy difference is enormous in the (110) surface due to the more assertive Lewis acidity of Al_{III} ions. According to thermodynamic stability, (100) becomes completely dehydrated above 600K, whereas some hydroxyl groups remain stable at high temperatures on the (110) surface. Moreover, it was also shown that the sulfidation of the alumina (110) surface occurs only in specific conditions, while the (100) surface is not sulfided (no surface O/S exchange) [132]. This information is essential for our work, where we will investigate the sulfidation process of Mo-oxides supported on the (100) surface of alumina.

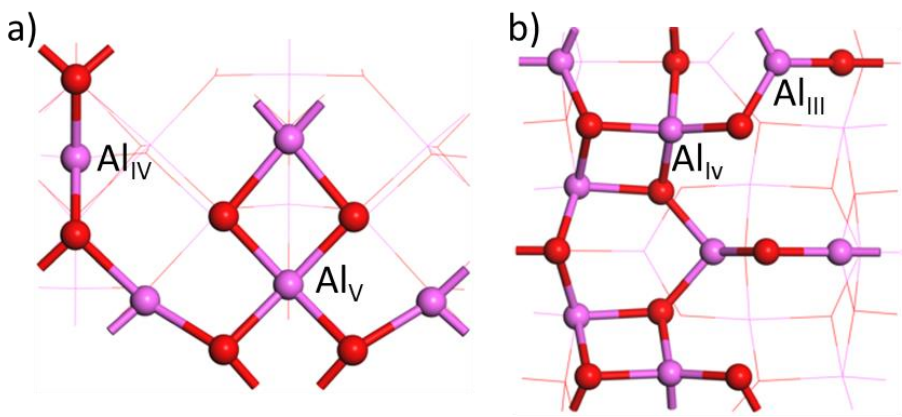

Figure 2-13: Clean dehydrated surfaces of γ-alumina. a) (100) surface exhibits octahedral Al_V and tetrahedral Al_{IV}, b) (110) surface shows Al_{IV} along with Al_{III}.

Earlier experimental studies suggest that the IR spectrum at higher frequencies (above 3000 cm^{-1}) contains about seven OH bands. Several proposals have been made in the

literature to explain the nature of the hydroxyl groups. The first proposition was made by Tsyganenko et al., who claimed five prominent OH peaks such as tripled bridge OH (3700 cm^{-1}), bridged OH (3740 cm^{-1}), OH linked to Al_V (3730 cm^{-1}), terminal OH (3790 cm^{-1}), and OH related to Al_{III} (3800-3770 cm^{-1})[142]. The second proposal made by Knozinger and Ratnasamy considered the different crystal planes effect and indicates morphology dependence of OH bands[143]. Later, Busca proposed explaining the multiplicity of OH bands, that it is essential to understand cation vacancies present on the surface (Figure **2-14**)[144]. The degree of aluminum crystallinity has also been proposed as one factor that can influence the OH band.

Digne et al. performed the DFT calculation and calculated the vibrational frequencies of OH groups for various hydroxyl coverage on the surface[14, 15]. Different OH bands have surface orientation dependence according to DFT calculations, indicating the IR peaks to be sensitive towards morphology as Knozinger and Ratnasamy proposed. However, they somehow revisited each band's previous assignment according to the coordination number of OH groups and Al sites. Furthermore, vacancy is not required to explain the spectra. μ_1-OH has three different peaks related to Al_{IV}(100), Al_{VI} (100), and Al_V(110). μ_3-OH has the lowest frequency, followed by μ_2-OH and μ_1-OH, aligning with the Busca study(Figure **2-14**)[144].

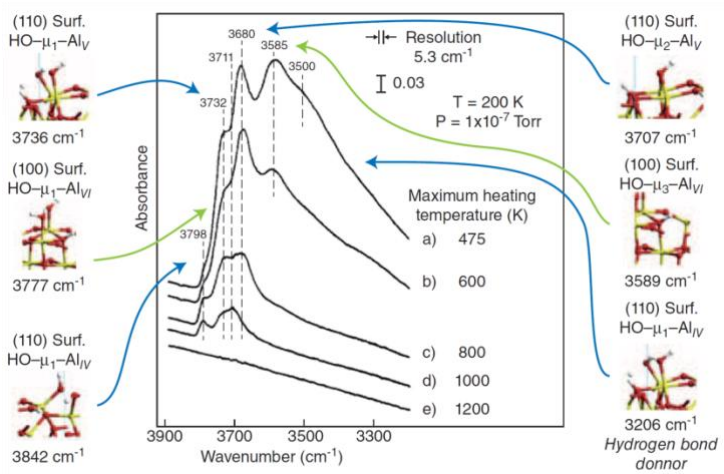

Figure 2-14: OH stretching frequencies calculated by DFT [14, 15] and compared with experimental [145] frequencies.[7, 14, 15] (figure taken from ref. [7])

At this stage, it is essential to underline that this knowledge of the nature of surface hydroxyls may become crucial for a better understanding of its interaction with the active phase precursors or with the activated phase, as underlined in the previous sections.

2.2.6. Description of Mo-oxide on the support

As it is proposed in the literature for various catalytic applications (not only HDS), molybdenum oxides can be found in a highly dispersed form on various oxide surfaces and could even exist as isolated MoO_x species [16, 100, 146, 147]. With the help of different experimental techniques such as Raman, IR, and EXAFS, it is speculated that molybdenum centers may exist as tetrahedral or square pyramidal coordination on alumina along with mono-oxo or di-oxo under dry conditions [100, 148–152]. DFT investigations have been undertaken to understand the interactions between various Mo/W-oxide forms supported by Al_2O_3 [17, 153], TiO_2 [154–157], and SiO_2[158]. Some of them have studied on larger polyoxometalates on a support such as Mo_8S_{26} [156], while others have focused on tiny entities of Mo-oxides as small as monomer and dimers supported on alumina [17, 153] and titania [154, 155]. As our study concerns Mo-oxides on alumina, we will concentrate mainly on those studies in more detail.

Several plausible mono-oxo and di-oxo Mo centers for MoO_3 and Mo_2O_6 species have been studied on γ-alumina (100) and (110) surfaces using DFT [17, 153]. Monomers were observed to be more stable than dimers on the (110) surface; however, a reverse effect was witnessed on the (100) surface. This indicated the presence of monomeric species on the surface even at high Mo loading and was later verified by Raman spectroscopy[159]. For monomers, di-oxo Mo-center is more stable on (100) surface but mono-oxo Mo-center on (110). However, mono-oxo Mo-centers were observed to be more stable on (110) surface than monomers. But, one of the molybdenum centers is di-oxo, and another one is mono-oxo for the most stable dimer on (100) surface.

Recently, multilayers of α-MoO_3 on two different γ-alumina models have also been considered using DFT. Monolayers of MoO_3 were more stable than the bilayers on γ-alumina. Interfacial interaction takes place through charge transfer from the surface of γ-alumina to α-MoO_3. γ-alumina supported MoO_3 was observed to be more active than

isolated MoO_3, especially on (100) surface, among others[160]. A recent theoretical study, accompanied by experiments, shows that doubly charged polyoxomolybdates can transform from chain to ring and, finally, compact structures as a function of size (Figure **2-15**) [161]. Inspired by these studies, we will also consider a few of these structures as oxide precursors on γ-alumina and their sulfidation under HDS conditions.

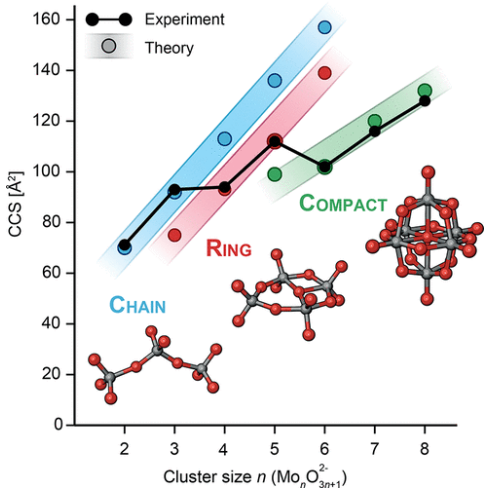

Figure 2-15: Evolution of polyoxomolybdates as a function of size.[161]

2.2.7. Sulfidation of Mo-oxide

Almost no DFT study has been undertaken to apprehend the sulfidation process of Mo-oxide on supported alumina. Only a few DFT studies have attempted to rationalize the sulfidation thermodynamics in bulk MoO_3 [162] and in monolayer or large clusters of bulk MoO_3 [163–165]. In general, it was observed that creating a vacancy and replacing the oxygen with sulfur on the terminal oxo-site (Mo=O) is slightly more favorable and exothermic in nature in contrast with bridging (twofold) or tridentate oxygen sites where the O/S exchange is highly endothermic. Moreover, O-vacancy creation increases the reactivity of sulfiding agents (H_2S or S_2), which means that the use of hydrogen would enhance the sulfidation rate. As more terminal oxygens are being replaced by sulfur, they can form S-dimer. The formation of these S_2-dimer leads to ~0.5 eV additional stabilization from its monomer's counterpart [164].

Alternatively, a danish DFT study investigated the thermochemistry of sulfur-oxygen exchange at the edges of the MoS_2 nano-crystallite [54] to identify the possible residual Mo-O chemical bonds after sulfidation. It was suggested that the S-edge is the most difficult to sulfide and maybe the location of residual oxidized Mo sites.

Interestingly, one experimental study proposed kinetic modeling of the sulfidation process of MoO_3 supported on alumina [166]. The kinetic model analyzes the two-step process: sulfidation of MoO_3 and growth of MoS_2 phase, for which it evaluates the respective apparent activation energies of 23 kJ/mol and 43 kJ/mol.

To the best of our knowledge, only one DFT study reported thermodynamic trends in thiolysis energies of Mo oxide precursors as a function of various supports described by molecular clusters [167]. The authors proposed a correlation between thiolysis energy descriptor and sulfidation degree and/or dispersion. However, we may ask to which extent the small size clusters represent the support and how the kinetic effect may impact these results.

As a consequence, almost no DFT study has been undertaken combining the thermodynamic and kinetic effect of support on the sulfo-reductive mechanisms of Mo-oxide species. Therefore, it is essential to understand the sulfidation process at the molecular level and the evolution of oxide precursors under a sulfiding environment.

2.2.8. Alumina supported MoS_2

Addressing the reactions of the "genesis" of the MoS_2 based active phase remains far more challenging primarily for two reasons: the first one is due to the complexity of the supported system itself, and the second one is the complexity of the molecular mechanisms involved during the sulforeduction process.

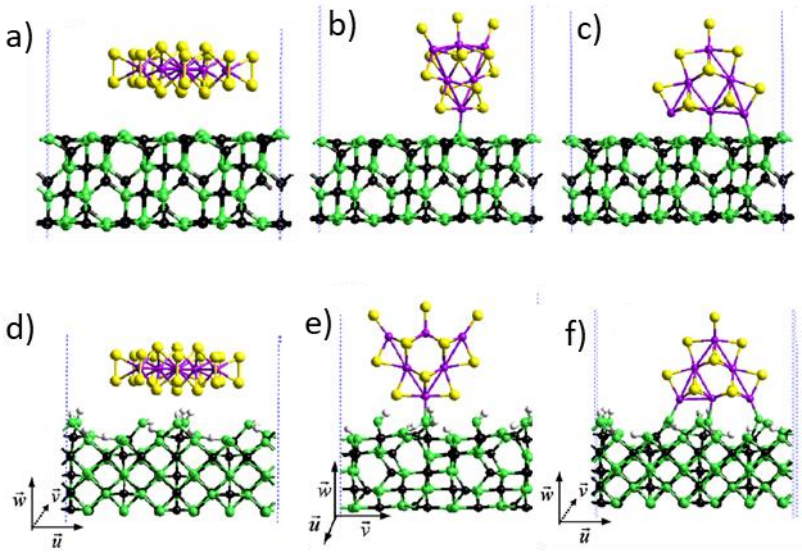

Figure 2-16 : Various Mo_6S_n clusters on a) (100) and b) (110) surface of g-alumina interacting through van-der-Waals interactions or Mo-O-Al linkage (image taken from ref. [77])

To reveal the interaction between MoS_2 and support (γ-alumina/TiO_2), Arrouvel C et al. performed various DFT calculations of Mo_6S_n clusters on γ-alumina and TiO_2 [77]. Triangular Mo_6S_n clusters were considered as relevant models for active phase, truncated either as Mo-edge or S edge; these edges could interact with the alumina surfaces or act as an active site of catalyst (Figure **2-16**). Authors have performed a systematic study by changing the number of sulfur atoms (n) as a function of the chemical potential of sulfur according to conditions of HDS process conditions such as T, $p_{H2,}$ and p_{H2S}. The different behavior of Mo_6S_n was observed for γ–alumina and TiO_2 for distinct surfaces.

At a highly reducing environment, the Mo_6S_{24} cluster is more stable at horizontal (aligned to the surface) orientation than the vertical orientations on γ-alumina support with both the surface (100) and (110). The stability factor is mild electrostatic interaction of S-species with γ-alumina. Moreover, OH frequency shift is firm evidence of the interaction of hydroxyl groups present on the surface with S of the cluster [168]. However, a change in orientation was observed for the lower reducing environment due to strong interaction via the Mo-O-Al bond at the corner of the cluster. In contrast to γ–alumina, on TiO_2, Mo_6S_n ($10 \leq n \leq 14$) cluster are stabilized for $\Delta\mu_s$ below -0.21 eV, and an epitaxial relationship were observed (101) surface of TiO_2 due to multiple Mo-O-Ti and Mo-S-Ti bond formation. Due to four-membered ring formation, the Mo_6S_{14} cluster was tilted at 52° from the surface plane. On (001) surface of TiO_2, there are two different types of 4 membered ring formed

Mo-S-Ti-S-Mo and Mo-O-Ti-O-Mo, which affect the orientation of Mo_6S_{14} cluster with respect to the TiO_2 (001) and (101) surfaces.

Effect of promotors has also been investigated using DFT by Costa D et al. [101] for CoMoS nanocluster on γ-alumina. The weakening of edge interactions was observed through Co promotion. The smaller particle size of MoS_2 was observed in the case of Co promotion compared to the non-promoted case due to weaker adhesion energy and ligand effect of promotor on γ-alumina. The reason behind different HDS activity was indicated to be a lower S-edge/Mo-edge ratio on TiO_2 than γ-alumina. Moreover, the promotion effect weakens the interaction between the active phase (MoS_2) and support.

Although this work did not investigate the sulfidation mechanism, it is an example that illustrates how the chemical interaction with the support may impact the stability and orientation of MoS_2 layers. This residual chemical interaction through Mo-O-Al bonds may result from the sulfo-reductive activation process. Thus, one of the critical questions is understanding better how the sulfidation process transforms Mo-oxides to Mo-disulfides on support like alumina.

2.3. Conclusions and strategy of the thesis

As we have underlined in this chapter, there exists a very diverse range of applications for MoS_3 – MoS_2 based nanomaterials. These are widely used in HDS catalyst and have been suspected of offering new applications as HER catalysis, cathode material for batteries, solid lubricant, mercury capture, and many others. Despite these various applications and the intense research on MoS_3, the atomistic scale understanding of the MoS_3 phase remains still uncertain. The rational knowledge of Mo-oxides to Mo-sulfides reduction, precise nature of oxide precursors, and involved intermediate species remains insufficient.

To the best of our knowledge, no theoretical study based on density functional theory (DFT) investigated the sulfo-reduction mechanisms of Mo-oxides on supported alumina with a consistent comparison between oxysulfide and trisulfide pathways for the sulfo-reduction as invoked in the experimental literature. A clearer atomistic scale description

is also needed to elucidate the anchoring sites of alumina for oxide precursors and how they may influence the sulfidation steps. Additionally, the structure (chain vs. triangular) and stability of the amorphous MoS_3 phase remain to be highlighted to reveal the sites of MoS_3 as a catalyst for the diversified appliance.

We believe that this DFT study will give more refined insights into the mechanistic insights about the sulfidation process and the nature of crucial intermediate such as the MoS_3 phase and provide some comprehension about morphology and its evolution as a function of size. Furthermore, it will serve as a companionway to improve the control of the activation step, in particular by identifying the O-sites which are the most reluctant to sulfidation from a thermodynamic or kinetic aspect is mandatory.

The first part of the research project reported in Chapter 4, which is the core of the thesis, will investigate the effect of the alumina support on the various possible sulfo-reduction mechanisms oxides clusters for the small size, such as monomer, dimer, and trimer. Since the large size Mo-oxide cluster would be difficult to simulate at a DFT level due to expensive computational simulation time. A precise description of these small entities containing relevant O-sites to be sulfided would enable us to rationalize the behavior of bigger-size Mo-oxide precursors appropriately. Moreover, it has been shown that such depolymerized Mo-oxides could be involved in the liquid sulfidation process. Starting from such molecular oxide precursors, their thermodynamic stability (and structures) on (100) γ-alumina surfaces will be calculated, which can be correlated with available EXAFS and spectroscopic data. After that, we will probe the lability of oxygen sites for sulfur/oxygen replacement, transformation into oxy-sulfides, and their thermodynamic trends. The role of alumina anchoring sites will also be examined as it has been invoked in the literature.

The sulfidation likelihood will be complemented by a systematic kinetic investigation of these O/S exchanges. Further conversion of oxy-sulfides to MoS_3 or direct transformation to MoS_2-active phase by the sulfo-reductive process will also be explored along with MoS_3 to MoS_2 transformation. It will be interesting to examine how these intermediate steps will appear on a thermodynamic scale because MoS_3 coexists as competing steps with

other oxy-sulfide intermediates. The effect of temperature would also be considered to mimic the conditions of the experiment.

The critical question about the growth of the sulfided phase, whether it starts at the trisulfide phase or subsequent to disulfide phase formation, would depend on the transformation-kinetics of the trisulfide phase to disulfide phase. To answer this question, the effect of size and diffusion of these species on support must be contemplated. We will also propose some aspects of these questions in this study, such as interaction energy and size effect on small entities.

The second part of the research project reported in Chapter 5 will deal with the investigation of non-supported structures of the MoS_3 phase and its growth which may be considered to a continuity of the previous part. Therefore, we have neglected the effect of support on the growing part of the MoS_3 phase to see if it can be considered as a precursor of the targeted MoS_2 phase. We will thus simulate various plausible structures for MoS_3 clusters and increase their degree of complexities. We will take advantage of already proposed structures for the MoS_3 phase and endeavor the other possibilities based on chemical intuitions. After finding the most prominent structures for the respective size, we will directly compare triangular and chain-like models. Structural analysis will be compared with EXAFS, and the IR spectrum of relevant polymorphs will be compared with available experimental IR of the bulk-MoS_3 phase. The thermodynamic stability will reveal the most stable structures among all the explored ones without support.

Additionally, we will probe the critical spectroscopic descriptors on the phase and calculate the IR spectrum, moreover, its comparison with the experimental IR spectrum. This will provide insights into the effect of size on spectroscopic descriptors. We also revisit the experimental IR peak assignment. To explore the large potential energy surface, Ab Initio Molecular Dynamics will also be performed. Finally, we will propose some mechanistic pathways to transform one cluster into another.

Overall, we hope that this thesis will enable the reader to push further his current understanding of the genesis of one relevant catalytic active phase supported on alumina

through quantum simulation approaches. Since quantum simulation will be the fundamental technique used in the present research work, we present in Chapter 3 the fundamental aspects of the computational methods used….

Chapter 3: Methods and computational details

Density functional theory (DFT) is an eminent tool to rationalize the ground state electronic structure properties. DFT is extensively used across chemistry, material science, and condensed matter physics. Its popularity is based on its practical utility, such as affordable cost and sufficient accuracy. This chapter discusses some underlying theory of DFT and its practical implications, DF perturbation theory for calculating the infrared spectra, and nudged elastic band calculation for determining the transition state that we have applied in this PhD investigation.

3.1. Density Functional Theory

The condensed matter cohesion, such as a catalyst, results from the electrostatic interaction between all its constitutive electrons and nuclei. These interactions are described by the Hamiltonian operator[1] (H), which corresponds to total energy, the sum of kinetic and potential energies. To understand the material's fundamental level, we need to solve the many-body Schrödinger equation, which describes the quantum mechanical system. Time independent stationary state Schrödinger equation of a multi-electron and nuclei system:

$$\boldsymbol{H_{tot}\Psi_{tot}(r,R) = E_{tot}\Psi_{tot}(r,R)} \qquad \textbf{3-1}$$

Where, H_{tot} is the Hamiltonian operator of the system, $\Psi_{tot}(r,R)$ is the total stationary state wave function of the system dependent on the positions of electrons (r) and nuclei (R). $\Psi_{tot}(r,R)$ contains all the information about that particular state of the system. E_{tot} is the total energy of the system. Hamiltonian of a system can be written as a summation of all the kinetic energies and potential energies:

[1] Operator is a function of physical state which operates on a function and transform it to another function.
For example: operator $\hat{O}$ operate on a function $f(x)$ and transform it into $g(x)$. Such as $\hat{O}\,f(x) = g(x)$ and if $g(x) = cf(x)$, here c is called as eigenvalue of the operator $\hat{O}$ and $f(x)$ is the eigenfunction. And every observable quantities in quantum world, are expressed as expectation value of some operators.

$$\boldsymbol{H_{tot} = T_n + T_e + V_{nn} + V_{ee} + V_{ne}} \qquad \textbf{3-2}$$

Here, T_n is the kinetic energy of all the nuclei, T_e the kinetic energy of all the electrons, V_{nn} The Coulomb interaction energy between nuclei-nuclei, $V_{ee}$the interaction energy between electron-electron, and V_{ne} is the interaction energy between electrons and nuclei. Therefore, $T_n = \sum_A -\frac{\hbar^2}{2M_A}\nabla^2_{\boldsymbol{R}_A}$, $T_e = \sum_i -\frac{\hbar^2}{2m_i}\nabla_{\boldsymbol{r}_i}^2$, $V_{nn} = \frac{1}{2}\frac{1}{4\pi\epsilon_o}\sum_{A\neq B}\frac{+e^2 Z_A Z_B}{|\boldsymbol{R}_A - \boldsymbol{R}_B|}$, $V_{ee} = \frac{1}{2}\frac{1}{4\pi\epsilon_o}\sum_{i\neq j}\frac{-e^2}{|\boldsymbol{r}_i - \boldsymbol{r}_j|}$, and $V_{ne} = \frac{1}{4\pi\epsilon_o}\sum_{i,A}\frac{-e^2 Z_A}{|\boldsymbol{r}_i - \boldsymbol{R}_A|}$. [169, 170]

Where m_i and r_i: mass and position of ith electron of the system and M_A and R_A: mass and position of Ath nuclei of the system.

If we could solve this equation exactly, we could explain every property of the material which can ever be known about that material. However, this equation cannot be solved precisely for more than one electron system[169]. DFT is an alternative method to solve the many-body Schrödinger equation at reasonable computational cost and convenient accuracy[170]. Our goal is thus to solve equation **3-1** and $\boldsymbol{H_{tot}}$ is expressed in equation **3-2**. Adiabatic and Born-Oppenheimer approximation (BOA) are the approximation to solve the equation(**3-1**). BOA discard the movement of nuclei due to high mass ratio between nuclei and electron. Hereafter, nuclei are considered as fixed-point charge and point mass. After applying the BOA, we only need to solve the electronic part of the Hamiltonian that has parametric dependence on the position of the nuclei[171].

From equation **3-2**, T_n and V_{nn} would behave as a constant potential for H_{tot} due to their dependence on nuclei position. The electronic part of the Hamiltonian is $H_e = T_e + V_{ne} + V_{ee}$ need to be solved for static nuclei.

$$\boldsymbol{H_{ele}\Psi_{ele}(r;R) = E_{ele}\Psi_{ele}(r;R)} \qquad \textbf{3-3}$$

Eigenvalues obtained from equation **3-3** would serve as a potential for the Schrödinger equation for a particular position of nuclei and can be solved if we know the solution of the electronic part of the Schrödinger equation. Despite assuming nuclei as static, the electronic part of the Schrödinger equation still cannot be solved due to non-local term like electron-electron repulsive interaction (V_{ee}). Hohenberg and Kohn came up with two

theorems, which transform the equation from the position as a fundamental variable to the density as a fundamental variable without losing any information about the system. This reduces the dimensionality of the many-body Schrödinger equation from 3N (positions) to 3 (density) [170].

3.1.1. Hohenberg and Kohn theorems

Theorem 1: *For any system of interacting particles in an external potential $V_{ext}(r)$, the density is uniquely determined (in other words, the external potential is a unique functional[2] of the density and vice versa).*[172]

This theorem says that there cannot be two different external potentials that give rise to the same ground-state density. So, total energy can be written in terms of ground-state electron density ρ_0 as follows:

$$\boldsymbol{E_0[\rho_0] = T[\rho_0] + E_{ee}[\rho_0] + E_{ext}[\rho_0]} \qquad \textbf{3-4}$$

Where $E_{ext}[\rho_0]$ is coming from external potential $E_{ext}[\rho_0] = \int \rho(r) V_{ext}\, dr$.

Here in equation **3-4**, the first term is system dependent, and the second one is universally valid (independent of V_{ext}), which is known as *Hohenberg-Kohn functional* $F_{HK}[\rho_0]$. If we know the form of F_{HK} functional, we can get the ground state energy. This F_{HK}, also known as universal functional, is entirely independent of the system taken into account. However, the explicit form of the two terms, i.e., $T[\rho_0]$ and $E_{ee}[\rho_0]$ is not known. $E_{ee}[\rho_0]$ could be written as electron-electron interaction and non-classical interaction corrections:

$$\boldsymbol{E_{ee}[\rho\ \ ] = \int\int \left(\frac{\rho(r_1)\rho(r_2)}{r_{12}}\right) dr_1 dr_2 + E_{ncl}[\rho]} \qquad \textbf{3-5}$$

where $\rho(r) = \langle \Psi_0 | \rho | \Psi_0 \rangle = \int \Pi_{i=1}^{N} dr_i |\Psi_0(r_1 r_2 r_3 \dots r_N)|^2$ *and* $N = \int \rho(r) dr$.

[2] A function maps numbers onto (real or complex) numbers, $f: \mathbb{R} \to \mathbb{R}: x \mapsto f(x)$, and Functional usually referred as "function of a function" which means A functional maps functions onto (real or complex) numbers $F: \mathcal{F} \to \mathbb{C}: f \mapsto \mathcal{F}[f]$.

The first term in equation **3-5** also includes the spurious interaction of the electrons with itself. An additional self-interaction correction term included in $E_{ncl}[\rho]$ to correct the self-interaction error. This non-classical term of electron-electron interaction ($E_{ncl}[\rho]$) also contains exchange-correlation due to the fact that electrons are indistinguishable particles, so their exchange energy would also need to be considered. However, the explicit form of this ($E_{ncl}[\rho]$) functional is not known. Only the ground state density contains the information about positions and charges of the nuclei, allowing the mapping from density to an external potential.

Theorem 2: *A universal functional for the energy* $\boldsymbol{E}\ [\boldsymbol{\rho}(\boldsymbol{r})]$ *can be defined in terms of density. The exact ground state is the global minimum value of this functional*.[172]

The ground state energy can be obtained variationally: the density that minimizes the total energy is the ground state energy. The corresponding density would be the exact ground-state density.

$$\boldsymbol{E_0[\rho_0] \leq E[\rho] = T[\rho] + E_{ext}[\rho] + E_{ee}[\rho] = \min_{\Psi\to\rho_0} \langle \Psi | \hat{H} | \Psi \rangle} \qquad \textbf{3-6}$$

Any trial density $\rho(r)$ defines its Hamiltonian H and its own wave function Ψ and this wave function can now be taken as a trial wave function for the Hamiltonian generated from true external potential V_{ext}. *Hohenberg-Kohn* framework illustrated that the ground state wavefunction itself could determine the Hamiltonian.

3.1.2. Kohn-Sham DFT

Even after reformulating the problem from wavefunction to density that reduces the 3N dimensional equation to 3 dimensions, it still remains unsolvable. One year after Hohenberg and Kohn's paper, Kohn and Sham suggested a practical way to compute the Hohenberg-Kohn functional ($F_{HK} = T[\rho_0] + E_{ee}[\rho_0]$). They mapped the system of interacting electrons onto a fictitious scenario of non-interacting ones, however having the exact same electron density. This provides a set of independent particle equations which are practically possible to solve numerically.

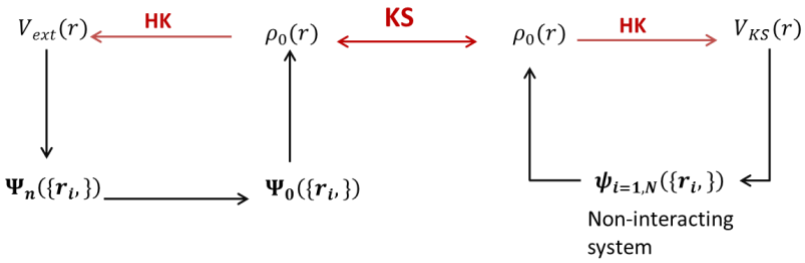

Figure 3-1: Kohn-Sham (KS) mapping of interacting electrons to fictitious non-interacting one with same ground state electron-density [173].

Earlier, solving the Schrödinger equation by wavefunction methods, Hartree also proposed independent particle approximation. The wavefunction of the multi-electron system is described as a product of all single electron wavefunction, also known as the Hartree product. However, this approximation fails to take into account the antisymmetric principle[3]. The wavefunction can be represented as the antisymmetrized product of wavefunction to solve this issue. The antisymmetrized product of the wavefunctions is also known as the Slater determinant. For the N electron system, the wave function could be written as:

$$\boldsymbol{\Psi} = \frac{\mathbf{1}}{\sqrt{\boldsymbol{N}!}} \begin{vmatrix} \chi_1(x_1) & \cdots & \chi_N(x_1) \\ \vdots & \ddots & \vdots \\ \chi_1(x_N) & \cdots & \chi_N(x_N) \end{vmatrix} \qquad \textbf{3-7}$$

Where, $\chi_i(x_i)$ is single electron wavefunction including spin coordinates and $\sqrt{N!}$ is a normalization factor.

The assumption, an electron moves independently of other electrons except that the moving electron will feel an average Coulomb potential due to the presence of all other electrons made by Kohn-Sham, is equivalent to the Slater determinant.

[3] Antisymmetric principle: The wavefunction which describe the system should be antisymmetric with respect to the interchange of coordinates for a pair of electrons. This is a corollary of the "Pauli exclusion principle".

In HK formulation, the problem was the unknown precise expression of kinetic energy and potential energy in the form of density addressed by KS [169, 174]. By using the fictitious kinetic energy and actual density, the total energy expression of the interacting system can be transformed as:

$$\boldsymbol{E_{KS_{DFT}} = T'[\rho(r)] + E_{eN}[\rho(r)] + J[\rho(r)] + E_{XC}[\rho(r)]} \qquad \textbf{3-8}$$

Where T' $[\rho(r)]$ is the kinetic energy of a non-interacting system with the density of $\rho(r)$, $E_{eN}[\rho(r)]$ is potential energy from nuclei and $J[\rho(r)]$ is the classical Coulomb interaction term. The last one is the exchange-correlation term which contains the non-classical electrostatic interaction energy that arises from the antisymmetry of the many-body wavefunction (known as exchange-correlation) and the difference between kinetic energy of the interacting (real) and non-interacting (fictitious) system. The last term is a small fraction of total energy, so it can be approximated, though it also has to be a functional of density. Now, to find the ground state density $\rho_0(r)$ for the non-interacting system, we simply solve the single electronic Hamiltonian, also known as Kohn-Sham equations.

$$\boldsymbol{\left[-\frac{1}{2}\nabla^2 + V_{KS}(r)\right]\psi_i(r) = \epsilon_i\psi_i(r)} \qquad \textbf{3-9}$$

For N single-particle state $\psi_i(r)$ represented by Slater determinant of constituent basis sets with the energy ϵ_i and V_{KS} Kohn-Sham potential depends on density $\rho(r)$ that means it is necessary to solve these equations self-consistently, which is initiated by choosing an initial density $\rho(r)$ thereby constructing the Kohn-Sham equation after solving these equations again and later calculating the resultant density. Then a new Kohn-Sham equation is built and so on until the density does not change appreciably anymore. The energy of the non-interacting system could be written as:

$$\boldsymbol{\Sigma_{i=1}^{N}\epsilon_i = T'\ [\rho(r)] + \int dr\rho(r)V_{KS}(r)} \qquad \textbf{3-10}$$

So, the total energy of the interacting system $E_{KS_{DFT}}$ can be written in terms of eigenvalues of KS equations as:

$$\boldsymbol{E_{KS_{DFT}} = \Sigma_{i=0}^{N} \epsilon_i - \int dr\rho(r)V_{ext}(r) - J[\rho(r)] + E_{xc}[\rho]} \qquad \textbf{3-11}$$

Hereafter, the problem reduces to determine or approximate the $E_{xc}[\rho]$ term. If $E_{xc}[\rho]$ is approximated well enough we can calculate total energies, forces, and electronic structures, etc.

3.1.3. Exchange-Correlation functional

KS-DFT can be called an independent particle theory (in a practical aspect), and it is astonishingly simple. Yet, it provides an exact density and energy (at least in principle) of any interacting system. However, the crucial question is how well the exchange-correlation functional and derivative of it is defined. The functional exists, but its explicit form is not yet known. It is one of the most complicated challenges in the field of development of DFT currently. KS proposed a simple approximation for the exchange-correlation energy, which works reasonably well, and is called the local density approximation (LDA). The LDA approximates the XC functional at any position r as the XC energy per electron in a uniform homogeneous electron gas of density $\rho(r)$[169, 171]. The LDA expression for $E_{xc}[\rho]$ is:

$$\boldsymbol{E_{xc}[\rho] = \int dr\epsilon_{xc}[\rho(r)]\rho(r)} \qquad \textbf{3-12}$$

Where $\epsilon_{xc}[\rho(r)]$ is the exchange-correlation energy of homogeneous electron gas of density $\rho(r)$. LDA works quite well but tends to overestimate the cohesive energies, bond strength and highly underestimate the energy gaps in insulators and semiconductors.

In order to improve exchange-correlation functional various attempt have been made, such as decoupling the exchange and correlation part as the exchange part is dominant in E_{xc}. Therefore, it is crucial to formulate E_x more accurately than E_c. In a similar spirit, one

more attempt was the GGA approximation. GGA uses the information about the density $\rho(r)$ at a particular point r including the information about the gradient of charge density $\rho(r)$ in order to take into account the non-homogeneity of the actual electron density. The exchange-correlation energy can be represented in the following form:

$$\boldsymbol{E_{xc}^{GGA}[\rho\ \ ] = \int f(\rho\ \ ,\nabla_{\rho}\ \ )dr} \qquad \textbf{3-13}$$

∇_{ρ} is the gradient of the electron density. This simple improvement brings down the tendency of overestimation significantly, which was the case in LDA. However, GGA still slightly overestimates the bond strength and cohesive energies.

Apart from GGA, various other functional types have been formulated in the literature, such as meta-GGA, hybrid non-local, and virtual orbital dependent functionals. Meta–GGA is the extension of the GGA concept: besides considering the local density and its gradient, meta-GGA also incorporates the dependence on local kinetic energy density or Laplacian of electron density. Hybrid functionals are the mixture of local DFT (Kohn-Sham) exchange and non-local Hartree-Fock exchange in some specific proportions. Hybrid functionals usually predict more accurate geometries, total energies, and band-gaps than meta-GGA, GGA, and LDA[175] as it lowers the orverbinding of bonded interactions. However, hybrids are significantly expensive compared to GGA or Meta-GGA. They are technically challenging to apply on periodic systems, so the functional choice depends on the requirement according to the system.

In the present PhD work, we used the Perdew-Burke-Ernzerhof (PBE) [176] functional, which belongs to the GGA family representing a good quality/efficiency compromise for the large molecular models to be simulated and the targeted accuracy. However, since GGA functionals do not consider dispersion corrections by essence, we used the formalism described in the following section to overcome this limitation.

3.1.4. Dispersion Corrections

The dispersion energy is part of the correlation energy for short and medium electron-electron interatomic distance that has not been incorporated in GGA-KS-DFT. Standard exchange-correlation (LDA, GGA, and meta-GGA) functionals are the functionals of local electron density or the gradient of electron density, neglecting the long-range electron-correlations such as London dispersion. The London terms (attractive in $-C/R^6$) of the van-der-Waals forces correspond to the instantaneous response of electrons within a region of space to a fluctuation of the electronic density within another region of space. The interaction between the dipoles induced by this fluctuation is known as London dispersion. So, physically, these interactions are always present but not treated in KS-DFT.

Furthermore, it is essential to accurately calculate long-range dispersion corrections since they could represent a significant contribution depending on the systems (adsorption of large molecules on a surface, for instance). These so-called weak interactions may be very substantial for large molecules (or a large number of small molecules).

$$\boldsymbol{E_{tot} = E_{el} + E_{disp}} \qquad \textbf{3-14}$$

In the present PhD work, we used the density-dependent dispersion coefficient (dDsC)[177], which takes care of these corrections parametrically to consider these interactions. dDsC is based on exchange-hole dipole moment formalism of dispersion coefficient proposed by Becke and Johnson and damping parameter. The atomic ionization energies and polarizabilities are needed to calculate it apart from the density-based information and fitting parameters[178]. As it is dependent on density, it is expected to offer a more accurate picture of highly polarized and charged systems. There are several other types of dispersion corrections; some of the popular ones also include DFT-D2 [179], DFT-D3 [180], TS-vdW [181], XMD [182], and DFT-NL [183].

3.1.5. Solving KS-equations self-consistently

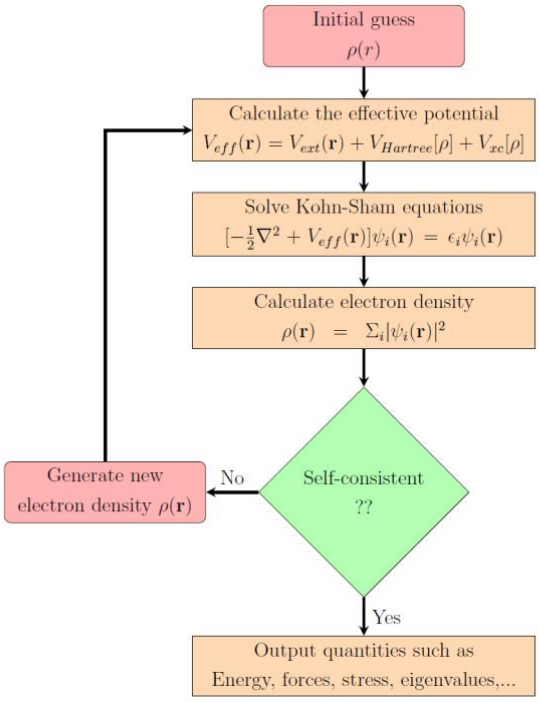

Figure 3-2: SCF cycle to solve the Kohn-Sham single electron equations for molecular orbitals [173].

Now to get the eigenfunction of KS equations, we need to solve the KS equations selfconsistently. The self-consistency cycle has been given in Figure **3-2**. The first step is to choose the basis set and initial guess for density $\rho(r)$ then construct V_{eff} , $V_{eff} = V_{ext} + V_H + V_{xc}$ with the V_{eff} solve the KS equations, calculate new electron density. If convergence criteria are met, one proceeds to calculate total energies, force, etc. If convergence is not achieved, the new density is used as the new guess, and the procedure is repeated [173, 184].

To solve the Kohn-Sham equations self-consistently, we have to make an initial guess $\rho(r)$. To construct the initial guess for electron density, we will expand the unknown orbitals of the KS equation as basis sets.

3.1.6. Plane-wave basis set

Basis sets are essential to solve the Schrödinger equation numerically, whether by wavefunction or density-functional-based methods. Most of the electronic structure methods are dependent on some kind of basis function. The unknown wavefunction of the system has to be expanded in terms of these basis functions in order to solve the equations numerically. These have usually been referred to as a set of non-orthogonal single electron functions used to build molecular orbitals. Molecular orbitals (MOs) are the linear combination of atomic orbitals (LCAO-MO approximation). In computational chemistry, an orbital is a single electron function. Depending on the requirement, the properties of basis sets change. For example, atomic-centered basis sets are commonly used for molecules, but plane-wave basis sets are for condensed matter or periodic systems.

There are thus two dominant classes of basis set available in quantum chemistry: Plane-wave basis sets and localized basis sets. We have used the plane-wave basis set in our PhD investigation; therefore, we will discuss them in more detail.

The use of plane-wave for solids or periodic systems has many advantages over localized basis sets. The easy transformation from real space to reciprocal space representations, simplicity for calculating Hellmann-Feynman forces-stress (see equation **3-20**-**3-23**), and no basis sets superposition error[4] (BSSE) are primary.

For periodic systems, the use of plane waves is beneficial because each electronic wavefunction can be written as a product of a plane wave and lattice part:

$$\boldsymbol{\phi_k}(\boldsymbol{r}) = \boldsymbol{e}^{\boldsymbol{ik\cdot r}}\boldsymbol{u_k}(\boldsymbol{r}) \qquad \textbf{3-15}$$

[4] BSSE is the error arising due to overlap of atomic centered basis sets of an interacting molecule. As the interatomic distance shrinks among individual atoms, the consisting basis set changes to minimize the total energy of the system. This change in basis set (used in energy minimization) as a function of interatomic distance would lead to an overestimation of interaction energy (known as BSSE).

Where index k represents a set of plane waves within the primitive unit cell of the periodic system and $u_k(r)$ possesses the same periodicity as the unit-cell[5] and can be expanded as:

$$\boldsymbol{u_k(r) = 1/\Omega\, \Sigma_G C_{k,G} e^{iG\cdot r}} \qquad \textbf{3-16}$$

Where G is the reciprocal lattice vector and Ω is the volume of the unit cell. The plane waves ($\phi_k(r)$) that appear in the above expansion (equation **3-15**) can be represented as a grid in reciprocal space. Each electron occupies a state of definite k. In principle, infinite number of plane waves are required to describe the electron's wavefunction perfectly, but in practice, higher-order terms of the Fourier component have negligible contribution [185]. So we can truncate the expansion at some value of |k + G| as:

$$\boldsymbol{E_{cut} = \frac{\hbar^2|k+G|^2}{2m} = \frac{\hbar^2}{2m} G_{cut}^2} \qquad \textbf{3-17}$$

Using the finite number of plane waves will introduce some error that can be reduced by systematically improving the convergence of the property of interest while increasing the number of plane waves. Despite having many advantages such as orthogonal, simple to calculate, an easy transformation from real to reciprocal space, and being independent of atomic position, using plane waves has some disadvantages. A large number of basis sets are required to describe the KS orbitals accurately. The scaling size of the basis set depends on the simulation volume that makes the large vacuum-containing cells expensive to simulate. The requirement of a considerable number of basis functions can be reduced by using pseudopotential and frozen core approximation that we will discuss next.

3.1.7. Projector augmented wave method

From the perspective of chemical interactions, core electrons[6] are not involved in the bonding and in some physical and chemical properties which define the system. Those are influenced mainly by relatively loosely bonded valence electrons. Thus, we can

[5] In a periodic system potential (V) satisfies $V(r+R) = V(r)$ condition, where R is Bravais lattice vector and $u_k(r+R) = u_k(r)$.

[6] Core electrons usually defined as the rare gas configuration. These are tightly bounded inner electrons, occupied low energy levels and commonly unaffected by chemical reactions. As they don't participate during the reaction, the wavefunction of core electrons doesn't change significantly. Valence electrons are, in contrast, outermost electrons which participate in chemical reactions and wavefunctions of valence electrons change substantially after reaction.

simplify the treatment of the core region. The nuclear potential diverges near the nucleus ($V_{nuc} \propto -Z/r$), which leads to computational problems, especially while using plane waves. The wavefunction of core electrons are highly localized and chemically inactive. Further, due to the constraining of the Pauli exclusion principle (orthogonality condition), the outer shell valence orbitals are oscillating rapidly near the core region.

To represent such a highly oscillating function, one needs many plane waves that will make it very expensive in terms of computational cost. As we know that the core electrons are chemically inert, they can be neglected for most practical purposes (also known as frozen core approximation), and the valence electron wavefunction can be smoothened near the nucleus by a pseudo wavefunction. Consequently, the valence electrons do not experience full coulomb potential but just an effective potential (pseudopotential). The cutoff radius (r_c) is defined so that pseudopotential's behavior is identical to all-electron potential after r_c. The inner part of pseudopotential (below r_c) would be replaced by effective potential. Similarly, the core region of the wavefunction is defined up to r_c (Figure **3-3**). After that, valence states wavefunction would be identical to the all-electron wavefunction. The cutoff will be defined in such a way so that it can mimic the physical properties of the system significantly accurately with the least required computational cost. This approximate way reduces the computational cost dramatically with a little loss in accuracy.

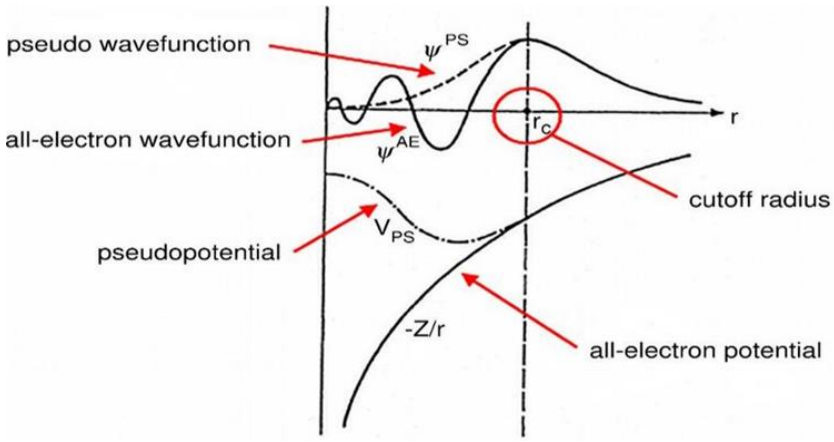

Figure 3-3: Comparison of the pseudo wavefunction and pseudopotential with all-electron wavefunction and potential. (image taken from [186])

Pseudopotential and linearized augmented plane wave (LAPW) methods are a specific case of the projector augmented wave (PAW) method. PAW was proposed by Blöchl in order to improve the efficiency of pseudopotential methods and reduce the computational cost. The PAW method allows us to transform the all-electron wavefunction to auxiliary wavefunctions by some transformation operator while conserving the orthogonality between the core and the valence orbitals. Beyond augmentation radius, auxiliary wavefunctions and all-electron wavefunction behave identically. But within the augmentation sphere, pseudo wavefunctions are approximated by frozen core approximation[187]. By unifying the all-electron and pseudopotential methods, the PAW approach provides a much more computationally efficient way to solve KS-equations[188].

3.1.8. Ab initio molecular dynamics (AIMD)

Born-Oppenheimer molecular dynamics (BOMD)

Ab initio molecular dynamics is a powerful tool to generate the finite-temperature dynamical geometries by solving Newton's equation of motion from calculated forces from electronic structure calculations. AIMD is one step ahead of static nuclei KS-DFT. A structural minimization of static nuclei system is highly dependent on the initial guessed geometry. Thanks to AIMD, the system's dynamical properties can be computed at finite temperature, in principle independent of the starting point.

The system consists of N nuclei and N_e electrons; within the BOA, nuclei of the system are considered to be point charges and point masses during the ground state. The obtained energy from Kohn-Sham equations is the nuclei's function (which we deemed to be fixed). Derivative of this energy concerning nuclei coordinates would act as interatomic potential. This potential is required to compute the instantaneous force in Newton's equation of motion to move the atom. Therefore, the calculated gradient of energy (obtained by DFT at a fixed position of nuclei) will provide the force responsible for the motion of nuclei. For a given time step, new positions would be calculated, and the process would be repeated. During the course of dynamics, we assume that the electrons will stay in the adiabatic ground state; nuclei will move on the ground state potential energy

surface and follow classical Newton's equation of motions. Newton's equations of motion for nuclei within the framework of BOA can be written as[189, 190]:

$$\boldsymbol{M_A \ddot{R}_A(t) = -\nabla_R \min_{\psi} \langle \Psi_0 | H_{ele} | \Psi_0 \rangle} \qquad \textbf{3-18}$$

M_A is the mass of Ath nuclei, $\ddot{R}_A(t)$ is velocity gradient, $\nabla_R$is differential operator, Ψ_0 is ground state wavefunction solved at particular R and H_{ele} is electronic Hamiltonian parametrically dependence on R. In most simplistic case of AIMD, we solve the equation **3-18** numerically at every time step.

In the present PhD work, we have used a simplified scheme for AIMD based on a velocity-scaled algorithm to accelerate the exploration of some configurational states of complex systems.

3.2. Simulation of spectroscopic properties

3.2.9. Vibrational analysis within harmonic approximations

The vibrational frequencies, ν, would be evaluated by the eigenvalues of Hessian matrices of the potential energy surface E(R) within the BO approximation, scaled by nuclear masses[191].

$$\boldsymbol{det \left| \frac{1}{\sqrt{M_A M_B}} \frac{\partial^2 E(R)}{\partial R_A \partial R_B} - \nu^2 \right| = 0} \qquad \textbf{3-19}$$

M_A, M_B, and R_A, R_B are the mass and atomic positions of nuclei A and B, respectively, and ν is the frequency of the normal mode. It is important to point out that the underlying theory of vibrational mode is within the harmonic approximation, which means the interatomic potential energy is expanded to second-order. The resulting Hamiltonian would be the sum of all the independent harmonic oscillators. The Hellmann-Feynman theorem assures that the non-degenerate eigenvalue of the first derivative of Hamiltonian concerning any parameter λ corresponds to the first derivative of energy eigenvalue of that Hamiltonian.

$$\frac{\partial E}{\partial \lambda} = \langle \Psi \quad \left|\frac{\partial H_\lambda}{\partial \lambda}\right| \Psi \quad \rangle \qquad \textbf{3-20}$$

Here, Ψ and E are the eigenfunction and eigenvalue of the operator H_λ respectively and H_λ has parametric dependence on λ. As we already discussed earlier, within the BOA, Hamiltonian has parametric reliance on nuclei position. So for nucleus A, the electronic ground state would be[191]:

$$F_A = -\frac{\partial E(R)}{\partial R_A} = -\langle \Psi \quad (r, R) \left|\frac{\partial H_R}{\partial R_A}\right| \Psi \quad (r, R)\rangle \qquad \textbf{3-21}$$

After combining equations **3-20** and **3-21**, we can write the F_A as:

$$F_A = -\int \frac{\rho \quad (r)\partial V_{ne}(r)}{\partial R_A}\, dr - \frac{\partial E(R)}{\partial R_A} \qquad \textbf{3-22}$$

Where V_{ne} is the electron-nucleus interaction (equation **3-22**), $\rho(r)$ is ground state electron density, and F_A is the force felt when atom A is displaced. By derivating the Hellman-Feynman forces concerning ionic positions are hessian matrices, also known as the matrices of interatomic force constants[191]:

$$\frac{\partial^2 E(R)}{\partial R_A \partial R_B} \equiv -\frac{\partial F_A}{\partial R_B} \qquad \textbf{3-23}$$

3.2.9.1. Finite difference methods for vibrational modes and frequencies

The force-constant matrix is calculated by displacing each atom in the unit cell from its equilibrium position and calculating the restraining force on every other atom of the unit cell. This method is also called frozen phonons due to the fixed amplitude of displacement while calculating its derivative. A schematic of this method is shown in Figure **3-4**. The finite difference method is straightforward and straightforward to implement; therefore, available for semilocal DFT, hybrid DFT, forcefields, or dynamical mean-field theory but limited to the small size of supercells. However, because this method requires the

construction of a supercell making the computation expensive, after applying the FD method, the interatomic force-constants matrix can be written as:

$$\frac{\partial^2 E(R)}{\partial R_A \partial R_B} \equiv -\frac{\partial F_A}{\partial R_B} \approx -\frac{F_A}{\Delta R_B} \qquad \textbf{3-24}$$

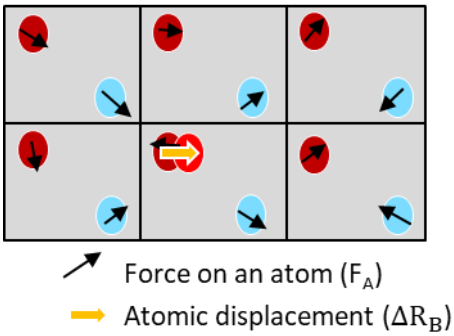

Figure 3-4: Schematic representation finite difference method to calculate the vibrational modes (image adopted from an online source). One atom is displaced, and the acting forces on all the other atoms are being measured.

3.2.9.2. Density functional perturbation theory and linear response method for vibrational spectra

Based on how the system reacts to some sort of perturbation, various physical and spectroscopic properties can be determined. IR spectrum, Raman spectrum, polarizabilities, and phonons are some of them. Density functional perturbation theory (DFPT) is an effective method for calculating such properties and comprehending these phenomena. A perturbative potential is added to the system, and the system's behavior under this perturbative potential is observed. The system response can be examined under varying applied perturbation by calculating single-point energy calculations of every corresponding change induced by the perturbation.

The perturbation could be a slight atomic displacement, expansion or contraction of a primitive cell, external electric or magnetic field, etc. Response to all these perturbations

mentioned above would give insight into specific properties of the system. The observation of the response to the electric field can be used to elucidate various linear optical properties, Born effective charges (BEC), and vibrational frequencies[192]. For equilibrium geometry, the forces acting on individual nuclei should be zero. In DFPT, the Hessian matrix is calculated in the following way:

$$\frac{\partial^2 E(R)}{\partial R_A \partial R_B} \equiv -\frac{\partial F_A}{\partial R_B} \qquad \textbf{3-25}$$

$$= \int \frac{\partial \rho_R(r)}{\partial R_B} \frac{\partial V_{ne}(r)}{\partial R_A} dr + \int \rho_R(r) \frac{\partial^2 V_{ne}(r)}{\partial R_A \partial R_B} dr + \frac{\partial^2 E_{ion}(R)}{\partial R_A \partial R_B}$$

Where R_A and R_B and atomic parameters. This expression closely links the second derivatives of the total energy to the ground state electron density $\rho_R(r)$ and the linear response of the charge density to a displacement of the ions, $\frac{\partial \rho_R(r)}{\partial R_B}$. $V_{ne}(r)$ is the electron-ion interaction and $E_{ion}(R)$ the direct ion-ion interaction.

The DFPT approach has been implemented in VASP for PAW potentials[192] as well as its application for vibrational spectroscopy of adsorbed molecules on the surface [193]. Within the framework of dipole approximation[194], the intensity of active infrared modes is directly proportional to the square of the change in dipole moment along the normal mode direction:

$$I_\lambda \propto |D(\lambda) - D_0|^2 \qquad \textbf{3-26}$$

$D(\lambda)$ is the new dipole moment after displacing the atom in the direction of vibrational mode λ, and D_0 is the permanent dipole moment when the system is at equilibrium. The intensity can be calculated by evaluating the first order in Taylor series expansion of the dipole moment:

$$\boldsymbol{I_\lambda} \propto \sum_{\alpha=1,3} \left| \sum_{\substack{i=1,N \\ \beta=1,3}} \boldsymbol{\nabla_{i\beta} D^\alpha e_i^\beta(\lambda)} \right|^2 \qquad \textbf{3-27}$$

Where, $\nabla_{i\beta} D^\alpha$ is the first derivative of polarization vector with respect to ionic coordinates, also known as Born effective charge (BEC) tensor and $e_i^\beta(\lambda)$ is the β component of polarization vector of vibrational mode λ. [195, 196] Moreover, the BEC tensor of an atom i can be calculated in the following way:

$$\boldsymbol{\nabla_{i\beta} D^\alpha = Z_i^{\alpha\beta} = \frac{\partial^2 E_{tot}}{\partial \varepsilon_\beta \partial \tau_\alpha}} \qquad \textbf{3-28}$$

Where, E_{tot} is the total energy of the cell, ε_β is the electric field along the direction $\boldsymbol{\beta}$ and τ_α is the atomic displacement along the direction α of the lattice. The electric field ε_β is generated due to the long-range character of Coulomb interactions [195].

We have used this approach for all IR-spectra plotted in the PhD thesis and to evaluate the vibrational contribution of some thermodynamic analyses after checking that it is equivalent to the finite difference method described before. For the sake of simplicity, the standard method for evaluating various thermodynamic terms with the use of vibrational frequencies are reported in Appendix A.

3.2.10. Core level shift and binding energies

X-ray photoelectron spectroscopy is a crucial technique to understand surface chemistry and, more particularly, analyze the chemical states of key elements of the materials. The distinction among various chemical forms is based on core level atomic binging energy (BE). The shift of core level binding energy with respect to its reference gives insights into the chemical environment around the targeted atom. Calculating the binding energy involves initial and final state approximations. Initial state approximation assumes the

energy level of core orbitals is directly related to core electron energy based on Koopman's theorem [197], and final state approximation assumes the energy of excited state would be related to the core orbital energy of the excited state. Here, the energy of the excited state can be obtained by calculating the energy of the system ($E(n_c-1)$) where one electron is transferred to the lowest unoccupied molecular orbital (LUMO) from one of its particular atom's core and creating a system with core-hole [198, 199]. Therefore, the BE expression can be written as:

$$\boldsymbol{BE = E(n_c - 1) - E(n_c)} \qquad \textbf{3-29}$$

$E(n_c)$ is the ground state energy, and $E(n_c-1)$ is the energy of the excited state; the difference between these two states will provide information about the binding energy of the electron that is being excited of the particular atom. VASP implementation of PAW formalism of all-electron method with frozen core approximation allows us to generate the corresponding energy of core orbitals of the respective atom. A system with a core-hole can be created by putting an additional nuclear charge to the core of the system along with one electron in a valence state to keep the charge neutrality. This is also known as the Z+1 approximation. The binding energy in equation **3-29** can be evaluated by the Slater-Janak theorem [200, 201].

$$\boldsymbol{BE = E(n_c - 1) - E(n_c) \ \sim -\epsilon_c\left(n_c - \frac{1}{2}\right)} \qquad \textbf{3-30}$$

Where, $-\epsilon_c(n_c - 1/2)$ is the Kohn-Sham eigenvalues of the given core level eigen state with half electron decrease in the occupation. We can not compare the direct BE because the reference is not the same in theory and experiments. But the difference in BE (ΔBE) can be directly compared with experimentally obtained XPS data.

Other possibilities consider that one or half electron is removed from the system and kept in a vacuum (JS_n and FS_n in Figure **3-5**). All these approaches work well for molecules and clusters, and the JS_n approach also shows more promising results for molecular moieties on the surfaces than FS, JS, and FS_n [202]. In our investigation, we have tested FS and JS approach on the MoS_3 polymorphs. We did not observe any significant difference between them, and here we report only the data on the FS approach.

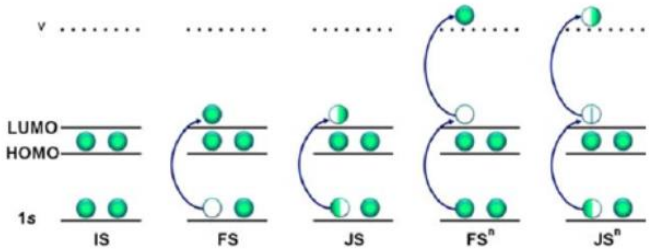

Figure 3-5: IS- initial state, FS- final state, JS- Jana-Slater, FS_n, and JS_n are the modified version of FS and JS[202].

3.3. Approach to find minimum energy paths and saddle points

A key question in computational chemistry applied to catalysis is evaluating the rate-limiting steps and determining the transition states for chemical reactions. During these chemical events, the atomic configuration of the system changes in many ways involving bond formation and breaking. These events usually occur many orders of magnitude slower than the vibrations of the system. Suppose one excludes standard or even biased AIMD approaches, which would be too much computational time consuming for the systems studied in this PhD work. In that case, one common approach is to use static methods to explore the minimum energy path of the reaction to identify transition states (TS) and apply TS theory (TST) to evaluate rate constants.

Besides the Born-Oppenheimer approximation, TST has two other main assumptions: i) the process is slow enough to maintain the Boltzmann distribution in the reactants, and ii) the dividing surface has one fewer degree of freedom (N-1) than the reactants (N). Besides, to reach the final state, it travels over this dividing surface only once. That means that the PES must contain only one "saddle point"[7] between two intermediate points if no stable intermediate exists between the saddle points. The highest point on the dividing surface would give us information about the barrier. Now the problem is to determine the

[7] A point on the surface of two variables would be called a saddle point if the partial derivation of the function with respect to individual variable ($\frac{\partial f}{\partial x} = \frac{\partial f}{\partial y} = 0$) is zero and $\frac{\partial^2 f}{\partial x^2}\frac{\partial^2 f}{\partial y^2} - \left[\frac{\partial^2 f}{\partial x \partial y}\right]^2 < 0$.

saddle point of this diving surface, which is challenging. The reaction coordinate of this saddle point would correspond to the transition mode of the process that will be normal mode with imaginary frequency.

The minimum energy path (MEP) is commonly used to determine the reaction coordinates for transitions (rare events). MEP may include one or more minima, corresponding to the stable intermediates between the initial and the final point. Given that case, MEP will exhibit two or more maxima, indicating a corresponding saddle point. To estimate the rate accurately, one needs to find the highest saddle point along with MEP that will correspond to the rate-limiting step. The first-order saddle points are a maximum in one direction and a minimum in all others. This will be obtained by minimizing all the degrees of freedom except one that will be maximized. [203]

Once the saddle point is known, we can evaluate the activation energy that will give insights into the reaction rate. The energy difference between the initial image and the saddle point (E_A) estimates the exponential term in the empirical Arrhenius rate equation[8] or even more precisely in the Eyring-Polanyi equation. This equation assumes that the nuclei are classical particles; activated complex, we call them now transition state, are in quasi-equilibrium with reactants and products; and the TS would be converted into reactants or products once they are formed. The Eyring-Polanyi equation states as following [205, 206]:

$$\boldsymbol{k = \frac{\kappa k_B T}{h} e^{-\frac{\Delta G^{\ddagger}}{RT}}} \qquad \textbf{3-31}$$

Where κ is the transmission coefficient, k_B is the Boltzmann's constant, h is Planck's constant, and $\Delta G^{\ddagger}$ is the Gibbs energy of activation. The transmission coefficient is the fraction of flux going through TS and converted into a product; if we assume the reaction is non-reversible, this coefficient would be equal to 1. The Gibbs energy can breakdown into two components, and the equation can be rewritten as (for $\kappa = 1$):

$$\boldsymbol{k = \frac{k_B T}{h} e^{-\frac{\Delta S^{\ddagger}}{R}} e^{-\frac{\Delta H^{\ddagger}}{RT}}} \qquad \textbf{3-32}$$

[8] Swedish chemist Svante Arrhenius proposed that the rate constant of a reaction would exponentially decay based on the ratio of activation energy and temperature: $k = Ae^{-E_A/RT}$, where E_A is the activation energy of the, R is gas constant, T is kelvin temperature and A is frequency factor. [204].

$\Delta S^{\ddagger}$ and $\Delta H^{\ddagger}$ is the entropy of the activation and enthalpy of activation, respectively.

If we determine the activated complex (transition state or saddle point), we can directly deduce the rate constant of the reaction by DFT calculations of $\Delta S^{\ddagger}$ and $\Delta H^{\ddagger}$ (see appendix-A). Several methods have been proposed in the literature to estimate MEPs and saddle points. We will describe only the ones that have been used in this PhD project: Nudged Elastic Band (NEB), Climbing image (CI)-NEB, dimer methods, and intrinsic reaction coordinates (IRC). [203]

3.3.11. The NEB method

The nudged elastic band (NEB) method connects the initial point (reactants), **I**, and the final point (product), **F**, with several images between **I** and **F** through a spring (elastic band). These images can be generated through linear interpolation of initial (**I**) and final (**F**) image. After the image has been generated, an optimization algorithm is applied to minimize these images along with MEP. Apart from providing an estimate of the saddle point, the NEB method also theoretically allows us to have a global overview of the potential energy landscape.

These generated images are relaxed towards the MEP by implementing a force projecting scheme. In this scheme, the potential forces operate perpendicular to the elastic band, and spring forces operate along with the band (Figure **3-6**). These force projections are made by defining a tangent along the path ($\widehat{\tau}$) as the unit vector from the lower energy image to the neighboring higher energy image. To avoid the abrupt change in the $\widehat{\tau}$ direction, a linear interpolation between neighboring images is used. The force component on NEB image i is defined as:

$$\boldsymbol{F}_i^{NEB} = \boldsymbol{F}_i^{\perp} + \boldsymbol{F}_i^{\parallel} \qquad \textbf{3-33}$$

Where $\boldsymbol{F}_i^{\perp}$ is the force component perpendicular to the elastic band and $F_i^{\parallel}$ is the parallel to elastic band which is spring force.

$$\boldsymbol{F}_i^{\perp} = -\nabla \mathbf{E}(\boldsymbol{I}_i) + \nabla \mathbf{E}(\boldsymbol{I}_i) \cdot \widehat{\boldsymbol{\tau}}_i \widehat{\boldsymbol{\tau}}_i \qquad \textbf{3-34}$$

And the spring force

$$F_i^{\parallel} = k(|I_{i+1} - I_i| - |I_i - I_{i-1}|)\hat{\tau}_i \qquad \textbf{3-35}$$

In this expression I_i is the coordinates of ith image and k is the spring constant for image i in connection with $i-1$ and $i+1$ within the harmonic approximation. Now, these forces on each image are minimized along with the MEP. [207]

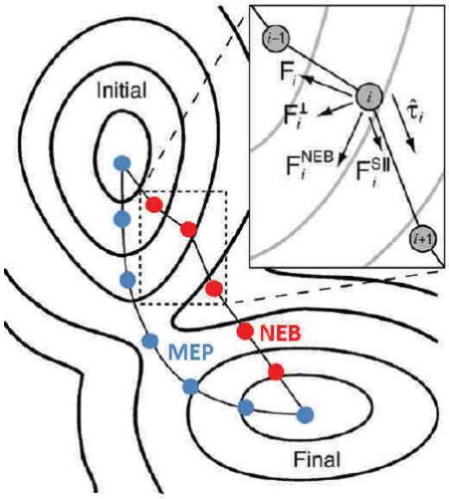

Figure 3-6: MEP and NEB description on a potential energy surface (PES) and the force component description on NEB image (adopted from ref [208])

3.3.12. CI-NEB method

Climbing image (CI)-NEB is a further improvement over classical NEB. This approach saved us from the necessity to optimize the forces on every single image. After performing a few relaxation steps and finding out the highest energy image, this highest energy image moved uphill. In other words, this image does not feel any spring force along the downhill tangent (Figure **3-7**). The force which will cause to move the image uphill:

$$F_{imax}^{climb} = -\nabla \mathrm{E}(I_{imax}) \cdot \hat{\tau}_{\parallel}\hat{\tau}_{\parallel} \qquad \textbf{3-36}$$

The direction of the movement of this maximum energy image is determined by the neighboring images of I_{imax} unless there is only one image between the initial and final state, there is no assurance that the TS would connect to the final and initial point in both these methods (NEB/CI-NEB). These images are linearly interpolated, which is an

approximate way to have an idea about the MEP. In order to confirm that the observed TS connect the initial and final image, we have to perform intrinsic reaction coordinate (IRC) analysis (section 3.3.14). [209–211]

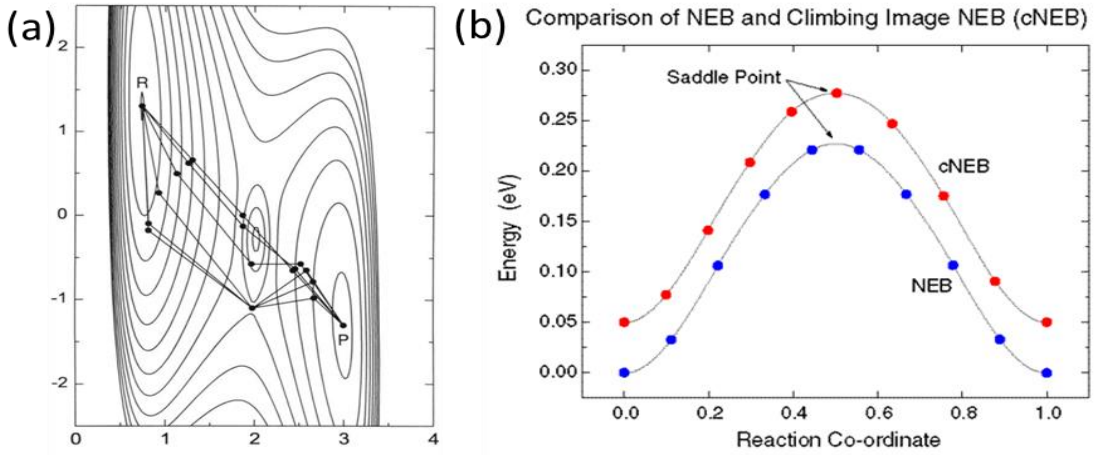

Figure 3-7: (a) The CI-NEB method between the reactant (R) and product (P). (b) Comparison of potential energy surface calculated by NEB and CI-NEB, and the difference in saddle point [209].

Force-based optimizers are commonly used to minimize the energy for every image on the current path towards the MEP and saddle point. In general, quasi-Newton and quick-min are the default VASP force-based optimizers used for NEB/CI-NEB. The Henkelman group has developed several complementary force-based optimizers such as conjugate gradient (CG), Limited-memory Broyden-Fletcher-Goldfarb-Shannon(L-BFGS), Global-LBFGS, Fast internal relaxation engine (FIRE), and steepest descents (SD). [208]

In this thesis, we have mainly used the VASP default optimizer that is CG, where the TS was not very complex. However, in some cases, where the complicated TS is involved, CG optimization doesn't converge, FIRE or L-BFGS have been utilized. Predominantly, for DBT hydrogenolysis (appendix : D), we have used the L-BFGS and FIRE; FIRE is more robust in the case of troublesome convergence issues.

3.3.13. The Dimer method

To determine the saddle point when the final state is not known is even more challenging than the earlier problem of finding the saddle point when the final image is known. Usually, this search requires the second derivatives of the energy with respect to the atomic coordinates, which means the entire Hessian matrix has to be calculated. Besides,

the matrix needed to be diagonalized to find the normal modes, and this calculation is considerably expensive. Henkelman et al. have proposed a method that does not require calculating the second derivative and can be applied only with the first energy derivative.

A set of two images close to TS, called "dimer," is a prerequisite (Figure **3-8**) to apply this method. The dimer evolution during optimization should lead to the saddle point instead of going to the minima. This is because the acting force direction on the center of the dimer has been inverted while optimizing. The acting force on the center is obtained by interpolating the forces on both images of the dimer. The direction of the normal mode that has the lowest frequency would give the active force direction. The normal mode direction is obtained by minimizing the energy concerning its orientation. The reverse effective central force will lead the dimer to the saddle point after optimization. Several different initial configurations could be needed to obtain a reasonable (or the appropriate) saddle point that leads out of the minimum basins. Furthermore, this method does not connect the initial and final image through the saddle point, unlike NEB or CI-NEB. [212]

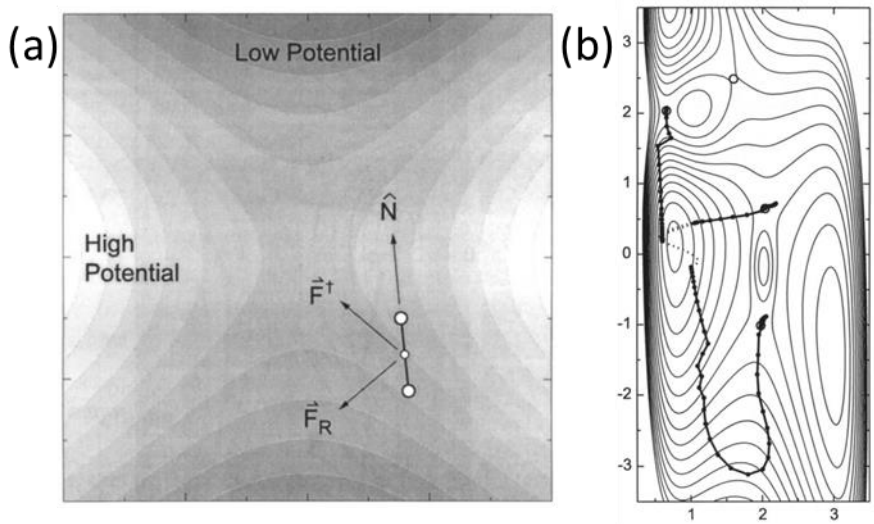

Figure 3-8: (a) Effective force calculation in dimer method. An image pair is generated and rotated to determine the direction of the lowest frequency mode. (b) An example of the dimer method; three different starting points were generated to follow the dimer approach, and all three lead to distinct saddle points[212].

The improved dimer method further improves the Henkelman dimer method by Heyden et al. [213]. Earlier, the first derivative of the energy was required to reach the saddle point; this was replaced by the energy calculations, which reduced the computational cost many folds. A good initial guess is given; the improved dimer method can provide the reasonable saddle point even when reaction coordinates do not correspond to the eigenvector of the lowest eigenvalue mode, where the earlier dimer method is likely to fail. [213]

Finding an appropriate TS is relatively time-consuming even after choosing our favorite optimizer, and convergence is difficult to achieve in many cases. We have used an approach by combining CI-NEB and (improved)dimer methods to reduce the time. We first run the CI-NEB for a hundred steps. If the convergence has not been achieved, we use the half-optimized TS image as an input in the (improved)dimer approach to finding the saddle point. However, it requires calculating the frequencies twice, once to get the direction of acting force towards saddle point and the second time to confirm that TS is a first-order saddle point.

3.3.14. Intrinsic Reaction coordinate (IRC)

To determine the authenticity of the optimized TS from earlier described methods, we first need to calculate the frequencies. The TS is a first-order saddle point, so it should contain only one single imaginary frequency. After the TS was verified, it has to go to another confirmation to be able to prove that this is the TS that connects the two minima; one corresponds to the reactant (initial image/substrate) and another one to the product (final-image/product) (Figure **3-9**). Once the saddle point has been found, the mapping can be made from the gradient of energy downhill in both directions to connect it with its initial and final state with a minimum energy path (MEP). [203] IRC is a mass-weighted reaction coordinate on the steepest descent path in both directional vectors (reactant and product). [210, 211, 214, 215]

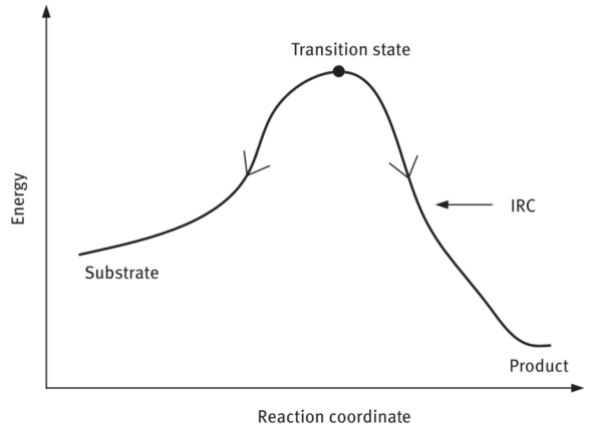

Figure 3-9: Intrinsic reaction coordinate (IRC) calculation in both forward and backward direction that leads to substrate and product. The transition state corresponds to the actual TS connecting through reactant and product.

This approach was mandatory for the research project reported in Appendix-D, where some complex TS have been determined. For the research work described in the next chapter, this was not mandatory since most TS involved primarily only H-transfers.

3.4. Conclusions

We will use the static approach in this thesis to investigate the mechanism of stepwise activation process. However, the static method is limiting when the potential energy surface is very complex, and several local stationary points exist on PES. Because in the static approach, the energy minimization is highly dependent on an initial guess, and to guess an adequate starting point could be difficult due to complex PES. Nevertheless, we will remain within the framework of the static approach in this thesis. Starting from an initial guess, the total-energy and acting forces of the system are being calculated. If these forces are not below some reasonable threshold, the atoms are moved according to the acting forces on them, and new total-energy and forces are being calculated. This process is repeated until we reach the desired threshold of forces and change in total-energy from its previous step. In this approach, the great majority of the geometry optimizations were performed at 0 K, excepting some specific AIMD simulations to explore configurations systematically. Thermal and entropy effects were included *a posteriori* by the thermostatistics approach.

This chapter presented a brief summary of the underlying theory and methods we have used in this thesis. We have described the approximation used in theory and their limitations in some cases, basis set and exchange-correlation functional for the investigation, methods to search the TS NEB, CI-NEB, dimer, and calculating the frequencies and IR spectra (FD and DFPT). The methods section of the upcoming chapters will describe specific details about the computational methods, parameters, and used cutoff. We have used DFT as implemented in VASP with plane-wave basis sets, PBE exchange-correlation functional within GGA approximation, PAW pseudopotential, and dDsC dispersion correction. The choice of the basis sets, pseudopotentials, and dispersion corrections are based on the earlier benchmarks done in the group.

Chapter 4: Genesis of MoS_2 from Mo-oxide precursors on γ-alumina

The genesis of the MoS_2 phase by activation of the HDS catalyst is one of the crucial and complex processes in the refining industry. The activation dependency on several influencing parameters challenges having an enviable understanding of the process. This chapter explores how sulfidation occurs on Mo-oxides through our model oxide precursors, involved intermediates, and what path sulfidation prefers to go after oxysulfide vs. trisulfide on the (100)-surface of γ–alumina.

4.1. Introduction

As highlighted in the general introduction, MoS_2 based materials represent a wide interest for various catalytic and electrocatalytic applications such as hydrodesulfurization process, hydrogen evolution reaction, etc. However, the catalytic performances strongly depend on the sulfidation state resulting from the preparation steps. More particularly, the final activation step is crucial for the transformation of the oxide precursor into the targeted sulfided Mo material.

As detailed in the bibliography, the preparation of such Mo disulfides may require specific Mo oxides precursors (such as polyoxomolybdates) impregnated on oxide support (such as alumina) followed by various possible thermal treatments (drying/calcination). The resulting supported Mo-oxides are finally activated by sulforeduction under H_2/H_2S gas phase or with organo-sulfur compounds in the liquid phase at elevated temperature (350°C).[7]

The activation step of γ-alumina supported molybdenum oxide precursor by sulfo-reductive treatment remains a crucial step for the genesis of the industrial disulfide molybdenum (MoS_2) based active phase. Therefore, to improve the resulting properties of these catalysts, it remains critical to understand better the genesis and activation steps of these active phases from their oxide precursors.

Even though the activation step of supported molybdenum oxide precursor by sulfo-reductive treatment has been the subject of many experimental studies,[27, 35, 36, 106, 216, 217] several mechanistic questions remain open e.g.: the nature and role of MoO_xS_y oxysulfides and MoS_3 trisulfide intermediates, and the kinetically limiting steps.

Scheme:

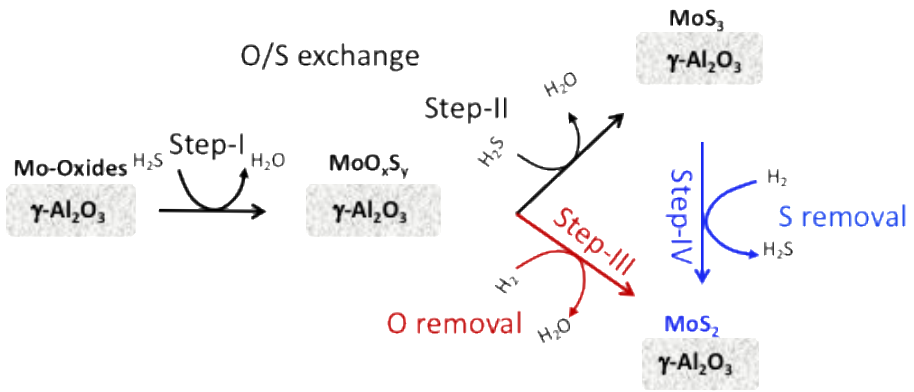

Figure 4-1: Schematic diagram of sulfidation of Mo oxide precursors by H_2S into Mo oxysulfides, and from oxysulfides to MoS_2 following two pathways: direct reduction to MoS_2 by H_2 (steps I and III) or sulfidation into MoS_3 followed by transformation to MoS_2 (steps I, II and IV).

The oxidation state of Mo changes from VI to IV during activation. The widely accepted key intermediates are oxysulfides,[27, 98, 100, 216, 218] and the formation of *a*-MoS_3.[40, 104–106, 216, 217, 219] These oxysulfides or trisulfides are complex amorphous compounds interacting with γ-alumina. The structural understanding of these amorphous compounds remains challenging. For instance, we will show in **Error! Reference source not found.**, the wide structural diversity of *a*-MoS_3 polymorphs as a function of size even without support effect.[220] The structural insight about Mo oxysulfides is even more elusive, particularly in the presence of the alumina support.

No H_2 consumption has been observed at the first stage, and only H_2S intake is seen in temperature-programmed sulfidation (TPS).[98, 100, 218] Further conversion of trisulfides to disulfide phase produces a substantial quantity of H_2S as reported by in situ XAS.[217] This significant H_2S emission supports the hypothesis of reduction of trisulfides rather than oxysulfides supported by many other studies.[27, 40, 105, 106, 216, 217]

Furthermore, it has been shown by some studies that H_2S is the key reactant to allow the formation of the MoS_2 phase even without H_2 uptake at an early stage.[98, 100, 104, 218, 221]. Therefore, if the MoS_3 intermediate is involved, the activation process is proposed to occur in two stages: O/S exchange with H_2S[107, 218] leading to MoS_3-phase[103, 104, 216] from MoO_3-like species (steps I and II in Figure **4-1**), followed by its transformation to MoS_2 phase thanks to H_2 reduction (step IV). However, the possibility of direct reduction of oxysulfide to the disulfide phase also exists (step-III).

At the same time, the various Mo-oxysulfides intermediate ($Mo^{IV}O_xS_y$, $Mo^{V}O_xS_y$, $Mo^{VI}O_xS_y$,) supported on alumina are highly reactive towards sulfidation. Thus, identifying and characterizing them remains crucial but challenging from an experimental point of view. Time-resolved XAS and Raman spectroscopy on NiMo catalyst supported by Al_2O_3 gave some essential insights due to its capacity to resolve pure spectra of intermediate species by using multivariate curve regression with altering least-squares (MCR-ALS) method for curve fitting.[222] Probing the intermediates is accomplished by using the solid dehydrating condition that reduces the catalyst's reactivity towards H_2S.[223, 224] In particular, in situ EXAFS enabled to follow the evolution of key bond lengths such as Mo-O, Mo-S, Mo-Mo…[99, 106, 217] and to reveal some key intermediates such as MoO_xS_y and MoS_3. Also, by in situ Laser Raman Spectroscopy, the disappearance of some characteristic top oxo-species Mo-O_t and the appearance of S_2^{2-} and S^{2-} species was analyzed as a function of temperature.[217]

In addition, the final active state and respective intermediates could also be affected by various other factors such as type of sulfidation (liquid or gas phase),[98, 99, 225], the pressure of H_2/H_2S,[226] and chelating agent[219] added at impregnation. Gas-phase sulfidation is commonly performed at 10-15% H_2/H_2S and 350-400°C, and liquid phase sulfidation using real feed stoke (gasoil) and/or dimethyl-disulfide (DMDS) along with H_2 flow. Therefore, the source of H_2S may be dissolved in the liquid phase once it is generated through DMDS decomposition at 230°C. This induces that sulfidation starts at a relatively higher temperature around 230 °C in comparison with the gas phase where it starts as early as around room temperature.[99, 227, 228] After 230 °C, as soon as the DMDS dissociated and H_2S is available for sulfidation, oxysulfide intermediates are rapidly transformed into MoS_3 and finally into MoS_2. The initial slow rate might not be due to the

liquid phase's intrinsic slower reactivity but rather because no H_2S sulfiding agent is available before the decomposition of DMDS.[98]

The key descriptors: Mo-O_t, Mo-O-Mo, Mo-S-Mo, Mo-Mo, and Mo-Al were identified for both types of sulfidation. In addition, the absence of a shorter Mo-S bond leads to specific proposals for oxysulfide intermediates.[99] Another exciting difference revealed by in-situ XAS is that during liquid phase sulfidation, the delayed sulfidation temperature induces the depolymerization of the polyoxomolybdate precursor between 80 to 230°C.[99] Hence, the smaller Mo-oxide oligomers (as small as dimers or trimers) highly dispersed on the support are generated and will be the relevant oxide species involved in sulfidation. For that reason, as explained in what follows, we will consider such Mo-oxide oligomers as the starting species for the investigation of sulforeduction mechanisms.

Moreover, the gas phase sulfidation gives 1.5-1.8 times higher MoS_2 stacking than that of the liquid phase with similar mean particle size, and an increase in pressure affects the activation positively. Furthermore, the remaining Mo, which is not sulfided, could be independent oxidic or oxysulfide species separated from MoS_2 stacked phase[226] interpreted from Mo-O EXAFS data.

From a theoretical point of view, as it was presented in the bibliography, some DFT studies focused on the stability of Mo-oxide oligomers either as isolated charged polyoxomolybdates[154–157] or supported on alumina.[17, 153] Other DFT studies focused on the interfacial structures of MoS_2 clusters[33, 68, 229, 230] on alumina,[74, 77, 101] as a function of sulfo-reductive conditions found in the reactive environment or on the thiolysis mechanisms of Mo-O-X linkages for X being various elements composing the support such as Ti, Al, Si…[16, 167, 231]

However, to the best of our knowledge, there exists no published DFT investigation of the sulfidation of Mo-oxides. In particular, numerous open questions remain about the molecular-scale mechanisms of S/O exchanges and reduction steps involved in the activation of Mo-oxides primarily when dispersed on a support such as an alumina.

We have chosen to consider the sulfidation of small $Mo_{\mathrm{n}}O_{3\mathrm{n}}$ oligomers (n=1, 2 and 3) for several reasons. Of course, such small size oligomers are more easily tractable by quantum simulation. However, this is not the main reason. These have been suggested to be present on numerous oxide support (including alumina)[16, 146–152] under drying conditions. The Mo-oxysulfides intermediates formed in the course of sulfidation are also reported by EXAFS analysis to exhibit a small Mo-Mo coordination number.[100, 222] Moreover, as mentioned before, they are involved in liquid phase sulfidation of polyoxomolybdates resulting from depolymerization.[99] Finally, Mo-oxide trimmers supported on alumina exhibit numerous O-species (top-oxo, bridging oxo, O-interfacial), representing key relevant O-sites of reactivity with respect to H_2S and H_2 might differ significantly as encountered in the real experimental system.

In this chapter, we thus investigate the interaction of small Mo-trioxide precursors with alumina and their sulfidation using H_2S. We will unveil the kinetic and thermodynamic aspects of sulfidation and involved intermediates. The transformation from oxysulfides and trisulfide to the disulfide phase will be examined. We will compare the kinetic and thermodynamic behavior of the trisulfide and disulfide pathways. The stability of chain vs. triangular models and the possibility of their transformation from one to another at various stages of the process would be scrutinized. We will also discuss the effect of size during this whole process. Only the key results are presented here; many of the detailed information about gas-phase sulfidation, vacancy creation, and thermodynamic and kinetics other sulfidation pathways, triangular vs. chain comparison, and frequency analysis are reported in Appendix-B. We will refer to these details in the following part of the chapter wherever it is needed.

4.2. Methods

For all total energy calculation, density functional theory (DFT) as implemented in VASP[232–234] has been used relying on the Perdew-Burke-Ernzerhof (PBE)[176] functional within the framework of generalized gradient approximation (GGA). The long-range interactions were included through a density-dependent dispersion correction (dDsC).[177, 178] The projector augmented-wave (PAW) method[235] was chosen to describe the electron-ion interaction. The kinetic energy cut-off for the plane-wave basis

set has been fixed at 400 eV. Furthermore, for the minimization of the electronic energy, Gaussian smearing with a width of 0.2 eV was chosen.

A mixture of the blocked-Davidson scheme and residual minimization method direct inversion in the iterative subspace has been applied. Spin-polarized calculations were performed to obtain the ground state of the clusters. Electronic convergence was assumed to be achieved at 10^{-5} eV. For geometry optimization, the conjugate gradient algorithm was used. Geometric convergence cut-off has been set to 0.02 eV/Å.

All structures have been optimized for frequency calculations with tighter convergence criteria such as 10^{-7} eV for electronic properties and 0.01 eV/Å for geometry. The finite difference method has been used to calculate the frequencies and the DFPT method to simulate the IR spectra as implemented in VASP.

For determining the adsorption energy (ΔE) of the starting Mo_nO_{3n} (n=1 to 3) oxides oligomers on alumina at 0 K, the following equation was used:

$$\gamma - \mathbf{Al_2O_3} + \mathbf{n} \times \mathbf{MoO_{3(bulk)}} \rightarrow \mathbf{Mo_nO_{3n}}@\gamma - \mathbf{Al_2O_3} \qquad \textbf{4-1}$$

$$\mathbf{\Delta E} = \frac{\mathbf{1}}{\mathbf{n}}\left[\mathbf{E}(\mathbf{Mo_nO_{3n}}@\gamma - \mathbf{Al_2O_3}) - \mathbf{n} \times \mathbf{E}\left(\mathbf{MoO_{3(bulk)}}\right) - \mathbf{E}(\gamma - \mathbf{Al_2O_3})\right] \qquad \textbf{4-2}$$

where $E(Mo_nO_{3n}@\gamma - Al_2O_3)$ is the electronic energy of the adsorbed Mo_nO_{3n} oligomers (n=1, 2 and 3), $E(MoO_3)$ is the energy of bulk-MoO_3 and $E(\gamma - Al_2O_3)$, the energy of the alumina slab representing the surface.

This study focused on the (100) surface of γ-alumina. This slab has been constructed following the procedure by Digne et al.[14, 15] according to the bulk alumina model defined by Krokidis et al.[135]. Moreover, it has been shown that in sulfur-reduction conditions as encountered in this work, the surface remains dehydrated and is not sulfided[132],[72](Figure **4-2**). We have relaxed the first two layers of the surface, and the bottom two layers have been kept fixed.

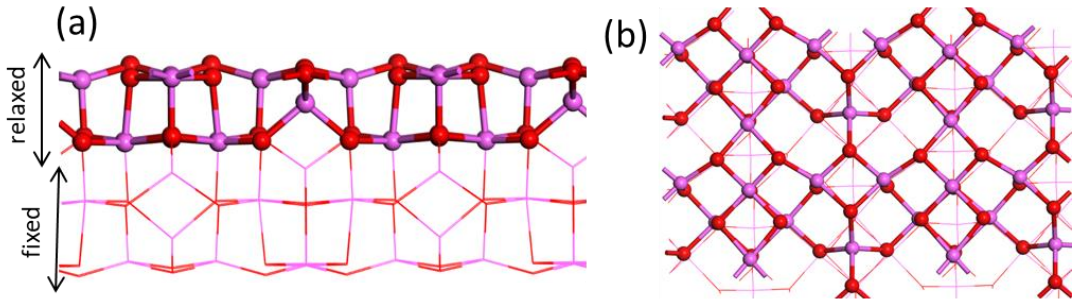

Figure 4-2: Molecular model of the (100) surface of γ-alumina[132]. a) side view and b) top view of the surface. Balls and sticks represent the movable slab, and lines represent the fixed slab. (Color code–Red: O, pink: Al).

Once we have identified the most stable adsorption site for the Mo-oxide cluster on the surface, we assume that the adsorbed cluster will not move or diffuse on the surface in the course of the sulfo-reduction mechanism. This assumption is based on the strong Mo-oxide or Mo-oxysulfide support interaction shown later in the results section. This does not exclude that locally the anchoring sites evolve as a function of sulfidation.

To determine the O/S exchange thermochemistry energy at 0K, which occurs through H_2S adsorption either on oxide-cluster or support, we used the following equation:

$$\mathbf{Mo_nO_{3n}@\gamma - Al_2O_3 + xH_2S \rightarrow Mo_nO_{3n-x}S_x@\gamma - Al_2O_3 + xH_2O} \qquad \textbf{4-3}$$

$$\mathbf{\Delta E = [E(Mo_nO_{3n-x}S_x@\gamma - Al_2O_3) + xE(H_2O) - E(Mo_nO_{3n}@\gamma - Al_2O_3) - xE(H_2S)]} \qquad \textbf{4-4}$$

where $E(Mo_nO_{3n-x}S_x@\gamma - Al_2O_3)$ is the energy of alumina supported oxysulfide after x number of O/S exchanges, $E(H_2O)$ is the energy of water, $E(Mo_nO_{3n}@\gamma - Al_2O_3)$ is the energy of pure oxide, and $E(H_2S)$ is the energy of H_2S. To calculate the energy change during a single O/S exchange, we have used the following equation:

$$\boldsymbol{Mo_nO_{3n-x}S_x}@\gamma \mathbf{- Al_2O_3 + H_2S \rightarrow} \boldsymbol{Mo_nO_{3n-x-1}S_{x+1}}@\gamma \mathbf{- Al_2O_3 + H_2O} \qquad \textbf{4-5}$$

$$\mathbf{\Delta E = \begin{bmatrix} E(Mo_nO_{3n-x-1}S_{x+1}@\gamma - Al_2O_3) + E(H_2O) \\ -E(Mo_nO_{3n-x}S_x@\gamma - Al_2O_3) - E(H_2S) \end{bmatrix}} \qquad \textbf{4-6}$$

The reaction energy of the reduction of $Mo_nO_nS_{2n}$ oxysulfides or Mo_nS_{3n} trisulfides occurring under H_2 (g), was calculated according to :

$$\mathbf{Mo_nO_{n-x}S_{2n}@\gamma - Al_2O_3 + H_2 \rightarrow Mo_nO_{n-x-1}S_{2n} \ @\gamma - Al_2O_3 + H_2O} \qquad \textbf{4-7}$$

$$\mathbf{\Delta E = \left[E\left(Mo_nO_{n-x-1}S_{2n} \ @\gamma - Al_2O_3\right) + E(H_2O) - E(Mo_nO_{n-x}S_{2n}@\gamma - Al_2O_3) - E(H_2)\right]} \qquad \textbf{4-8}$$

where $E\left(Mo_nO_{n-x-1}S_{2n} \ @\gamma - Al_2O_3\right)$ is the energy of supported $Mo_nO_{n-x-1}S_{2n}$ intermediate oxysulfides.

The underlying assumption is that the reduction of oxysulfide starts when it reaches a S/Mo stoichiometry of 2. This assumption is based on our observation of the endothermic process of water removal from pure oxides by using H_2. Similarly, for the reduction of trisulfide (Mo_nS_{3n}) into disulfide oligomers (Mo_nS_{2n}) by H_2:

$$\boldsymbol{Mo_nS_{3n-x}}\mathbf{@\gamma - Al_2O_3 + \boldsymbol{H_2} \rightarrow \boldsymbol{Mo_nS_{3n-x-1}} \ @\gamma - Al_2O_3 + \boldsymbol{H_2S}} \qquad \textbf{4-9}$$

$$\mathbf{\Delta E = \left[E\left(Mo_nS_{3n-x-1} \ @\gamma - Al_2O_3\right) + E(H_2\boldsymbol{S}) - E(Mo_nS_{3n-x}@\gamma - Al_2O_3) - E(H_2)\right]} \qquad \textbf{4-10}$$

where, $E\left(Mo_nS_{3n-x-1} \ @\gamma - Al_2O_3\right)$ is the energy of supported Mo_nS_{3n-x-1} oligomer and $E(Mo_nS_{3n-x}@\gamma - Al_2O_3)$ is the energy of Mo_nS_{3n-x} oligomers.

During these sulfo-reduction steps into the final disulfides, we identify the limiting steps and corresponding activation energies. To determine the activation energy, we computed the energy of the transition state (TS). We used the Nudged Elastic Band (NEB) method in conjunction with constrained force-based optimizers to determine the geometry of the TS.[203, 208, 209, 213] To generate the intermediate images between reactant and product, we used the Opt'npath open-source code.[236] We performed the frequency calculations to confirm TS as a first-order saddle point on the potential energy surface with only one imaginary frequency, and that imaginary mode corresponds to the

restoring force along the direction of reactant or product from TS. We have used an open-source code to trace the reaction energy plots.[237]

All aforementioned electronic energies were corrected by the contribution of zero-point energy, thermal corrections at T=623K, and entropy in order to determine the vibrational free energy (details are given in the appendix-A) :

$$\boldsymbol{\Delta G = \Delta H - T\Delta S} \quad \textbf{4-11}$$

$$\mathbf{\Delta H = \Delta U + P\Delta V} \quad \textbf{4-12}$$

$$\mathbf{\Delta U(S) = \Delta U(S)_{ele} + \Delta U(S)_{\boldsymbol{vib}} + \Delta U(S)_{\boldsymbol{rot}}} \quad \textbf{4-13}$$

where $U(S)_{rot}$ and $U(S)_{trans}$ = 0, for adsorbed species assuming that the Mo_nO_{3n}, $Mo_nO_xS_{3n-x}$, and Mo_nS_{3n} clusters are immobile on the alumina surface due to anchoring points. We included the translations and rotational contributions for gas-phase molecules such as H_2O, H_2S, and H_2.

4.3. Results

4.3.1. Oxides precursors interaction with γ-alumina

Based on the experimental insights detailed above, we have chosen monomer (Mo_1O_3), dimer (Mo_2O_6), or trimer (Mo_3O_9) as the starting Mo-oxides dispersed on alumina. To determine the optimal interaction and the adsorption/anchoring sites of γ-alumina, we performed a careful preliminary exploration of the energetic stability of the Mo_1O_3, Mo_2O_6, and Mo_3O_9 species on the (100) γ-alumina surface.

4.3.1.1. Monomer and Dimer

Handzlik and Sautet previously investigated monomeric and dimeric Mo oxides in interaction with γ-alumina using DFT with PW91-GGA exchange correlational functional without dispersion corrections.[17, 153] We confirmed that the di-oxo Mo_1O_3 conformers adsorbed on (100) surface were found to be more stable by about 12 kJ.mol^{-1} than the mono-oxo one. However, the most stable adsorption site we found is different from the one reported by Handzlik and Sautet,[17] which may be due to an effect of dispersion corrections included in the present work. The energy difference between the two sites is

about 0.25 eV in favor of our revised data. In our revised configuration, we find slightly shorter Mo-O-Al (1.83 Å vs. 1.86 Å[17]) and Mo-O_{surf} (1.98 Å vs. 2.16 Å[17]) bonds featuring much stronger interaction between Mo-oxides and surface (Figure **4-3**a and b). For the dimeric species, we find the configuration illustrated in Figure **4-3**c, very similar to the one reported by Handzlik et al.: one Mo-atom bearing a mono-oxo species and another Mo bearing a di-oxo. Moreover, the formation energy of the supported dimer (with respect to supported monomers) is also consistent (115 kJ/mol vs. 123[153] kJ/mol).

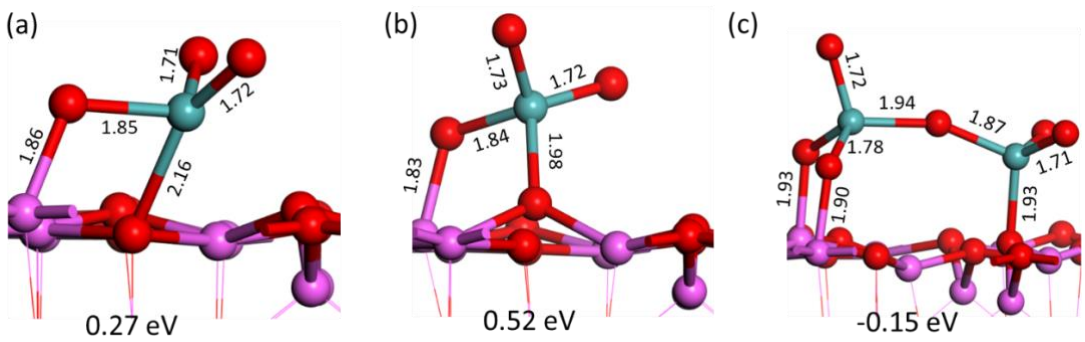

Figure 4-3: The most stable di-oxo conformers of Mo_1O_3 on alumina: a) most stable proposed by Handzlik and Sautet and b) most stable in this study, and c) conformers for Mo_2O_6. Bond lengths of various Mo-O and O-Al bonds are given in Å. The energy represented here is relative to bulk MoO_3 and normalized to one formula unit. (Color code–Red: O, Pink: Al, and Blue: Mo).

4.3.1.2. Trimer

As a natural extension of monomers and dimers, the interaction of Mo_3O_9 trimer with the same γ–alumina surface was analyzed. As for the Mo_3S_9 (Mo-trisulfide) clusters which can exhibit two main shapes: either a chain[35, 38, 41] or a triangular[40] one as proposed in previous experimental[35, 37, 40, 42, 56] and theoretical[38, 39, 220] works. Similarly, The Mo_3O_9 precursor may also exist in two families of conformers: either cyclic or chain-like (Figure **4-4**). The cyclic conformer is more stable than the chain by about 1 eV in the gas phase (Figure B-1), similar to our previous finding for Mo_3S_9 clusters in the gas phase.[220] However, the strong support effect induces an inversion of the relative stability of the two Mo_3O_9 conformers is inverted: the chain conformer becomes more stable by -0.42 eV. The support interaction enables the formation of new Mo-O-Al and Mo-

O_{surf} bonds, which prevent the under-coordination of Mo-atoms present in the chain and leads to an octahedral/square-pyramidal environment for Mo-atom that is more stable than tetrahedral. In the absence of support, the under-coordination of Mo atoms is stabilized by the Mo-O-Mo cyclization (B1.1). The interaction with support also impacts the nature of oxygen atoms which will be involved in the sulfur/oxygen exchange process, as described in the following.

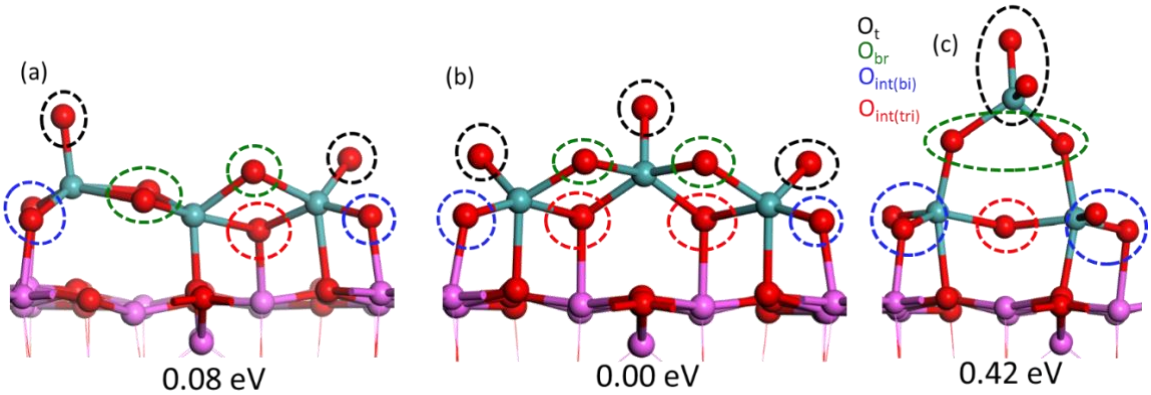

Figure 4-4: Most stable trimer (Mo_3O_9) on (100) surface of alumina. a) chain-1, b) chain-2 represent the most stable conformer, and c) represents the most stable cyclic. (Red: O, Pink: Al, and Blue: Mo).

There are four distinct classes of oxygens present in the Mo_3O_9-chain system (Table **4-1**): terminal oxo-species (O_t), bridging (O_{br}), interfacial-bidentate ($O_{int(bi)}$), and interfacial-tridentate ($O_{int(tri)}$) (Figure **4-4**). Terminal oxo-species (O_t) connected to one Mo center only. Bridging oxo- (O_{br}) bonded to two Mo-atoms (Mo-O-Mo) only. Interfacial-bidentate ($O_{int(bi)}$) are initial terminal oxo- that also interacts with the aluminum site of support, becoming bridging species (Mo-$O_{int(bi)}$-Al). Interfacial tridentate ($O_{int(tri)}$) are initial bridging oxo- that also becomes bonded to aluminum sites of support ($^{Mo-O-Mo}_{\quad Al}$). These different types of oxygen are present on the chain and triangular conformers (Figure **4-4**).

The most stable chain conformer of Mo_3O_9 on alumina exhibits three-terminal oxo (O_t) species (Figure **4-4**b), and the second most stable conformer has two O_t (Figure **4-4**a) species. Both conformers are thermodynamically equivalent (ΔE=~0.08 eV) while the local structures of two Mo atoms differ slightly from the relative positions of the types of Mo-sites. Both conformers contain a Mo atom in a distorted square pyramidal. This Mo is coordinated to five O belonging to the cluster. In one conformer, it is the central atom; in

the other one, it is one Mo atom located at the edge. Both structures contain two Mo-atoms with a distorted trigonal bipyramidal structure with four O ligands belonging to the cluster and one O to alumina. As a consequence, this implies that the distribution of O sites also differs (Table **4-1**): one chain conformer exhibits three interfacial O, whereas the second one exhibits four interfacial O, including two tridentate ones.

The structure of the most stable cyclic trimer is quite similar among the various conformers except for the local structure of the "central" Mo-atom located at a larger distance from the support. This central Mo-atom has a tetrahedral configuration(Figure **4-4**c), while the two other Mo-atoms are of distorted trigonal bipyramidal structure with 4 O ligands belonging to the cluster and one O to alumina. This cyclic trimer has two oxo species, two bridgings, four interfacial-bidentate, and one interfacial-tridentate type of oxygens. The chain and triangular both models exhibit the most stable conformer at the same adsorption site of alumina.

The support has thus a significant impact on the relative stability and structures of these MoO_3 oligomers with respect to their gas-phase structures. For Mo_1O_3, Mo_2O_6, and Mo_3O_9 (chain, cyclic), Mo-atom prefers mainly a tetrahedral structure in the gas phase (except the central atom of the chain, which exhibits the square pyramidal shape in the gas phase). On the support, Mo_3O_9 chain-conformer exhibit two isoenergetic structures called chain-1 and chain-2 in what follows.

Table 4-1: Various types of oxygen observed in the system (notation and their respective description).

Notation	Description	Chain-1	Chain-2	Cyclic
O_t	Terminal oxo- singularly bonded to one Mo atom	2	3	2
O_{br}	Bridging oxo- bonded to two Mo (Mo-O-Mo)	3	2	2
$O_{int(bi)}$	Interfacial oxygen bonded to one Mo and one Al of alumina (Mo-O-Al)	3	2	4

$O_{int(tri)}$	Interfacial oxygen bonded to two Mo of cluster and on Al of support (Mo—O—Mo / Al)	1	2	1
O_{surf}	Oxygen from support interacting with Mo of the cluster	2	2	2

4.3.2. Oxygen/Sulfur exchange Mo-oxides on alumina

4.3.2.3. Thermodynamic aspects

The supported oxide oligomers are expected to undergo a sulfo-reduction process to form oxysulfides or trisulfides intermediates, followed by their further transformation to the final disulfide phase. The cyclic conformers are more stable in the gas phase than the chain along the entire sulfidation path leading to the trisulfide phase (Figure B-5). By contrast, the support reverses this, which highlights the strong effect of alumina (Figure **4-5**). Thus, on alumina, we will focus on the chain conformers. The thermodynamic analysis of the oxygen/sulfur exchange involving H_2S as reactant and H_2O as a product (Figure **4-5**) will give insights into which oxygens are easily exchangeable and which ones are more energy demanding in order to select the most relevant paths for the subsequent kinetic analysis

According to the various types of oxygen sites identified earlier (Table **4-1**), we examined the O/S exchange for chain-1, chain-2, and cyclic (Figure **4-5**). Two possible paths (path-1 and -2) were found for the chain-1 conformer.

The O/S replacement on path-1 of chain-1 occurs in a more homogeneous way than on path-2 (Figure B-8 and Figure B-9). On path-1, the three Mo-atoms become all partially sulfided (connected to one S-atom, Figure B-8) at step 2 already, whereas on path-2, only two Mo-atoms are sulfided up till 5' (Figure B-9). The first two steps of path-1 and path-2 are similar and involve bridging O-sites in O/S exchange. However, the main difference arises at the third and fourth steps where path-1 replaces the terminal oxygen, while path-2 prefers the interfacial ($O_{int(bi)}$).

Even though step three is slightly less promising for path-2, the gain in free energy at the 4th step for path-2 is huge, about -0.8 eV (Figure **4-5**). This enhanced stability comes from the formation of S_2-dimer replacing two adjacent $O_{int(bi)}$ by S. Path-1 favors the replacement $O_{int(bi)}$ and $O_{int(tri)}$ after the bridging and terminal oxygen. At step seven, path-1 can be linked to path-2 by dissociation the half-bridged dimer formed at step 6 and creating a new dimer with S appeared at step 7. The dissociation requires activation energy of 0.45 eV, and the formation of new terminal S_2 dimer results in -0.5 eV stabilization.

Thus, we propose that either the two paths co-exist or that a mixed solution combining path-1 until step 7 and a transition to path-2 after step 7 will lead to the formation of the most stable chain-Mo_3S_9. Path-2 also discards the compatibility of chain-2 as the formed trisulfide is almost 1 eV less stable.

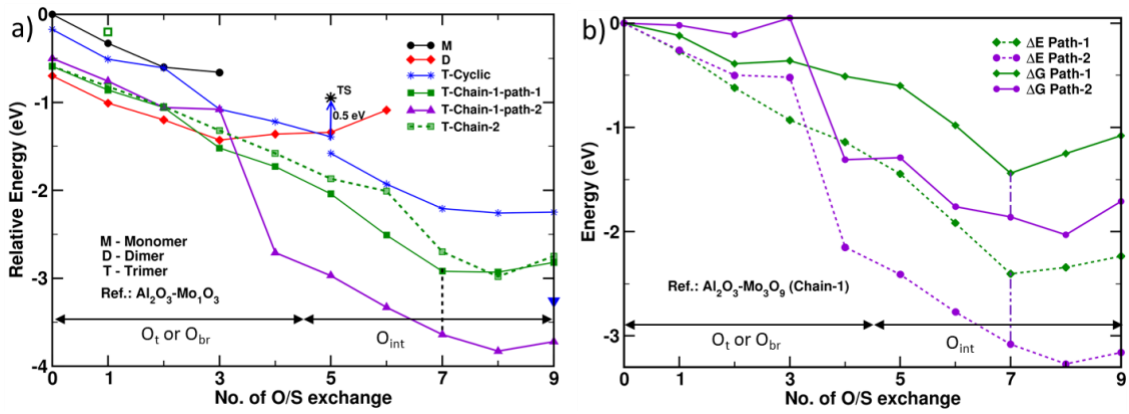

Figure 4-5: Thermodynamic energy profile of O/S exchange a) at 0 K for various Mo-oxide on alumina with alumina adsorbed Mo_1O_3 as a reference and b) electronic energy at 0 K and Gibbs free energy at 625 K for the chain-1-trimer Mo_3O_9 according to path-1 and path-2 with alumina adsorbed Mo_3O_9 as reference. The possible transition between Path-1 to Path-2 exists at step 7.

Chain-2 (Figure B-11) and cyclic (Figure B-7) conformers follow the general trend of O/S exchange: the bridging and terminal oxo-sites are being replaced first, followed by $O_{int(bi)}$ and $O_{int(tri)}$. The possibility of a similar effect of $O_{int(bi)}$ being replaced first and leading to the formation of S_2-dimer providing additional stability also exists for chain-2 and cyclic conformers. The appearance of the S_2-dimer increases the stability of chain-2 and cyclic by 0.44 eV and 0.46 eV from their non-dimer states, respectively. This observation is

consistent with an earlier DFT study of MoO_3 O/S exchange, where the S_2-dimer formation results in ~0.5 eV further stabilization.[164]

By following the O/S exchange path, the final cyclic Mo_3S_9 structure is less stable than the chain-1-path-2 and chain-1-path-1 structure. Actually, we also found another triangular trisulfide conformer that exhibits an intermediate level of stability between chain-1-path-2 and chain-1-path-1. We will come back to this point later in the discussion on structural reconstruction aspects.

The O/S exchange energy of bridging and terminal oxygens have a minor difference. Thus, they can be exchanged simultaneously from a thermodynamic perspective, while kinetics may play a significant role (see next section). Changing the $O_{int(tri)}$ instead of bridging/terminal oxygen cost almost 0.65 eV additional energy concerning terminal/bridging oxygen being exchanged. Every exchange step of the sulfidation is exergonic by about -0.2 eV to -0.5 eV except for the last three steps. Interestingly, this remains consistent in monomer, dimer, even in trimer chain-2, and cyclic also (Figure **4-5** a). This trend suggests that the last few O/S replacements are more arduous than earlier ones; however, to have a more coherent understanding, we must investigate the kinetics of the crucial oxygen types.

4.3.2.4. Structural and vibrational analysis of key intermediates

During the S/O replacement, various changes in the local chemical environment occur, resulting from the disappearance of several Mo-O bonds and the simultaneous formation of new Mo-S and S-S ones. We compare here some structural and spectroscopic descriptors of relevant oxide, oxysulfide, and trisulfide intermediates with EXAFS and IR/RAMAN data reported in the literature[27, 100, 106, 217, 238] and analyze their evolution.

For this spectroscopic analysis, we focus on the chain-1 conformers, which are the most favorable thermodynamically. The observation may slightly depend on the type of path we are considering since they may involve different conformer types. The structural conformers of the critical intermediates are shown in Figure **4-6**, and the respective

evolution of key Mo-O(S) bond lengths and coordination number in Figure **4-7** and compared with EXAFS values.[217, 222]

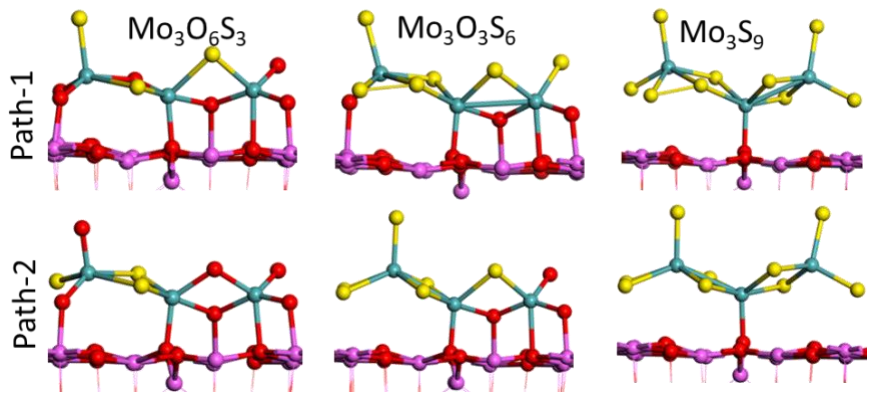

Figure 4-6: Key oxysulfides and trisulfides for path-1 and path-2 have been simulated to analyze IR spectra. (Red: O, Pink: Al, Blue: Mo, and Yellow: S.)

We observed similar local Mo-O descriptors for Mo-oxides as reported in the literature regarding the chain Mo-oxide species. However, these descriptors might occur in different sizes in the real systems depending on the preparation and the activation process. The terminal oxo-site exhibits the shortest Mo-O_t bond (calculated at 1.71 Å vs. 1.74 Å experimentally[100, 217]). Among all Mo-O bonds, the bridging oxo-site (Mo-O-Mo) reveals the longest bond at 2.10 Å (2.26 Å[106]). The interfacial oxygens (Mo-O-(Al) and Mo-O_{surf}) have an intermediate bond length around 1.86-2.28 Å (1.96Å [217]).

No short Mo-Al bond was seen for Mo-oxide species reported by some EXAFS data[100, 106, 222], but we observed a rather long one with a Mo-Al bond of 3.06 Å (3.06 Å[106, 217, 222]). The absence of a short Mo-Al bond is identified across the whole sulfidation steps of our models. Nonetheless, the presence of long Mo-Al is visible in oxides, oxysulfides and slowly vanishes in trisulfides. The oxysulfide species ($Mo_3O_6S_3$ and $Mo_3O_3S_6$) exist on two distinct pathways (Path-1 and Path-2), as discussed earlier. The so-called homogeneous Path-1 involves the replacement of terminal and bridging oxygen first and later the interfacial ones ($O_{int(tri)}$ and $O_{int(bi)}$), while the heterogeneous Path-2 exchanges the two bridgings followed by two $O_{int(bi)}$ out of three, then terminal ones, and finally $O_{int(tri)}$ and $O_{int(bi)}$, respectively.

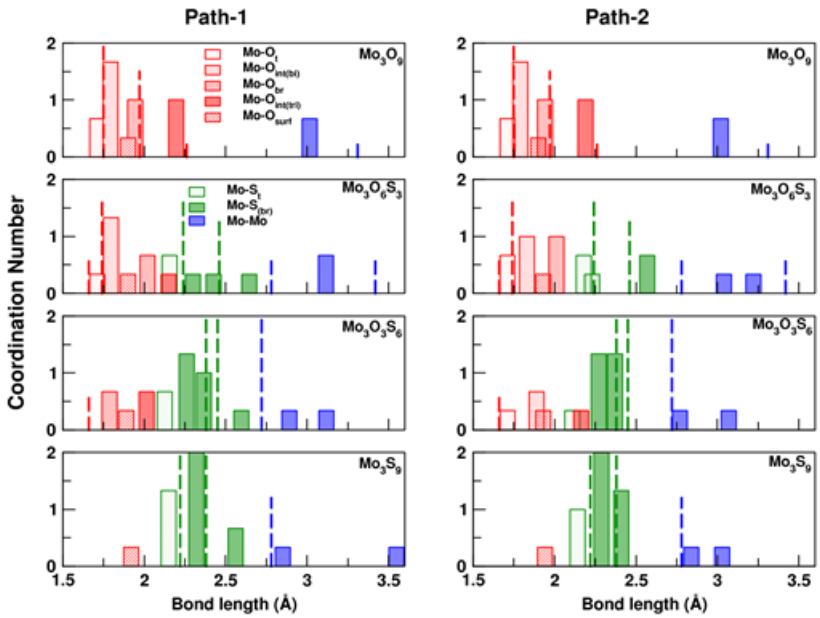

Figure 4-7: Evolution of various types of bond lengths and their coordination number for path-1 and path-2 during oxide to trisulfide sulfidation. The dashed lines represent the respective bond length with coordination number measured by EXAFS[217]. The coordination number is an average coordination number per Mo-atom (no. of bonds/3).

Oxysulfides ($Mo_3O_6S_3$ and $Mo_3O_3S_6$) contribute to several new emerging Mo-S bonds as more oxygens are replaced by sulfur from $Mo_3O_6S_3$ and $Mo_3O_3S_6$ (Figure **4-7**). For instance, new terminal Mo-S bonds of 2.14 Å (2.24 Å[217]) and Mo-S-Mo bonds of 2.41 Å (2.38 Å[217]) appear and are evidence of the presence of different S species such as S_2^{2-} and S^{2-} as also confirmed by IR/Raman,[27, 40, 217] while Mo-O_t may vanish as more S replaced the oxygen (Figure **4-7**). However, EXAFS revealed that the short Mo-O bond might be present in oxysulfides intermediates.

In some cases, only one small Mo-O bond (1.68 Å),[106] and in others, two Mo-O bonds (1.66Å and 1.74Å)[217] were observed. Nonetheless, it is not easy to precisely recognize the sulfidation stage of the intermediate identified by EXAFS that corresponds to our DFT calculations. EXAFS seems to indicate that the short Mo-O_t bonds still exist for intermediate components with a stoichiometry as $Mo_3O_2S_7$, which is a pretty late stage of S/O exchange[217] (Figure **4-7**).

For our investigation, if we follow Path-1, the terminal and bridging oxo are the first ones to be replaced, and the $Mo_3O_3S_6$ intermediates do not contain such Mo-O_t anymore. If we follow Path-2, the terminal would be retained until $Mo_3O_3S_6$, which is a slightly later stage of sulfidation for chain models. In the case of cyclic, we made an almost identical observation as for Path-1 (Figure **4-5**b and Figure B-7). Hence, this would mean that the heterogeneous path-2 where the sulfidation occurs on one part of the Mo-oxide, leaving the other part unsulfided seems to contribute to the EXAFS spectrum.

Mo-S bonds (2.41 Å) agree well with EXAFS (2.38 Å[100, 217]). The interaction between Mo-Mo becomes stronger as the Mo-Mo bond shrinks from 3.31 Å to 2.86 Å. Nevertheless, one long Mo-Mo bond always remains there, which seems to be not identified in the EXAFS of oxysulfide or trisulfide. Even though the trisulfide Mo_3S_9 species are formed, one Mo-O(-Al) bond (1.94 Å) involving the central Mo atom and one alumina-oxygen remain. According to some earlier studies, such residual Mo-O bond (measured at 2.06 Å) was proposed to come from oxygen atoms due to reluctant Mo-oxides/oxysulfide species that have not been fully sulfided.[226] However, we suspect that this Mo-O bond can also involve interfacial O atoms belonging to the alumina surface.

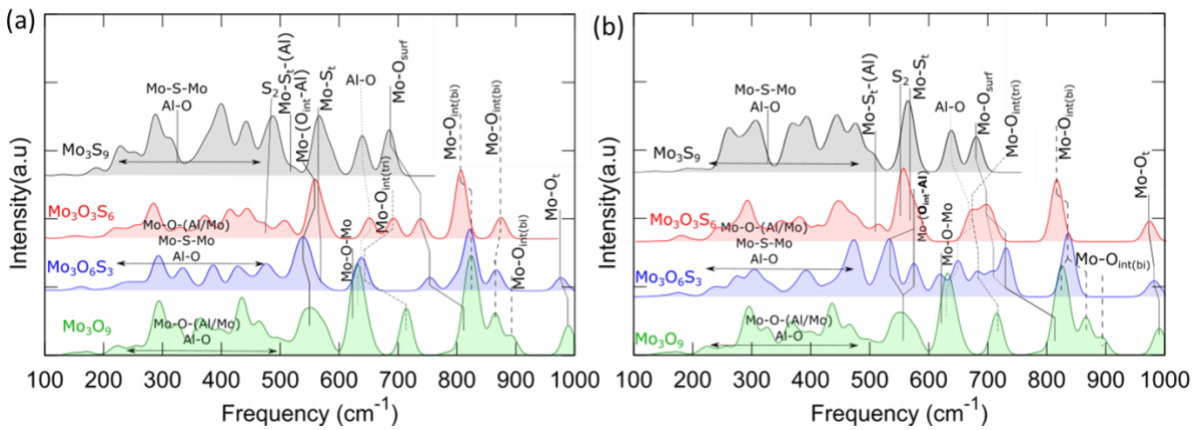

Figure 4-8: Simulated IR-spectrum for relevant intermediates during oxide to trisulfides transformation: a) Path-1 and b) Path-2.

The simulated IR spectrum of various Mo-oxides, oxysulfides, and trisulfides for Path-1 (Figure **4-8**a) and Path-2 (Figure **4-8**b) using a DFPT approach allows monitoring all the fundamental frequency modes of the oxysulfides clusters and their evolution during sulfidation. The contribution of alumina has been kept limited to the atoms located in the closest interacting region around the cluster (all other bulk atoms are being frozen).

Unambiguously, we recover the highest band at 980 cm^{-1} corresponding to the Mo-O_t vibrational mode;[27, 147] Mo-$O_{int(bi)}$ appears between 800 to 900 cm^{-1}. Mo-$O_{int(bi)}$ exhibits three peaks for three different Mo-O_{int} bonds due to variation in bond strength.

Interaction of Mo with surface oxygen peak occurs around 700-750 cm^{-1} (Mo-O_{Surf}). Interfacial tridentate have a lower frequency (715 cm^{-1}) than interfacial bidentate. All the lower modes appear below 500 cm^{-1} (combination of Mo-O-Mo, Al-O-Al, and Mo-O-Al). The modes concerned with alumina are present almost everywhere underneath. We see an apparent change in the simulated IR spectra going from oxide to trisulfide. As the bridging oxygens are being replaced, several Mo-O, Mo-O-Al, and Al-O-Al peaks start diminishing, mostly below 500 cm^{-1} ($Mo_3O_6S_3$), while new peaks of newly formed Mo-S-Mo appear (around 500 cm^{-1} and below). Similarly, when terminal oxygens are being exchanged, Mo-O_t peak disappears (about 980 cm^{-1}), and a new Mo-S_t peak arises at 560 cm^{-1}. As discussed for EXAFS, the disappearance of Mo-O_t peak occur at a later sulfidation degree for path-2.

Furthermore, a slight shift of Mo-O_t peak towards lower frequency is detected while increasing sulfidation, as reported in the literature.[27] The evolution towards lower frequency is even true for Mo-O_{int} and Mo-O_{surf} and indicates the weakening of the interaction between oxysulfides and alumina. Mo-O_{int}-Al also disappears as more and more S are being replaced, and Mo-S-Mo (below 430 cm^{-1}) and S_2-dimer (540 cm^{-1}) peaks come into existence. The spectroscopic analysis clearly shows structural changes during the transformation; though, the alumina modes underneath complicate this analysis somewhat.

4.3.3. Mechanism and kinetics of O/S exchange from MoO_3 to MoS_3 (step I and II)

After the detailed thermodynamic investigation, we focus now on the kinetics with the systematic determination of free energies of activations of the sulforeduction mechanisms (under H_2S/H_2) Mo_3O_9 supported on the alumina (100) surface. From preliminary calculations, we found that the reduction of Mo_3O_9 by hydrogen is endothermic (0.2 eV – 1.14 eV for first oxygen removal and 0.51 eV – 1.89 eV for the second oxygen removal). Thus, we assume hydrogen will not react at the first stage of the process to create O-vacancy on Mo_3O_9; instead, we must consider that O/S exchange

utilizing H_2S adsorption and H_2O removal is thermodynamically favored, which is in line with the proposal earlier made by Muijsers et al.[103].

However, we will address the question at which stage the reduction by H_2 becomes competitive with H_2S or even more advantageous. For simplicity, it is reasonable to assume that hydrogen will play its role after oxysulfides have enough S species to be transformed into MoS_2 without using additional H_2S to fulfill the requirement of deficient S. In that way, we can comprehend whether it is reasonable to undergo further sulfidation until MoS_3 (proposed by many experimental investigations[35, 36, 40, 104, 105, 216, 218, 219] or follow a more direct reduction from some oxysulfide intermediate to MoS_2 (as suggested by others[27, 98, 100, 216, 218]). Moreover, The hypothesis of using the first H_2S is also in line with some experimental observations that observed MoS_2 formation even without the explicit use of H_2.[104, 221] Thus, we will first focus on the role of H_2S and its reactivity on oxides/oxysulfides to trisulfides conversion (Figure **4-1** step-II), and further, we will analyze the possible role of H_2 to allow the transformation either from trisulfide to disulfide (Figure **4-1**, step-IV), or from oxysulfide to disulfide (Figure **4-1**, step-III)

Oxygen to sulfur exchange by H_2S will involve four crucial steps: i) adsorption and activation of H_2S, ii) H_2S dissociation with the formation of SH, OH, iii) proton transfer (formation of H_2O), and iv) desorption of water.

i)	$* + H_2S(g) \rightarrow *\text{-}SH_2$	H_2S adsorption
ii)	$*\text{-}O + *\text{-}SH_2 \rightarrow *\text{-}OH + *\text{-}SH$	H_2S dissociation
iii)	$*\text{-}OH + *\text{-}SH \rightarrow *\text{-}OH_2 + *\text{-}S$	Proton transfer
iv)	$*\text{-}OH_2 \rightarrow * + H_2O(g)$	H_2O desorption
Total	$*\text{-}O + H_2S\ (g) \rightarrow *\text{-}S + H_2O\ (g)$	

Apart from these four main steps, there might be some supplementary ones such as SH or OH reorientation, S migration. We have examined all four types of oxygen sites as described in Figure **4-4** and their respective O/S replacement mechanism steps.

According to the previous thermodynamic investigation, bridging/terminal oxygen are the easiest ones to be replaced, and interfacial ones can be challenging.

4.3.3.5. Bridging-oxygen sites

Adsorption and activation of H_2S would be the first step towards sulfidation of the starting Mo_3O_9 oxide. The adsorption energy (0 K) is exothermic at -0.48 eV (Figure **4-9** and Figure B-13). However, by applying entropy and thermal corrections, this step becomes endergonic at 625 K ($\Delta G_{br_{0\to1}} = +0.55$ eV) due to the loss of rotational and translational degrees of freedom of H_2S from the gas phase to the adsorbed state. Since the targeted replaceable oxygen atoms are the bridging ones, we restrict the adsorption Mo-sites closer to the reactive site. The central Mo-atom was observed to have the strongest capacity to hold H_2S. The availability of its octahedral environment with one empty site makes it the natural choice for H_2S adsorption. However, we explore the other possible adsorption sites in close proximity.

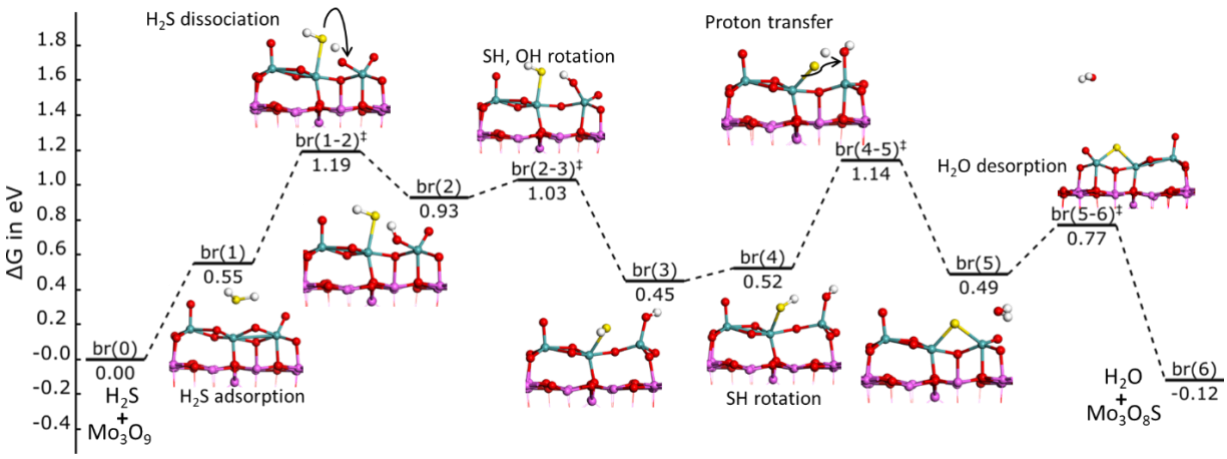

Figure 4-9: Free energy profile of O/S exchange involving bridging oxygen and H_2S. (Red: O, Blue: Mo, Pink: Al, Yellow: S, and White: H)

Then the H_2S dissociation and proton moves to the targeted oxygen is the next step. The activation free energy for this H_2S dissociation is $\Delta G^{\ddagger}{}_{br_{1\to2}} = +0.64$ eV, which is expected

to be accessible in sulforeductive conditions (T = 625 K). The H_2S is dissociated; after that, one of its protons is transferred to the bridging oxygen leading to the scission of one Mo-O bond and the simultaneous formation of one OH group. Consequently, the Mo-S bond evolves as H_2S dissociates (from 2.79 Å as H_2S to 2.42 Å as SH), and the strong interaction of the SH group with the Mo-site is suspected to be enforced with respect to H_2S.

It can be observed that the energy of the product is quite close to the TS energy (br(2) and br(2-3)‡, $\Delta G^{\ddagger}{}_{br_{2\to3}} = +0.10$ eV) due to their structural similarity. A slight internal arrangement, SH, OH rotation, occurs before the next proton transfer, which involves weak activation energy around 0.07 eV - 0.15 eV (activation for H-rotation is not shown here), which is far lower than the barrier of other key steps. Therefore, it is reasonable to neglect these activation steps and assume that they will not significantly impact the overall process.

After these rearrangements, the proton transfer step occurs and is coupled with S migration from top to bridging site with water formation. It is essential to underline that the S bridging process is mandatory to promote water formation and further desorption; otherwise, the undercoordinated Mo-site is highly unstable. The free energy of activation of this step is $\Delta G^{\ddagger}{}_{br_{4\to5}} = +0.62$ eV, which is somewhat similar to the first one.

The final step concerns the removal of water which exhibit about free energy of activation of $\Delta G^{\ddagger}{}_{br_{5\to6}} = +0.28$ eV. The entropy of water makes the overall path slightly exergonic (-0.12 eV). All the bridging oxygen have similar local chemical environments; as a result, we assume that the kinetics of other bridging oxygen would not differ significantly from what we have seen in this case. Therefore, all the bridging oxygen will exhibit a similar activation free energy of $\Delta G^{\ddagger}{}_{br} = \sim 1.2$ eV.

4.3.3.6. Top-oxygen sites

According to the preliminary thermodynamic study, terminal oxygen would not differ significantly from bridging oxygens, albeit the kinetics may vary greatly. Therefore, we explored the O/S exchange mechanism for terminal oxygen on a $Mo_3O_7S_2$ oxysulfide where the two bridging atoms have been substituted (Figure **4-10**). The same central Mo-

site exhibits a slightly weaker molecular adsorption of H_2S, consequently higher $\Delta G_{t_{0\to1}} = +0.79$ eV in contrast with the previously discussed O/S exchange. Moreover, the free energy of H_2S dissociation is about +0.97 with a corresponding activation free energy barrier ($\Delta G^{\ddagger}{}_{t_{1\to2}} = +0.18$ eV) that is lower than the bridging O/S exchange due to the proximity of available terminal oxygen, and no Mo-O bond scission is required at this step. Here again, the energy of the product is similar to the TS (t(1-2) and t(2)) due to their structural similarity.

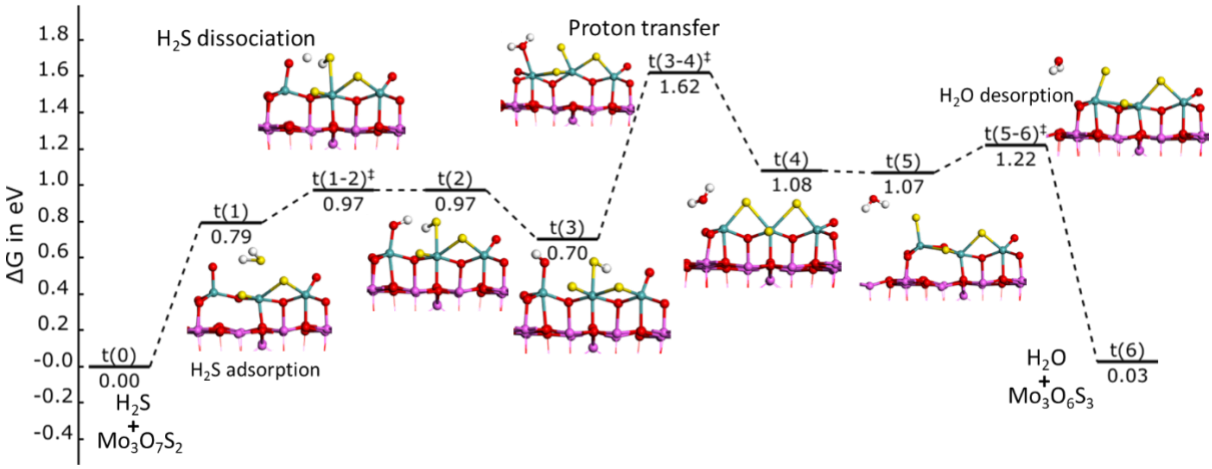

Figure 4-10: Free energy profile of O/S exchange involving terminal oxygen and H_2S. (Red: O, Blue: Mo, Pink: Al, Yellow: S, and White: H)

After subsequent SH/OH rotation (t(2) → t(3)), the second proton transfer takes place. This step is also coupled with S migration (from top to bridging site) in a similar manner as the bridging O. The proton transfer associated with S migration is the rate-limiting step for terminal O/S exchange, and it is significantly higher (+0.43 eV) than the rate-limiting step of bridging one with the cost of $\Delta G^{\ddagger}{}_{t_{3\to4}} = +0.92$ eV activation energy. The excessive activation energy could be because of a concerted mechanism. After water formation, migration of S from bridging site to top site is one more easy, intermediate step that is a precursor to the water desorption.

No activation was observed for S migration in this case. $\Delta G^{\ddagger}{}_{t_{5\to6}} = +0.15$ eV energy is required to take out the water from the system. As in the previous case (bridging), the S atom stabilizes the O-vacancies on top of the Mo site, which also justifies why the S/O exchange is preferred to the alternative direct O-removal by H_2, for instance. The creation of O-vacancies on top of the Mo site in the Mo_3O_9 cluster upon H_2/H_2O exchange is

thermodynamically energy demanding (1.14 eV to 1.76 eV at 0K) due to the instability of the corresponding Mo_3O_{9-x} cluster (See B2.1 Figure B-6). In the presence of H_2S, the O-vacancy site is thus immediately cauterized by the S atom.

4.3.3.7. Interfacial-bidentate oxygen sites

Until now, all the bridging and terminal oxygens are being replaced, and we reach the point where the interfacial oxygens, apparently the difficult ones, are needed to be exchanged using H_2S. We consider a $Mo_3O_4S_5$ oxysulfide where sulfide species have replaced all bridging and top oxo sites for this step. Now we will shine the light on the mechanism of interfacial oxygen sites, which seem to be the most challenging ones according to our thermodynamic analysis. Interfacial oxygen can be considered as top/bridging sites that interact directly with Al through Mo-O-Al linkage. There are two intrinsic complexities for these oxygens being sulfided: their sterical accessibility for adsorbed H_2S and their stronger interaction with alumina. The adsorption of H_2S on the central Mo-atom is relatively weak compared to the previous stage of sulfidation. Most of the interfacial oxygen would not be accessible with such pre-adsorbed H_2S on this site. Consequently, we had to consider that H_2S is adsorbed on one of the Al sites of support located in the close vicinity of the interfacial oxygen to be exchanged.

As support sites initiate the reaction mechanism, some intermediate steps might differ from the previous steps, but the four key steps for the exchange process will remain unaffected. H_2S is adsorbed on support exhibits a stronger interaction than that on Mo-site. The strength of H_2S adsorption on support may vary depending on the adsorption site and the orientation of H_2S. For example, H_2S adsorption for $O_{int(bi)}$ and $O_{int(tri)}$ differs by 0.18 eV (at 0 K). Both are adsorbed on the octahedral site of Al and differs by a 45° rotation of H_2S. Better hydrogen bonding through the oxygen of support (2.72 Å vs. 3.36 Å) and direct access to the octahedral Al site for H_2S adsorption (2.58 Å vs. 2.76 Å) contribute to the additional stability. At 625 K, $\Delta G_{int-bi_{0\rightarrow1}} = +0.43$ eV is needed for the adsorption step (Figure **4-11**).

After the adsorption of H_2S on support, H_2S dissociates by migrating the hydrogen to the replaceable oxygen with the activation energy of $\Delta G^{\ddagger}{}_{int-bi_{1\rightarrow2}} = +1.39$ eV. A relatively large distance between O to be protonated and S (S—H--O) coming from H_2S could be a reason for significantly high activation free energy compared to previous cases. No

intermediate can be observed along the axis of O—H—S but found perpendicular to it. The reason we suspect is the O coordination with Al and Mo no available orbital to interact with H. Moreover, this proton transfer weakens the associated Mo-O bond (2.03 Å vs. 1.81 Å). H_2S dissociation is the rate-limiting step for this O/S exchange path. Contrary to the bridging O site of the cluster, neither Mo-O nor Al-O bond scission occurs during the H_2S dissociation, suggesting that the O atom is weakly destabilized and forms μ_2-OH (Figure **4-11**).

Furthermore, the instability of SH on the Al site keeps the other intermediates at high energy. This SH group and the subsequent S atom are more stable on Mo-site by 0.54 eV and 0.2 eV, respectively than on Al-site. Therefore, the overall path remains at a high energy level. After SH rotation, the proton transfer step also occurs at relatively high energy but lower than the first one ($\Delta G_{int-bi_{3\to4}} = +1.70$ eV vs. $\Delta G_{int-bi_{1\to2}} = +1.82$ eV). This second transfer induces water formation associated with Mo-O bond weakening (2.03 Å vs. 2.05 Å). After water formation, the H_2O molecule remains to adsorb to the Al site of the support and diffuse on the support before desorbing. In parallel, the S atom formed on the support migrates to the cluster and bonds with a bridging S atom. Though these steps are not exhibiting higher activation energies, they make the overall exchange mechanism much more complex(Figure **4-11**).

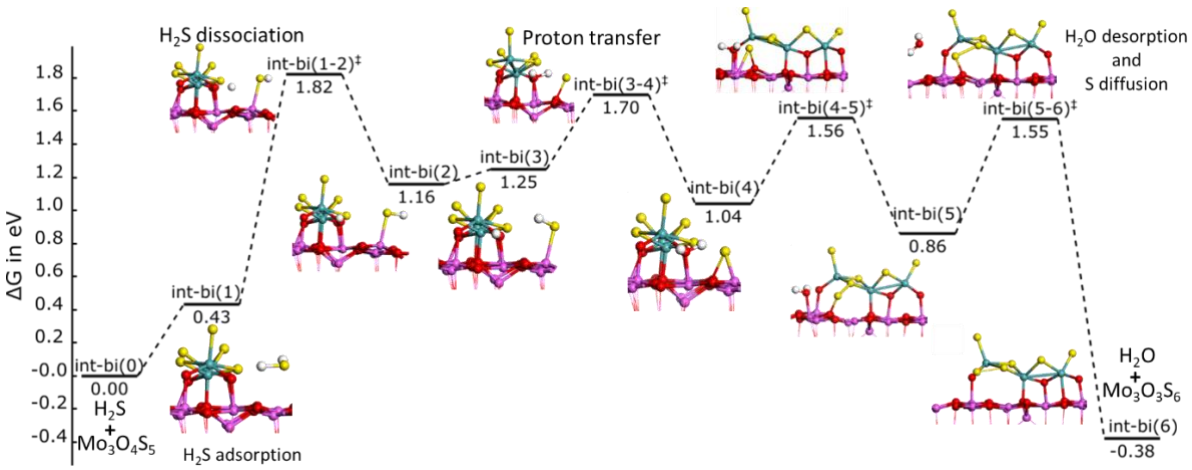

Figure 4-11: Free energy profile of O/S exchange involving interfacial bidentate oxygen and H_2S. (Red: O, Blue: Mo, Pink: Al, Yellow: S, and White: H)

4.3.3.8. Interfacial-tridentate oxygen site

We consider a MoO_2S_7 oxysulfide containing one $O_{int(bi)}$ and one $O_{int(tri)}$ site for this step. The alumina adsorption site for H_2S adsorption ($\Delta G_{int-tri_{0\to1}} = +0.37$ eV) is similar to

the previous case, while the subsequent mechanism will be significantly different. Indeed, the hydrogen of H_2S cannot directly reach the targeted oxygen site; it has first to diffuse on the alumina surface. Hence, the H_2S dissociation occurs by hydrogen migration from the S-atom of H_2S to a neighboring alumina μ_3-oxygen and transforms into μ_2-OH with a weak activation energy of $\Delta G^{\ddagger}{}_{int-tri_{1\to2}} = +0.37$ eV (Figure **4-12**). Thereafter, it is transferred to the $O_{int(tri)}$ atom forming μ_3-OH. This H_2S dissociation exhibits a rather high activation free energy ($\Delta G^{\ddagger}{}_{int-tri_{2\to3}} = +1.00$ eV).

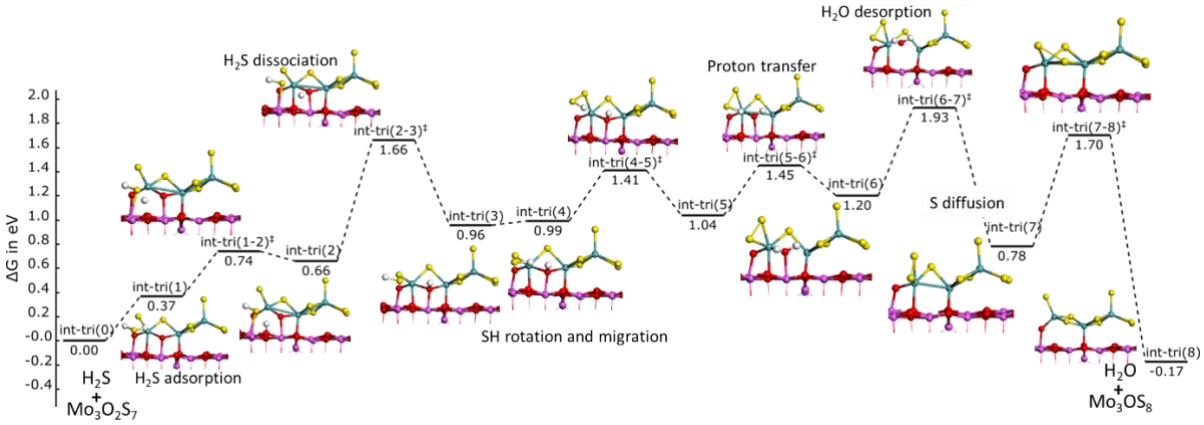

Figure 4-12: Free energy profile of O/S exchange involving interfacial tridentate oxygen and H_2S. (Red: O, Blue: Mo, Pink: Al, Yellow: S, and White: H)

As for the $O_{int(bi)}$, none of the Mo-O or Al-O bonds is broken, so that a μ_3-OH group is formed, and resulting the energy levels will remain relatively high along the reaction path. At this moment, the SH proton is not within the proximity of the $O_{int(tri)}$, and the S atom is also too far away to exchange it. After SH rotation, this group diffuses on alumina and binds to an available terminal sulfide to form a Mo-S-S-H species with a lower activation free energy ($\Delta G^{\ddagger}{}_{int-tri_{4\to5}} = +0.42$ eV). Through this S-S-H species, the proton is more easily accessible to oxygen and can be transferred smoothly with a moderate activation free energy of $\Delta G^{\ddagger}{}_{int-tri_{5\to6}} = +0.41$ eV (Figure **4-12**).

Once water is formed; one Mo-O bond is broken while keeping water in strong interaction with alumina and Mo, which makes the water desorption step very demanding with $\Delta G^{\ddagger}{}_{int-tri_{6\to7}} = +0.73$ eV, similar to the $O_{int(bi)}$ site in contrast with water desorption from the cluster. In general, we observe that water desorption from support is kinetically more limited than from the Mo site of the cluster (~0.7 eV vs. 0.23 eV), where the exchanged S atom helps for this step. After the desorption of water, the O-vacancy should be replaced by S, which currently exists as S-S dimer with terminal S. The splitting of the S-S bond requires an activation free energy of $\Delta G^{\ddagger}{}_{int-tri_{7\to8}} = +0.92$ eV (Figure **4-12**).

4.3.4. Transformation of Mo_3S_9 trisulfides into Mo_3S_6 disulfides (step IV)

In this section, we focus on the further transformation of Mo-trisulfide into disulfide species and its kinetics. This corresponds to step IV in Figure **4-1**, where only H_2 can be involved as reactant and H_2S is produced. The three main elementary steps are i) adsorption of H_2, ii) dissociation of H_2 leading to the formation of SH, SH, iii) proton transfer, and iv) H_2S desorption.

i)	2 *-S + H_2 → *-SH + *-SH	H_2 activation
ii)	*-SH + *-SH → *-SH_2 + *-S	Proton transfer
iii)	*-SH_2 → * + H_2S (g)	H_2S desorption
Total:	*-S + H_2 → * + H_2S (g)	

Like in previous cases, some intermediate SH reorientation and S diffusion or rearrangement will be involved. The thermodynamic diagram in Figure **4-13**a indicates that the removing first S from alumina supported-Mo_3S_9 is endothermic by 0.24 eV. However, the subsequent second step is exergonic (-0.5 eV), and the third is thermodynamically neutral (0.09 eV). The gain in energy during second S removal comes from reconstructing the cluster (chain-like conformer to triangular-like conformer). Though thermodynamics is not energetically limiting but kinetic can be.

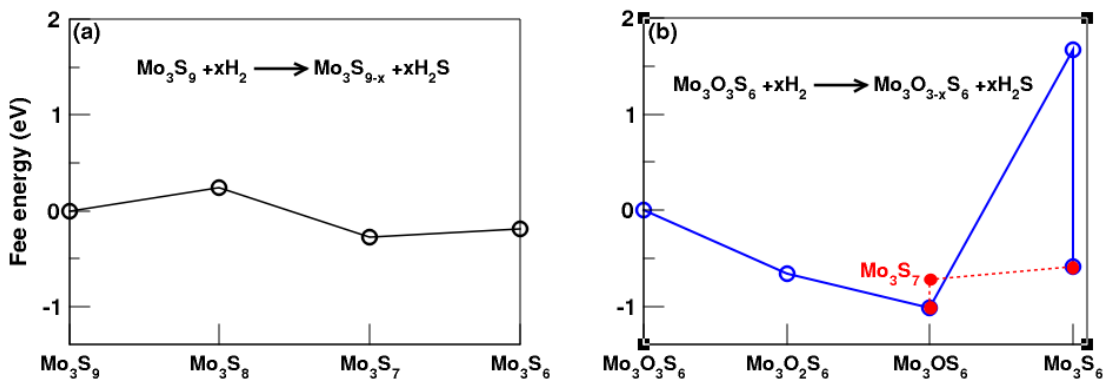

Figure 4-13: Thermodynamic energy plot for a) trisulfide to disulfide transformation and b) oxysulfide to disulfide reduction by H_2.

4.3.4.9. $Mo_3S_9 + H_2 \rightarrow Mo_3S_8 + H_2S$

It must be underlined that several Mo_3S_9 conformers have been proposed in the literature, such as triangular[39, 40, 123] or chain-like ones.[34, 37, 38, 41, 42] We have tested both, and we found that the chain-like one is more stable by 0.46 eV on the alumina support. This trend is inverted in the gas phase, where the triangular conformer is predominant for such a small size; the gas phase MoS_3 polymorphs will be discussed in the next chapter of this thesis in great detail.[220] The evolution of the stability as a function of size will be shown, and at which stage the chain-like species become more stable than triangular-like, which is more stable for the smallest size. Considering these species on the support, the interaction with the alumina site is thus a strong stabilizing factor for the chain conformer over triangular, involving significant reconstruction of the chain and triangular with respect to their gas-phase ground-state structures.

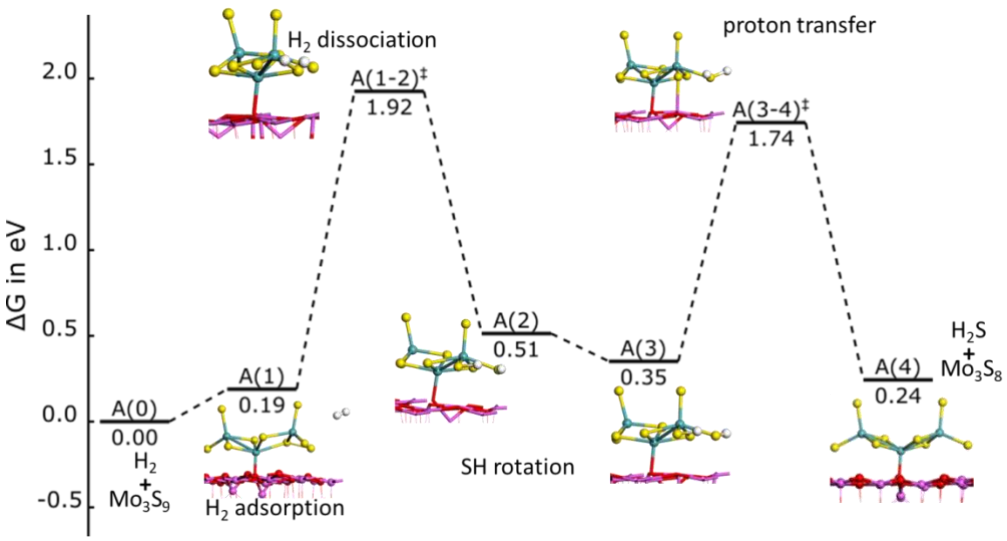

Figure 4-14: Free energy profile of S removal using H_2, $Mo_3S_9 + H_2 \rightarrow Mo_3S_8 + H_2S$. (Red: O, Blue: Mo, Pink: Al, Yellow: S, and White: H)

We screened the various possible sites for S removal and observed that the S_2 dimer is thermodynamically the most prominent one as it leads to a symmetrical structure. Since the activation free energy of breaking the S_2 dimer along with dissociative adsorption of H_2 is relatively high $\Delta G^{\ddagger}{}_{A_{1\rightarrow 2}} = +1.73$ eV (Figure **4-14**), this step would be a rate-limiting step. It is followed by SH rotation, and the third step is proton transfer from one SH to the neighboring SH leading to the formation of H_2S with activation energy ($\Delta G^{\ddagger}{}_{A_{3\rightarrow 4}}$) of +1.39 eV. The proton transfer and H_2S desorption are a concerted process. From Mo_3S_9 to Mo_3S_8**,** it must be noticed that the cluster remains in a chain-like conformer (Figure **4-14**).

4.3.4.10. $Mo_3S_8 + H_2 \rightarrow Mo_3S_7 + H_2S$ and $Mo_3S_7 + H_2 \rightarrow Mo_3S_6 + H_2S$

Analogous to the previous case, we screened different possible S sites for the second S removal. In this case, the bridging sulfur would be thermodynamically more advantageous than the terminal ones. Pulling out the bridging S creates a vacancy causing a strong reconstruction. As mentioned earlier, the first step would be H_2 dissociation that requires about $+1.25\ eV$ ($\Delta G^{\ddagger}{}_{B_{1\rightarrow 2}}$) as activation energy (Figure **4-15**). SH rotation leads to a slightly less stable intermediate that will be the precursor for further proton transfer.

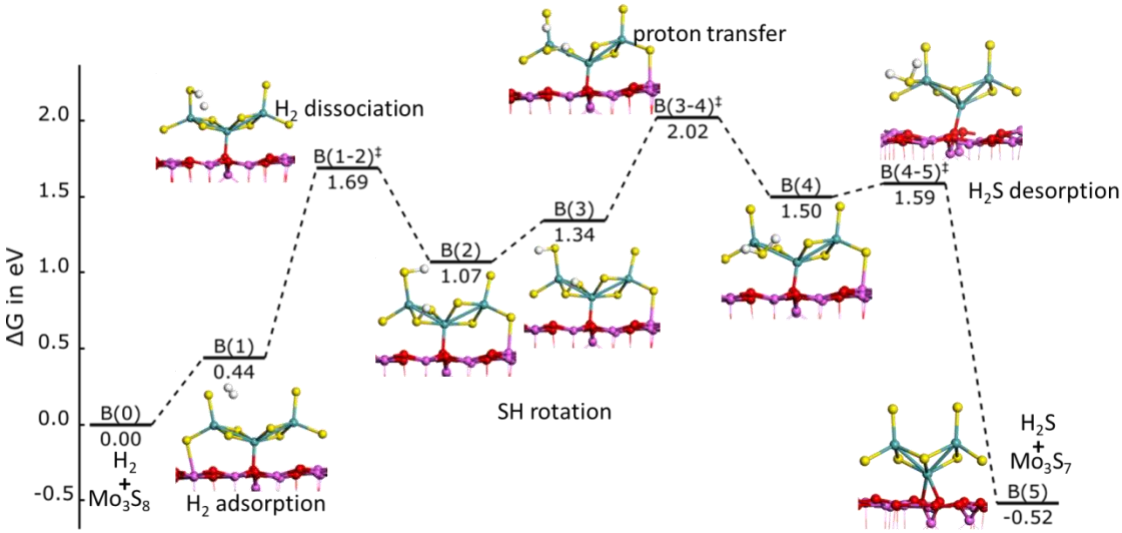

Figure 4-15: Free energy profile of S removal using H_2, $Mo_3S_8 + H_2 \rightarrow Mo_3S_7 + H_2S$. (Red: O, Blue: Mo, Pink: Al, Yellow: S, and White: H)

The proton transfer and the formation of H_2S requires $+0.68\ eV$ ($\Delta G^{\ddagger}{}_{B_{3\rightarrow 4}}$). Although the intrinsic activation energy of this step is not high, it is the highest TS of the whole path with overall activation energy for the path is $+2.02\ eV$ ($\Delta G^{\ddagger}{}_{B_{0\rightarrow 4}}$), so the proton transfer would be the rate-limiting step. The desorption of H_2S creates S vacancy and induces a reconstruction leading to the formation of a triangular conformer converting bridging sulfur (μ_2-S) into apical sulfur (μ_3-S). Surprisingly, this reconstruction step (B4→B5) occurs with a negligible barrier. Due to this reconstruction, the overall S-removal process from Mo_3S_8 into Mo_3S_7 is exergonic, contrasting with the previous endergonic S removal.

The remaining excessive sulfur of Mo_3S_7 is removed identically. Subsequently, after H_2 adsorption, it dissociates with an activation energy of $+1.27\ eV$ ($\Delta G^{\ddagger}{}_{C_{0\to2}}$) and a proton transfer exhibiting the highest TS at $+1.39\ eV$ ($\Delta G^{\ddagger}{}_{C_{0\to4}}$) followed by easy H_2S desorption (Figure **4-16**). This is the easiest S removal among the three involved ones. The proton transfer step is combined with S migration. As in the previous case, the H_2S removal is associated with a further reconstruction, and terminal μ_1-S converted into bridging μ_2-S, which closes the triangular ring of the Mo_3S_6 disulfide. This structure is reminiscent of the triangular pattern observed in MoS_2 phases. We will come back to this reconstruction in the discussion.

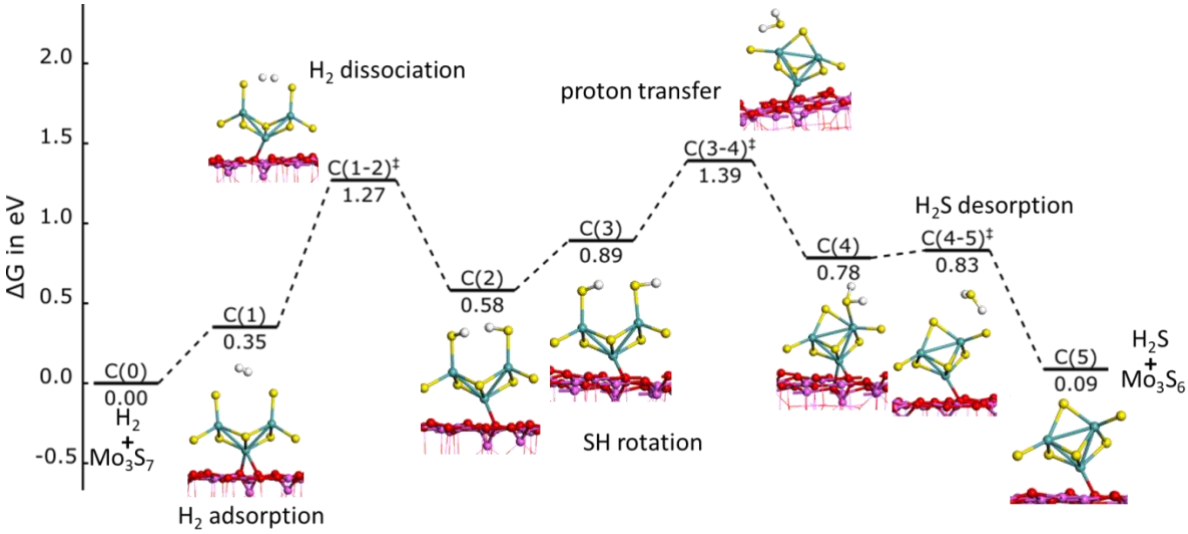

Figure 4-16: Free energy profile of S removal using H_2, Mo_3S_7 + H_2 → Mo_3S_6 +H_2S. (Red: O, Blue: Mo, Pink: Al, Yellow: S, and White: H)

4.3.5. Reduction of oxysulfides to disulfides by H_2 (step III)

$Mo_3O_3S_6$ has the suitable S/Mo stoichiometry to be directly transformed into Mo_3S_6 by H_2 reduction without the further use of H_2S. To determine the preferable site of O removal, we probed all the possible sites thermodynamically. After every step of removing O, cluster reconstruction takes place. The thermodynamic plot indicates that the first two steps are exergonic, but the final oxygen removal leads to a high energy intermediate (Figure **4-13**b). Therefore, we will propose an alternative path for sulfidation for this last oxygen. The mechanisms proposed here will be pretty similar to the one for the trisulfide Mo_3S_9 to disulfide Mo_3S_6 transformation: i) adsorption of H_2, ii) H_2 dissociation leads to the formation of SH, OH, iii) proton transfer from SH to OH group and formation of water, and finally, iv) water desorption.

i)	*-O+ *-S + H_2 → *-OH + *-SH	H_2 activation
ii)	*-OH + *-SH → *-OH_2 + *-S	Proton transfer
iii)	*-OH_2 → * + H_2O(g)	H_2O desorption
	Total: *-O + H_2 → * + H_2O (g)	

We examined the rate-limiting steps for oxygen removal (instead of S-removal as in the previous case). The final stable Mo_3S_6 cluster exhibits a triangular geometry (Figure **4-16**), whereas the current state of $Mo_3O_3S_6$ oxysulfide is linear (chain-like). Therefore, we will also investigate at which stage the chain to triangular transformation occurs. In $Mo_3O_3S_6$, all remaining oxygen sites are interfacial ones observed to be kinetically the most complicated ones for sulfidation. Investigating the role of hydrogen will help to comment on whether it is kinetically more promising to reduce the oxysulfide into disulfide or if the trisulfide pathway should be preferred.

4.3.5.11. $Mo_3O_3S_6 + H_2 \rightarrow Mo_3O_2S_6 + H_2O$ and $Mo_3O_2S_6 + H_2 \rightarrow Mo_3OS_6 + H_2O$

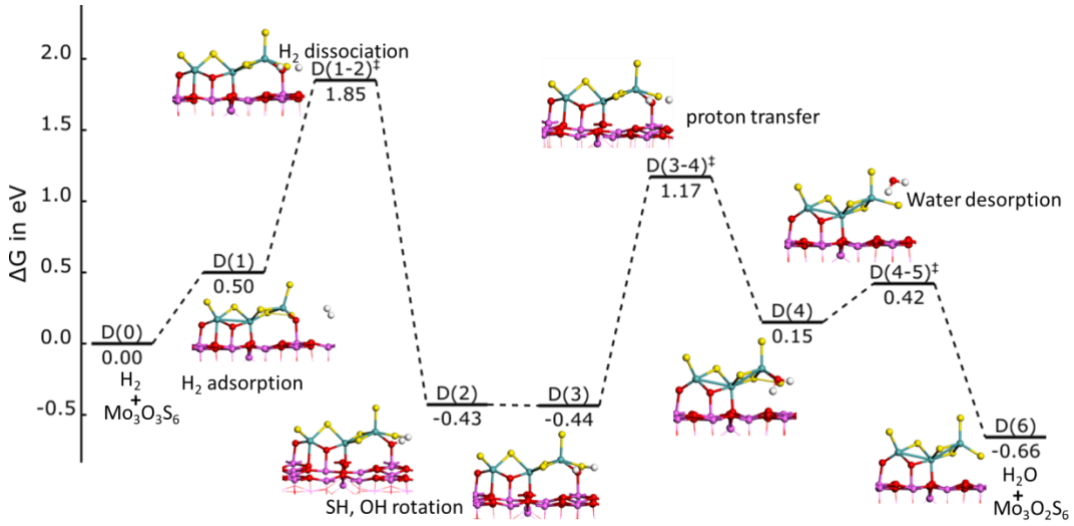

Figure 4-17: Free energy profile of oxygen removal according to the following reaction: $Mo_3O_3S_6 + H_2 \rightarrow Mo_3O_2S_6 + H_2S$. (Red: O, Blue: Mo, Pink: Al, Yellow: S, and White: H)

The activation free energies for H_2 dissociations are relatively high (+1.85 $(\Delta G^{\ddagger}{}_{D_{0\rightarrow 2}})$ and +1.91 eV $(\Delta G^{\ddagger}{}_{E_{0\rightarrow 2}})$ in both cases, this leads to the formation of one SH and one OH group (Figure **4-17** and Figure **4-18**). These values are similar to the activation for H_2

dissociation on Mo_3S_9 ($\Delta G^{\ddagger}{}_{A_{0\to2}} = +1.92\ eV$). This H_2 dissociation is followed by SH and OH rotations and proton transfer from SH to OH to produce H_2O. Interestingly, the water desorption is kinetically easier than in the case of O/S exchange ($\Delta G^{\ddagger}{}_{D_{4\to5}} = +0.39$ eV and $\Delta G^{\ddagger}{}_{int-tri_{6\to7}} = +0.73$ eV) However, in O/S exchange the S diffusion and water desorption are concerted, explaining the excessive energy cost for water desorption. In the $Mo_3O_2S_6 \to Mo_3OS_6$ transformation, after the removal of the water, a slight rearrangement with modest activation energy ($\Delta G^{\ddagger}{}_{E_{4\to5}} = +0.46\ eV$) leads to a triangular kind of Mo_3OS_6 entity as in the case of $Mo_3S_8 \to Mo_3S_7$.

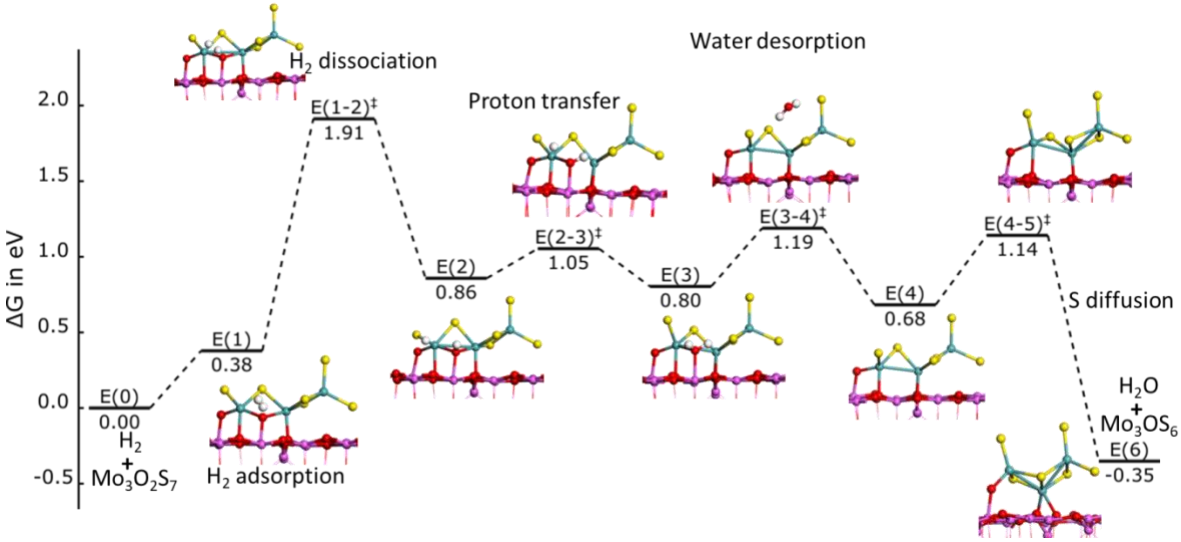

Figure 4-18: Free energy profile of oxygen removal according to the following reaction: $Mo_3O_2S_6 + H_2 \to Mo_3OS_6 + H_2S$. (Red: O, Blue: Mo, Pink: Al, Yellow: S, and White: H)

4.3.5.12. $Mo_3OS_6 + H_2S \to Mo_3S_7 + H_2$

Considering the last reduction step, $Mo_3OS_6 \to Mo_3S_6$, we found that the process is thermodynamically unfavorable ($+2.68\ eV$) because it goes through a high-energy Mo_3S_6 intermediate (Figure **4-22**) which must then reconstruct into the most stable triangular Mo_3S_6. Since removing the final oxygen seems to be a difficult step, we propose to come back to an O/S exchange process as already studied for the previous steps to overcome this issue. Similarly, the elementary steps combine H_2S adsorption, dissociation of H_2S, and formation of SH, OH groups, SH-OH reorientation, proton transfer that leads to water formation. The TS of the proton transfer exhibits the highest free energy level ($\Delta G^{\ddagger}{}_{F_{0\to5}} = +2.07\ eV$, Figure **4-19**). Once Mo_3S_7 is formed, it will follow the S removal path already studied before ($Mo_3S_7 \to Mo_3S_6$, Figure **4-16**).

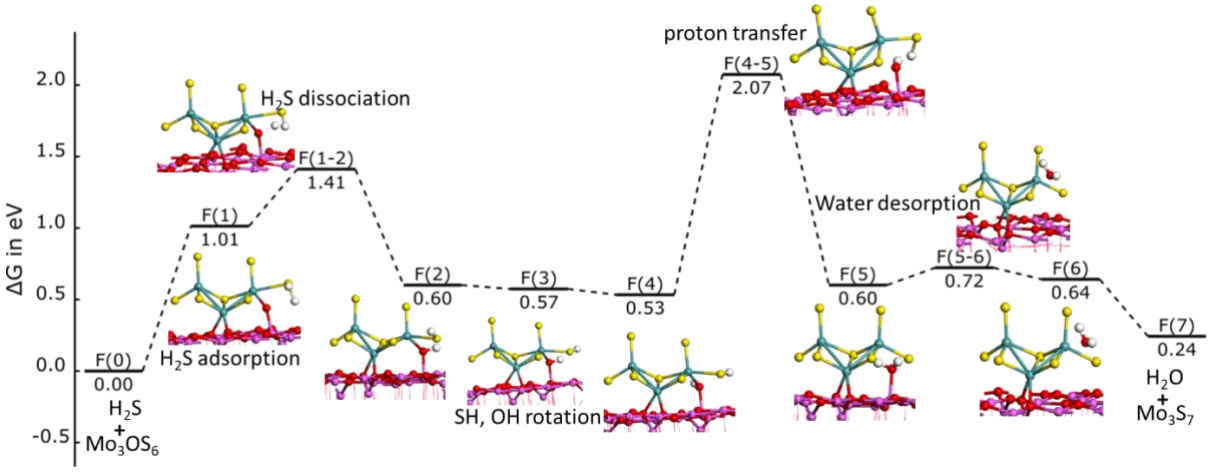

Figure 4-19: Free energy profile of O/S exchange involving interfacial tridentate oxygen and H_2S. ($Mo_3OS_6 + H_2S \rightarrow Mo_3S_7 + H_2O$). (Red: O, Blue: Mo, Pink: Al, Yellow: S, and White: H)

4.4. Discussion

4.4.6. Sulfidation from Mo_3O_9 to $Mo_3O_3S_6$ (step I)

Considering first Step I of Figure **4-1**, our study reveals that the sulfidation of highly dispersed small oxide species involves a S/O exchange mechanism, as previously proposed in the literature.[27, 103, 104] This mechanism involves four successive elementary steps: i) adsorption of H_2S on Mo site, ii) dissociation of H_2S by migrating the proton to neighboring O, iii) proton transfer from SH to OH resulting in water formation, and d) water desorption. In several cases, the first or the second proton transfer was the most energy-demanding step and would limit the reaction rate.

Simultaneously, we understand the nature of oxy-sulfide species and quantify their interaction with alumina support from thermodynamic and kinetic aspects. Though the thermodynamic energy favors the $O_{int(bi)}$ replacement to form S-S dimer, kinetically, these oxygens have greater energy demand, which might prohibit the sulfidation of these oxygens before bridging or terminal ones. Similarly, $O_{int(tri)}$ would be one of the last oxygens to be replaced due to the excessive energy barrier and lower accessibility.

If we consider the thermodynamic diagram (Figure **4-4**, Path-1 vs. Path-2), O/S exchange will follow path-1 at the early stage of sulfidation since bridging and terminal oxygens are

easily replaceable kinetically. It is also in line with some earlier DFT studies on different unsupported MoO_3 systems.[163–165] Nevertheless, once the second interfacial oxygen is being replaced ($Mo_3O_3S_6 \rightarrow Mo_3O_2S_7$), a transition from path-1 to path-2 should occur. Path-1 corresponds to a more homogeneous S/O exchange process, while path-2 involves the sulfidation of one side of the Mo_3O_9 cluster preferentially. If path-2 occurs preferentially, the oxysulfide intermediate such as $Mo_3O_3S_6$ will retain the oxo (terminal) species for a longer sulfidation degree, which would be compatible with EXAFS observations showing the presence of the smallest Mo-O bonds also for $Mo_3O_3S_6$.[106, 217]

By considering an energetic span analysis,[239] we compare the energies and free energies of activation of the TOF determining transition states (TDTS) as shown in Figure **4-20**. Analyzing first the effect of entropy and thermal corrections, we notice that these corrections increase the barriers by +0.6 eV to +0.8 eV for bridging and terminal oxygen, albeit the rate-limiting step remains unchanged. However, the barriers for $O_{int(bi)}$ and $O_{int(tri)}$ are increased by only +0.4 eV.

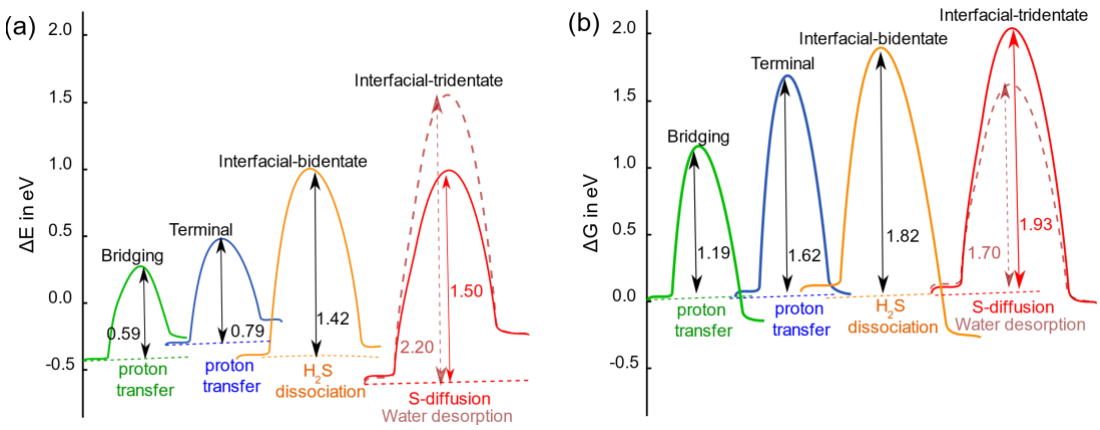

Figure 4-20: Step-II of Figure 4-1, a) Electronic energy comparison for various types of O/S exchange at 0K with respective rate-limiting step, activation energy barrier, and oxygen type. b) Gibbs free energy comparison various types of O/S exchange at 0K with respective rate-limiting step, activation energy barrier, and oxygen type.

This entropy effect is found to be directly proportional to the adsorption energy of H_2S either on the Mo cluster or on the support. The weakest H_2S adsorption is for terminal

oxygen (-0.34 eV) due to weak hydrogen bonding through present O/S on the cluster, and acquire the highest entropy effect +0.79 eV, leading to the more considerable enhancement in the activation energy difference of the terminal and bridging oxygen. Likewise, $O_{int\text{-}tri}$ has the most substantial adsorption (-0.67 eV) and obtain the weakest destabilization (+0.37 eV) due to entropy and thermal contributions. Consequently, including entropy and thermal contributions reveal that the activation free energies for O/S exchange between terminal oxo-species and interfacial O-species are less pronounced than without the corrections. The difference in activation energy of terminal and interfacial reduces to 0.2 eV, which makes even the terminal oxygens kinetically difficult to exchange while the bridging species are kinetically favored. Therefore, combining this kinetic results with the thermodynamics of path-1 and path-2 may explain why terminal oxo-species can remain present in $Mo_3O_3S_6$ as observed by EXAFS.[106, 217]

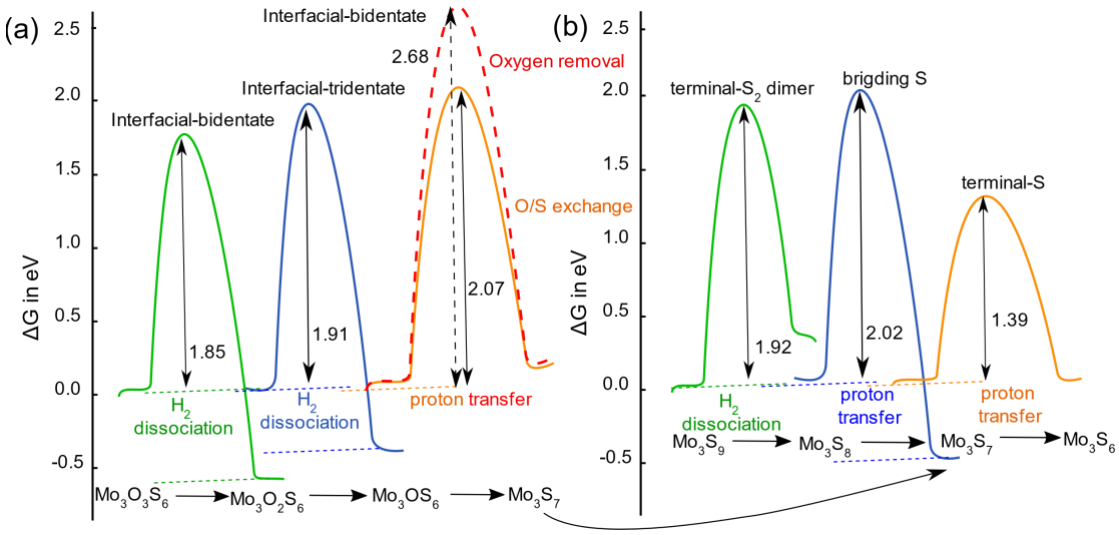

Figure 4-21: Free energy comparison of Mo_3S_6 formation following the a) oxysulfide reduction pathway step III and b) trisulfide reduction pathway step IV with respective rate-limiting step and involve oxygen or sulfur type.

4.4.7. Competition between sulfidation from $Mo_3O_3S_6$ to Mo_3S_9 (step II) and reduction from $Mo_3O_3S_6$ to Mo_3S_6 (step III)

Considering now the kinetic competition between step II and step III of Figure **4-1**, Figure **4-21** summarizes the free energy of activations for the identified TDTS. H_2 dissociation is the TDTS for the first two O-removal steps on oxysulfides, whereas it is TDTS for the first

S-removal on the Mo_3S_9 trisulfide only. For Mo_3S_9, the dissociation of dimer and H_2 is concerted. This leads to increasing the activation energy for this step. In the other cases, proton transfers are TDTS.

Starting from Mo-oxysulfide ($Mo_3O_3S_6$), removing interfacial oxygen with H_2 requires relatively comparable free activation energies as replacing the same oxygen sites by S. Moreover, thermodynamically the O/S exchange also competes with reduction accompanied by oxygen removal. Figure **4-21** summarizes this thermodynamic and kinetic balance between steps II and III of Figure **4-1**. Therefore, it seems challenging to discriminate between O/S exchange leading to Mo_3OS_8 (step II) and oxygen removal (step III) leading to Mo_3OS_6 starting from the common $Mo_3O_3S_6$ intermediate. By contrast, the last O-removal on Mo_3OS_6 reveals an explicit limitation due to the considerably high-energy intermediate generated (Mo_3S_6) before its reconstruction towards the most stable one.

Instead of removing the last oxygen in Mo_3OS_6 alternatively, it can be replaced by the O/S exchange, which reveals free activation energy of +2.07 eV (Figure 4-22), the highest value among all the activation energies found for the mechanisms studied in this work. Considering this last step, the full O-removal path seems to be disfavored with respect to the trisulfide path.

4.4.8. Chain to triangular cluster reconstruction

As it will be analyzed in the next chapter for the non-supported MoS_3 polymorphs, the relative stabilities of chain-like and triangular morphologies of the $Mo_3O_xS_y$ (including MoS_3) intermediates may be critical for the growth of the targeted MoS_2 phase. MoS_2 phase exhibits a triangular pattern of Mo_3 building block where Mo-atoms are connected by μ_3 sulfur atoms.

As we mentioned several times, the alumina support has a strong tendency to stabilize chain-like species. This is true for the Mo_3O_9 tri-oxide, the Mo_3S_9 tri-sulfide, and for some $Mo_3O_xS_y$ oxysulfides (Figure **4-22**). By contrast, the Mo_3S_6 species is stabilized with a triangular shape. Several elementary steps are thus suspected to involve the chain to the triangular reconstruction of $Mo_3O_xS_y$ intermediates. This was, in particular, the case for the following steps:

- removing bridging site oxygen/sulfur ($Mo_3O_2S_6 + H_2 \rightarrow Mo_3OS_6 + H_2S$ and $Mo_3S_8 + H_2 \rightarrow Mo_3S_7 + H_2S$) with 0.46 eV activation energy due to interfacial oxygen atoms

- removing the sulfur from Mo_3S_8 follows the natural transformation to triangular Mo_3S_7 and then towards true triangular Mo_3S_6 with small activation energies

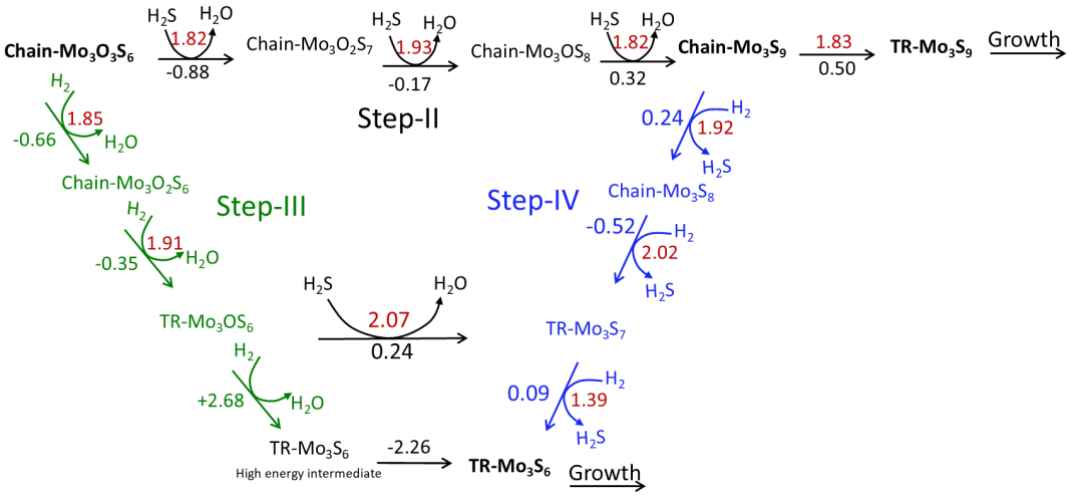

Figure 4-22: Oxysulfides to trisulfides sulforeduction by H_2S (black arrows), trisulfides to disulfides transformation using H_2 (blue arrows), and direct reduction from oxysulfide to disulfides by H_2 (green arrows). The formalism for step-II, step-III, and step-IV and color coding is the same as in Figure 4-1. Activation free enthalpies (red number) and reaction free enthalpy (black/blue/green numbers) are given in eV. For the respective molecular models, see Figure B-30

Regarding the Mo_3S_9 trisulfide species, the support induces a thermodynamic stabilization of the chain-like morphology by about -0.50 eV (Figure **4-22**). However, this reconstruction must be questioned with respect to the competing sulfur removal steps occurring on the chain Mo_3S_9, which requires quite high free activation energies (greater than 1.9 eV for the first two S-removals). After the formation of chain-Mo_3S_9, we thus explored an alternate path where the reconstruction to a triangular conformer may take place before S-removal.

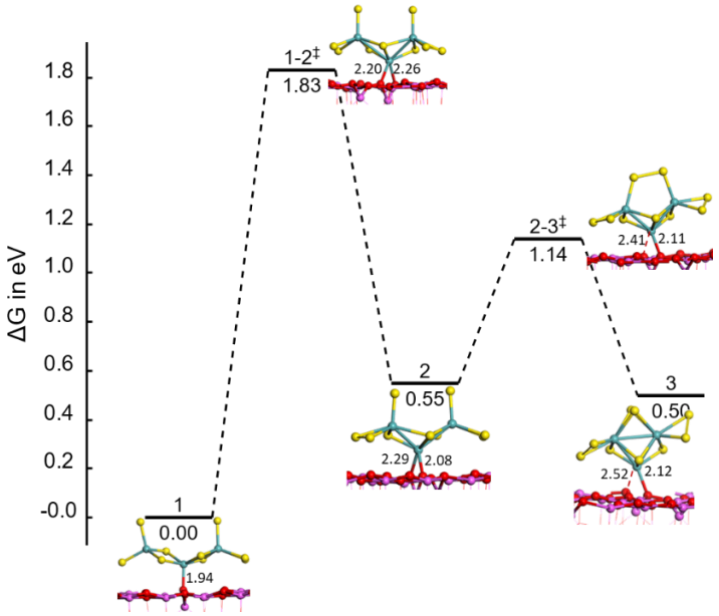

Figure 4-23: Free energy profile of Chain-Mo_3S_9 to TR-Mo_3S_9 transformation ($\Delta G = G_{product} - G_{chain\text{-}Mo3S9}$).

The exploration of this alternate path is also justified by the fact that the trisulfide Mo_3S_9 phase has a much weaker interaction with the support than all other chain-like oxysulfide intermediates (as explained in the next section 4.4.9), suggesting that this transformation should be more accessible at the trisulfide stage than at the oxysulfide stage. Figure **4-23** reports the chain-triangular transformation mechanism. Diffusing the S from its bridging site to the terminal site enables us to form a terminal dimer. This requires the breaking of the Mo-S bond, μ_2-S--μ_1-S gives rise to μ_2-S_2 species, and μ_2-S converted into μ_3-S. Breaking of Mo-S bond requires a significant free energy cost of $\Delta G^{\ddagger}{}_{1\rightarrow 2}$ = 1.83 eV. It must be underlined that the corresponding RDTS is stabilized by shifting the position of the Mo central atom on the alumina. This Mo atom becomes in a bridging position between two oxygen atoms of alumina, whereas it was located on top of one oxygen before with a short Mo-O bond length (1.94 Å). This bridging position is highly symmetric at RDTS (Mo-O=2.20 and 2.26 Å) and becomes asymmetric when the reconstruction proceeds further (Mo-O=2.12 and 2.52 Å, for the final product).

Further S-S bridging is the next step towards the formation of TR-Mo_3S_9. Although the activation energy for the first step is high, it remains still lower than the activation energies found for the direct transformation to MoS_2 through S-removal. This implies that once chain Mo_3S_9 is formed, its reconstruction into triangular Mo_3S_9 is a possible pathway.

4.4.9. Mobility and growth of intermediates

Mobility and growth for intermediates will also be addressed in the next chapter. However, it is already interesting to discuss the possibility of determining at least which intermediates might be the most prone to grow on alumina. For that, the interaction energy descriptor reported in Figure **4-24** could provide some preliminary insights about the stability and diffusion of these species on the alumina support. However, the diffusion will be not only dependent on the interaction energy but also on the following adsorption site and respective changes in the geometry of the cluster.

As shown in Figure **4-24**, we have evaluated the interaction energy for some relevant oxide, oxysulfide, trisulfide, and disulfide species. The stronger interaction of Mo oxides with alumina support through Al-O-Mo linkage is coherent with results invoked in the literature.[96] The interaction energy systematically goes down as a significant number of oxygens are being replaced by sulfur. The interaction could be weaker for Mo sulfides due to weaker Al-S-Mo linkage or even primarily Van-der-Waal interaction reported for MoS_2.[77] The diffusion of oxide precursors and oxysulfide species on support seems to be excluded due to strong interaction through Mo-O-Al linkage compared to sulfides, where only one Mo-O-Al bridge exists. Moreover, it is also essential to notice that the interaction energy of all chain-like clusters (including Mo_3S_9) is significantly higher than triangular (or cyclic) ones. This significantly weaker interaction of triangular-Mo_3S_9 and Mo_3S_6 implies that they would be the more mobile species diffusing on the surface and allowing the formation of larger MoS_3 or MoS_2 clusters.

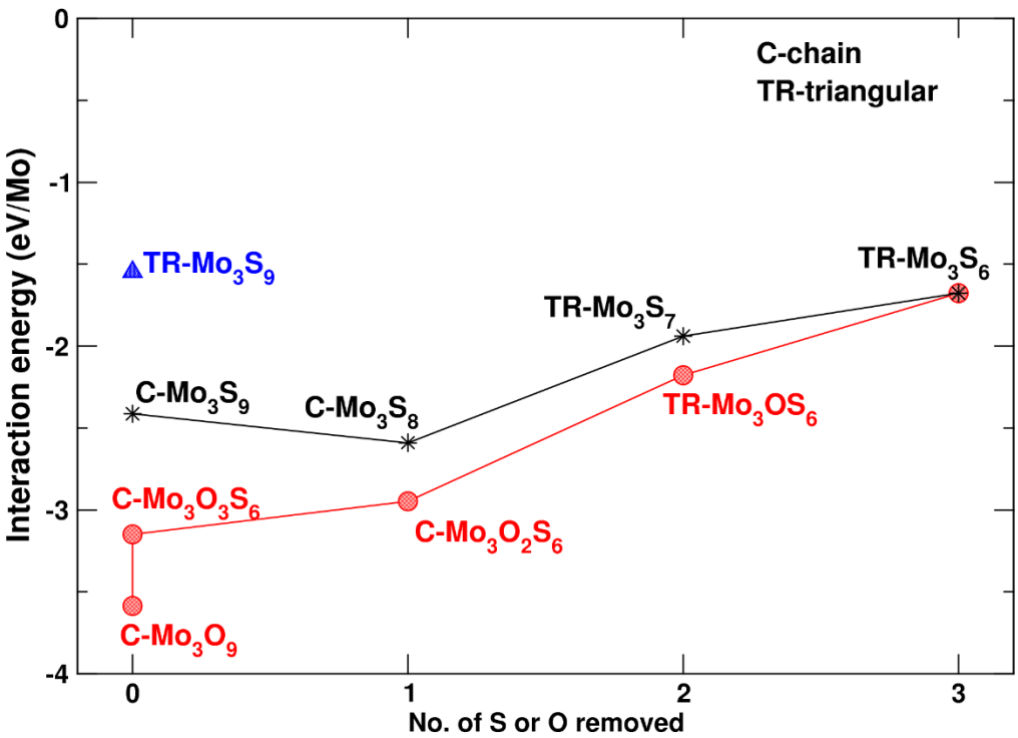

Figure 4-24: Interaction energy of Mo-oxide, -oxysulfides, -sulfides and intermediates with the alumina (100) surface as a function of S or O removals normalized by per Mo. (interaction energy = $E_{*clusters} - E_{*} - E_{cluster}$; * is surface)

If we consider that forming Mo_3S_9 triangular species are favored with respect to Mo_3S_6, we may expect that the growth of MoS_3-polymorphs may be predominant before their ultimate transformation into the MoS_2 active phase, as suggested by EXAFS studies.[99, 106, 217] The next chapter will show that the oligomerization of triangular Mo_3S_9 into larger $Mo_{3n}S_{9n}$ 2D patches is highly exergonic. Thus, we could suspect that such $Mo_{3n}S_{9n}$ 2D patches will be the precursor of the MoS_2 active phase. The S-removal step would occur on such larger size $Mo_{3n}S_{9n}$ 2D patches rather than on the small size Mo_3S_9 for which the S-removal is energetically too demanding.

4.4.10. Size effects

We provide some insights into the effect of cluster size on the kinetics of O/S exchange and S-removal for monomeric species (MoO_3 or MoS_3 and compare it with the trimer case (Figure **4-25**a). The detailed stepwise mechanism and limiting steps are shown in appendix-B (Figure B-28 and Figure B-29). Interestingly, the kinetic limitation to replace

interfacial oxygen remains also valid for monomers. Interfacial oxygen exchange costs 1.35 eV as compared to 1.08 eV for terminal oxygen. In both cases, the proton transfer remains the rate-limiting step. The comparison of the monomer and the trimer reveals that the O/S exchange for monomer is more advantageous than for trimer, and its activation free energy is by 0.58 eV lower, while thermodynamic aspects are equivalent. We suspect the stronger coordination for small Mo_1O_3 entities compare to larger ones (Mo_3O_9); therefore, O/S exchange should be difficult, but we observe the reverse. This unexpected observation indicates that the sulfidation mechanism is faster with small size species such as MoO_3. In particular, these small entities cannot explain the presence of residual non-sulfided Mo species as often observed experimentally.[106, 217]

By contrast, the further S removal from Mo_1S_3 to Mo_1S_2 is found to be impossible kinetically (free activation energy of 3.06 eV, Figure **4-25**), which is far much greater than for Mo_3S_9 species (1.91 eV). At the same time, it is thus more beneficial to sulfide Mo_1O_3, and essentially impossible to transform into Mo_1S_2. However, more calculations are required to validate this point. This result may indicate that smaller trisulfides entities are less prone to change into disulfides than larger ones. This would imply that the growth towards larger $Mo_{3n}S_{9n}$ oligomers (such as 2D patches of 1T'-MoS_3 described in the next chapter) would enhance the S-removal step leading to $Mo_{3n}S_{6n}$ disulfides.

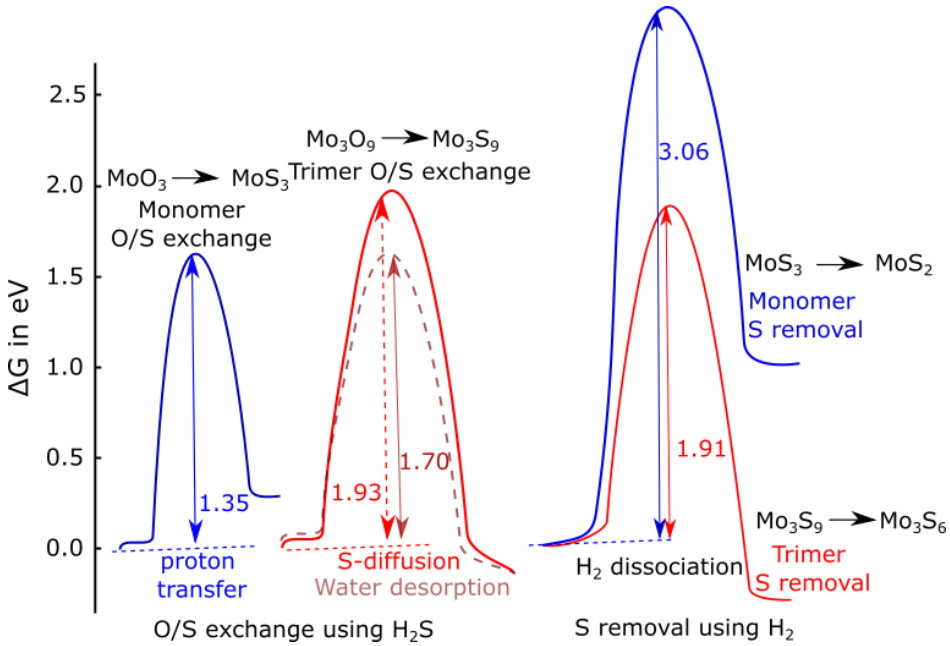

Figure 4-25: Comparison of Gibbs free energy of activation for the monomer (MoO_3) and the trimer (Mo_3O_9) for O/S exchange using H_2S.

As explained before, the growth at the trisulfide state is coherent with the fact that the triangular-Mo_3S_9 supported on alumina has the weakest interaction energy (Figure **4-24**), even lower than Mo_3S_6. It implies that the mobility of Mo_3S_9 is greater than Mo_3S_6 or chain-Mo_3S_9. Chain-Mo_3S_9 exhibits almost 1.5 times stronger interaction than that of TR-Mo_3S_9. However, further investigations on diffusion barriers and on S-removal on larger size $Mo_{3n}S_{9n}$ would be required to confirm this hypothesis.

4.5. Conclusions

Using DFT calculations, we examined the mechanisms of the genesis of the active phase on the (100) surface of γ-alumina support in detail. Firstly, we probed the stability of Mo_1O_3, Mo_2O_6, and Mo_3O_9 on alumina. Secondly, the stability of these models in the gas phase and on the support have been compared. Structural and spectroscopic properties were calculated for various critical $Mo_3O_xS_y$ intermediates formed during the S/O exchange.

Thirdly, the presence of various types of oxygen sites and their chemical reactivity were investigated. The thermodynamics and kinetics of these different O-sites were analyzed for the exchange of O/S. The reduction path was inquired. We compared the two competing pathways, oxysulfide and trisulfide, for the genesis of the active phase by energetic span analysis. Fourthly, the effect of the size of sulfidation/reduction was studied. The possibility of transforming one conformer to other (chain to triangular) was also probed. The impact of entropy and the thermal correction was also considered for some key pathways and intermediates. Based on current understanding, we propose some possible routes for the growth of the *a*-MoS_3/active phase.

The support shows a substantial impact on energetics and structures. Cyclic-Mo_3O_9 and triangular Mo_3S_9 are more stable in the gas phase, while support stabilizes the linear conformers. This thermodynamic trend was also be found to be true for the whole sulfo-reduction pathway, which revealed the key role of the support interaction to control the genesis of the sulfide phase.

Four types of specific oxygen sites are present on the Mo_3O_9 conformers: terminal, bridging, interfacial bi-, and tri-dentate. They all have specific spectroscopic and structural features. We monitored the evolution of these critical features during sulfo-reduction and compared them with available EXAFS data and IR/Raman characteristic peaks. Thermodynamically, the terminal and bridging oxygens are labile to be exchanged, and interfacial oxygens are challenging to exchange by using H_2S. However, kinetically the bridging one is the easiest one to be replaced, the terminal one is moderately hard, and the interfacial ones are the most challenging ones to be replaced.

The trisulfide Mo_3S_9 route to Mo_3S_6 is slightly favored over the reduction of $Mo_3O_3S_6$ to Mo_3S_6 due to the last difficult reduction step of Mo_3OS_6. However, the S-removal on small Mo_3S_9 chain-like entities exhibits a high activation free energy (>1.9 eV) instead. Alternatively, though the chains are more stable for the oxysulfide and trisulfide phase, we propose that Mo_3S_9-chain transform into triangular at a competing cost and then diffuse to condense with other Mo_3S_9 in order to form larger $Mo_{3n}S_{9n}$ that will transform into $Mo_{3n}S_{6n}$. The mobility of these TR-Mo_3S_9 species would be significantly less demanding than the Chain-Mo_3S_9, oxysulfides, and disulfide species as a consequence of their lower interaction energy with alumina. The formation of the larger MoS_3 species on alumina by the diffusion and sintering of small MoS_3 species would need further investigation. Furthermore, their transformation to the disulfide phase also requires more attention to confirm the easier sulfur removal with increasing MoS_3 cluster size.

For that, it is necessary to determine the structural and energetics of MoS_3 polymorphs as a function of sizes, which is the topic of the next chapter. The investigation will be carried out in the absence of alumina support to quantify the intrinsic trends related to the MoS_3 polymorphs. Moreover, as we have already seen, the tri-sulfides have weaker interaction than oxides or oxysulfides; this interaction would be even weaker for the larger size. Therefore, it is reasonable to drop the effect of support while investigating MoS_3 phase stability.

Chapter 5: Amorphous MoS_3: Size-dependent structural properties, spectroscopic, and energetic analysis

This chapter reproduced the text published in the paper https://doi.org/10.1021/acs.cgd.0c00981. [220]

Despite the growing interest in the a-MoS_3 phase due to its diversified applications, many open voids exist about its structural understanding. In this chapter, we undertake some of them, such as triangular vs. chain, Mo-Mo bond types, sulfur species, and their respective spectroscopic signature. We also determine the evolution of MoS_3 polymorphs as a function of size and their possible transformation scheme from one polymorph to another.

5.1. Introduction

As we have discussed the importance of the MoS_3 phase (section 2.1.4), over the past few decades, amorphous MoS_3 (*a*-MoS_3) based nanomaterials have gained significant attention from the scientific community because of their versatile properties valuable for industrial applications as well as for numerous emerging applications in new energies. The *a*-MoS_3 phase was shown to play a crucial role as electro-and photo-chemical (pre-)catalysts for hydrogen evolution reaction (HER).[128, 240, 241] It was also found to exhibit attractive capacity and rate capability when used in electrode materials for batteries.[20, 21, 28, 58, 242] The use of *a*-MoS_3 was also suggested to improve the recovery of Hg capture from the flue gas.[24, 243] Finally, in the synthesis of industrial MoS_2 based catalysts used in hydrodesulfurization (HDS), *a*-MoS_3 is known to be a key precursor formed during the activation of the 2H-MoS_2 nano-crystalline phase.[7, 104] Moreover, MoS_3 improves the catalytic activity if used as a precursor for the preparation of the HDS catalyst.[111]

Several experimental[36, 40, 41, 112–115] and a few theoretical[38, 39] approaches have been applied to provide the atomic-scale understanding of the nature of the MoS_3 phase

and its reactivity. The amorphous nature and attractive properties of its 1D- or 2D nano-structure make it an intriguing system to study. The presence of various sulfur species such as S^{2-} and S_2^{2-} gives flexibility to the structure and is suspected to be a potential active site for HER or other applications. [19, 53, 56, 116, 117]

Despite the attractive interest of *a*-MoS_3 based nanomaterials, the amorphous nature of the MoS_3 phase makes it challenging to control and understand its chemical reactivity. In particular, the type of the structural building unit such as Mo_3 triangular[39, 40, 123] vs. Mo chain[34, 41, 42, 120] is still debated. In contrast, the ambivalent interpretation of the nature of sulfur species (S^{2-}, S_2^{2-}) and types of present Mo-Mo[41, 118][35, 120–122] bonds leads to ambiguous interpretations of spectroscopic data and reactivity. IR peak assignment based on $(NH_4^+)_2[Mo_3S_{13}^{2-}]$ remains questionable where no μ_1-S and μ_1-S_2 descriptor exist in the reference compound.[40]

By density functional theory (DFT), we simulate the energetic, structural, and spectroscopic features of relevant 0D-, 1D- and 2D-MoS_3 triangular, chain-like polymorphs. Moreover, we will also shed light on some unprecedented 0D-2D-nano-structures (ring, wave, and helix) of the MoS_3 polymorphs and revisit the interpretation of EXAFS, IR-RAMAN, and XPS experimental data. To validate the reliability of the newly proposed structures, we will analyze the various structures and compare them with available EXAFS data. The relative stability of the multiple polymorphs will be determined as a function of sizes. We explore how Mo_kS_{3k} clusters of a few k atoms may grow up to infinite MoS_3 polymorphs (periodic replica). The computed IR spectra within the density functional perturbation theory level will be compared with a reference experimental IR spectrum of bulk-MoS_3.[40] We also discuss the core level shift (ΔBE) with the corresponding XPS signals. We finally propose the possible transformation of MoS_3 polymorphs upon oligomerization by analyzing molecular dynamics simulations and growth energy profiles. Only the key results are presented here; some of the detailed information about explored structures for triangulars and chains, and spectroscopic analysis of various species is given in Appendix-C. We will refer to these details in this chapter wherever it is needed.

5.2. Methods

For all the calculations, density functional theory (DFT) as implemented in VASP[232–234] has been used relying on the Perdew-Burke-Ernzerhof (PBE)[176] functional within the framework of generalized gradient approximation (GGA). The long-range interactions were included through a density-dependent dispersion correction (dDsC)[177, 178]. The projector augmented-wave (PAW) method[235] was chosen to describe the electron-ion interaction. The kinetic energy cut-off for the plane-wave basis set has been fixed at 500 eV. Furthermore, for the minimization of the electronic energy, a Gaussian smearing with a width of 0.2 eV was chosen. In contrast, a mixture of the blocked-Davidson scheme and residual minimization method direct inversion in the iterative subspace has been applied. Spin-polarized calculations were performed to obtain the ground state of the clusters. Brillouin zone integration has been adapted as a function of each simulated system, either cluster or periodic structure.

To represent the MoS_3 polymorphs, we simulated two types of molecular models: Mo_kS_{3k} clusters of various finite sizes and periodic structures of infinite size in one dimension. A large vacuum has been used to minimize the spurious interactions with neighboring images along with the nonperiodic directions of the respective models. To optimize the structures of the various polymorphs, the conjugate gradient algorithm was used. Electronic and geometric convergence cut-off has been set to 10^{-6} eV and 0.02 eV/Å, respectively. For the clusters' geometry optimization, a large cubic supercell was used to avoid the spurious interactions of the clusters with its periodic images. For the periodic structures, the ionic positions and cell parameters along the periodic replica have been optimized.

The exploration of some complex structures has been refined by ab initio molecular dynamics (AIMD) with the scaled velocity Verlet algorithm to solve Newton's equations of motions (time step of 5 fs and T = 1000 K).

For frequency calculations, the structures have been optimized with tighter convergence criteria such as 10^{-7} eV for electronic properties and 0.01 eV/Å for geometry. To calculate the frequencies and corresponding infra-red intensities, the linear response method with

density functional perturbation theory (DFPT) has been used as implemented in VASP.[193] We convoluted the IR intensity peaks by a normal distribution with the variance of 80 cm^{-1} to compare with the experimental IR.

To calculate the core-level binding energy (ΔBE), we use the Janak-Slater transition state approach[200, 202, 244], where a half electron is shifted to the lowest unoccupied molecular orbital (LUMO) from its core rather than creating a full core-hole. We compare this ΔBE with available XPS data.

For determining the thermodynamic stability of the various oligomers, the following equation has been used to calculate the relative growth energy ΔE at 0 K:

$$\boldsymbol{Mo_3S_9 \rightarrow \frac{3}{k}\, Mo_kS_{3k}} \qquad \textbf{5-1}$$

$$\boldsymbol{\Delta E = \frac{3}{k}[E(Mo_kS_{3k}) - E(Mo_3S_9)]} \qquad \textbf{5-2}$$

where $E(Mo_kS_{3k})$ is the electronic energy of the Mo_kS_{3k} cluster or periodic structure, and $E(Mo_3S_9)$ is the energy of the Mo_3S_9 cluster used as a reference. The effect of zero-point energy, thermal corrections, and entropy have been included in calculating the free energy variation (details are given in appendix C) :

$$\boldsymbol{\Delta G = \frac{3}{k}[G_{vib}(Mo_kS_{3k}) - G_{vib}(Mo_3S_9)]} \qquad \textbf{5-3}$$

We have assumed that the Mo_kS_{3k} clusters or infinite structures are immobile, and thus they have no translational and rotational contributions.

5.3. Structure analysis

5.3.1. 0D- and 1D-model of triangular oligomers (TO)

Inspired by the earlier experimental work by Weber et al.[40], we first optimized the numerous possible structures of the Mo_3S_9 triangular monomers. All these structures differ by the nature, number, and location of sulfur species:

- S_2^{2-} dimers, either on top (also called μ_1-S_2 in what follows) or in bridging site (μ_2-S_2),
- S^{2-} atoms, either on top (μ_1-S), or in the bridging site (μ_2-S), or in the hollow site (μ_3-S).

The most stable structure is shown in Figure **5-1**a), while other metastable structures with relative energies are given in Figure C-1 and Figure C-2. This stable structure exhibits :

- two S_2^{2-} dimers : one μ_1-S_2 and one μ_2-S_2,
- four S^{2-} atoms : two μ_1-S, two μ_2-S, and one μ_3-S.

None of the empirically proposed structures by Weber et al.[40] corresponds to the most stable one: their energy is at least +0.65 eV higher than the one reported in Figure **5-1**a, see Figure C-1). Weber's proposals were made on the assumption of the experimentally observed +4 oxidation state of Mo. Actually, our minimal energy structure of Mo_3S_9 exhibits an average formal oxidation state of +4.67 (assuming a formal $2e^-$ charge for the S-atom and S_2 dimers). Previous DFT calculations also showed that Weber's structures are subject to strong reconstructions, and resulting Mo exhibits formal oxidation states higher than +4.[39] This apparent discrepancy indicates that such Mo_3S_9 triangular monomers are not the dominant species in *a*-MoS_3. Nevertheless, they might co-exist with other oligomeric structures with an average oxidation state close to +4.

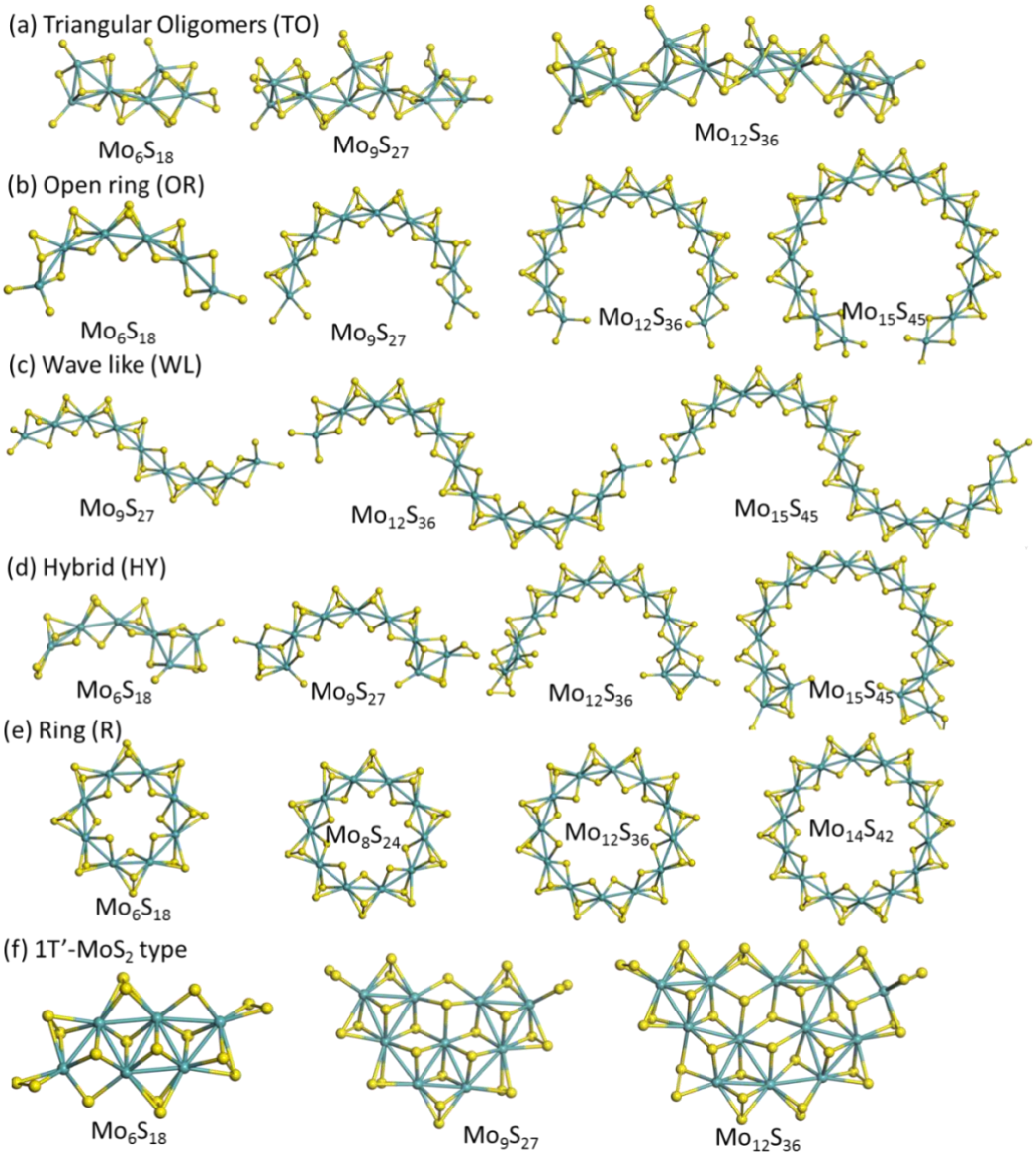

Figure 5-1: Most stable structures of Mo_kS_{3k} for some relevant k values: a) Triangular oligomers (TO), b: open-ring (OR), c): wave-like (WL), d) hybrid (HY) models, e): ring (R) structures and f) 1T'-MoS_2 type. Yellow balls: S, Blue balls: Mo.

Interestingly, our most stable Mo_3S_9 structure exhibits two distinct types of Mo-Mo bond length: one short Mo-Mo bond at 2.72 Å and two long Mo-Mo bonds at 2.96 Å, which are compatible with some experimental EXAFS studies: 2.75 and 3.16 Å, respectively,[35, 41] although we noticed a slight underestimation of 0.18 Å for the long Mo-Mo bond. Also, the mean Mo-S bond length (2.35 Å) is in close agreement with the experimental value (2.41 Å).

However, as suggested experimentally, *a*-MoS_3 could actually consist of larger oligomers made of Mo_3S_9 triangular clusters interconnected by S species. [40, 128] Exploring the size effects on triangular oligomers (TO) requires the simulations of various TO conformers. For Mo_6S_{18} this revealed that the interconnection of two Mo_3S_9 triangular units occurs through one S_2 dimer and one S atom (initially μ_2-S) becoming μ_3-S (Figure **5-2**a). Hence, this interconnection does not involve only one or two S-atoms as originally suggested,[40] but three S-atoms. This structural trend is further confirmed for the larger oligomers Mo_9S_{27}, $Mo_{12}S_{36,}$ and $Mo_{15}S_{45}$ (Figure **5-1**b). The average formal oxidation state of Mo in these oligomeric structures continuously decreases from +4.67 for Mo_3S_9 to +4.16 for $Mo_{15}S_{45}$ TO. This evolution is due to the vanishing contribution of μ_1-S_1 species located at the edges when size increases. Note that we will call "edges" the two terminal units of the chain-like model in the following.

To go beyond the 0D structures, we have optimized the corresponding 1D structure of TO systems. According to the spatial rotation of each Mo_3S_9 triangular unit along the TO chain, the smallest periodic structure allowing the chain interconnection between two neighboring supercells was found for $Mo_{18}S_{54}$ (Figure **5-3**a). For this 1D TO-periodic (TO-P) chain, no μ_1-S species remains as a consequence of periodicity. Moreover, the mean Mo oxidation state reaches the limit of +4 for TO-P, while it is 4.11 for $Mo_{18}S_{54}$, both of which are very close to the experimental value.[40]

Considering the local interatomic distances, the short and long Mo-Mo and Mo-S bond-lengths slightly expand as a function of the oligomer size (Table C-3). We determine these bond lengths for the Mo18S54 TO-P structure (Table **5-1**) by calculating the pair correlation functions (PCF, Figure C-5). The short Mo-Mo bond length is about 2.76 Å, and the long Mo-Mo bond becomes 3.08 Å which is in closer agreement with the experimental EXAFS data (Table **5-1**).[41] As the size of TO increases, the long Mo-Mo bond present in triangular monomers such as Mo_3S_9 shortens (Figure **5-2**a), while the long Mo-Mo bond is located at the interconnection of two triangular monomers along the chain. The mean Mo-S bond length also slightly expands to 2.42 Å with the size increase, in good agreement with EXAFS.

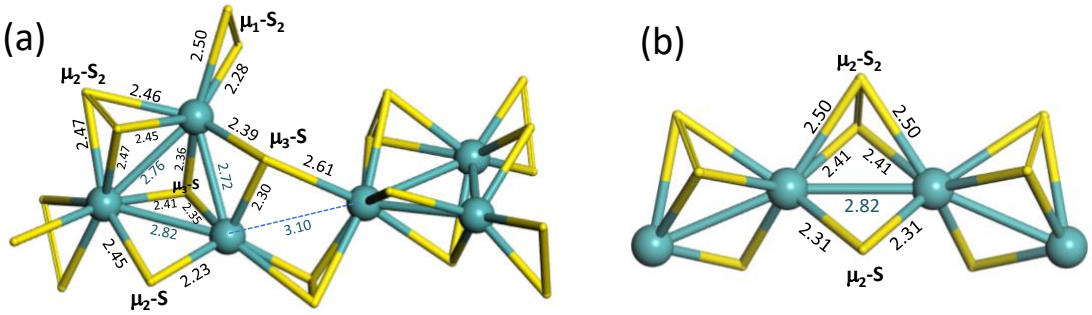

Figure 5-2: Local structures of (a) 1D-TO-P polymorphs and (b) R-P, 1D-WL-P or 1D-H-P polymorphs. Distances (in Å) represent local values only (not averaged values).

At this stage, we must recall that many EXAFS studies do not report the long Mo-Mo bond length[120], which may raise the question about the precise assignment of the structure on the basis of the Mo-Mo distance. Therefore, we also investigate alternative structures below.

5.3.2. 0D and 1D-Chains: Open-ring (OR), wave-like (WL), linear (L), and helical (HL).

Within the chain-like models, two competing ones were initially proposed: one strictly linear made of $Mo^{5+}(S^{2-})_2(S_2^{2-})_{1/2}$[34, 41] and one distorted made of $Mo^{4+}(S^{2-})(S_2^{2-})$.[38] Hence, we started by investigating two periodic structures of strictly linear chain-like models involving either $Mo^{5+}(S^{2-})_2(S_2^{2-})_{1/2}$ or $Mo^{4+}(S^{2-})(S_2^{2-})$. For the Mo^{5+} model, the optimized structure (Figure C-4) confirms the presence of two Mo-Mo bond lengths (2.70 and 3.28 Å) compatible with Ref.[34] while for the Mo^{4+} model (Figure **5-3**b), the structure exhibit one short Mo-Mo bond only (2.90 Å) longer than the one usually reported by EXAFS (Table **5-1**).[120] Moreover, the DFT energies show that the Mo^{4+} model is more stable by 0.11 eV per MoS_3 unit. This preliminary result may be consistent with Hibble's proposal.[38]

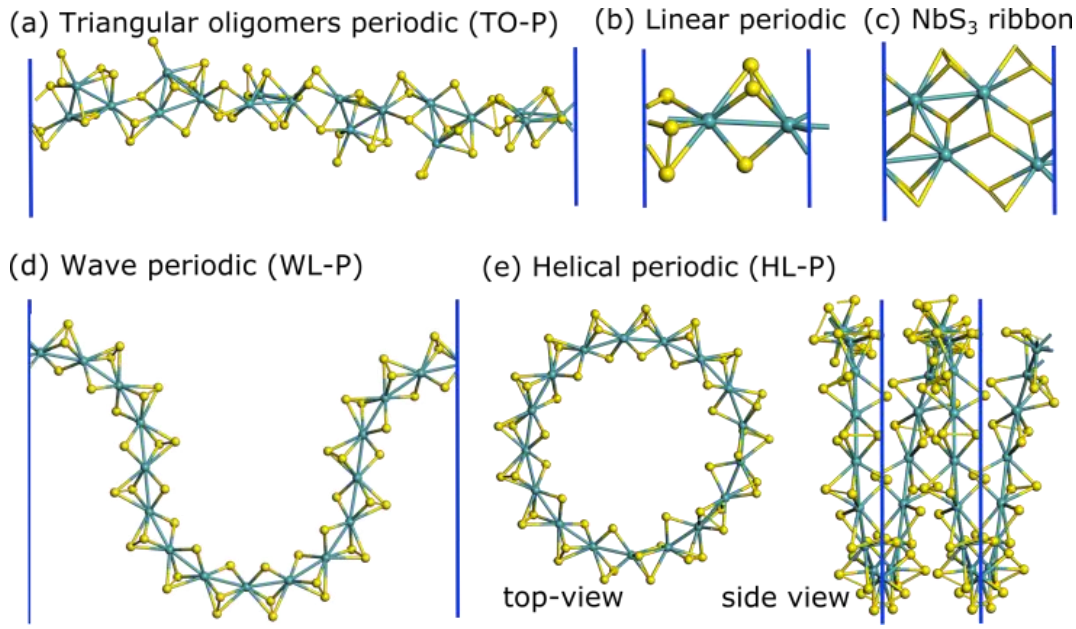

Figure 5-3: Various MoS_3 nanostructures : a) Triangular oligomers $Mo_{18}S_{54}$ (TO-P), (b) Linear periodic Mo_2S_6 (L-P), (c) NbS_3-ribbon (Mo_4S_{12}) (d) $Mo_{16}S_{48}$ Wave-like (WL-P), and (e) $Mo_{17}S_{51}$ Helical (HL-P). The direction perpendicular to the blue lines is the direction of periodicity.

Releasing the periodic constraint, any attempt to stabilize a finite size Mo_kS_{3k} clusters of $Mo^{5+}(S^{2-})_2(S_2^{2-})_{1/2}$ formal unit relaxed into a curved chains of $Mo^{4+}(S^{2-})(S_2^{2-})$: open-ring (OR, Figure **5-1**b) and wave-like (WL, Figure **5-1**c). The observed curvatures are induced by the relative position of two successive S_2 dimers. In OR, the relative tilting angle of two successive dimers is always ~60° (Figure **5-4**). When this alternate tilting of two successive S_2 dimers is locally broken at a chain's point, the chain curvature changes, which leads to a WL-type structure (Figure **5-1**c). In the extreme case of a linear chain, the relative tilting angle between two successive dimers is ~90° (Figure **5-4**).

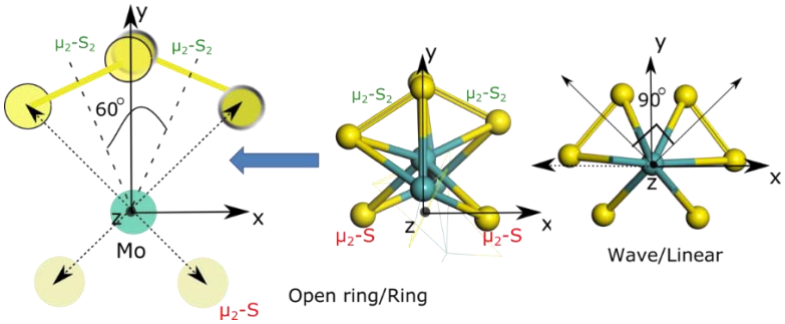

Figure 5-4: Side view of open-ring (OR) structure and orientation of dimers w.r.t. the plane of Mo-Mo arc (yz plane).

As for TO polymorphs and linear chains, we explore the construction of 1D-periodic structures for the curved structures. One original structure directly inherited from OR, is the closed ring (R) represented for $Mo_{14}S_{42}$ in Figure **5-1**e, which resembles MoS_2 nanotubes.[245] In that case, OR is locked by bridging the two edges through Mo-S-Mo bonds involving the dangling S and S_2 species at OR edges. Nevertheless, this lock of the cycle only occurs for an even number of Mo atoms because of the tilting alternation of the S_2 dimer invoked before. The cycle tension depends on the size and, hence, the relative stability of R models depends on their sizes (Figure **5-1**e). OR and R structures exhibit one type of short Mo-Mo bond length (about 2.72-2.79 Å) with very small variation according to size (Table C-3).

Table 5-1: Mo-Mo and Mo-S bond lengths (in Å) for various types of MoS_3 polymorphs.

Bond	TO-P	Ring	WL-P	HL-P	L-P	1T'-like	EXAFS*	EXAFS**
$Mo\text{-}Mo_{short}$	**2.76**	**2.75**	**2.77**	**2.76**	**2.90**	**2.79**	**2.75**	**2.75**
$Mo\text{-}Mo_{long}$	**3.08**	**--**	**--**	**--**	**--**	**3.16**	**3.16**	**--**
$Mo\text{-}S_{short}$	**2.27**	**2.29**	**2.30**	**2.31**	**2.31**	**2.33**	**--**	**--**
$Mo\text{-}S_{long}$	**2.46**	**2.46**	**2.45**	**2.46**	**2.46**	**2.47**	**--**	**--**
$Mo\text{-}S_{avg}$	**2.42**	**2.39**	**2.39**	**2.40**	**2.40**	**2.44**	**2.44**	**2.44**

*according to Ref.[35], ** according to Ref.[120]

1D periodic structures (WL-P) containing various numbers of Mo per unit cell depending on the wave amplitude were optimized (Figure **5-5**and Figure **5-3**d). Finally, a more complex structure consists of a helical periodic (HL-P) structure, as shown in Figure **5-3**e,

which results from 3D distortion of the R structures induced by the change of the relative orientation of successive S_2 dimers. Interestingly, these more complex 3D structures are very similar to the one proposed by Hibble et al.[38] Table **5-1** shows that these periodic structures also exhibit one short Mo-Mo bond (about 2.76-2.77 Å) as for OR and R structure. The Mo-Mo PCF analysis (Figure C-5) reveals that the structural feature of this polymorph family clearly differs from TO. The mean Mo-S bond length is ~2.40 Å, while the S-S bond length in S_2 bridging dimer is ~2.05 Å (whatever the size, except for the smallest constrained Mo_6S_{18} ring, Table C-3).

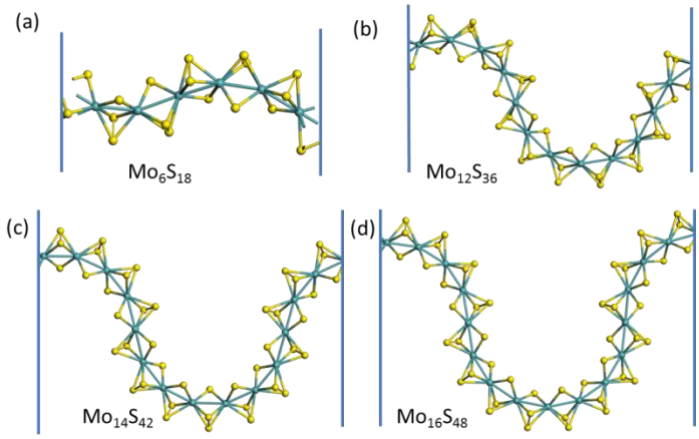

Figure 5-5: Various 1D-periodic wave-like nano-structures with different number of Mo-atoms in unit cell. Corresponding structures with relative energy (w.r.t. per Mo_3S_9 of TO) (a)-2.45, (b) -2.69, (c)-2.71 and (d) -2.72 in eV.

Comparing the Mo-Mo and Mo-S bond-lengths of various explored structures with EXAFS data (Table **5-1**), we observe that all the chain-like structures (linear, WL, WL-P, HL-P, and R) have only one Mo-Mo bond in contrast with TO. This type of polymorph would thus explain the fact that EXAFS data do not identify the longer Mo-Mo distance in some experimental MoS_3 samples, whereas it may exist in other ones, which would be of TO type.[120]

5.3.3. MoS_3 patches with 1T'-MoS_2 like structure

Ab-initio molecular dynamics (AIMD) was performed to explore if new possible structures can be revealed. Starting AIMD from TO metastable conformers identified at 0 K after geometry optimization (such as the one highlighted for Mo_6S_{18} in Figure C-2), the

system rapidly explored an ample configurational space. The structural evolutions of the Mo_6S_{18} and Mo_9S_{27} oligomers (Figure **5-6** and Figure **5-7**) show that the triangles rapidly interconnect by one μ_2-S_2 species plus one μ_3-S species as we found by static optimization. Moreover, the dynamic evolution proceeds further and reaches, after a few picoseconds, more condensed rearrangements exhibiting respectively 4 and 8 adjacent triangular clusters interconnected by μ_3-S species.

Figure **5-1**f illustrates the final products obtained after quenching at 0 K for both Mo_6S_{18} and Mo_9S_{27} condensed structures. For $Mo_{12}S_{36}$, the corresponding optimized structure is represented in Figure **5-1**f. The structural patterns of these triangular Mo_3 in Mo_6S_{18}, Mo_9S_{27}, and $Mo_{12}S_{36}$ are very similar to the one found in the 1 T' polymorph of MoS_2, where μ_3-S atom are located in hollow sites of Mo_3 triangles, with an alternate position either above or below the Mo plane. Note, however, that the edge/surface ratio needs to be appropriate to keep the nominal MoS_3 stoichiometry. Indeed, as discussed below, a nanoribbon with similar stability satisfies this constraint.

Actually, the PCF analysis of $Mo_{12}S_{36}$ reveals that two main Mo-Mo distances are observed: one short at 2.79 Å and one long at 3.16 Å (Table **5-1** and Figure **5-4**). This implies that the $Mo_{12}S_{36}$ condensed structure is actually closer to the 1 T' phase of MoS_2 with the specific ordering of the contracted and expanded Mo_3 triangles within the structure, whereas one single long Mo-Mo bond is reported for the 1T phase.[246] Interestingly, the NbS_3 structure could also exhibit a nanoribbon made of two infinite Nb rows arranged in a similar way as in Mo_6S_{18} cluster.[126, 247] The simulation of an analogous 2D-periodic MoS_3 nanoribbon (Figure **5-8**) reveals the presence of short Mo-Mo distances co-existing with significantly longer ones. We will now discuss how the triangular cluster can transform into 1T'-MoS_3.

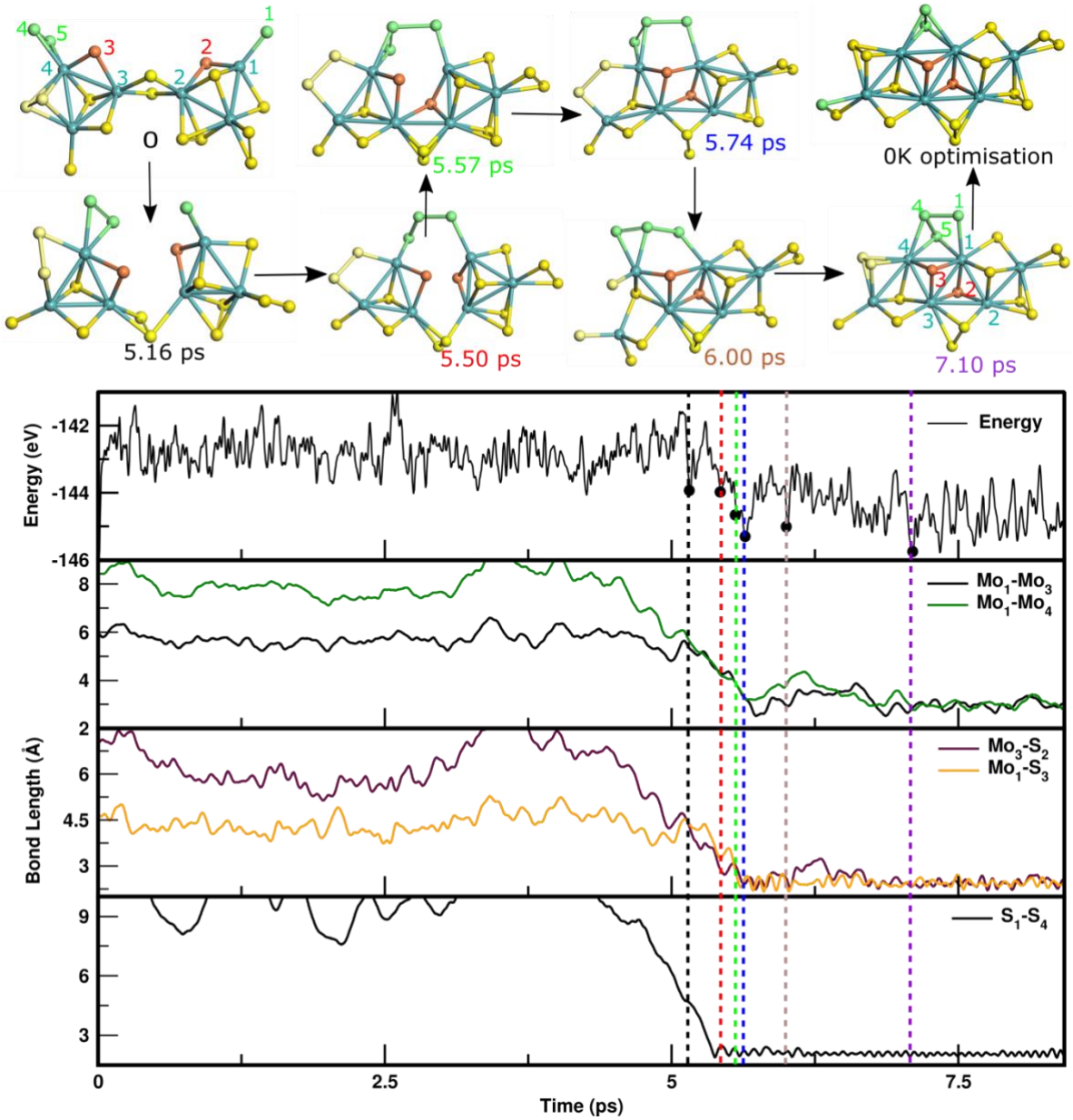

Figure 5-6: Panel 1: Relevant intermediate structures observed during AIMD simulation (T = 1000 K) of the transformation of Mo_6S_{18} TO into 1T'-MoS_2 like phase. Color legend: Blue balls: Mo atoms, yellow balls: S atoms not directly involved in the transformation, red balls: μ_2-S becoming μ_3-S in the newly formed Mo_3 triangles, green balls: μ_1-S and μ_1-S_2 interacting during MD. Panel 2: Total energy evolution as a function of time; black dots represent the energy of the intermediate structures given in Panel 1. Panel 3: Evolution of the Mo-Mo distances for the two newly formed Mo-Mo bonds. Panel 4: Evolution of the Mo-S distances for the two newly formed Mo-S bonds. Panel 5: Evolution of the S-S distance for the newly formed S_1-S_4 bond distance.

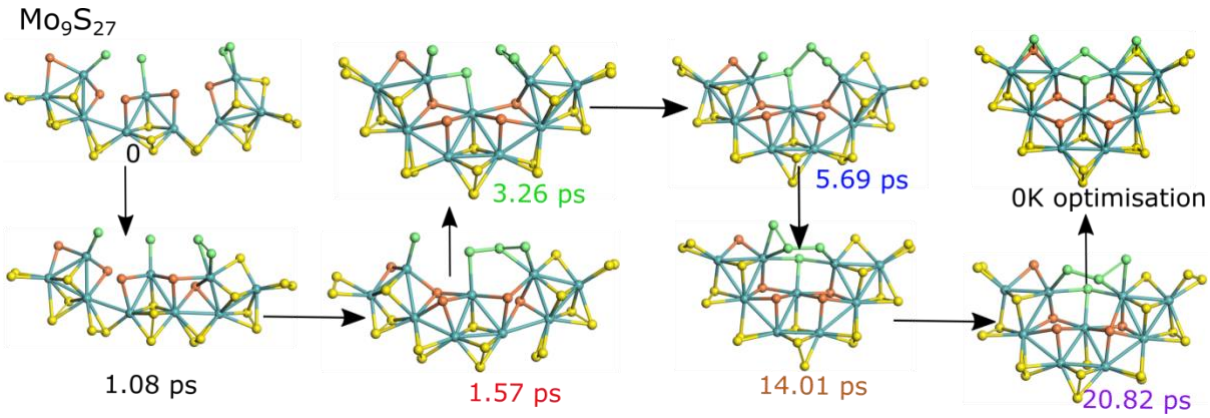

Figure 5-7: Relevant intermediate structures observed during AIMD simulation (T = 1000 K) of the transformation of Mo_9S_{27} TO into 1T'-MoS_2 like phase. Color legend: Blue balls: Mo atoms, yellow balls: S atoms not directly involved in the transformation, red balls: μ_2-S becoming μ_3-S in the newly formed Mo_3 triangles, green balls: μ_1-S and μ_1-S_2 interacting during MD.

While observing the successive intermediates formed as well as the associated transformation mechanisms in both cases, we notice in Figure **5-6** and Figure **5-7**, two main families of S species playing a key role in the formation of the 1T'-type MoS_3 structure. The first ones are the μ_2-S atoms (red balls Figure **5-6** and Figure **5-7**) which are becoming μ_3-S atoms located in the hollow site of the newly formed Mo_3 triangles. As the analysis of the Mo-S distance shows it for the Mo_6S_{18} (see steps 5.50 ps and 5.57 ps and Mo-S distances in Figure **5-6**), the μ_2-S atoms are becoming closer to two Mo-atoms belonging to the two triangular clusters and thus allow the formation of new Mo-S bonds inside the newly formed adjacent triangles. Simultaneously the Mo-Mo distance decreases. It must also be underlined that the relative position of these bridging S-atoms is critical to forming the 1T'-type pattern since they must become μ_3-S (apical) in the hollow sites located above and below the Mo plane. Otherwise, the formation of the 1T'-type is impossible.

The other S-atoms involved are μ_1-S and μ_1-S_2 (green balls in Figure **5-6** and Figure **5-7**), which interact by forming transient S_3 trimers, which also help for the condensation mechanisms by bridging the distant triangles close together (steps 5.50 ps and 5.57 ps in Figure **5-6** and S-S distance).

Finally, it is important to stress that all the μ_2-S_2 remains uninvolved in the transformation. Since they are located at the edges of the cluster, they potentially hinder the growth of the 1T'-structure. The present transformation is induced by the thermal effect, and it could be accelerated in the presence of hydrogen gas which will easily remove some excess S-atoms, particularly those of μ_2-S_2 and μ_1-S_2. Such sulfo-reductive conditions are often used to activate the MoS_2 phases experimentally, as discussed in the previous chapter.

Finally, this dynamic evolution of the structure is clearly featured by the energy profile (Figure **5-6** shows that after 5ps, the energy drops as the oligomer starts to condense and finally reaches a low energy plateau when the 1T'-type structure is formed. To compare the energies of these 1T'-type structures consistently with the former ones as reported in Figure **5-9**, we perform a static geometry optimization at 0 K on the AIMD structures obtained at the final energy plateau. Figure **5-9** shows that for three sizes Mo_6S_{18}, Mo_9S_{27}, and $Mo_{12}S_{36}$, the 1T'-type structures are more stable by -0.56 to -0.73 eV with respect to TO structures. The infinite extension of such kind of 1T'-MoS_3 can be similar to NbS_3 ribbon structures shown below (Figure **5-8**).

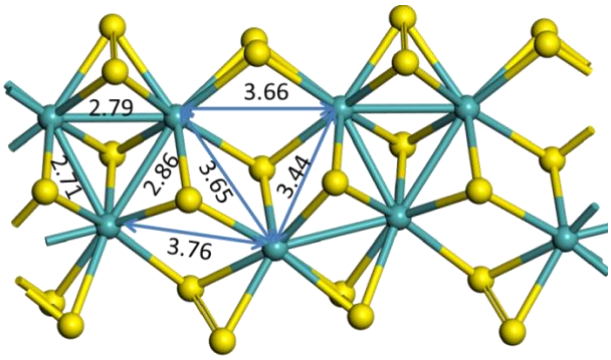

Figure 5-8: MoS_3 1D-periodic structure (double supercell) inherited from NbS_3 ribbon structure.[114]

The structural analysis indicates that if EXAFS reports the presence of two types of Mo-Mo bonds (short or long), it is difficult to discriminate whether they are due to the formation of one single polymorph or a mixture of polymorphs. To go beyond, we evaluate in what follows the relative stability of these various polymorphs.

5.3.4. Energetics analysis

Figure **5-9** reports the growth energy (at 0 K, without ZPE corrections) as a function of the size of the various polymorphs described in the previous section. The impact of ZPE and temperature is reported in Figure **5-10**, which shows that it is more pronounced for the larger size clusters as compared to smaller size ones. In most cases, entropy and thermal corrections stabilize the clusters for higher temperatures. However, these thermal and entropic effects influence only moderately the main energetic trends, so we primarily discuss the results considering 0 K energies.

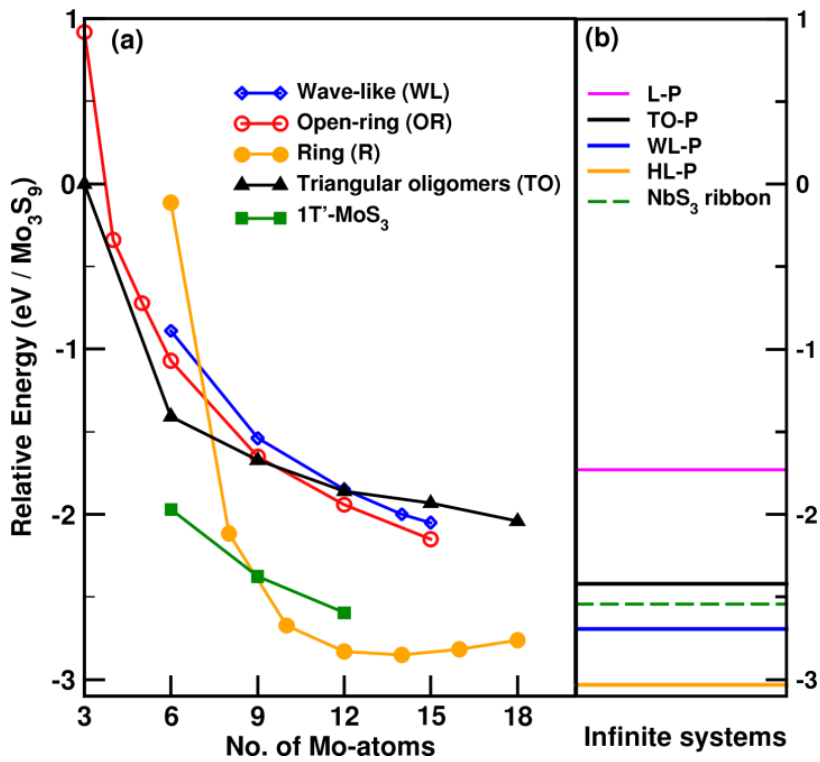

Figure 5-9: Growth energies of (a) 5 relevant types of MoS_3 polymorphs as a function of size (reference energy is the Mo_3S_9 triangular cluster), (b) corresponding periodic structures: L-P, TO-P, WL-P, HL-P, and NbS_3-like MoS_3 ribbon.

On the growth energy diagram (Figure **5-9**), as expected, all curves (except the one of R) exhibit a continuously decreasing trend as a function of size, with a constantly decreasing

slope. However, even for large sizes considered in the present study (up to 16 Mo), a plateau in energy is not yet reached, and the asymptotic limit value for infinite size can only be estimated of the polymorphs placed in periodic supercells as described before for L-P, TO-P, WL-P, and HL-P.

The OR and WL polymorphs share a similar internal structure. Hence, they are nearly iso-energetic, and their relative energy remains constant as a function of the size. Nevertheless, WL is slightly less favored compared to OR due to the point defects induced by the change in the tilting angle of the S_2 dimer (as described before).

The relative energies between other families of MoS_3 polymorphs of different types are, however, size-dependent. Considering first the 0D TO and OR structures, the energy values of the smallest Mo_3S_9 and Mo_6S_{12} clusters reveal that TO is strongly stabilized with respect to OR by ~1 eV for Mo_3S_9. By contrast, the infinite TO-P polymorph is less stable than WL-P and HL-P. The inversion of stability between TO and OR or WL occurs for 9-12 Mo atoms. For larger oligomers, OR or WL is more stable.

If we consider the lowest energy L-P model (pink in Figure **5-9**), it is evident that it is significantly less stable than all other polymorphs and cannot be considered relevant for the *α*-MoS_3 phase. Our more stable models preferentially exhibit curved or bent chains such as those found in OR/WL/HL. This is in qualitative agreement with Hibble's bent chain models indicating numerous elbows.[38]

The most striking energetic result concerns the R model. Indeed, for a size greater than 8 Mo, the R models emerge as the thermodynamically most stable arrangement except for the HL-P polymorph, which is competitive with the lowest energy R structure reached at 14 Mo. The R models are strongly stabilized with respect to OR due to the absence of edge energies after ring closure. This edge effect is generally stronger for OR/WL than for TO, which also explains the higher energies of OR/WL for small sizes. In agreement with these considerations, the stabilization of the periodic TO-P system with respect to the larger TO is less pronounced than for WL. The periodicity in WL-P also enables to wipe this edge effect out. So, the stability of WL-P may compete with R, when the ring strain is non-negligible.

As we have explained in the previous section, OR may grow in a helical structure HL/HL-P, which has the lowest energy we could identify for MoS_3 models. This stabilization is induced by the close proximity of two helical rings, which supplements Van-der-Waals interactions, not present in any other periodic system.

Finally, Figure **5-9** demonstrates that the stability of the 1T'-like MoS_3 polymorph, including the NbS_3-like nanoribbon, strongly competes with many other phases. This result is also consistent with the AIMD simulation, which highlighted the fast transformation from TO into 1T'-like MoS_3 clusters. For sizes up to 12 Mo atoms, 1T'-like MoS_3 clusters are more stable than OR/WL and TO. For the 1D structures, the MoS_3 nanoribbon is slightly more stable than TO-P but less stable than WL-P. Hence, here again, this would mean that the size effect will modulate the relative stability of this polymorph which would be favored at small sizes.

We calculate the corrections for two different temperatures to check the sensitivity of free energy values with respect to temperature (Figure **5-10**). However, we did not observe any substantial effect of these corrections. The result is very mild for small clusters; it is negligible, and for larger ones, it slightly stabilizes the polymorphs. At 0K, the crossing point between TO and OR occurs after size=9, which is shifted before size=9, for T=625 K. 1T'-MoS_3 polymorphs remains unaffected by thermochemistry.

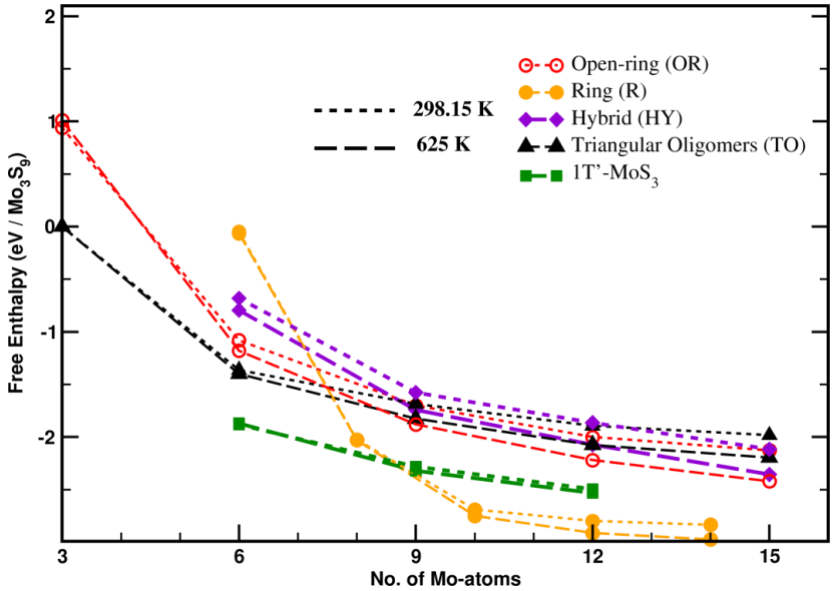

Figure 5-10: Growth free energy of clusters as a function of the number of Mo-atoms, including the zero-point energy correction and thermal corrections.

5.4. Spectroscopic analysis

5.4.5. Comparison of the simulation of $[Mo_3S_{13}]^0$, $[Mo_3S_{13}]^{2-}$ and $[Mo_3S_9]^0$ clusters with the reference $[Mo_3S_{13}^{2-}]$ compounds

The current experimental assignment of the characteristic peaks at 470 cm^{-1} refer to μ_3-S (also called apical S), 520 cm^{-1} as μ_1-S_2 (also usually called terminal S_2), and 545 as μ_2-S_2 (bridging S_2) are based on the spectrum of the reference spectrum of $(NH_4^+)_2[Mo_3S_{13}^{2-}].H_2O$.[40] However, as we show in what follows, this interpretation must be considered with great care because firstly, Mo_3S_{13} is fully saturated by S atoms: S/Mo stoichiometry is equal to $4+\frac{1}{3}$ which is far above the one of MoS_3 and lac the key descriptors. Secondly, the Mo_3S_{13} entity is negatively charged, whereas *a*-MoS_3 is neutral.[40]

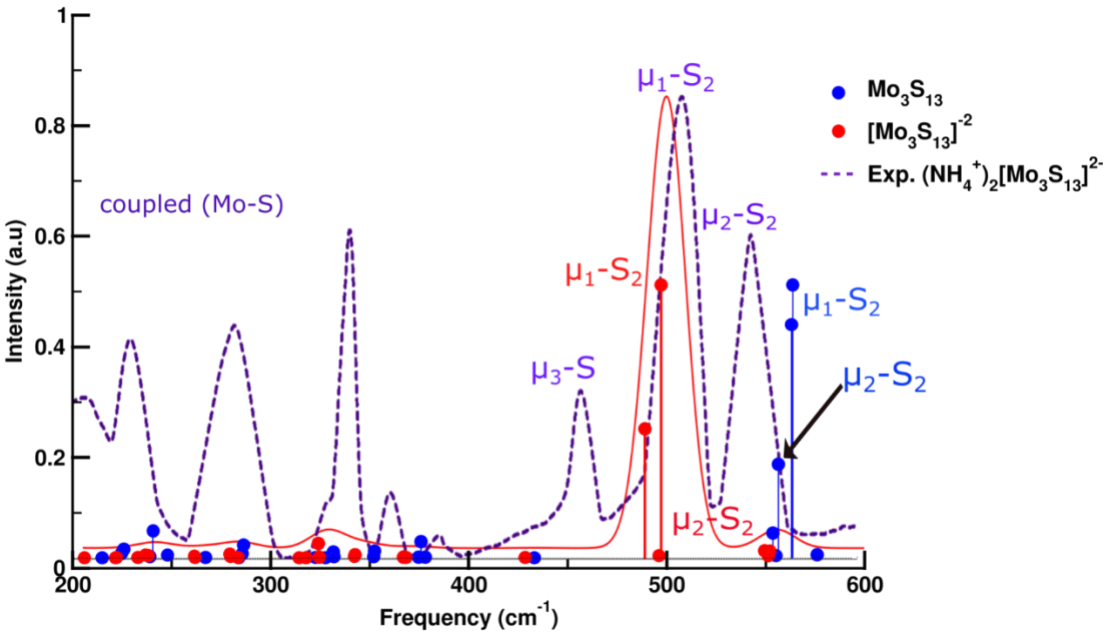

Figure 5-11: Simulated spectrum of Mo_3S_{13} (charged and uncharged) and its comparison with experimental IR spectrum of $(NH4^+)_2[Mo_3S_{13}]^{2-}$.

We simulated two species $[Mo_3S_{13}]^0$ and $[Mo_3S_{13}]^{2-}$ to better understand the charge effect on the vibrational frequencies of S-S modes, either as μ_1-S_2 or μ_2-S_2 species. The results reported in Figure **5-11** highlight a clear red-shift of the vibrational S-S mode of the μ_1-S_2 species by about 60 cm^{-1} in $[Mo_3S_{13}]^{2-}$ with respect to $[Mo_3S_{13}]^0$. By contrast, the vibrational frequency of μ_1-S_2 mode is not affected by the charge. We undertook a Bader charge analysis (Table **5-2**) to delve deeper into this effect, revealing that charge accumulates on the terminal μ_1-S_2 species, inducing an S-S bond stretching by 0.029 Å and thus a shift of the vibrational S-S modes to a lower frequency. By contrast, the charge of μ_2-S_2 remains almost constant, and therefore it results in a weaker change in vibrational frequency. Thus, in the case of the reference $[Mo_3S_{13}]^{2-}$ charged compound, a clear distinction (by about 50 cm^{-1}) can be made between μ_1-S_2 and μ_2-S, whereas this discrimination vanishes for the neutral $[Mo_3S_{13}]^0$. Moreover, the effect of the over-stoichiometry is also highlighted in Figure **5-11** since the S-S frequencies in μ_1-S_2 and μ_2-S_2 are also red-shifted by 16/18 cm^{-1} in $[Mo_3S_{13}]^0$ with respect to $[Mo_3S_9]^0$. In addition, two μ_1-S and μ_2-S species are present in $[Mo_3S_9]^0$ with lower frequencies at about 530 and 440-460 cm^{-1} respectively, not present neither in $[Mo_3S_{13}]^0$ nor in $[Mo_3S_{13}]^{2-}$.

Table 5-2: Bond lengths, Bader charges, and vibrational frequency of S_2 and S species present in $[Mo_3S_{13}]^0$, $[Mo_3S_{13}]^{-2}$ and $[Mo_3S_9]^0$

			S-S bond (Å)	charge on S_2	Vib. Freq. (cm^{-1})
	Exp.	μ_1-S_2	-	-	505
		μ_2-S_2	-	-	545
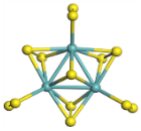	$[Mo_3S_{13}]^0$	μ_1-S_2	1.999	6.29	560
		μ_2-S_2	2.028	6.41	555
		μ_3-S	-	-	436
	$[Mo_3S_{13}]^{2-}$	μ_1-S_2	2.028	6.54	500
		μ_2-S_2	2.032	6.49	550
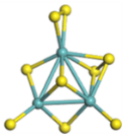		μ_3-S	-	-	431
	$[Mo_3S_9]^0$	μ_1-S_2	2.053	6.64	542
		μ_2-S_2	2.057	6.37	539
		μ_1-S	-	-	532, 527
		μ_2-S	-	-	443, 466
		μ_3-S	-	-	422

As a consequence, the IR assignment of MoS_3 exclusively based on the $(NH_4^+)_2[Mo_3S_{13}^{2-}]$ reference could be seriously misleading. In particular, the usual empirical assignment of the characteristic peaks at 520 cm^{-1} for μ_1-S_2 and 545 cm^{-1} for μ_2-S_2 is not confirmed. From this, we can thus indicate that the μ_1-S_2 or μ_2-S_2 would be challenging to differentiate, while other species such as μ_1-S or μ_2-S have never been invoked for the IR assignment, whereas they exist in $[Mo_3S_{13}]^0$ as well as in larger TO identified.

5.4.6. IR spectrum of TO polymorphs

As discussed in the previous section, the empirical IR assignment of MoS_3 based on $(NH_4^+)_2[Mo_3S_{13}]^{2-}$ reference compound[40] must be questioned due to the effects of the $2e^-$ charge and S/Mo over-stoichiometry involved in this reference compound. Weber et

al.[40] have assigned the two characteristic peaks at 520-525 cm^{-1} to μ_1-S_2 and 545-555 cm^{-1} to μ_2-S_2. While the simulation confirms that in $[Mo_3S_{13}]^{2-}$ the two characteristic peaks at 520-525 cm^{-1} and 545-555 cm^{-1} can be assigned to μ_1-S_2 and to μ_2-S_2 respectively, the S-S vibrational frequencies of these two species cannot be easily distinguished anymore in the neutral $[Mo_3S_9]^0$ due to the significant shift of the S-S frequency in μ_1-S_2 with or without charge. Moreover, μ_1-S or μ_2-S species exist in $[Mo_3S_9]^0$ as well as in the larger TO previously identified, while they are not present in $[Mo_3S_{13}]^{2-}$.

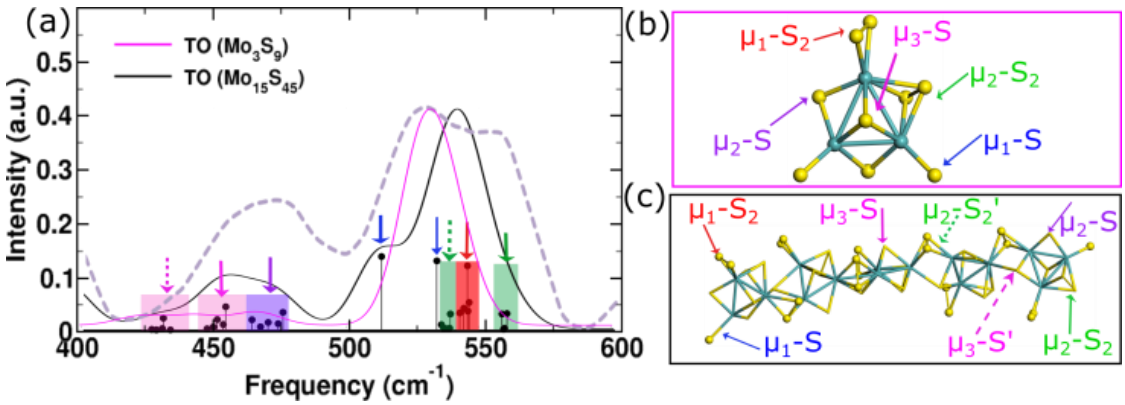

Figure 5-12: (a) IR spectra of Mo_3S_9 (pink line), TO $Mo_{15}S_{45}$ (black line), Colored arrows point to the contributions of the various S species as defined in the structural models of (b) triangular Mo_3S_9 and (c) TO $Mo_{15}S_{45}$. All simulated spectra have been renormalized while keeping the highest intensity peak fixed. Experimental IR spectrum (dashed line) from ref.[40]

The simulation of IR spectra performed (e.g., Figure **5-12**a) are compared with the *a*-MoS_3 bulk IR spectrum provided in Ref.[40], similar to other published spectra.[36, 128] Since the region below 400 cm^{-1} involves mixed vibrational modes of Mo-S and Mo-Mo, we focus on the following on the region 400-600 cm^{-1}. As we expect from the preliminary analysis of Mo_3S_9, all modes involving S_2 dimers such as μ_2-S_2 or μ_1-S_2 appear between 535-558 cm^{-1} (Table C-4). For TOs larger than Mo_3S_9 (including $Mo_{15}S_{45}$ in Figure **5-12**), two types of μ_2-S_2 exist: one located on each triangular cluster (545-558 cm^{-1}) and the one at the interconnection of two triangles (535-539 cm^{-1}). Furthermore, μ_1-S_2 appears in between two types of μ_2-S_2 (538-546 cm^{-1}) and exhibits the highest intensity of the S_2 species. Since the frequencies of μ_2-S_2 and μ_1-S_2 are very close, they produce a single broad peak in this spectrum region. Thus, considering only these two S species, it is impossible to explain the origin of the two high-intensity peaks revealed in the experimental IR spectrum's 500-

575 cm-1 region. However, the two μ_1-S_1 species of the triangular Mo_3S_9 give rise to two high-intensity peaks at 512 cm^{-1} and 532 cm^{-1} which may thus contribute to the region observed in the experimental data at about 525 cm^{-1}. This interpretation has never been proposed in the experimental literature due to the use of the $(NH_4^+)_2[Mo_3S_{13}^{2-}]$ reference, which does not contain μ_1-S_1 species. Figure C-6 illustrates the effect of TO size on the evolution of the IR spectra: the intensity of the first μ_1-S_1 high-intensity peak decreases with increasing size because μ_1-S_1 are located at TO edges.

Finally, in the broad region between 425 and 475 cm^{-1}, the simulation reveals a contribution of three types of species:

- μ_3-S on each triangular cluster at ~430 cm^{-1},
- μ_3-S at the interconnection of the triangular clusters at ~425 cm^{-1},
- μ_2-S species on each triangular cluster at 446-475 cm^{-1}.

Increasing the size of TO up to the infinite TO-P enhances the intensity of this broad low wavenumber region with respect to the 500-575 cm^{-1} region (Figure C-6).

However, considering one single type of TO polymorph makes it challenging to recover the experimental IR spectrum. As the previous energetic analysis showed that TO polymorphs are less stable for large size than chain-like ones (OR, R, WL) or 1T'-MoS_3 clusters, we investigate their spectroscopic features next.

5.4.7. IR spectrum of chain-like (OR, R, and WL) polymorphs

The simulated spectra of chain-like models OR and R reveal that they exhibit all very similar features (Figure C-7 and Figure C-8): as an example, R $Mo_{14}S_{42}$ is also reported in Figure **5-13**. It is important to recall that no μ_1-S_2 species are present and that μ_2-S_2 and μ_2-S are predominantly located in the internal chain (Figure **5-13**). Thus, the simulated spectra are dominated by one intense region between 531 to 547 cm^{-1} due to μ_2-S_2 species (Table C-4). Increasing the size of OR and R induces a slight shift to higher frequencies of the μ_2-S_2 region. This trend correlates with the slight increase of the S-S bond length (from 2.053 Å to 2.067 Å) when the size increases. OR also contains 4 μ_1-S at edges with a peak at ~508 cm^{-1}, whose intensity decreases with increasing size due to the loss of edge

effects. Finally, the μ_2-S modes contribute to the broad region 450-475 cm^{-1}, depending on sizes (Table C-4). Due to the absence of the μ_3-S contributions and the IR intensity quenching interaction between μ_2-S species, this low-frequency region is much less intense for the chain-like models than in TO polymorphs.

WL exhibits a similar trend as TO for the regions due to μ_2-S_2 and μ_2-S contributions (Figure C-9). In addition, the four μ_1-S at edges imply the appearance of a marked shoulder around 515 cm^{-1} for the small sizes. As for OR, this edge effect vanishes for considerable and infinite size, such as in WL-P. Here again, the broad region 450-475 cm^{-1} exhibits a very weak intensity. To enhance this region, one should break the high symmetry of the R, WL, and OR systems by generating a helical system as shown for HL-P in Figure **5-13**. In this case, the 3D-distortion of the chain enhances the contributions μ_2-S, which are not all perfectly located in the plane of the circular region of HL.

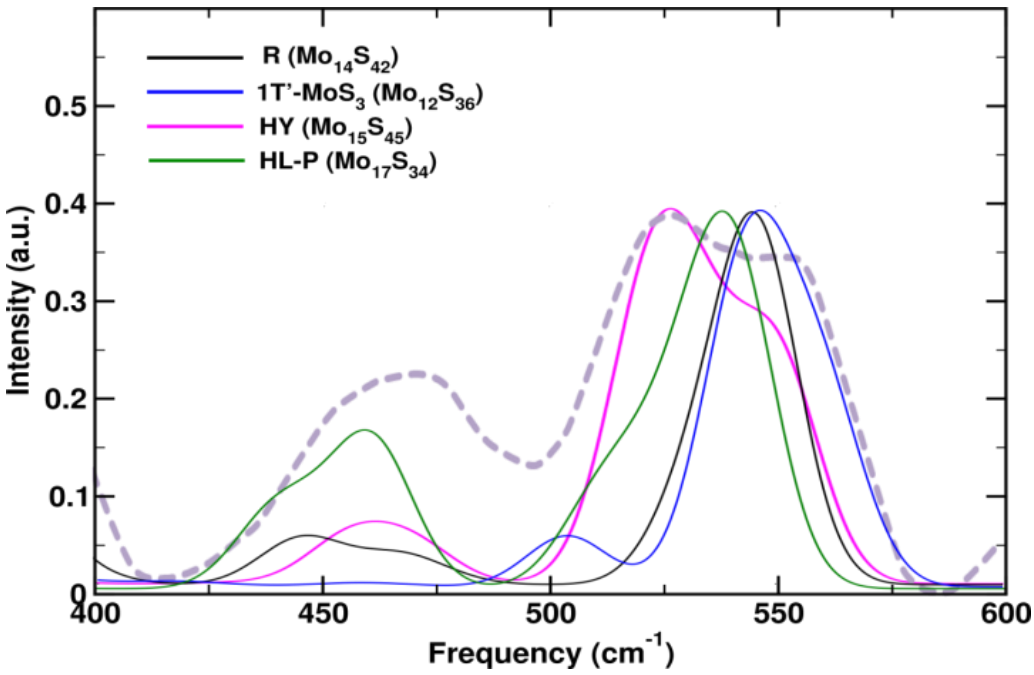

Figure 5-13: IR spectrum of R, HL-P, HY, and 1T'-MoS_3 polymorphs (solid lines). All simulated spectra have been renormalized while keeping the highest intensity peak fixed. Dashed curve: experimental IR spectrum from ref.[40]

Finally, Figure **5-13** reports the simulated IR spectrum for the 1T'-MoS_3 cluster ($Mo_{12}S_{36}$), revealing that the predominant μ_2-S_2 species and the two μ_1-S_2 presents at edges exhibit

a slightly broad region at about 550 cm^{-1}, which matches well the high-frequency region of the experimental spectrum.

5.5. Discussion

Our revisited assignment of the IR spectrum of MoS_3 reveals that the higher region at 545-555 cm^{-1} is assigned to both μ_1-S_2 and μ_2-S_2 when they exist as in TO polymorphs (with at least 6 Mo), or to μ_2-S_2 only as in chain-like models (R, OR, WL, HL), or to edges of 1T'-MoS_3. The IR region at 520-525 cm^{-1} is reproduced only if μ_1-S species are present either at the edges of the chain-like and TO models or on the triangular Mo_3S_9.

Moreover, the energetic analysis showed that TO models are thermodynamically stable only for the smallest size as Mo_3S_9, whereas for larger sizes, the chain-like (OR, R, WL, HL) or the 1T'-MoS_3 cluster become more stable. Hence, the MoS_3 phase is actually constituted of various polymorphs as a function of the size of the oligomers. This is reflected in the IR spectrum resulting from the contribution of these multiple polymorphs. At this stage, we can propose the two following possible combinations of polymorphs:

- Triangular Mo_3S_9 (contributing to the region 520-525 cm^{-1}) and 1T'-MoS_3 cluster such as $Mo_{12}S_{36}$ or even NbS_3-ribbon for larger size (contributing to the region 545-555 cm^{-1})
- Triangular Mo_3S_9 (contributing to the region 520-525 cm^{-1}) and larger chain-like models such as OR, R, WL, or HL (contributing to the region 545-555 cm^{-1} and to the region 520-525 cm^{-1} when μ_1-S species are present at edges).

To further investigate the combination of Triangular Mo_3S_9 with chain-like models, we simulated a Hybrid (HY) structure combining both one OR structure with two triangular Mo_3S_9 clusters located at its edges (Figure **5-1**d). As expected, this composite structure recovers the two high-frequency regions (Figure **5-13**) of the experimental spectrum. The μ_1-S species of the triangular Mo_3S_9 give rise to a broad region at 520 cm^{-1} (Figure C-10). In addition, one μ_1-S_2 of the triangular Mo_3S_9 and μ_2-S_2 of the triangles and of the OR chain gives rise to the upper part of the experimental spectrum (533-552 cm^{-1}). With increasing size, this upper region gains relative intensity due to more numerous μ_2-S_2 contributions with respect to μ_1-S. Similarly, the lowest broad region between 450 and 500 cm^{-1} is also

increasingly visible due to the increased number of μ_2-S within the chain (Figure C-7). To enhance the intensity of this region 450-500 cm^{-1}, 3D-chain distortion as in HL is required.

XPS experiments of MoS_3 usually reveal two species, μ_2-S_2 and μ_1-S_2, in the S 2p region with respective binding energies of 162.9 eV and 161.6 eV. In other words, the corresponding relative binding energy, ΔBE=BE(μ_2-S_2)-BE(μ_1-S_2), is +1.3 eV.[40] The DFT calculation of the core level shift between μ_2-S_2 and μ_1-S_2 species yield a ΔBE of 1.55 eV in 1T'-MoS_3 and 1.57 eV in TO $Mo_{18}S_{54}$ (Table **5-3**). Given the DFT accuracy, this value is in reasonable agreement with the experiment.

However, in chain-like models, μ_2-S_1 are present instead of μ_1-S_2, which may raise a question about the coherence with XPS. Our DFT calculations show that ΔBE=BE(μ_2-S_2)-BE(μ_2-S) fluctuates between 1.14 eV and 1.65 eV for various WL and OR models. So, these models also remain compatible with the S 2p XPS spectrum, i.e., XPS does not allow discrimination between these different models.

Table 5-3: Binding energy (in eV) of different Sulfur species present in various polymorphs by core-level shift calculation.

Species	ΔB.E = BE(μ_2-S_2) – BE(μ_1-S_2)	ΔB.E = BE(μ_2-S_2) – BE(μ_1-S)	ΔB.E = BE(μ_2-S_2) – BE(μ_2-S)	ΔB.E = BE(μ_2-S_2) – BE(μ_3-S)
TO	**1.57**	**2.84**	**1.56**	**1.3**
TO-P	**0.75**	--	**0.87**	**1.09**
OR	--	**2.23**	**1.66**	--
WL	--	**2.31**	**1.14**	--
WL-P	--	--	**1.48**	--
HL-P	--	--	**1.75**	--
1T'-MoS_3	**1.55**	--	--	**1.43**

Regarding the μ_1-S species present at edges of TO, WL, and OR, the question of compatibility with XPS must also be addressed. Here, ΔBE=BE(μ_2-S_2)-BE(μ_1-S) is shifted to significantly higher energy: +2.84 eV in TO $Mo_{15}S_{45}$, +2.31 eV in WL (Mo=14) and +2.23 eV in OR (Mo = 15) also meaning that the binding energy of μ_1-S_2 is significantly greater

than the one of μ_1-S. However, these μ_1-S species are not identified in the S 2p XPS spectrum. As a consequence, if these μ_1-S exist, they must be present in very low concentrations, i.e., significantly smaller than the other S species. This low concentration of μ_1-S does not contradict the IR spectrum since we noticed that in our proposed models, their number is comprised between 2 and 4 per polymorph. For the model $Mo_{15}S_{45}$, this represents less than 10% of S species. Since the bulk MoS_3 phase comprises polymorphs of various sizes going beyond $Mo_{15}S_{45}$, this percentage is undoubtedly much lower. Due to the higher sensitivity of IR to these μ_1-S species, their low concentration does not prevent them from being visible in IR spectra while XPS does not see them.

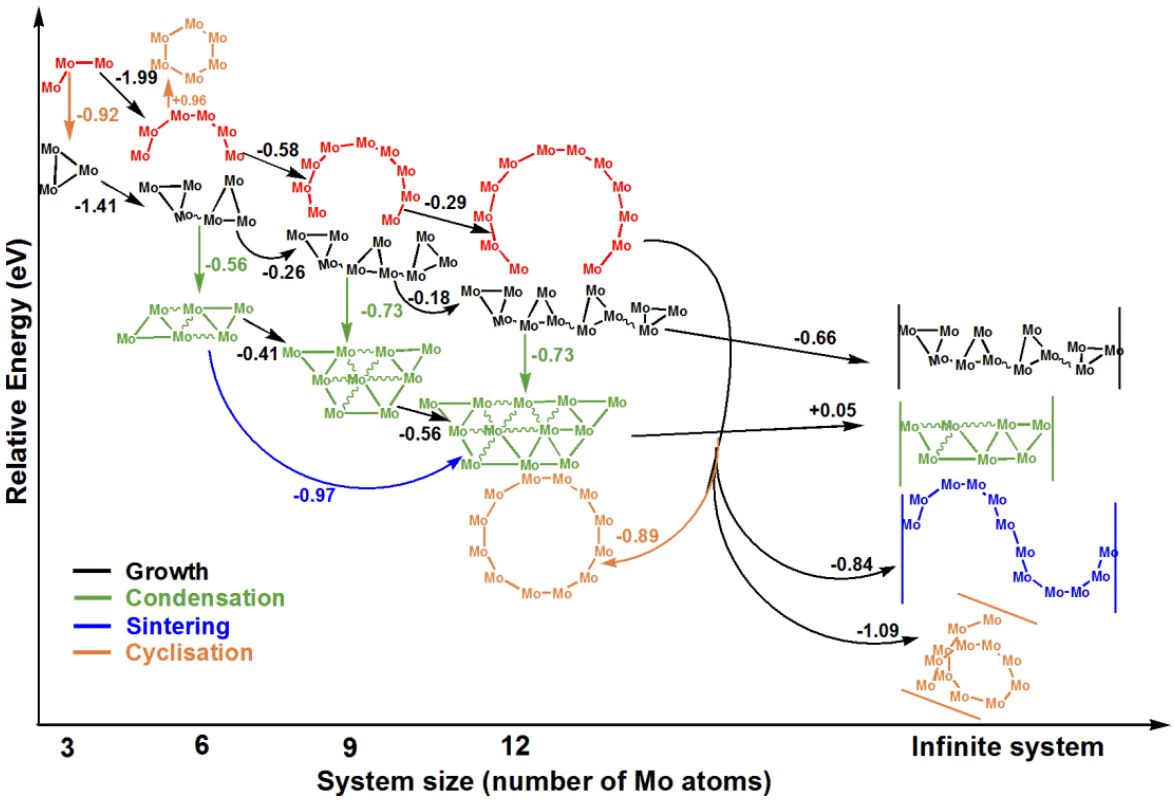

Figure 5-14: Possible transformation pathways of the MoS_3 polymorphs and correspondingly free energy change.

In both aforementioned combinations of MoS_3 polymorphs, the Mo-Mo bond length should exhibit the short (~2.72-2.75 Å) and long (2.96-3.16 Å) contribution as reported by some EXAFS analysis.[35] Depending on the proportion of triangular Mo_3S_9, we may suspect that the long Mo-Mo bond vanishes and the short one only becomes predominant. This could explain that other EXAFS analyses reported this short Mo-Mo bond only.[35, 120, 122, 241] These different observations may also originate from the genesis

(synthesis pathway) of the MoS_3 phase, which may result in atomically different *a*-MoS_3 phases depending on the experimental conditions.

As illustrated by the thermodynamic energy plot (Figure **5-9**), the triangular Mo_3S_9 is the most stable one for the smallest size. If the nucleation of MoS_3 starts from such triangular clusters, it is highly improbable that it transforms into a chain-like OR Mo_3S_9 because of the high reaction endergonicity (ΔG~1 eV at T=298.15 K, Figure **5-10**). Concomitantly, if the nucleation generates OR Mo_3S_9, the reverse reaction to TO is exergonic. For larger TO, the transformation into chain-like oligomers (OR, R, WL, HL) would be thermodynamically favored (Figure **5-10**). Although further investigations are needed, it is strongly suspected that the kinetic limitations of breaking several Mo-S and Mo-Mo bonds to open the interconnected triangular Mo_3S_9 clusters will prevent the transformation from TO into the chain-like polymorphs. Hence, the formation of chain-like polymorphs would need to be promoted during the genesis of the Mo_3S_9 embryos through specific reaction conditions (precursors or even support effects).

Assuming that the triangular Mo_3S_9 clusters are first formed, they could grow by connecting one to each other to form TO oligomers of increasing sizes. Nevertheless, as we have shown by AIMD, the small TO intermediates Mo_6S_{18}, Mo_9S_{27}, and $Mo_{12}S_{36}$ are prone to be further transformed into 1T'-MoS_3 clusters through a condensation step (Figure **5-14**). This striking dynamic behavior reveals that metastable TO conformers might readily convert into a 1T'-like MoS_3 polymorph.

The TO into 1T'-MoS_3 transformation is exergonic (ΔG~-0.56 eV to -0.73 eV for the three Mo_6S_{18}, Mo_9S_{27}, and $Mo_{12}S_{36}$ clusters). As revealed by the AIMD simulation, this condensation mechanism occurs if the relative positions of the various dimeric and monomeric S species are optimal. Otherwise, it is blocked, and the oligomerization of the triangular species can continue. Once the first embryos of the 1T'-MoS_3 phase are generated in the form of the structures identified by our AIMD, they could probably follow a sintering process to produce larger MoS_3 ribbons inspired by the NbS_3 structure.[114, 126] Note that the transformation of TO-P into MoS_3 ribbons (NbS_3-like) is also exergonic.

In the present AIMD simulations (constant chemical composition), the obtained 1T'-like phase is thus over-stoichiometric with respect to 1T'-MoS_2, and the excess S atoms are located at the edges of the 1T'-nanostructure.

Similarly, over-stoichiometric triangular or hexagonal nanostructures have been reported for 2H-MoS_2.[32, 248] The removal of the excess sulfur from the edge sites in the presence of H_2 as it is usual in sulfo-reductive conditions may lead to 1T'-MoS_2[7], which can further transform into 2H-MoS_2.[249–256] The easy formation of the 1T'-MoS_3 cluster also justifies the above proposal of coexistence of triangular Mo_3S_9 and 1T'-MoS_3 clusters to recover the experimental IR spectrum.

However, we cannot exclude that right from the early stage; the nucleation forms a chain like a cluster (if stabilized by support effect or nature of precursor) which rapidly grows by adding "linearly" other Mo atoms before transforming into TO that is energetically preferred in the gas-phase for small clusters. Furthermore, if the growth of OR proceeds further, the cyclization process from OR to R would be likely considering the significant free energy gain ($\Delta G \sim -0.89$ eV at T=298.15 K, for $Mo_{12}S_{36}$). The fact that such ring structures have not been yet reported so far may indicate that the first scenario is common. However, we propose that the improvement of synthesis or characterization methods could allow for identifying the R structures. Alternatively, the reconstruction of the terminal units of the OR structures could result in the HY structures where triangular clusters and a chain are interconnected. We have shown above that the simulated IR spectrum of these HY polymorphs is also compatible with the experimental one.

5.6. Conclusions

By means of DFT calculations, the present work provided a detailed analysis of the structural, energetic, and spectroscopic properties of the *a*-MoS_3 amorphous phase. The challenging question of the amorphous nature of this phase was addressed by identifying several structures of possible conformers such as chain-like and triangular oligomers either previously invoked in the experimental literature or newly proposed. By simulating cluster models and periodic structures, we showed how size effects impact the relative stability of these various polymorphs.

We first ruled out the strictly linear models of $Mo^{5+}(S^{2-})_2(S_2^{2-})_{1/2}$[34, 41] and of $Mo^{4+}(S^{2-})(S_2^{2-})$, which are both significantly less stable than triangular models or curved chains. The curvature is induced by the specific orientation of S_2 dimers as found in open-ring (OR), ring (R), wave-like (WL), or helical (HL) structures.

For small sizes, the triangular Mo_3S_9 is more stable than the chain-like models. Nevertheless, the free energy rapidly becomes favorable to chain-like models when increasing size. In particular, for the largest oligomers studied here ($Mo_{15}S_{45}$), OR and R becomes more stable than TO, while the periodic structures such WL-P and HL-P confirm that chain-like models are favored.

To the best of our knowledge, the stable ring structures were never observed experimentally. So, as a first perspective to favor the formation of this appealing ring structure, we suggest that experimental studies may explore alternative synthesis pathways to prevent the formation of triangular clusters and to prompt the cyclization process.

We proposed possible transformation pathways for the MoS_3 oligomers: from their nucleation to growth, accompanied eventually by condensation and cyclization steps. In particular, the AIMD simulation revealed the easy transformation of the MoS_3 TOs into a so-called "1T'-MoS_3" phase with the typical structural pattern of the 1T'-MoS_2 phase. The corresponding periodic structure should be MoS_3-ribbon inherited from the NbS_3 phase.

Our large variety of explored structures allowed us to revisit the interpretation of experimental EXAFS, IR, and XPS spectra. The DFPT simulation of IR spectra highlighted the particular contribution of the Mo-S mode of μ_1-S species in the 525 cm^{-1} region. In comparison, the S-S modes of μ_1-S_2 and μ_2-S_2 contribute to the 550 cm^{-1} region. The core-level shift calculations reveal the XPS compatibility of all S species, excepting μ_1-S species present at the edges of the chain-like model or in the triangular Mo_3S_9, which, therefore, should at most exist in very low concentrations. To recover the IR spectrum, we proposed relevant combinations of polymorphs. These combinations of polymorphs may also explain why EXAFS data report either one or two types of Mo-Mo bond lengths depending on the relative concentrations of each polymorph. The curved chain-like model contains

only one short Mo-Mo bond, whereas the TO model contains one short and one long Mo-Mo bond length.

This in-depth theoretical study of the MoS_3 phase provides a rational understanding of the amorphous MoS_3 phase, which could be helpful in improving its reactivity as well as the genesis of MoS_2 phases (1T or 2H) used in many applications: hydrotreatment, hydrogen evolution reaction, storage materials… We propose in the general conclusions to revisit the principal results of the genesis of the MoS_2 phase obtained in Chapter 4 and 5.

Chapter 6: Conclusions and perspectives

In this thesis, we have addressed four objectives under the critical questions of the genesis of the γ-alumina-supported MoS_2 catalyst. The first objective was to understand the interaction of oxide precursors and the nature of alumina anchoring sites, how the support influences the structure (triangular vs. chain), and the stability of molybdenum oxide precursors represented by small oligomers. The second objective was devoted to the mechanistic insights into the sulfo-reduction of these molybdenum oxide precursors and the impact of the support. We provided a fundamental understanding and a quantitative analysis by identifying the various types of oxygen sites and their potentiality towards sulfo-reduction. The combination of thermodynamics and kinetics of the process offers information on the involved intermediates and limiting steps. In particular, the competition of oxysulfide and trisulfide pathways has been examined. The third objective was to probe various key effects on two sulfidation pathways: the size of Mo-oxysulfide and trisulfide oligomers and structural reconstruction (triangular vs. linear). Finally, the fourth objective was to determine the nature of the MoS_3 phase, growth, and morphological evolution (chain vs. triangular) as a function of size (in the absence of any support effect). We have attempted to make the bridge with numerous experimental data (IR, EXAFS, XPS…) published in the literature for each objective.

In what follows, we summarize the critical findings related to these objectives. Besides, we highlight the limitation of the current study and the questions which still remain open. Therefore, we will also propose some further DFT investigations in the spirit of unfolding those challenges.

6.1. Sulfo-reduction of Mo-oxides on supported alumina

Monomer (Mo_1O_3), dimer (Mo_2O_6), and trimer (Mo_3O_9) as a model of oxide precursors have been investigated on the (100) surface of alumina. The support has a considerable effect on the conformation of Mo-oxides and their stability. Mo_2O_6 structures are modified by support with respect to its gas-phase conformer. The support stabilizes the chain-Mo_3O_9 vs. cyclic-Mo_3O_9 through the anchoring point of Mo-Ol-Al and Mo-O_{surf} linkage. Indeed, the support reverses the relative stability between the two arrangements with respect to the gas-phase. The support also leads to a stronger deformation of chain-Mo_3O_9 compared to the cyclic model. The larger the deformation of the structure from its gas phase, the greater the impact on

stability was observed. Four chemically different classes of oxygens were found on supported Mo-oxides: terminal (O_t), bridging (O_{br}), interfacial-bidentate ($O_{int\text{-}bi}$), and interfacial-tridentate ($O_{int\text{-}tri}$). These oxygens, with their various chemical environment, play a crucial role during sulfo-reduction.

O/S exchange is the most commonly invoked chemical phenomenon in the literature for the sulfidation process. Generally, O/S exchange is thermodynamically favorable and results in an energy gain of 0.3-0.5 eV. However, thermodynamically neutral or even endergonic steps, for some last couple of O/S exchanges, suggest intrinsic difficulties at the end of the process. Terminal and bridging oxygens are equally prone to exchange and more favorable than O_{int} thermodynamically. If two adjacent interfacial oxygens are first exchanged (heterogeneous sulfidation), an S_2-dimer can be formed, which provides a strong stabilization (~1 eV). This stabilizing effect of the dimer is also consistent in other chains and cyclic-Mo_3O_9 models. Moreover, the S_2-dimer formation is also an indication of reducing the oxidation state of Mo.

We propose an interpretation of EXAFS data based on the simulated oxysulfide intermediates' analysis and suspect that the short Mo-O_t bonds observed in EXAFS are the signature of a heterogeneously sulfided Mo-oxysulfides.

Regarding the mechanisms, the necessary steps to replace the oxygen with sulfur are H_2S adsorption, H_2S dissociation, proton transfer, and water desorption. In most cases, the H_2S dissociation or the proton transfer step is the rate-limiting step (for O_t, $O_{br,}$ and $O_{int\text{-}bi}$). However, $O_{int\text{-}tri}$ is limited by water desorption and sulfur diffusion. Bridging oxygen (O_{br}) is the easiest to be replaced by sulfur, requiring ~1.2 eV. The terminal oxygens (O_t) are moderately expensive and feature an activation free energy of ~1.6 eV. However, for interfacial oxygen atoms, due to strong interaction with support, the interfacial oxygens demand excessive energy for sulfidation (larger than 1.7 eV). If we follow this path till the end, a trisulfide Mo_3S_9 oligomer with a chain-like structure anchored on the support is obtained (Figure **6-1**).

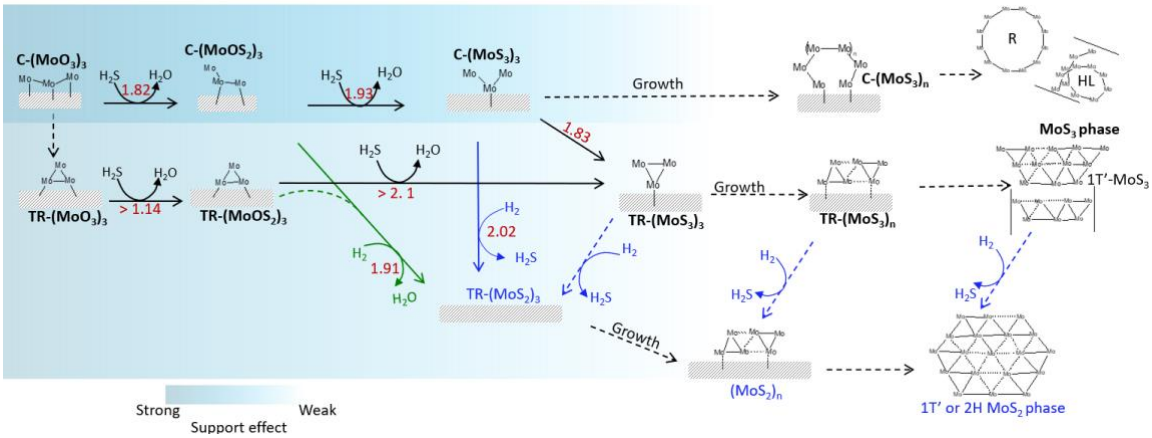

Figure 6-1: Schematic representation of the entire activation process, starting from Mo-oxide precursors to final MoS_2 active phase. The solid arrows indicate the current work, and the dashed arrows imply the perspectives of this work.

Further transformation of chain-Mo_3S_9 into triangular Mo_3S_6 phase is feasible but with relatively high activation energy (2.0 eV) resulting from S-vacancy creation by H_2 reduction. Hence, we suspect that the reconstruction of chain-Mo_3S_9 into triangular- Mo_3S_9 would be kinetically preferred (1.8 eV), although it is slightly less stable. This triangular Mo_3S_9 will rapidly grow to triangular $(Mo_3S_9)_n$ 1T'-patches, possible precursors of the 1T-MoS_2 phases (Figure **6-1**).

As the last few interfacial oxygen sites are challenging to exchange and removing sulfur, we compare if H_2 could help to remove them and form directly MoS_2 species instead of MoS_3. The process involves four key steps: H_2 adsorption, H_2 dissociation, proton transfer, and water desorption. The dissociation of hydrogen is usually the rate-limiting step. Thermodynamics favors the first two oxygen removal with activation energies of about 1.9 eV, similar to O/S exchange (Figure **6-1**). However, the final oxygen removal leads to a very high energy intermediate that may block the full path and forced it to return to an O/S exchange. Furthermore, if we compare the oxysulfides vs. trisulfide pathway, the activation energy of removing the S from Mo_3S_9 is very similar to oxygen removal or exchange. Therefore, we suspect that the reconstruction of chain Mo_3S_9 followed by the rapid growth of triangular Mo_3S_9 entities could be the preferred pathway.

The evaluation of the interaction energies of oxides, oxysulfides, trisulfides, and disulfides species with the support revealed that oxides have the strongest interaction with alumina, dominated mainly by Mo-O-Al linkage, whereas the disulfides and trisulfides exhibit the weakest ones. Interestingly, triangular-Mo_3S_9 demonstrates the weakest interaction with alumina, which may enhance their surface diffusion and growth. Moreover, since the kinetics of sulfo-reduction of monomeric Mo_1O_3 species is far more complicated, we deduce that the growth of TR-Mo_3S_9 is more probable. However, this point should be validated by further investigations as proposed in the perspectives.

6.2. MoS_3 phase: triangular, chain, ring, or hybrid?

Using DFT, we systematically examined not only the various proposed models of MoS_3 either by theoretical investigations or by experimental observations such as triangles and chains but also some unprecedented ones such as ring, helical, and 1T'-MoS_3. We have compared the effect of size and their structural stability. The strictly linear MoS_3 is significantly less stable than the triangular or curved chains and is therefore not part of the likely constituents of amorphous MoS_3.

We have compared some of the key descriptors such as Mo-Mo and Mo-S bonds with available EXAFS data for our investigation models. Triangular models have two Mo-Mo bonds as proposed by some EXAFS, and chain models have only a short Mo-Mo bond as described by others. For the smallest size (No. of Mo-atoms (n) = 3), MoS_3 is most stable as triangular; for size n=6 and 9, it is most stable as 1T'-MoS_3; and for size n > 9, it is most stable as a ring, based on thermodynamic energy. Curved-chain models are more stable for a larger size than triangular oligomers. Even for the infinite size, the helical structure, which is an extension of the open-ring model, is the most stable one, followed by wavelike and NbS_3-ribbon.

We re-examine the IR-peak assignment for various models. We found a discrepancy with the earlier peak assignment based on the over-sulfided Mo_3S_{13} compound. The terminal and bridging-S_2 do not give rise to two different peaks but instead, appear at a similar frequency. Not a single model is able to reproduce the amorphous bulk-MoS_3 spectrum, so we suspect the presence of a mixture of various structures in the experimental bulk-MoS_3 samples, such as triangular, open-ring, hybrid, and a so-called 1T'-MoS_3.

We showed the transformation pathways from one polymorph to another, indicating at what stage the transformation could occur. By utilizing AIMD, we have revealed how triangular $(Mo_3S_3)_n$ may evolve to a 1T'-MoS_3 phase resembling the 1T-MoS_2 phase. The latter phase would then be transformed by S-diffusion into 2H-MoS_2.

6.3. Impact of the support

The easy transformation of triangular $(Mo_3S_9)_n$ into 1T'-MoS_3 2D patches as revealed by AIMD, induces that this process could be a favorable pathway for the further evolution of TR-Mo_3S_9 toward the 1T-MoS_2. However, this process will be possible only if the support does not favor the formation of C-Mo_3S_9 (Figure **6-1**). The stabilization of TR-Mo_3S_9 could be inherited from the cyclic-Mo_3O_9 precursors, which are stabilized in the absence of support, as shown by our calculations. Hence, a weakening of Mo-support interaction could be beneficial not only to the removal of O-species (particularly those located at the interface) but also to favor triangular species' formation, acting as the first embryos of the MoS_2 phase.

However, if a too weak metal support interaction takes place, chain-like MoS_3 polymorphs (such as helical or ring) become thermodynamically stabilized upon growing (for a size greater than 9 in the gas phase), as shown by our calculations. Once these long-chain MoS_3 polymorphs are formed, it may be difficult to reconstruct them into triangular entities, which may restrict further MoS_2 formation (see the whole scheme in Figure **6-1**).

Hence, even if more investigations are required, we suspect that an intermediate metal-support interaction that stabilizes triangular entities should be sought in order to optimize the genesis of the MoS_2 phase.

6.4. Open questions and perspectives

We have tried to unfold many challenging aspects of the genesis of the active phase on supported alumina. However, several interesting questions remain open. We propose in what follows some short-term and a few long-term perspectives to tackle those issues.

In the short term, we plan to investigate the TR-Mo_3S_9 to TR-Mo_3S_6 transformation through S-removal and compare the required activation energies with the chain-Mo_3S_9 to TR-Mo_3S_6 that we already determined. This will allow determining if the structure of Mo_3S_9 influences the S-removal step.

Moreover, we need to calculate the S removal for larger triangular MoS_3 structures to provide a better comprehension of the size effect of the MoS_3 phase on supported alumina. Furthermore, we will determine the energy barriers for the diffusion of the chain-Mo_3S_9 entities on the O-sites of the (100) surface of alumina.

In the longer term, the growth of the MoS_3 and MoS_2 phases should also be investigated. To have a clearer perspective about at which step the growth begins, whether the MoS_3 grows first and then transforms into MoS_2 or small MoS_3 transforms into MoS_2, and these MoS_2 patches grow afterward. As we know, the strength of interaction with support and activation required to remove the S from MoS_3 has a considerable impact on the growth of the trisulfide or disulfide phase. Calculating the S removal barrier for large MoS_3 species, diffusion barriers, and sintering barriers would help to understand what may happen during this process. Moreover, we think that the growth, if it occurs at the trisulfide stage, should be in triangular form because the chain could be inadequate precursors for MoS_2 transformation.

However, our understanding will remain limited to the (100) alumina surface within this project. As the (110) surface is significantly different, it is crucial to understand what happens on the (110) surface. The stability, evolution, and kinetics of many species, which we have investigated, should be considered for the future on (110) surface of alumina. On the (110) surface, sites are much more complex due to the presence of OH species which may impact the whole sulfidation process, particularly the steps involving interfacial O atoms. Moreover, the presence of the Al_{IV} site is known to have stronger interaction and could impact the stability of the triangular vs. chain throughout the reaction path.

Furthermore, we have investigated the Mo_3O_9 species that are still very small compared to what might be present in some preparation protocols. Therefore, the extension on the effect of Mo-oxides size could also be considered.

From a methodological point of view, due to the great number of DFT data collected so far, this study can be combined with microkinetic models such as kinetic-Monte-Carlo or mean-field microkinetic models for the entire process to bridge the gap between its atomic-scale insights and macroscopic properties such as rate of reaction, reaction barriers, and order of the reaction.

Considering alternative applications, *α*-MoS_3 has shown potential application for HER. The activity of HER can be investigated on our newly proposed MoS_3 models as a function of size and morphologies. We could explore the active sites and their reactivity based on the size and morphology of MoS_3 polymorphs.

Similarly, we could also propose to investigate more precisely the electronic properties of such MoS_3 polymorphs. Preliminary results have shown that they would be semi-conductors that could be beneficial for photocatalysis applications.

Last but not least, the study could also be extended to understand the nature of the interaction with toxic metals, such as Hg, by creating the defects, as *α*-MoS_3 has been shown a potential candidate for Hg capturing. We can also investigate which model suits what kind of application.

REFERENCES

[1] IEA. World Energy Outlook – 2020. https://www.iea.org/reports/world-energy-outlook-2020?mode=overview.

[2] IEA. *World Energy Outlook 2019:* Paris, France, **2019**.

[3] BP. *Full report – BP Statistical Review of World Energy 2019*.

[4] IEA. Oil Market Report - May 2021 – Analysis - IEA. https://www.iea.org/fuels-and-technologies/oil.

[5] Basset, L. Net-zero 2050 - European Climate Foundation. https://europeanclimate.org/net-zero-2050/.

[6] Office, P. *European Parliament and of the Council, Directive 2009/30/EC*.

[7] Toulhoat, H.; Raybaud, P. *Catalysis by transition metal sulphides: From molecular theory to industrial application;* Editions Technip: Paris, France, **2013**.

[8] Sabatier, P. *La catalyse en chimie organique;* Nouveau Monde: Paris, **1920**.

[9] Masel, R.I. *Principles of adsorption and reaction on solid surfaces;* Wiley: New York, Chichester, **1996**.

[10] Toulhoat, H.; Raybaud, P. Kinetic interpretation of catalytic activity patterns based on theoretical chemical descriptors. *J. Catal.*, **2003**, *216,* 63–72.

[11] Munnik, P.; Jongh, P.E. de; Jong, K.P. de. Recent Developments in the Synthesis of Supported Catalysts. *Chem. Rev.*, **2015**, *115,* 6687–6718.

[12] Che, M. Interfacial Coordination Chemistry. In: *Guczi, Solymosi et al. (Ed.) 1993 – Studies in Surface Science*; Vol. *75*; pp. 31–68.

[13] Carrier, X.; La d'Espinose de Caillerie, J.-B.; Lambert, J.-F.; Che, M. The Support as a Chemical Reagent in the Preparation of $WO_x/\gamma\text{-}Al_2O_3$ Catalysts: Formation and Deposition of Aluminotungstic Heteropolyanions. *J. Am. Chem. Soc.*, **1999**, *121,* 3377–3381.

[14] Digne, M.; Sautet, P.; Raybaud, P.; Euzen, P.; Toulhoat, H. Hydroxyl Groups on γ-Alumina Surfaces: A DFT Study. *J. Catal.*, **2002**, *211,* 1–5.

[15] Digne, M.; Sautet, P.; Raybaud, P.; Euzen, P.; Toulhoat, H. Use of DFT to achieve a rational understanding of acid-basic properties of γ-alumina surfaces. *J. Catal.*, **2004**, *226,* 54–68.

[16] Handzlik, J.; Sautet, P. Active sites of olefin metathesis on molybdena-alumina system: A periodic DFT study. *J. Catal.*, **2008**, *256,* 1–14.

[17] Handzlik, J.; Sautet, P. Structure of Isolated Molybdenum(VI) Oxide Species on γ-Alumina: A Periodic Density Functional Theory Study. *J. Phys. Chem. C*, **2008**, *112,* 14456–14463.

[18] Yan, Y.; Xia, B.; Xu, Z.; Wang, X. Recent Development of Molybdenum Sulfides as Advanced Electrocatalysts for Hydrogen Evolution Reaction. *ACS Catal.*, **2014**, *4,* 1693–1705.

[19] Escalera-López, D.; Lou, Z.; Rees, N.V. Benchmarking the Activity, Stability, and Inherent Electrochemistry of Amorphous Molybdenum Sulfide for Hydrogen Production. *Adv. Energy Mater.*, **2019**, *9,* 1802614–1802631.

[20] Matsuyama, T.; Deguchi, M.; Hayashi, A.; Tatsumisago, M.; Ozaki, T.; Togawa, Y.; Mori, S. Structure Analyses of Amorphous MoS_3 Active Materials in All-solid-state Lithium Batteries. *Electrochemistry*, **2015**, *83,* 889–893.

[21] Ye, H.; Ma, L.; Zhou, Y.; Wang, L.; Han, N.; Zhao, F.; Deng, J.; Wu, T.; Li, Y.; Lu, J. Amorphous MoS_3 as the sulfur-equivalent cathode material for room-temperature Li-S and Na-S batteries. *Proc. Natl. Acad. Sci. U S A*, **2017**, *114,* 13091–13096.

[22] Sun, J.; Wang, R.; Yuan, C. MoS_3 nanoparticles on reduced graphene oxide. *Mater. Today*, **2018**, *21,* 193–194.

[23] Lince, J.R.; Pluntze, A.M.; Jackson, S.A.; Radhakrishnan, G.; Adams, P.M. Tribochemistry of MoS_3 Nanoparticle Coatings. *Tribol. Lett.*, **2014**, *53,* 543–554.

[24] Mei, J.; Wang, C.; Kong, L.; Liu, X.; Hu, Q.; Zhao, H.; Yang, S. Outstanding Performance of Recyclable Amorphous MoS_3 Supported on TiO_2 for Capturing High Concentrations of

Gaseous Elemental Mercury: Mechanism, Kinetics, and Application. *Environ. Sci. Technol.*, **2019**, *53,* 4480–4489.
[25] Zhang, W.; Zhou, T.; Hong, J.; Xu, R. MoS_3 loaded TiO_2 nanoplates for photocatalytic water and carbon dioxide reduction. *J. Energy Chem.*, **2016**, *25,* 500–506.
[26] Seo, B.; Joo, S.H. Recent advances in unveiling active sites in molybdenum sulfide-based electrocatalysts for the hydrogen evolution reaction. *Nano Converg.*, **2017**, *4,* 19–30.
[27] Weber, T.; Muijsers, J.C.; van Wolput, J.H.M.C.; Verhagen, C.P.J.; Niemantsverdriet, J.W. Basic Reaction Steps in the Sulfidation of Crystalline MoO_3 to MoS_2, As Studied by X-ray Photoelectron and Infrared Emission Spectroscopy. *J. Phys. Chem.*, **1996**, *100,* 14144–14150.
[28] Ye, H.; Wang, L.; Deng, S.; Zeng, X.; Nie, K.; Duchesne, P.N.; Wang, B.; Liu, S.; Zhou, J.; Zhao, F.; Han, N.; Zhang, P.; Zhong, J.; Sun, X.; Li, Y.; Li, Y.; Lu, J. Amorphous MoS_3 Infiltrated with Carbon Nanotubes as an Advanced Anode Material of Sodium-Ion Batteries with Large Gravimetric, Areal, and Volumetric Capacities. *Adv. Energy Mater.*, **2017**, *7,* 1601602–1601611.
[29] He, Z.; Que, W. Molybdenum disulfide nanomaterials: Structures, properties, synthesis and recent progress on hydrogen evolution reaction. *Appl. Mater. Today*, **2016**, *3,* 23–56.
[30] Lv, R.; Robinson, J.A.; Schaak, R.E.; Du Sun; Sun, Y.; Mallouk, T.E.; Terrones, M. Transition Metal Dichalcogenides and Beyond: Synthesis, Properties, and Applications of Single- and Few-Layer Nanosheets. *Acc. Chem. Res.*, **2015**, *48,* 56–64.
[31] Raybaud, P.; Hafner, J.; Kresse, G.; Kasztelan, S.; Toulhoat, H. Ab Initio Study of the H_2–H_2S/MoS_2 Gas–Solid Interface: The Nature of the Catalytically Active Sites. *J. Catal.*, **2000**, *189,* 129–146.
[32] Schweiger, H.; Raybaud, P.; Kresse, G.; Toulhoat, H. Shape and Edge Sites Modifications of MoS_2 Catalytic Nanoparticles Induced by Working Conditions: A Theoretical Study. *J. Catal.*, **2002**, *207,* 76–87.
[33] Kasztelan, S.; Toulhoat, H.; Grimblot, J.; Bonnelle, J.P. A geometrical model of the active phase of hydrotreating catalysts. *Appl. Catal.*, **1984**, *13,* 127–159.
[34] Chien, F.Z.; Moss, S.C.; Liang, K.S.; Chianelli, R.R. Local and intermediate-range structure of amorphous MoS_3: Model calculation study. *Phys. Rev. B*, **1984**, *29,* 4606–4615.
[35] Cramer, S.P.; Liang, K.S.; Jacobson, A.J.; Chang, C.H.; Chianelli, R.R. EXAFS studies of amorphous molybdenum and tungsten trisulfides and triselenides. *Inorg. Chem.*, **1984**, *23,* 1215–1221.
[36] Chang, C.H.; Chan, S.S. Infrared and Raman studies of amorphous MoS_3 and poorly crystalline MoS_2. *J. Catal.*, **1981**, *72,* 139–148.
[37] Hibble, S.J.; Feaviour, M.R.; Almond, M.J. Chemical excision from amorphous MoS_3; a quantitative EXAFS study. *J. Chem. Soc., Dalton Trans.*, **2001,** 935–940.
[38] Hibble, S.J.; Wood, G.B. Modeling the structure of amorphous MoS_3: a neutron diffraction and reverse Monte Carlo study. *J. Am. Chem. Soc.*, **2004**, *126,* 959–965.
[39] Jiao, H.; Li, Y.-W.; Delmon, B.; Halet, J.-F. The Structure and Possible Catalytic Sites of Mo_3S_9 as a Model of Amorphous Molybdenum Trisulfide: A Computational Study. *J. Am. Chem. Soc.*, **2001**, *123,* 7334–7339.
[40] Weber, T.; Muijsers, J.C.; Niemantsverdriet, J.W. Structure of Amorphous MoS_3. *J. Phys. Chem.*, **1995**, *99,* 9194–9200.
[41] Liang, K.S.; Cramer, S.P.; Johnston, D.C.; Chang, C.H.; Jacobson, A.J.; deNeufville, J.P.; Chianelli, R.R. Amorphous MoS_3 and WS_3. *J. Non-Cryst. Solids*, **1980**, *42,* 345–356.
[42] Hibble, S.J.; Walton, R.I.; Pickup, D.M.; Hannon, A.C. Amorphous MoS_3: Clusters or chains? The structural evidence. *J. Non-Cryst. Solids*, **1998**, *232-234,* 434–439.
[43] Tributsch, H.; Bennett, J.C. Electrochemistry and photochemistry of MoS_2 layer crystals. I. *J. Electroanal. Chem.*, **1977**, *81,* 97–111.
[44] Nørskov, J.K.; Bligaard, T.; Logadottir, A.; Kitchin, J.R.; Chen, J.G.; Pandelov, S.; Stimming, U. Trends in the Exchange Current for Hydrogen Evolution. *J. Electrochem. Soc.*, **2005**, *152,* J23-J26.

[45] Hinnemann, B.; Moses, P.G.; Bonde, J.; Jørgensen, K.P.; Nielsen, J.H.; Horch, S.; Chorkendorff, I.; Nørskov, J.K. Biomimetic Hydrogen Evolution: MoS_2 Nanoparticles as Catalyst for Hydrogen Evolution. *J. Am. Chem. Soc.*, **2005**, *127,* 5308–5309.
[46] Jaramillo, T.F.; Jørgensen, K.P.; Bonde, J.; Nielsen, J.H.; Horch, S.; Chorkendorff, I. Identification of Active Edge Sites for Electrochemical H_2 Evolution from MoS_2 Nanocrystals. *Science*, **2007**, *317,* 100–102.
[47] Zhang, L.; Wu, L.; Li, J.; Lei, J. Electrodeposition of amorphous molybdenum sulfide thin film for electrochemical hydrogen evolution reaction. *BMC Chem.*, **2019**, *13,* 88–97.
[48] Deng, J.; Li, H.; Xiao, J.; Tu, Y.; Deng, D.; Yang, H.; Tian, H.; Li, J.; Ren, P.; Bao, X. Triggering the electrocatalytic hydrogen evolution activity of the inert two-dimensional MoS_2 surface via single-atom metal doping. *Energy Environ. Sci.*, **2015**, *8,* 1594–1601.
[49] Gao, G.; Sun, Q.; Du, A. Activating Catalytic Inert Basal Plane of Molybdenum Disulfide to Optimize Hydrogen Evolution Activity via Defect Doping and Strain Engineering. *J. Phys. Chem. C*, **2016**, *120,* 16761–16766.
[50] Merki, D.; Hu, X. Recent developments of molybdenum and tungsten sulfides as hydrogen evolution catalysts. *Energy Environ. Sci.*, **2011**, *4,* 3878–3888.
[51] Shang, C.; Fang, Y.Q.; Zhang, Q.; Wang, N.Z.; Wang, Y.F.; Liu, Z.; Lei, B.; Meng, F.B.; Ma, L.K.; Wu, T.; Wang, Z.F.; Zeng, C.G.; Huang, F.Q.; Sun, Z.; Chen, X.H. Superconductivity in the metastable 1T' and 1T''' phase of MoS_2 crystals. *Phys. Rev. B*, **2018**, *98,* 184513–184523.
[52] Morales-Guio, C.G.; Hu, X. Amorphous Molybdenum Sulfides as Hydrogen Evolution Catalysts. *Acc. Chem. Res.*, **2014**, *47,* 2671–2681.
[53] Ting, L.R.L.; Deng, Y.; Ma, L.; Zhang, Y.-J.; Peterson, A.A.; Yeo, B.S. Catalytic Activities of Sulfur Atoms in Amorphous Molybdenum Sulfide for the Electrochemical Hydrogen Evolution Reaction. *ACS Catal.*, **2016**, *6,* 861–867.
[54] Hinnemann, B.; Nørskov, J.K.; Topsøe, H. A Density Functional Study of the Chemical Differences between Type I and Type II MoS_2-Based Structures in Hydrotreating Catalysts. *J. Phys. Chem. B*, **2005**, *109,* 2245–2253.
[55] Tsai, C.; Li, H.; Park, S.; Park, J.; Han, H.S.; Nørskov, J.K.; Zheng, X.; Abild-Pedersen, F. Electrochemical generation of sulfur vacancies in the basal plane of MoS_2 for hydrogen evolution. *Nat. Commun.*, **2017**, *8,* 15113–15121.
[56] Deng, Y.; Ting, L.R.L.; Neo, P.H.L.; Zhang, Y.-J.; Peterson, A.A.; Yeo, B.S. Operando Raman Spectroscopy of Amorphous Molybdenum Sulfide (MoS_x) during the Electrochemical Hydrogen Evolution Reaction: Identification of Sulfur Atoms as Catalytically Active Sites for H^+ Reduction. *ACS Catal.*, **2016**, *6,* 7790–7798.
[57] Yin, Z.; Zhao, J.; Wang, B.; Xu, Y.; Li, Z.; Ma, X. Insight for the effect of bridging S_2^{2-} in molybdenum sulfide catalysts toward sulfur-resistant methanation. *Appl. Surf. Sci.*, **2019**, *471,* 670–677.
[58] Chang, U.; Lee, J.T.; Yun, J.-M.; Lee, B.; Lee, S.W.; Joh, H.-I.; Eom, K.; Fuller, T.F. In Situ Self-Formed Nanosheet MoS_3/Reduced Graphene Oxide Material Showing Superior Performance as a Lithium-Ion Battery Cathode. *ACS nano*, **2019**, *13,* 1490–1498.
[59] Dockery, D.W.; Pope, C.A.; Xu, X.; Spengler, J.D.; Ware, J.H.; Fay, M.E.; Ferris, B.G.; Speizer, F.E. An Association between Air Pollution and Mortality in Six U.S. Cities. *N. Engl. J. Med.*, **1993**, *329,* 1753–1759.
[60] Dumon, A.S.; Sahu, A.; Raybaud, P. Hydrogenolysis and β–elimination mechanisms for C-S bond scission of dibenzothiophene on CoMoS edge sites. *J. Catal.*, **2021,** In press.
[61] Daage, M.; Chianelli, R.R. Structure-Function Relations in Molybdenum Sulfide Catalysts: The "Rim-Edge" Model. *J. Catal.*, **1994**, *149,* 414–427.
[62] Singhal, G.H.; Espino, R.L.; Sobel, J.E.; Huff, G.A. Hydrodesulfurization of sulfur heterocyclic compounds: Kinetics of dibenzothiophene. *J. Catal.*, **1981**, *67,* 457–468.
[63] Bataille, F.; Lemberton, J.-L.; Michaud, P.; Pérot, G.; Vrinat, M.; Lemaire, M.; Schulz, E.; Breysse, M.; Kasztelan, S. Alkyldibenzothiophenes Hydrodesulfurization-Promoter Effect, Reactivity, and Reaction Mechanism. *J. Catal.*, **2000**, *191,* 409–422.

[64] Egorova, M.; Prins, R. Hydrodesulfurization of dibenzothiophene and 4,6-dimethyldibenzothiophene over sulfided NiMo/γ-Al_2O_3, CoMo/γ-Al_2O_3, and Mo/γ-Al_2O_3 catalysts. *J. Catal.*, **2004**, *225,* 417–427.
[65] Euzen, P.; Raybaud, P.; Krokidis, X.; Toulhoat, H.; Le Loarer, J.-L.; Jolivet, J.-P.; Froidefond, C. Alumina. In: *Handbook of Porous Solids*. Schth, F., Sing, K.S.W., Weitkamp, J., Eds.; Wiley-VCH Verlag GmbH: Weinheim, Germany, **2002**; pp. 1591–1677.
[66] Ramirez, J.; Fuentes, S.; Díaz, G.; Vrinat, M.; Breysse, M.; Lacroix, M. Hydrodesulphurization activity and characterization of sulphided molybdenum and cobalt—molybdenum catalysts comparison of alumina-, silica—alumina- and titania-supported catalysts. *Appl. Catal.*, **1989**, *52,* 211–223.
[67] Huirache-Acuña, R.; Nava, R.; Peza-Ledesma, C.L.; Lara-Romero, J.; Alonso-Núez, G.; Pawelec, B.; Rivera-Muñoz, E.M. SBA-15 Mesoporous Silica as Catalytic Support for Hydrodesulfurization Catalysts—Review. *Materials*, **2013**, *6,* 4139–4167.
[68] Krebs, E.; Silvi, B.; Raybaud, P. Mixed sites and promoter segregation: A DFT study of the manifestation of Le Chatelier's principle for the Co(Ni)MoS active phase in reaction conditions. *Catal. Today*, **2008**, *130,* 160–169.
[69] Breysse, M.; Afanasiev, P.; Geantet, C.; Vrinat, M. Overview of support effects in hydrotreating catalysts. *Catal. Today*, **2003**, *86,* 5–16.
[70] Breysse, M.; Geantet, C.; Afanasiev, P.; Blanchard, J.; Vrinat, M. Recent studies on the preparation, activation and design of active phases and supports of hydrotreating catalysts. *Catal. Today*, **2008**, *130,* 3–13.
[71] Breysse, M.; Portefaix, J.L.; Vrinat, M. Support effects on hydrotreating catalysts. *Catal. Today*, **1991**, *10,* 489–505.
[72] Luck, F. A Review of Support Effects on the Activity and Selectivity of Hydrotreating Catalysts. *Bull. Soc. Chim. Belges*, **1991**, *100,* 781–800.
[73] Vrinat, M.; Breysse, M.; Geantet, C.; Ramirez, J.; Massoth, F. Effect of MoS_2 morphology on the HDS activity of hydrotreating catalysts. *Catal. Lett.*, **1994**, *26,* 25–35.
[74] Shimada, H. Morphology and orientation of MoS_2 clusters on Al_2O_3 and TiO_2 supports and their effect on catalytic performance. *Catal. Today*, **2003**, *86,* 17–29.
[75] Ramirez, J.; Cedeño, L.; Busca, G. The Role of Titania Support in Mo-Based Hydrodesulfurization Catalysts. *J. Catal.*, **1999**, *184,* 59–67.
[76] Ramírez, J.; Macías, G.; Cedeño, L.; Gutiérrez-Alejandre, A.; Cuevas, R.; Castillo, P. The role of titania in supported Mo, CoMo, NiMo, and NiW hydrodesulfurization catalysts: Analysis of past and new evidences. *Catal. Today*, **2004**, *98,* 19–30.
[77] Arrouvel, C.; Breysse, M.; Toulhoat, H.; Raybaud, P. A density functional theory comparison of anatase (TiO_2)- and γ-Al_2O_3-supported MoS_2 catalysts. *J. Catal.*, **2005**, *232,* 161–178.
[78] Beer, V. de; van der Aalst, M.; Machiels, C.J.; Schuit, G. The $CoOMoO_3$ γ-Al_2O_3 catalyst: VII. Influence of the support. *J. Catal.*, **1976**, *43,* 78–89.
[79] Gandubert, A.D.; Krebs, E.; Legens, C.; Costa, D.; Guillaume, D.; Raybaud, P. Optimal promoter edge decoration of CoMoS catalysts: A combined theoretical and experimental study. *Catal. Today*, **2008**, *130,* 149–159.
[80] Digne, M.; Marchand, K.; Bourges, P. Monitoring Hydrotreating Catalysts Synthesis and Deactivation using Raman Spectrometry. *Oil & Gas Science and Technology - Rev. IFP*, **2007**, *62,* 91–99.
[81] Costa, V.; Marchand, K.; Digne, M.; Geantet, C. New insights into the role of glycol-based additives in the improvement of hydrotreatment catalyst performances. *Catal. Today*, **2008**, *130,* 69–74.
[82] Iwamoto, R.; Grimblot, J. Influence of Phosphorus on the Properties of Alumina-Based Hydrotreating Catalysts. *Adv. Catal.*, **1999**, *44,* 417–503.
[83] Souchay, P. *Polyanions et polycations;* Gauthier-Villars: Paris, **1963**.
[84] Pope, M.T.; Jeannin, Y.; Fournier, M. *Heteropoly and Isopoly Oxometalates;* Springer Berlin: Berlin, **1983**.

[85] Shopov, D. *Heterogeneous catalysis: Proceedings of the sixth International Symposium;* Pub. House of the Bulgarian Academy of Sciences: Sofia, **1987**.
[86] Griboval, A.; Blanchard, P.; Payen, E.; Fournier, M.; Dubois, J.L. Alumina supported HDS catalysts prepared by impregnation with new heteropolycompounds. Comparison with catalysts prepared by conventional Co–Mo–P coimpregnation. *Catal. Today*, **1998**, *45,* 277–283.
[87] Griboval, A.; Blanchard, P.; Gengembre, L.; Payen, E.; Fournier, M.; Dubois, J.L.; Bernard, J.R. Hydrotreatment Catalysts Prepared with Heteropolycompound: Characterisation of the Oxidic Precursors. *J. Catal.*, **1999**, *188,* 102–110.
[88] Griboval, A.; Blanchard, P.; Payen, E.; Fournier, M.; Dubois, J.; Bernard, J. Characterization and catalytic performances of hydrotreatment catalysts prepared with silicium heteropolymolybdates: Comparison with phosphorus doped catalysts. *Appl. Catal. A*, **2001**, *217,* 173–183.
[89] Wang, L. On the genesis of molybdena-alumina catalyst. *J. Catal.*, **1980**, *66,* 251–255.
[90] Kasztelan, S.; Grimblot, J.; Bonnelle, J.P.; Payen, E.; Toulhoat, H.; Jacquin, Y. Preparation of Co-Mo-γAl_2O_3 and Ni-Mo-γAl_2O_3 catalysts by pH regulation of molybdenum solution. characterization of supported species and hydrogenation activities. *Appl. Catal.*, **1983**, *7,* 91–112.
[91] Spanos, N.; Lycourghiotis, A. Molybdenum-oxo Species Deposited on Alumina by Adsorption: III. Advances in the Mechanism of Mo(VI) Deposition. *J. Catal.*, **1994**, *147,* 57–71.
[92] Vissenberg, M.J.; Joosten, L.J.M.; Heffels, M.M.E.H.; van Welsenes, A.J.; Beer, V.H.J. de; van Santen, R.A. Tungstate versus Molybdate Adsorption on Oxidic Surfaces: A Chemical Approach. *J. Phys. Chem. B*, **2000**, *104,* 8456–8461.
[93] Goncharova, O.I.; Boreskov, G.K.; Yurieva, T.M.; Yurchenko, E.N.; Boldyreva, N.N. Active state of molybdenum in molybdenum-alumina catalysts for propylene oxidation. *React. Kinet. Catal. L.*, **1981**, *16,* 349–353.
[94] Le Bihan, L.; Blanchard, P.; Fournier, M.; Grimblot, J.; Payen, E. Raman spectroscopic evidence for the existence of 6-molybdoaluminate entities on an Mo/Al_2O_3 oxidic precursor. *J. Chem. Soc., Faraday Trans.*, **1998**, *94,* 937–940.
[95] Blanchard, P.; Lamonier, C.; Griboval, A.; Payen, E. New insight in the preparation of alumina supported hydrotreatment oxidic precursors: A molecular approach. *Appl. Catal. A*, **2007**, *322,* 33–45.
[96] Sarrazin, P.; Kasztelan, S.; Zanier-Szydlowski, N.; Bonnelle, J.P.; Grimblot, J. Interaction of oxomolybdenum species with γ-alumina and γ-alumina modified by silicon. The silica/γ-alumina system. *J. Phys. Chem.*, **1993**, *97,* 5947–5953.
[97] van Dillen, A.; Terörde, R.J.; Lensveld, D.J.; Geus, J.W.; Jong, K.P. de. Synthesis of supported catalysts by impregnation and drying using aqueous chelated metal complexes. *J. Catal.*, **2003**, *216,* 257–264.
[98] Texier, S.; Berhault, G.; Pérot, G.; Diehl, F. Activation of alumina-supported hydrotreating catalysts by organosulfides or H_2S: Effect of the H_2S partial pressure used during the activation process. *Appl. Catal. A*, **2005**, *293,* 105–119.
[99] Lesage, C.; Devers, E.; Legens, C.; Fernandes, G.; Roudenko, O.; Briois, V. High pressure cell for edge jumping X-ray absorption spectroscopy: Applications to industrial liquid sulfidation of hydrotreatment catalysts. *Catal. Today*, **2019**, *336,* 63–73.
[100] Leliveld, R.G.; van Dillen, A.J.; Geus, J.W.; Koningsberger, D.C. The Sulfidation of γ-Alumina and Titania Supported (Cobalt)Molybdenum Oxide Catalysts Monitored by EXAFS. *J. Catal.*, **1997**, *171,* 115–129.
[101] Costa, D.; Arrouvel, C.; Breysse, M.; Toulhoat, H.; Raybaud, P. Edge wetting effects of γ-Al_2O_3 and anatase-TiO_2 supports by MoS_2 and CoMoS active phases: A DFT study. *J. Catal.*, **2007**, *246,* 325–343.

[102] Jong, A.M. de; Borg, H.J.; van IJzendoorn, L.J.; Soudant, V.G.F.M.; Beer, V.H.J. de; van Veen, J.A.R.; Niemantsverdriet, J.W. Sulfidation mechanism by molybdenum catalysts supported on silica/silicon(100) model support studied by surface spectroscopy. *J. Phys. Chem.*, **1993**, *97,* 6477–6483.
[103] Muijsers, J.C.; Weber, T.; Vanhardeveld, R.M.; Zandbergen, H.W.; Niemantsverdriet, J.W. Sulfidation Study of Molybdenum Oxide Using MoO_3/SiO_2/Si(100) Model Catalysts and Mo_3^{IV}-Sulfur Cluster Compounds. *J. Catal.*, **1995**, *157,* 698–705.
[104] Payen, E.; Kasztelan, S.; Houssenbay, S.; Szymanski, R.; Grimblot, J. Genesis and characterization by laser Raman spectroscopy and high-resolution electron microscopy of supported molybdenum disulfide crystallites. *J. Phys. Chem.*, **1989**, *93,* 6501–6506.
[105] Nicosia, D.; Prins, R. The effect of phosphate and glycol on the sulfidation mechanism of $CoMo/Al_2O_3$ hydrotreating catalysts: An in situ QEXAFS study. *J. Catal.*, **2005**, *231,* 259–268.
[106] Rochet, A.; Baubet, B.; Moizan, V.; Pichon, C.; Briois, V. Co-K and Mo-K edges Quick-XAS study of the sulphidation properties of Mo/Al_2O_3 and $CoMo/Al_2O_3$ catalysts. *C. R. Chim.*, **2016**, *19,* 1337–1351.
[107] Scheffer, B.; van Oers, E.M.; Arnoldy, P.; Beer, V. de; Moulijn, J.A. Sulfidability and HDS activity of Co-Mo/Al_2O_3 catalysts. *Appl. Catal.*, **1986**, *25,* 303–311.
[108] Boer, M. de; van Dillen, A.J.; Koningsberger, D.C.; Geus, J.W. The Structure of Highly Dispersed SiO_2-Supported Molybdenum Oxide Catalysts during Sulfidation. *J. Phys. Chem.*, **1994**, *98,* 7862–7870.
[109] Stevens, G.C.; Edmonds, T. Electron spectroscopy for chemical analysis spectra of molybdenum sulfides. *J. Catal.*, **1975**, *37,* 544–547.
[110] Diemann, E. Radiale Verteilungsfunktionen. V. Strukturuntersuchungen an nichtkristallinem Molybdäntrisulfid, Wolframtrisulfid und Molybdäntriselenid. *Zeitschrift für anorganische und allgemeine Chemie*, **1977**, *432,* 127–135.
[111] Gao, Y.; Han, W.; Long, X.; Nie, H.; Li, D. Preparation of hydrodesulfurization catalysts using MoS_3 nanoparticles as a precursor. *Appl. Catal. B*, **2018**, *224,* 330–340.
[112] Bhattacharya, R.N.; Lee, C.Y.; Pollak, F.H.; Schleich, D.M. Optical study of amorphous MoS_3: Determination of the fundamental energy gap. *J. Non-Cryst. Solids*, **1987**, *91,* 235–242.
[113] Johnston, D.C.; Jacobson, A.J.; Silbernagel, B.G.; Frysinger, S.P.; Rich, S.M.; Gebhard, L.A. Magnetic susceptibility and electron spin resonance as probes of different magnetic species in MoS_3. *J. Catal.*, **1984**, *89,* 244–249.
[114] Sourisseau, C.; Gorochov, O.; Schleich, D. Comparative IR and Raman studies of various amorphous MoS_3 and Li_xMoS_3 phases. *Mater. Sci. Eng.*, **1989**, *3,* 113–117.
[115] Wang, J.; Ng, S.H.; Chew, S.Y.; Wexler, D.; Wang, G.X.; Liu, H.K. Characterization of Nanosize Molybdenum Trisulfide for Lithium Batteries and MoS_3 Structure Confirmation via Electrochemistry. *Electrochem. Solid-State Lett.*, **2007**, *10,* A204-A207.
[116] Afanasiev, P.; Jobic, H.; Lorentz, C.; Leverd, P.; Mastubayashi, N.; Piccolo, L.; Vrinat, M. Low-Temperature Hydrogen Interaction with Amorphous Molybdenum Sulfides MoS_x. *J. Phys. Chem. C*, **2009**, *113,* 4139–4146.
[117] Kibsgaard, J.; Jaramillo, T.F.; Besenbacher, F. Building an appropriate active-site motif into a hydrogen-evolution catalyst with thiomolybdate $[Mo_3S_{13}]^{2-}$ clusters. *Nat. Chem.*, **2014**, *6,* 248–253.
[118] Huntley, D.R.; Parham, T.G.; Merrill, R.P.; Sienko, M.J. An EXAFS study of the thermal decomposition of molybdenum trisulfide. *Inorg. Chem.*, **1983**, *22,* 4144–4146.
[119] G.F. Khudorozhko, I.P. Asanov, L.N. Maealov, E.A. Kravtsova. The study of electronic structure of molybdenum and tungsten trisulfides and their lithium intercalates by x-ray electron and x-ray emission and absorption spectroscopy. *J. Electron Spectrosc.*, **1994**, *68,* 199–209.

[120] Hibble, S.J.; Rice, D.A.; Pickup, D.M.; Beer, M.P. Mo K-edge EXAFS and S K-edge absorption studies of the amorphous molybdenum sulfides $MoS_{4.7}$, MoS_3, and $MoS_3.nH_2O$ (n ~ 2). *Inorg. Chem.*, **1995**, *34,* 5109–5113.

[121] Hédoire, C.-E.; Cadot, E.; Villain, F.; Davidson, A.; Louis, C.; Breysse, M. Preparation and characterization of molybdenum sulfide supported on β-zeolites obtained from $[Mo_3S_4(H_2O)_9]^{4+}$ precursor. *Appl. Catal. A*, **2006**, *306,* 165–174.

[122] Lassalle-Kaiser, B.; Merki, D.; Vrubel, H.; Gul, S.; Yachandra, V.K.; Hu, X.; Yano, J. Evidence from in situ X-ray absorption spectroscopy for the involvement of terminal disulfide in the reduction of protons by an amorphous molybdenum sulfide electrocatalyst. *J. Am. Chem. Soc.*, **2015**, *137,* 314–321.

[123] Müller, A.; Diemann, E.; Krickemeyer, E.; Walberg, H.J.; Bögge, H.; Armatage, A. $[Mo_3(IV)S(S_2)_6]^{2-}$ from amorphous MoS_3 by the reaction with OH^- and R= 0.015 strucutre of $(NH_4)_2[Mo_3(IV)S(S_2)_6]$ *Eur. J. Solid State Inorg. Chem.*, **1993**, *30,* 565–572.

[124] Onoda, M. Crystal Structures of Columnar Composite Crystals Sr_xTiS_3 (x=1.1-1.2). *Nihon Kessho Gakkaishi*, **1995**, *37,* 309–314.

[125] M, S.D.; G, D.; P, C.E. Raman Scattering in Fullerenes. *J. Raman Spectrosc.*, **1996**, *27,* 351–371.

[126] Rijnsdorp, J.; Jellinek, F. The crystal structure of niobium trisulfide, NbS_3. *J. Solid State Chem.*, **1978**, *25,* 325–328.

[127] Khudorozhko, G.F.; Asanov, I.P.; Mazalov, L.N.; Kravtsova, É.A.; Parygina, G.K.; Fedorov, V.E.; Mironov, Y.V. X-ray photoelectron, emission, and absorption studies of the electronic structure of molybdenum and tungsten trisulfides and their intercalates. *J. Struct. Chem.*, **1994**, *35,* 823–833.

[128] Tran, P.D.; Tran, T.V.; Orio, M.; Torelli, S.; Truong, Q.D.; Nayuki, K.; Sasaki, Y.; Chiam, S.Y.; Yi, R.; Honma, I.; Barber, J.; Artero, V. Coordination polymer structure and revisited hydrogen evolution catalytic mechanism for amorphous molybdenum sulfide. *Nat. Mater.*, **2016**, *15,* 640–646.

[129] Li, Y.; Yu, Y.; Huang, Y.; Nielsen, R.A.; Goddard, W.A.; Li, Y.; Cao, L. Engineering the Composition and Crystallinity of Molybdenum Sulfide for High-Performance Electrocatalytic Hydrogen Evolution. *ACS Catal.*, **2015**, *5,* 448–455.

[130] Baloglou, A.; Ončák, M.; Grutza, M.-L.; van der Linde, C.; Kurz, P.; Beyer, M.K. Structural Properties of Gas Phase Molybdenum Sulfide Clusters $[Mo_3S_{13}]^{2-}$, $[HMo_3S_{13}]^-$, and $[H_3Mo_3S_{13}]^+$ as Model Systems of a Promising Hydrogen Evolution Catalyst. *J. Phys. Chem. C*, **2019**, *123,* 8177–8186.

[131] Pan, Y.; Guan, W. Prediction of new stable structure, promising electronic and thermodynamic properties of MoS_3: Ab initio calculations. *J. Power Sources*, **2016**, *325,* 246–251.

[132] Arrouvel, C.; Toulhoat, H.; Breysse, M.; Raybaud, P. Effects of P_{H2O}, P_{H2S}, P_{H2} on the surface properties of anatase-TiO_2 and γ-Al_2O_3: a DFT study. *J. Catal.*, **2004**, *226,* 260–272.

[133] Larmier, K.; Chizallet, C.; Raybaud, P. Tuning the Metal–Support Interaction by Structural Recognition of Cobalt-Based Catalyst Precursors. *Angew. Chem. Int. Ed. Engl.*, **2015**, *54,* 6824–6827.

[134] Lippens, B.C.; Boer, J.H. de. Study of phase transformations during calcination of aluminum hydroxides by selected area electron diffraction. *Acta Crystallographica*, **1964**, *17,* 1312–1321.

[135] Krokidis, X.; Raybaud, P.; Gobichon, A.-E.; Rebours, B.; Euzen, P.; Toulhoat, H. Theoretical Study of the Dehydration Process of Boehmite to γ-Alumina. *J. Phys. Chem. B*, **2001**, *105,* 5121–5130.

[136] Wolverton, C.; Hass, K.C. Phase stability and structure of spinel-based transition aluminas. *Phys. Rev. B*, **2000**, *63,* 24102.

[137] Prins, R. Location of the Spinel Vacancies in γ-Al_2O_3. *Angew. Chem. Int. Ed. Engl.*, **2019**, *58,* 15548–15552.

[138] Batista, A.T.; Wisser, D.; Pigeon, T.; Gajan, D.; Diehl, F.; Rivallan, M.; Catita, L.; Gay, A.-S.; Lesage, A.; Chizallet, C.; Raybaud, P. Beyond γ-Al_2O_3 crystallite surfaces: The hidden features of edges revealed by solid-state 1H NMR and DFT calculations. *J. Catal.*, **2019**, *378,* 140–143.
[139] Raybaud, P.; Digne, M.; Iftimie, R.; Wellens, W.; Euzen, P.; Toulhoat, H. Morphology and Surface Properties of Boehmite (γ-AlOOH): A Density Functional Theory Study. *J. Catal.*, **2001**, *201,* 236–246.
[140] Lippens, B.C. Structure and texture of aluminas, **April 26, 1961**.
[141] Santos, P.d.S.; Coelho, A.C.V.; Santos, H.d.S.; Kiyohara, P.K. Hydrothermal synthesis of well-crystallised boehmite crystals of various shapes. *Mat. Res.*, **2009**, *12,* 437–445.
[142] Tsyganenko, A.A.; Filimonov, V.N. Infrared spectra of surface hydroxyl groups and crystalline structure of oxides. *J. Mol. Struct.*, **1973**, *19,* 579–589.
[143] Knözinger, H.; Ratnasamy, P. Catalytic Aluminas: Surface Models and Characterization of Surface Sites. *Catal. Rev.*, **1978**, *17,* 31–70.
[144] Busca, G.; Lorenzelli, V.; Ramis, G.; Willey, R.J. Surface sites on spinel-type and corundum-type metal oxide powders. *Langmuir*, **1993**, *9,* 1492–1499.
[145] Ballinger, T.H.; Yates, J.T. IR spectroscopic detection of Lewis acid sites on alumina using adsorbed carbon monoxide. Correlation with aluminum-hydroxyl group removal. *Langmuir*, **1991**, *7,* 3041–3045.
[146] Ohler, N.; Bell, A.T. Study of the Elementary Processes Involved in the Selective Oxidation of Methane over MoO_x/SiO_2. *J. Phys. Chem. B*, **2006**, *110,* 2700–2709.
[147] J.L.G. Fierro. *Metal Oxides: Chemistry and applications;* CRC PRESS, **2006**.
[148] Stencel, J.M.; Makovsky, L.E.; Sarkus, T.A.; Vries, J. de; Thomas, R.; Moulijn, J.A. Raman spectroscopic investigation of the effect of H_2O on the molybdenum surface species in MoO_3-Al_2O_3 catalysts. *J. Catal.*, **1984**, *90,* 314–322.
[149] Hu, H.; Wachs, I.E.; Bare, S.R. Surface Structures of Supported Molybdenum Oxide Catalysts: Characterization by Raman and Mo L_3-Edge XANES. *J. Phys. Chem.*, **1995**, *99,* 10897–10910.
[150] Xiong, G.; Li, C.; Feng, Z.; Ying, P.; Xin, Q.; Liu, J. Surface Coordination Structure of Molybdate with Extremely Low Loading on γ-Alumina Characterized by UV Resonance Raman Spectroscopy. *J. Catal.*, **1999**, *186,* 234–237.
[151] Desikan, A.N.; Huang, L.; Oyama, S.T. Structure and dispersion of molybdenum oxide supported on alumina and titania. *J. Chem. Soc., Faraday Trans.*, **1992**, *88,* 3357–3365.
[152] Mestl, G.; Srinivasan, T.K.K. Raman Spectroscopy of Monolayer-Type Catalysts: Supported Molybdenum Oxides. *Catal. Rev.*, **1998**, *40,* 451–570.
[153] Handzlik, J.; Sautet, P. Structure of Dimeric Molybdenum(VI) Oxide Species on γ-Alumina: A Periodic Density Functional Theory Study. *J. Phys. Chem. C*, **2010**, *114,* 19406–19414.
[154] Hamraoui, K.; Cristol, S.; Payen, E.; Paul, J.-F. Computational Investigation of TiO_2-Supported Isolated Oxomolybdenum Species. *J. Phys. Chem. C*, **2007**, *111,* 3963–3972.
[155] Hamraoui, K.; Cristol, S.; Payen, E.; Paul, J.-F. Structure and reducibility of titania-supported monomeric and dimeric molybdenum oxide entities studied by DFT calculations. *J. Mol. Struct. THEOCHEM*, **2009**, *903,* 73–82.
[156] Tougerti, A.; Berrier, E.; Mamede, A.-S.; La Fontaine, C.; Briois, V.; Joly, Y.; Payen, E.; Paul, J.-F.; Cristol, S. Synergy between XANES Spectroscopy and DFT to Elucidate the Amorphous Structure of Heterogeneous Catalysts: TiO_2-Supported Molybdenum Oxide Catalysts. *Angew. Chem. Int. Ed.*, **2013**, *52,* 6440–6444.
[157] Hu, H.; Oliveira de Souza, D.; Berrier, E.; Paul, J.-F.; La Fontaine, C.; Briois, V.; Cristol, S.; Tougerti, A. Investigation of the Reducibility of Supported Oxomolybdate Species for Mapping of Active Centers of Partial Oxidation Reaction: In Situ Mo K-Edge XAS and DFT Study. *J. Phys. Chem. C*, **2019**, *123,* 18325–18335.
[158] Kiani, D.; Sourav, S.; Taifan, W.; Calatayud, M.; Tielens, F.; Wachs, I.E.; Baltrusaitis, J. Existence and Properties of Isolated Catalytic Sites on the Surface of β-Cristobalite-Supported, Doped Tungsten Oxide Catalysts (WO_x/β-SiO_2, Na-WO_x/β-SiO_2, Mn-WO_x/β-SiO_2)

for Oxidative Coupling of Methane (OCM): A Combined Periodic DFT and Experimental Study. *ACS Catal.*, **2020**, *10,* 4580–4592.
[159] Drake, T.L.; Stair, P.C. Multiwavelength Raman Spectroscopic Characterization of Alumina-Supported Molybdenum Oxide Prepared by Vapor Deposition. *Top. Catal.*, **2017**, *60,* 1618–1630.
[160] Yu, M.; Qu, W.; Xu, S.; Wang, L.; Liu, B.; Zhang, L.; Peng, J. Interfacial stability, electronic property, and surface reactivity of α-MoO_3/γ-Al_2O_3 composites: DFT and DFT + U calculations. *Comput. Mater. Sci.*, **2018**, *153,* 217–227.
[161] Marianski, M.; Seo, J.; Mucha, E.; Thomas, D.A.; Jung, S.; Schlögl, R.; Meijer, G.; Trunschke, A.; Helden, G. von. Structural Characterization of Molybdenum Oxide Nanoclusters Using Ion Mobility Spectrometry–Mass Spectrometry and Infrared Action Spectroscopy. *J. Phys. Chem. C*, **2019**, *123,* 7845–7853.
[162] Shahrokhi, M.; Raybaud, P.; Le Bahers, T. On the understanding of the optoelectronic properties of S-doped MoO_3 and O-doped MoS_2 bulk systems: a DFT perspective. *J. Mater. Chem. C*, **2020**, *8,* 9064–9074.
[163] Hong, S.; Tiwari, S.; Krishnamoorthy, A.; Nomura, K.; Sheng, C.; Kalia, R.K.; Nakano, A.; Shimojo, F.; Vashishta, P. Sulfurization of MoO_3 in the Chemical Vapor Deposition Synthesis of MoS_2 Enhanced by an H_2S/H_2 Mixture. *J. Phys. Chem. Lett.*, **2021**, *12,* 1997–2003.
[164] Shi, X.-R.; Wang, J.; Hermann, K. Theoretical Cluster Studies on the Catalytic Sulfidation of MoO_3. *J. Phys. Chem. C*, **2010**, *114,* 6791–6801.
[165] Misawa, M.; Tiwari, S.; Hong, S.; Krishnamoorthy, A.; Shimojo, F.; Kalia, R.K.; Nakano, A.; Vashishta, P. Reactivity of Sulfur Molecules on MoO_3 (010) Surface. *J. Phys. Chem. Lett.*, **2017**, *8,* 6206–6210.
[166] Lai, W.; Xu, Y.; Zhao, Y.; Zheng, J.; Yi, X.; Fang, W. Modeling the kinetics of sulfidation over NiMo/Al_2O_3 catalyst for thiophene hydrodesulfurization. *React. Kinet. Mech. Catal.*, **2015**, *115,* 635–649.
[167] Joshi, Y.V.; Ghosh, P.; Daage, M.; Delgass, W.N. Support effects in HDS catalysts: DFT analysis of thiolysis and hydrolysis energies of metal–support linkages. *J. Catal.*, **2008**, *257,* 71–80.
[168] Topsoe, N.Y.; Topsoe, H. FTIR Studies of Mo/Al_2O_3-Based Catalysts: I. Morphology and Structure of Calcined and Sulfided Catalysts. *J. Catal.*, **1993**, *139,* 631–640.
[169] Thijssen, J.M. *Computational physics;* Cambridge University Press: Cambridge, **2013**.
[170] Koch, W.; Holthausen, M.C. *A Chemist's Guide to Density Functional Theory;* Wiley-VCH: Weinheim, **2015**.
[171] Frank, J. *Introduction to Computational Chemistry;* John Wiley & Sons, Inc, **2006**.
[172] Hohenberg, P.; Kohn, W. Inhomogeneous Electron Gas. *Phys. Rev.*, **1964**, *136,* B864-B871.
[173] Martin, R.M. *Electronic Structure: Basic Theory and Practical Methods;* Cambridge University Press: Cambridge, **2004**.
[174] Kohn, W.; Sham, L.J. Self-Consistent Equations Including Exchange and Correlation Effects. *Phys. Rev.*, **1965**, *140,* A1133-A1138.
[175] Hafner, J. Ab-initio simulations of materials using VASP: Density-functional theory and beyond. *J. Comput. Chem.*, **2008**, *29,* 2044–2078.
[176] Perdew, J.P.; Burke, K.; Ernzerhof, M. Generalized Gradient Approximation Made Simple. *Phys. Rev. Lett.*, **1996**, *77,* 3865–3868.
[177] Steinmann, S.N.; Corminboeuf, C. A generalized-gradient approximation exchange hole model for dispersion coefficients. *J. Chem. Phys.*, **2011**, *134,* 44117–44122.
[178] Steinmann, S.N.; Corminboeuf, C. Comprehensive Benchmarking of a Density-Dependent Dispersion Correction. *J. Chem. Theory Comput.*, **2011**, *7,* 3567–3577.
[179] Grimme, S. Semiempirical GGA-type density functional constructed with a long-range dispersion correction. *J. Comput. Chem.*, **2006**, *27,* 1787–1799.

[180] Grimme, S.; Antony, J.; Ehrlich, S.; Krieg, H. A consistent and accurate ab initio parametrization of density functional dispersion correction (DFT-D) for the 94 elements H-Pu. *J. Chem. Phys.*, **2010**, *132,* 154104-15423.
[181] Tkatchenko, A.; Scheffler, M. Accurate Molecular Van Der Waals Interactions from Ground-State Electron Density and Free-Atom Reference Data. *Phys. Rev. Lett.*, **2009**, *102,* 73005–73009.
[182] Becke, A.D.; Johnson, E.R. Exchange-hole dipole moment and the dispersion interaction: High-order dispersion coefficients. *J. Chem. Phys.*, **2006**, *124,* 14104.
[183] Vydrov, O.A.; van Voorhis, T. Nonlocal van der Waals density functional: The simpler the better. *J. Chem. Phys.*, **2010**, *133,* 244103–244112.
[184] Payne, M.C.; Teter, M.P.; Allan, D.C.; Arias, T.A.; Joannopoulos, J.D. Iterative minimization techniques for ab initio total-energy calculations: Molecular dynamics and conjugate gradients. *Rev. Mod. Phys.*, **1992**, *64,* 1045–1097.
[185] Sholl, D.S.; Steckel, J.A. *Density Functional Theory;* John Wiley & Sons, Inc: Hoboken, NJ, USA, **2009**.
[186] François, X.C. *DFT with plane waves, pseudopotentials:* Paris, **April 2010**.
[187] Barth, U. von; Gelatt, C.D. Validity of the frozen-core approximation and pseudopotential theory for cohesive energy calculations. *Phys. Rev. B*, **1980**, *21,* 2222–2228.
[188] Blöchl, P.E. Projector augmented-wave method. *Phys. Rev. B*, **1994**, *50,* 17953–17979.
[189] Kühne, T.D. Second generation Car-Parrinello molecular dynamics. *WIREs Comput. Mol. Sci.*, **2014**, *4,* 391–406.
[190] Paquet, E.; Viktor, H.L.; Atalay, Y. Computational Methods for Ab Initio Molecular Dynamics. *Adv. chem.*, **2018**, *2018,* 9839641–9839655.
[191] Pick, R.M.; Cohen, M.H.; Martin, R.M. Microscopic Theory of Force Constants in the Adiabatic Approximation. *Phys. Rev. B*, **1970**, *1,* 910–920.
[192] Gajdoš, M.; Hummer, K.; Kresse, G.; Furthmüller, J.; Bechstedt, F. Linear optical properties in the projector-augmented wave methodology. *Phys. Rev. B*, **2006**, *73,* 45112.
[193] Karhánek, D.; Bučko, T.; Hafner, J. A density-functional study of the adsorption of methane-thiol on the (111) surfaces of the Ni-group metals: II. Vibrational spectroscopy. *J. Phys. Condens. Matter.*, **2010**, *22,* 265006–265015.
[194] Brüesch, P. *Phonons: Theory and Experiments II: Experiments and Interpretation of Experimental Results;* Springer: Berlin, Heidelberg, **1986**.
[195] Baroni, S.; Gironcoli, S. de; Dal Corso, A.; Giannozzi, P. Phonons and related crystal properties from density-functional perturbation theory. *Rev. Mod. Phys.*, **2001**, *73,* 515–562.
[196] Esfarjani, K.; Hashi, Y.; Onoe, J.; Takeuchi, K.; Kawazoe, Y. Vibrational modes and IR analysis of neutral photopolymerized C_{60} dimers. *Phys. Rev. B*, **1998**, *57,* 223–229.
[197] Koopmans, T. Über die Zuordnung von Wellenfunktionen und Eigenwerten zu den Einzelnen Elektronen Eines Atoms. *Physica*, **1934**, *1,* 104–113.
[198] Johansson, B.; Mårtensson, N. Core-level binding-energy shifts for the metallic elements. *Phys. Rev. B*, **1980**, *21,* 4427–4457.
[199] Köhler, L.; Kresse, G. Density functional study of CO on Rh(111). *Phys. Rev. B*, **2004**, *70,* 165405–165414.
[200] Janak, J.F. Proof that $\partial E/\partial n_i = \varepsilon$ in density-functional theory. *Phys. Rev. B*, **1978**, *18,* 7165–7168.
[201] Lizzit, S.; Baraldi, A.; Groso, A.; Reuter, K.; Ganduglia-Pirovano, M.V.; Stampfl, C.; Scheffler, M.; Stichler, M.; Keller, C.; Wurth, W.; Menzel, D. Surface core-level shifts of clean and oxygen-covered Ru(0001). *Phys. Rev. B*, **2001**, *63,* 205419–205433.
[202] Pueyo Bellafont, N.; Viñes, F.; Hieringer, W.; Illas, F. Predicting core level binding energies shifts: Suitability of the projector augmented wave approach as implemented in VASP. *J. Comput. Chem.*, **2017**, *38,* 518–522.
[203] Henkelman, G.; Jóhannesson, G.; Jónsson, H. Methods for Finding Saddle Points and Minimum Energy Paths, 269–302.

[204] Arrhenius, S. Über die Dissociationswärme und den Einfluss der Temperatur auf den Dissociationsgrad der Elektrolyte. *Zeitschrift für Physikalische Chemie*, **1889**, *4U,* 96–116.
[205] Eyring, H. The Activated Complex in Chemical Reactions. *J. Chem. Phys.*, **1935**, *3,* 107–115.
[206] Evans, M.G.; Polanyi, M. Some applications of the transition state method to the calculation of reaction velocities, especially in solution. *Transactions of the Faraday Society*, **1935**, *31,* 875–894.
[207] Henkelman, G.; Jónsson, H. Improved tangent estimate in the nudged elastic band method for finding minimum energy paths and saddle points. *J. Chem. Phys.*, **2000**, *113,* 9978–9985.
[208] Sheppard, D.; Terrell, R.; Henkelman, G. Optimization methods for finding minimum energy paths. *J. Chem. Phys.*, **2008**, *128,* 134106–134116.
[209] Henkelman, G.; Uberuaga, B.P.; Jónsson, H. A climbing image nudged elastic band method for finding saddle points and minimum energy paths. *J. Chem. Phys.*, **2000**, *113,* 9901–9904.
[210] Fukui, K. Formulation of the reaction coordinate. *J. Phys. Chem.*, **1970**, *74,* 4161–4163.
[211] Fukui, K. The path of chemical reactions - the IRC approach. *Acc. Chem. Res.*, **1981**, *14,* 363–368.
[212] Olsen, R.A.; Kroes, G.J.; Henkelman, G.; Arnaldsson, A.; Jónsson, H. Comparison of methods for finding saddle points without knowledge of the final states. *J. Chem. Phys.*, **2004**, *121,* 9776–9792.
[213] Heyden, A.; Bell, A.T.; Keil, F.J. Efficient methods for finding transition states in chemical reactions: Comparison of improved dimer method and partitioned rational function optimization method. *J. Chem. Phys.*, **2005**, *123,* 224101–224115.
[214] Deng, L.; Ziegler, T. The determination of intrinsic reaction coordinates by density functional theory. *Int. J. Quantum Chem.*, **1994**, *52,* 731–765.
[215] Deng, L.; Ziegler, T.; Fan, L. A combined density functional and intrinsic reaction coordinate study on the ground state energy surface of H_2CO. *J. Chem. Phys.*, **1993**, *99,* 3823–3835.
[216] Cattaneo, R.; Weber, T.; Shido, T.; Prins, R. A Quick EXAFS Study of the Sulfidation of NiMo/SiO_2 Hydrotreating Catalysts Prepared with Chelating Ligands. *J. Catal.*, **2000**, *191,* 225–236.
[217] Rochet, A.; Baubet, B.; Moizan, V.; Devers, E.; Hugon, A.; Pichon, C.; Payen, E.; Briois, V. Intermediate Species Revealed during Sulfidation of Bimetallic Hydrotreating Catalyst: A Multivariate Analysis of Combined Time-Resolved Spectroscopies. *J. Phys. Chem. C*, **2017**, *121,* 18544–18556.
[218] Arnoldy, P.; van den Heijkant, J.; Bok, G.D. de; Moulijn, J.A. Temperature-programmed sulfiding of $MoO_3Al_2O_3$ catalysts. *J. Catal.*, **1985**, *92,* 35–55.
[219] Cattaneo, R.; Rota, F.; Prins, R. An XAFS Study of the Different Influence of Chelating Ligands on the HDN and HDS of γ-Al_2O_3-Supported NiMo Catalysts. *J. Catal.*, **2001**, *199,* 318–327.
[220] Sahu, A.; Steinmann, S.N.; Raybaud, P. Size-Dependent Structural, Energetic, and Spectroscopic Properties of MoS_3 Polymorphs. *Crystal Growth & Design*, **2020**, *20,* 7750–7760.
[221] Baubet, B.; Girleanu, M.; Gay, A.-S.; Taleb, A.-L.; Moreaud, M.; Wahl, F.; Delattre, V.; Devers, E.; Hugon, A.; Ersen, O.; Afanasiev, P.; Raybaud, P. Quantitative Two-Dimensional (2D) Morphology–Selectivity Relationship of CoMoS Nanolayers: A Combined High-Resolution High-Angle Annular Dark Field Scanning Transmission Electron Microscopy (HR HAADF-STEM) and Density Functional Theory (DFT) Study. *ACS Catal.*, **2016**, *6,* 1081–1092.
[222] Rochet, A.; Baubet, B.; Moizan, V.; Devers, E.; Hugon, A.; Pichon, C.; Payen, E.; Briois, V. Influence of the Preparation Conditions of Oxidic NiMo/Al_2O_3 Catalysts on the Sulfidation

Ability: A Quick-XAS and Raman Spectroscopic Study. *J. Phys. Chem. C*, **2015**, *119,* 23928–23942.
[223] Hardcastle, F.D.; Wachs, I.E. Determination of molybdenum–oxygen bond distances and bond orders by Raman spectroscopy. *J. Raman Spectrosc.*, **1990**, *21,* 683–691.
[224] Cornac, M.; Janin, A.; Lavalley, J.C. Structure of Mo catalysts supported on silica: IR and gravimetric results. *Polyhedron*, **1986**, *5,* 183–186.
[225] Y. Jacquin, J.P. Franck, G. Goubin, A. Elchenberger. 06/19/1985 Patent EP 0064429 B2.
[226] van Haandel, L.; Bremmer, G.M.; Hensen, E.; Weber, T. Influence of sulfiding agent and pressure on structure and performance of $CoMo/Al_2O_3$ hydrodesulfurization catalysts. *J. Catal.*, **2016**, *342,* 27–39.
[227] Eijsbouts, S.; van den Oetelaar, L.C.A.; Louwen, J.N.; van Puijenbroek, R.R.; van Leerdam, G.C. Changes of MoS_2 Morphology and the Degree of Co Segregation during the Sulfidation and Deactivation of Commercial Co−Mo/Al_2O_3 Hydroprocessing Catalysts. *Industrial & Engineering Chemistry Research*, **2007**, *46,* 3945–3954.
[228] Frizi, N.; Blanchard, P.; Payen, E.; Baranek, P.; Lancelot, C.; Rebeilleau, M.; Dupuy, C.; Dath, J.P. Genesis of new gas oil HDS catalysts: Study of their liquid phase sulfidation. *Catal. Today*, **2008**, *130,* 32–40.
[229] Paul, J.-F.; Cristol, S.; Payen, E. Computational studies of (mixed) sulfide hydrotreating catalysts. *Catal. Today*, **2008**, *130,* 139–148.
[230] Arancon, R.; Saab, M.; Morvan, A.; Bonduelle-Skrzypczak, A.; Taleb, A.-L.; Gay, A.-S.; Legens, C.; Ersen, O.; Searles, K.; Mougel, V.; Fedorov, A.; Copéret, C.; Raybaud, P. Combined Experimental and Theoretical Molecular Approach of the Catalytically Active Hydrotreating MoS_2 Phases Promoted by 3d Transition Metals. *J. Phys. Chem. C*, **2019**, *123,* 24659–24669.
[231] Yamamoto, K.; Chan, K.W.; Mougel, V.; Nagae, H.; Tsurugi, H.; Safonova, O.V.; Mashima, K.; Copéret, C. Silica-supported isolated molybdenum di-oxo species: formation and activation with organosilicon agent for olefin metathesis. *Chem. Comm.*, **2018**, *54,* 3989–3992.
[232] Kresse, G.; Hafner, J. Ab initio molecular dynamics for liquid metals. *Phys. Rev. B*, **1993**, *47,* 558–561.
[233] Kresse, G.; Furthmüller, J. Efficient iterative schemes for ab initio total-energy calculations using a plane-wave basis set. *Phys. Rev. B*, **1996**, *54,* 11169–11186.
[234] Kresse, G.; Furthmüller, J. Efficiency of ab-initio total energy calculations for metals and semiconductors using a plane-wave basis set. *Comput. Mater. Sci.*, **1996**, *6,* 15–50.
[235] Kresse, G.; Joubert, D. From ultrasoft pseudopotentials to the projector augmented-wave method. *Phys. Rev. B*, **1999**, *59,* 1758–1775.
[236] Paul Fleurat-Lessard. Opt'n Path. http://pfleurat.free.fr/ReactionPath.php.
[237] Angnes, R.A. mechaSVG. https://github.com/ricalmang/mechaSVG.
[238] Genuit, D.; Bezverkhyy, I.; Afanasiev, P. Solution preparation of the amorphous molybdenum oxysulfide $MoOS_2$ and its use for catalysis. *J. Solid State Chem.*, **2005**, *178,* 2759–2765.
[239] Kozuch, S.; Shaik, S. How to Conceptualize Catalytic Cycles? The Energetic Span Model. *Acc. Chem. Res.*, **2011**, *44,* 101–110.
[240] Merki, D.; Fierro, S.; Vrubel, H.; Hu, X. Amorphous molybdenum sulfide films as catalysts for electrochemical hydrogen production in water. *Chem. Sci.*, **2011**, *2,* 1262–1267.
[241] Tang, M.L.; Grauer, D.C.; Lassalle-Kaiser, B.; Yachandra, V.K.; Amirav, L.; Long, J.R.; Yano, J.; A, P.A. Structural and Electronic Study of an Amorphous MoS_3 Hydrogen-Generation Catalyst on a Quantum-Controlled Photosensitizer. *Angew. Chem. Int. Ed. Engl.*, **2011**, *50,* 10203–10207.
[242] Matsuyama, T.; Hayashi, A.; Ozaki, T.; Mori, S.; Tatsumisago, M. Electrochemical properties of all-solid-state lithium batteries with amorphous MoS_3 electrodes prepared by mechanical milling. *J. Mater. Chem. A*, **2015**, *3,* 14142–14147.

[243] Fu, W.; Yang, S.; Yang, H.; Guo, B.; Huang, Z. 2D amorphous MoS_3 nanosheets with porous network structures for scavenging toxic metal ions from synthetic acid mine drainage. *J. Mater. Chem. A*, **2019**, *7,* 18799–18806.
[244] Slater, J.C. Statistical Exchange-Correlation in the Self-Consistent Field. *Adv. Quantum Chem.*, *6,* 1–92.
[245] Ansari, R.; Malakpour, S.; Faghihnasiri, M.; Sahmani, S. An ab initio investigation into the elastic, structural and electronic properties of MoS_2 nanotubes. *Superlattice Microst.*, **2015**, *82,* 188–200.
[246] Chou, S.S.; Sai, N.; Lu, P.; Coker, E.N.; Liu, S.; Artyushkova, K.; Luk, T.S.; Kaehr, B.; Brinker, C.J. Understanding catalysis in a multiphasic two-dimensional transition metal dichalcogenide. *Nat. Commun.*, **2015**, *6,* 8311–8319.
[247] C. Sourrisseau; R.Cavagnat; M. Fouassier, and P. Maraval. Electronic, vibrational and resonance Raman spectra of the layered semiconducting compound NbS_3. *J. Raman Spectrosc.*, **1990**, *21,* 337–349.
[248] Lauritsen, J.V.; Kibsgaard, J.; Helveg, S.; Topsøe, H.; Clausen, B.S.; Lægsgaard, E.; Besenbacher, F. Size-dependent structure of MoS_2 nanocrystals. *Nature Nanotech.*, **2007**, *2,* 53–58.
[249] Kan, M.; Wang, J.Y.; Li, X.W.; Zhang, S.H.; Li, Y.W.; Kawazoe, Y.; Sun, Q.; Jena, P. Structures and Phase Transition of a MoS_2 Monolayer. *J. Phys. Chem. C*, **2014**, *118,* 1515–1522.
[250] Huang, Q.; Li, X.; Sun, M.; Zhang, L.; Song, C.; Zhu, L.; Chen, P.; Xu, Z.; Wang, W.; Bai, X. The Mechanistic Insights into the 2H-1T Phase Transition of MoS_2 upon Alkali Metal Intercalation: From the Study of Dynamic Sodiation Processes of MoS_2 Nanosheets. *Adv. Mater. Interfaces*, **2017**, *4,* 1700171–1700177.
[251] Zhu, J.; Wang, Z.; Yu, H.; Li, N.; Zhang, J.; Meng, J.; Liao, M.; Zhao, J.; Lu, X.; Du, L.; Yang, R.; Shi, D.; Jiang, Y.; Zhang, G. Argon Plasma Induced Phase Transition in Monolayer MoS_2. *J. Am. Chem. Soc.*, **2017**, *139,* 10216–10219.
[252] Huang, H.H.; Fan, X.; Singh, D.J.; Zheng, W.T. First principles study on 2H-1T' transition in MoS_2 with copper. *Phys. Chem. Chem. Phys.*, **2018**, *20,* 26986–26994.
[253] Oumahi, C.; Barros-Bouchet, M.I. de; Le Mogne, T.; Charrin, C.; Loridant, S.; Geantet, C.; Afanasiev, P.; Thiebaut, B. MoS_2 formation induced by amorphous MoS_3 species under lubricated friction. *RSC Adv.*, **2018**, *8,* 25867–25872.
[254] Wang, Z. 2H → 1T′ phase transformation in Janus monolayer MoSSe and MoSTe: An efficient hole injection contact for 2H-MoS_2. *J. Mater. Chem. C*, **2018**, *6,* 13000–13005.
[255] Jin, Q.; Liu, N.; Chen, B.; Mei, D. Mechanisms of Semiconducting 2H to Metallic 1T Phase Transition in Two-dimensional MoS_2 Nanosheets. *J. Phys. Chem. C*, **2018**, *122,* 28215–28224.
[256] Xia, Z.; Tao, Y.; Pan, Z.; Shen, X. Enhanced photocatalytic performance and stability of 1T MoS_2 transformed from 2H MoS_2 via Li intercalation. *Results Phys.*, **2019**, *12,* 2218–2224.
[257] McQuarrie, D.A. *Statistical mechanics;* Harper & Row: New York, London, **1976**.

Appendix A - Thermochemistry

To check the effect of thermal and zero-point energy corrections, we also incorporate the vibrational entropy contribution and thermal corrections. We assume the rotational and translational degree of freedom will not affect the energetics significantly, so we only take into account the vibrational contribution for the clusters and periodic systems. Furthermore, the equations described here assumes the system is noninteracting. This approximation will introduce some errors based on how far the studied system is from the ideal one. Besides that, the system is assumed to have remained in its ground state. As we know from classical thermochemistry, the free energy can be represented in terms of internal energy of the system and entropy contribution:

$$\boldsymbol{\Delta G = \Delta U - T\Delta S} \qquad \textbf{A- 1}$$

Where ΔU includes the sum of electronic energy and zero-point energy correction (ZPE), we calculate the ZPE from the sum of all the vibrational modes within the harmonic approximation at 0K.

$$\boldsymbol{\Delta G = \Delta E_{int} + ZPVE - T\Delta S_{vib}} \qquad \textbf{A- 2}$$

As we are not considering the electronic, rotational, and translational degree of freedom; we only consider the vibrational entropy term and can be computed from the following expression:

$$\boldsymbol{S_{vib} = R\,\Sigma_n \left(\frac{x_n}{e^{x_n} - 1} - \ln(1 - e^{x_n})\right)} \qquad \textbf{A- 3}$$

Here, $x_n = hc\nu_n/kT$, for the nth vibrational mode.[257]

Partition function (Q) is a function of state variables such as temperature and volume, which describes the statistical behavior of the system at thermodynamic equilibrium.

The internal energy of the system can be written in terms of partition function as:

$$U - U(0) = Nk_B T^2 \left(\frac{\partial \ln Q}{\partial T}\right)_v \qquad \text{A- 4}$$

And the entropy of the system can be written as:

$$S = \frac{U - U(0)}{T} + k \ln Q \qquad \text{A- 5}$$

The enthalpy and Gibbs energy of the system is defined as $H = U + pV$ and $G = H - TS$, respectively.

We can write G in term of Helmholtz energy as $G = U + pV - TS$.

The entropy of the system could be determined using the partition function:

$$S \quad = Nk_B + Nk_B \ln\left(\frac{q(V,T)}{N}\right) + Nk_B T \left(\frac{\partial \ln q}{\partial T}\right)_V \qquad \text{A- 6}$$

$$S \quad = Nk_B \left(\ln\left(\frac{q(V,T)}{N}\right) + T\left(\frac{\partial \ln q}{\partial T}\right)_V\right) \qquad \text{A- 7}$$

Suppose we assume that all the modes of the motions are independent of each other, such as rotational, vibration, translational and electronic. Then, the total partition function could be written as the product of an individual partition function.

$$q = \Sigma_i e^{-\beta\epsilon_i} = \Sigma_{i \in all\ states} e^{-\beta\epsilon_i^T - \beta\epsilon_i^R - \beta\epsilon_i^V - \beta\epsilon_i^E} \qquad \text{A- 8}$$

Herein, we assume the rotational and translational would be negligible as compare to vibrational contribution.

Therefore, within the framework of harmonic approximation, we can write the partition function as:

$$q \approx q_v = \Pi_n \frac{e^{-\frac{h\nu_n}{k_B T}}}{1 - e^{\frac{h\nu_n}{k_B T}}} \qquad \text{A- 9}$$

Here, n is the number of vibrational modes, h Planck's constant, ν frequency of vibrational mode. Now the vibrational entropy of the system could be written as:

$$S_{vib} = N_A k_B \left(ln\, q_v + T \left(\frac{\partial q}{\partial T} \right)_v \right) \qquad \textbf{A- 10}$$

$$S_{vib} = N_A k_B\, \Sigma_n \left(\frac{h\nu_n / k_B T}{e^{hc\nu_n / k_B T} - 1} - ln(1 - e^{-h\nu_n / k_B T}) \right) \qquad \textbf{A- 11}$$

Contribution to internal energy obtained from molecular vibration:

$$U_{vib} = N_A k_B\, \Sigma_n h\nu_n / k_B T \left(\frac{1}{2} + \frac{1}{e^{h\nu_n / k_B T} - 1} \right) \qquad \textbf{A- 12}$$

Zero-point energy has been calculated as the sum over energies of all the vibrational modes.

Appendix B - Complementary analysis on Mo-oxides

B1. Gas-Phase analysis

B1.1 Geometry analysis

We have first performed the structural and thermodynamic analysis of monomer (Mo_1O_3), dimer (Mo_2O_6), and trimer (Mo_3O_9) in the gas phase. We analyzed their ground state structures and the relative stability of these oligomers concerning monomers.

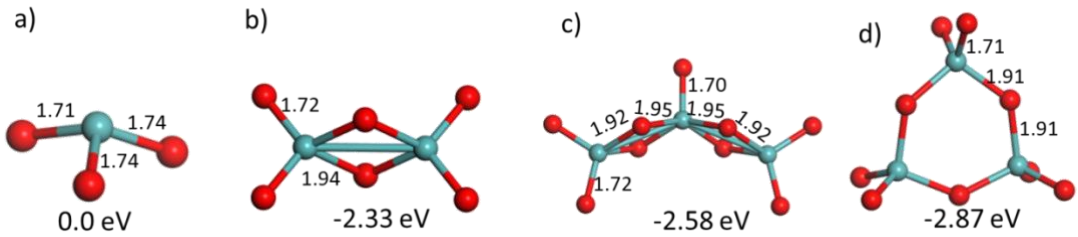

Figure B-1: gas-phase structures of a) monomer (Mo_1O_3), b) dimer (Mo_2O_6), and c)-d) trimer (Mo_3O_9) chain and cyclic conformers.

B1.2 Sulfidation in the gas phase

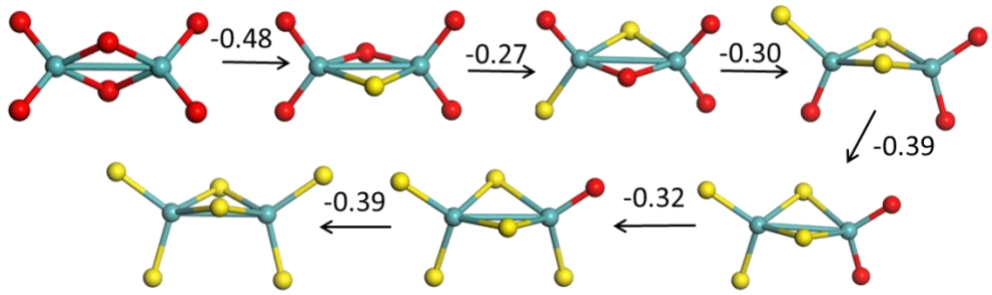

Figure B-2: Dimer (Mo_2O_6) sulfidation to Mo_2S_6 using H_2S/H_2O exchange.

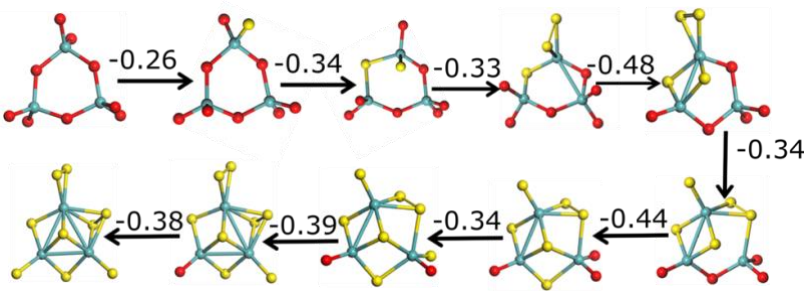

Figure B-3: Cyclic Mo_3O_9 to TR-Mo_3S_9 transformation by H_2S/H_2O exchange in the gas phase.

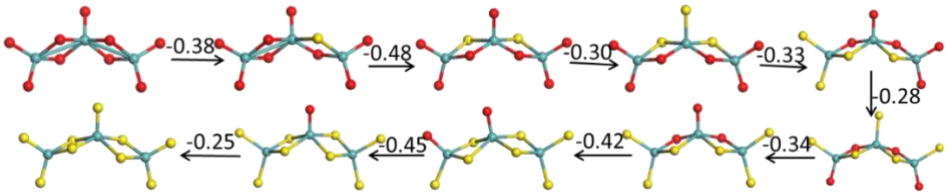

Figure B-4: Chain Mo_3O_9 to chain-Mo_3S_9 transformation by H_2S/H_2O exchange in the gas phase.

B1.3 Thermodynamics of gas-phase sulfidation

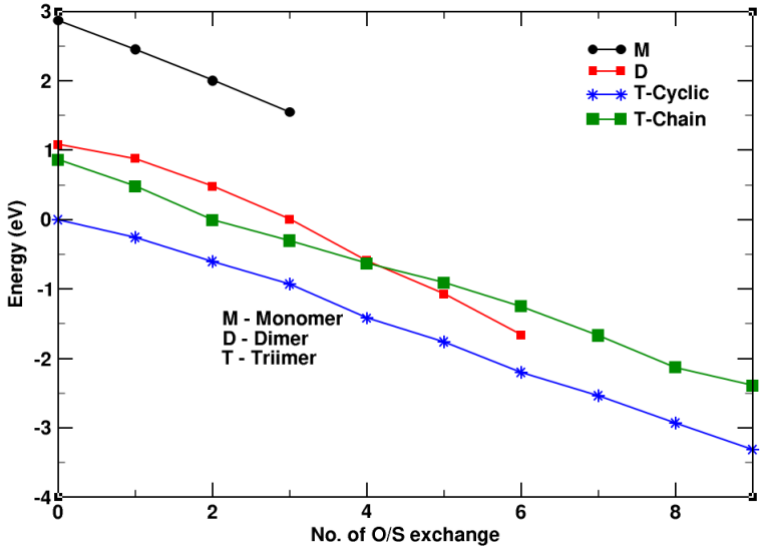

Figure B-5: Thermodynamic energy diagram of sulfidation of monomer, dimer, and trimer (chain and cyclic) as a function of O/S exchange.

B2. Alumina supported Mo_3O_9 and its sulfidation

B2.1 Vacancy creation on supported Mo_3O_9

Creating the O-vacancy from Chain-Mo_3O_9 is significantly endothermic. The ΔE of the following ($Mo_3O_9 + H_2 \rightarrow Mo_3O_8 + H_2O$) reaction may vary from 0.2 eV to 1.76 eV depending on the type of oxygen is being removed. Creating the vacancy site by removing the terminal oxygen is exceptionally high (at least 1.14 eV). However, removing the bridging and some of the interfacial oxygens are comparatively easy. The empty octahedral site is highly unfavorable but creating a tetrahedral site at the edge is less endothermic than octahedral

vacancy. Further removal of oxygen is even more expensive than the first one and could vary from 0.51- 1.89 eV based on the removing oxygen type.

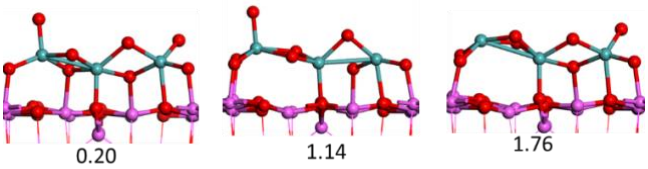

Figure B-6: Mo_3O_8 structures after creating vacancy using H_2 and respective reaction energy.

B2.2 Cyclic-Mo_3O_9 sulfidation

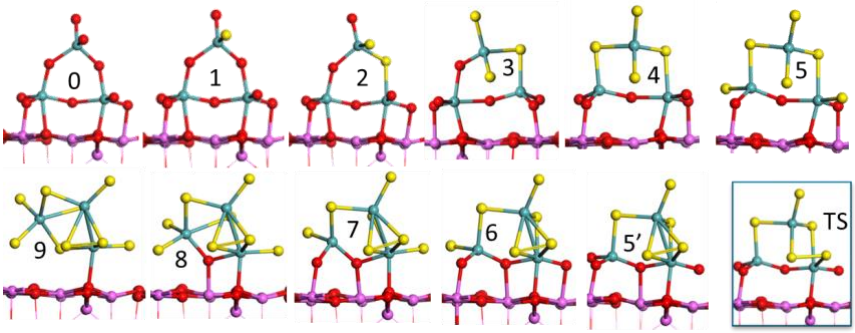

Figure B-7: Mo-Oxides to Mo-sulfides transformation by O/S exchange for cyclic-trimer ($Mo_3O_9 \rightarrow Mo_3S_9$).

Sulfidation of cyclic-Mo_3O_9 occurs similarly to chain-Mo_3O_9. The terminal and bridging oxygens are primarily the first ones to be replaced, followed by interfacial oxygens. The formation of dimers appeared after five O/S exchanges by costing the 0.5 eV of activation energy. Though the final Mo_3S_9 after all the O/S exchange is not the most stable one. The most stable supported TR-Mo_3S_9 is significantly different and needs various S diffusion to reach the most stable form.

B2.3 Chain1-Mo_3O_9 sulfidation through path-1

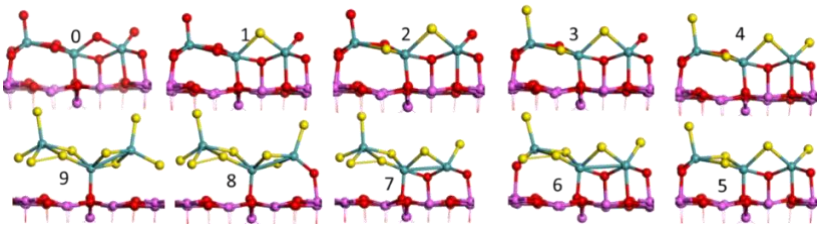

Figure B-8: Mo-Oxide to Mo-Sulfide step-wise O/S exchange structure for Path-1 ($Mo_3O_9 \rightarrow Mo_3S_9$) on support.

B2.4 Chain-1-Mo_3O_9 through path-2

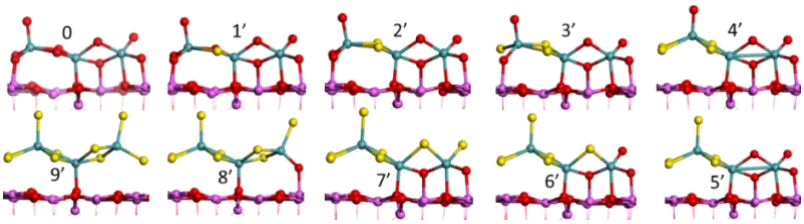

Figure B-9: Mo-Oxide to Mo-Sulfides step-wise O/S exchange structures for Path-2 ($Mo_3O_9 \rightarrow Mo_3S_9$) on support.

B2.5 Most relevant-Mo_3O_9 to Mo_3S_9 sulfidation path

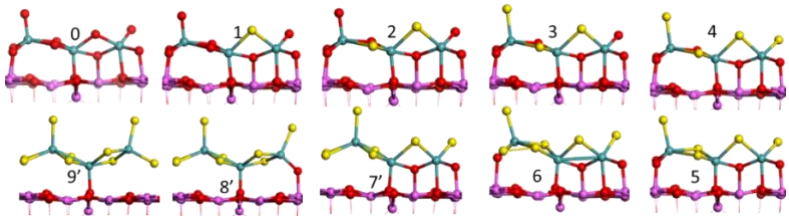

Figure B-10: Most relevant path for Mo-Oxides to Mo-Sulfides transformation by O/S exchange for chain-trimer ($Mo_3O_9 \rightarrow Mo_3S_9$) on support.

B2.6 Chain-2-Mo_3O_9 sulfidation

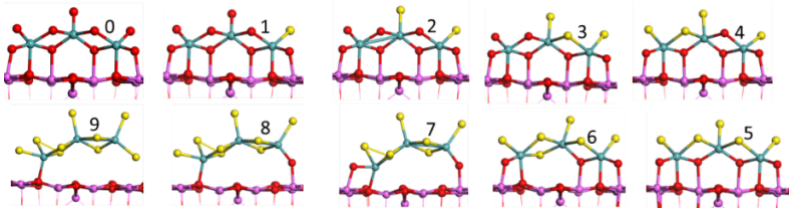

Figure B-11: Mo-Oxide to Mo-Sulfides step-wise O/S exchange structures for Chain-2 ($Mo_3O_9 \rightarrow Mo_3S_9$) on support.

B3. Thermodynamics of sulfidation of supported Mo_3O_9

Figure B-12 Illustrates the thermodynamically possible most favorable O/S exchange path, and below, we have shown the O/S exchange for cyclic trimer. As we have observed for chain trimer, in a similar fashion, the terminal and bridging oxygen are first and easily replaceable compared to the interfacial ones, even for cyclic trimer. A slight reconstruction is required to reach the most stable conformer of $Mo_3O_4S_5$, which costs about 0.5 eV (Figure B-12). The final structure is very similar to the triangular model of a-Mo_3S_9. Their thermodynamic comparison with other chain structures has been illustrated in Figure B-12.

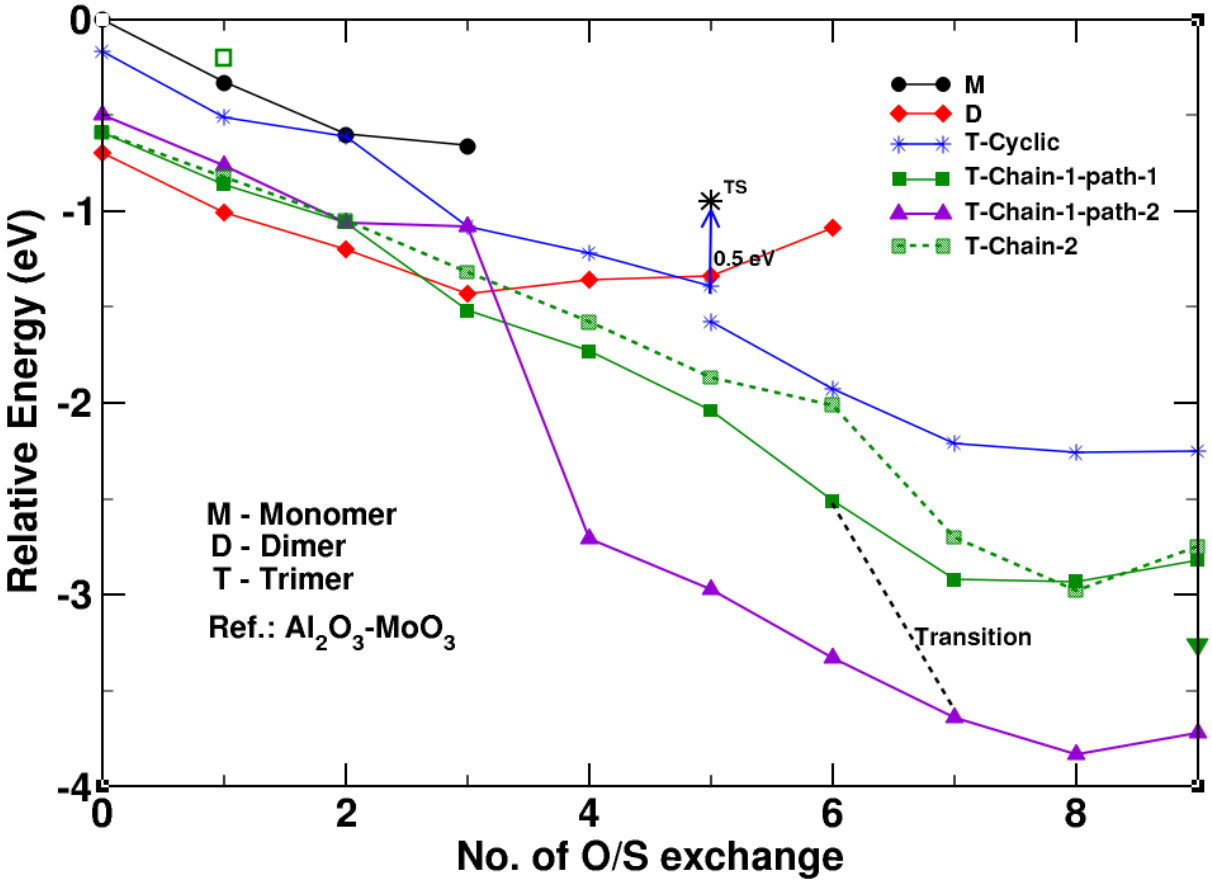

Figure B-12: Thermodynamic energy diagram of various Mo-oxide models. Monomer adsorbed on alumina has been taken as a reference. The cyclic structure shows a transition at $Mo_3O_4S_5$ with respective transition state (TS) for transformation to a more stable conformer.

Thermodynamic energy comparison for various sizes of $MoO_3 \rightarrow MoS_3$ raises some crucial points, such as every O/S exchange is thermodynamically favorable except for some interfacial oxygen. Interestingly, the cyclic trimer is far less stable than the cyclic chain for sulfides, almost 1.5 eV. This is particularly important, as, in its gas phase, the triangular is more stable by about 1 eV than the chain of Mo_3S_9. By these observations, it appears that the Mo3 size will mainly exist in chain form. For the larger size, the chains are also more stable in the gas phase. Therefore, they might be more stable on support too. However, the formations of such chains without deformation can be questioned and needs further examination.

B4. Kinetics of sulfidation of supported Mo_3O_9

B4.1 Electronic energy plot for various O/S exchange of supported chain-1-Mo_3O_9

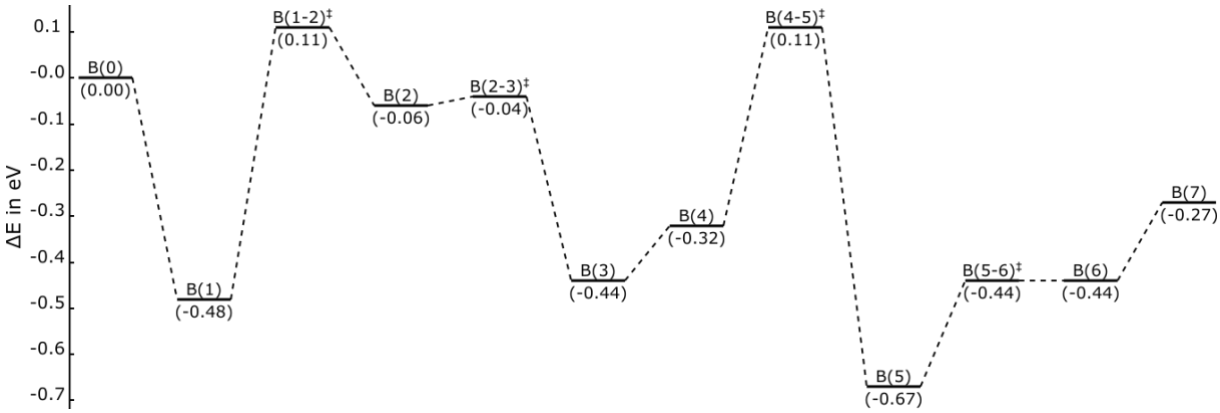

Figure B-13: ΔE plot for bridging oxygen replacement.

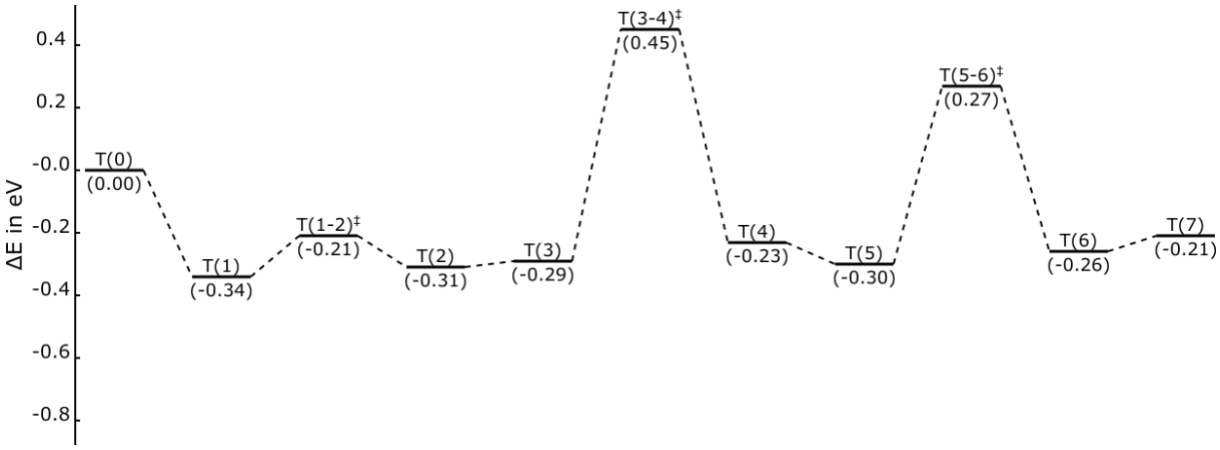

Figure B-14: ΔE plot for terminal oxygen replacement.

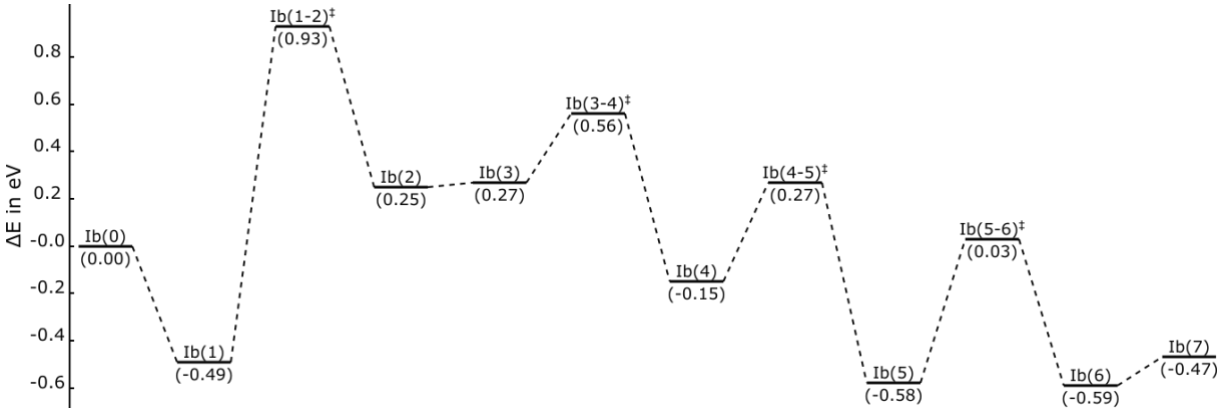

Figure B-15: ΔE plot for interfacial bidentate oxygen replacement.

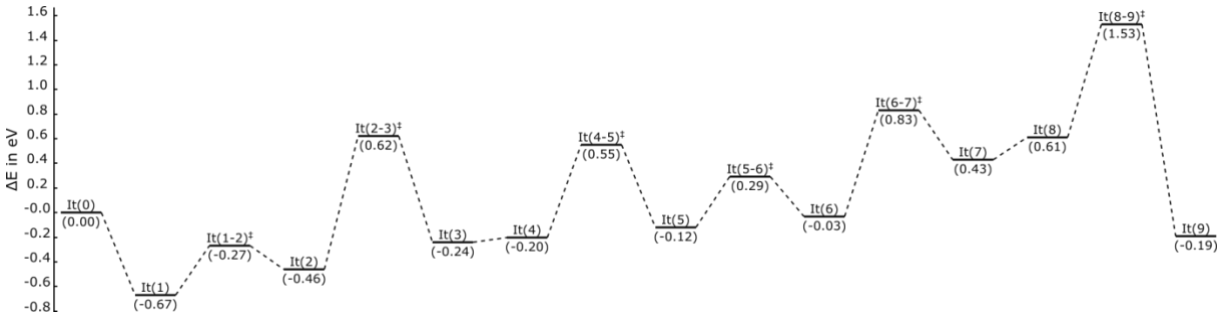

Figure B-16: ΔE plot for interfacial tridentate oxygen replacement.

B4.2 Electronic energy plot for O/S exchange supported cyclic Mo_3O_9

Terminal oxygen site

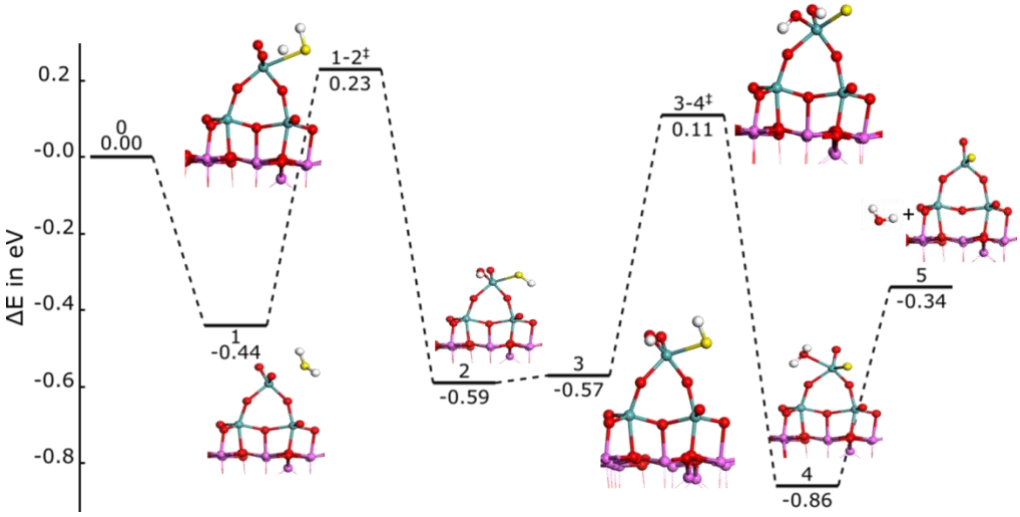

Figure B-17: Energetics of O/S exchange for terminal oxygen of cyclic trimer using H_2S (Mo_3O_9 + H_2S →Mo_3O_8S + H_2O) at 0K.

Terminal Oxygen: Starting from H_2S adsorption on the clusters followed by H_2S dissociation that involves the proton transfers to the oxygen and leads to the formation of SH, OH. The activation energy is similar to that of terminal oxygen in the chain (+0.67 eV). Some SH and OH rotations are required to get the appropriate intermediate for second proton transfer, leading to water formation. The final step is the desorption of water.

Bridging oxygen site

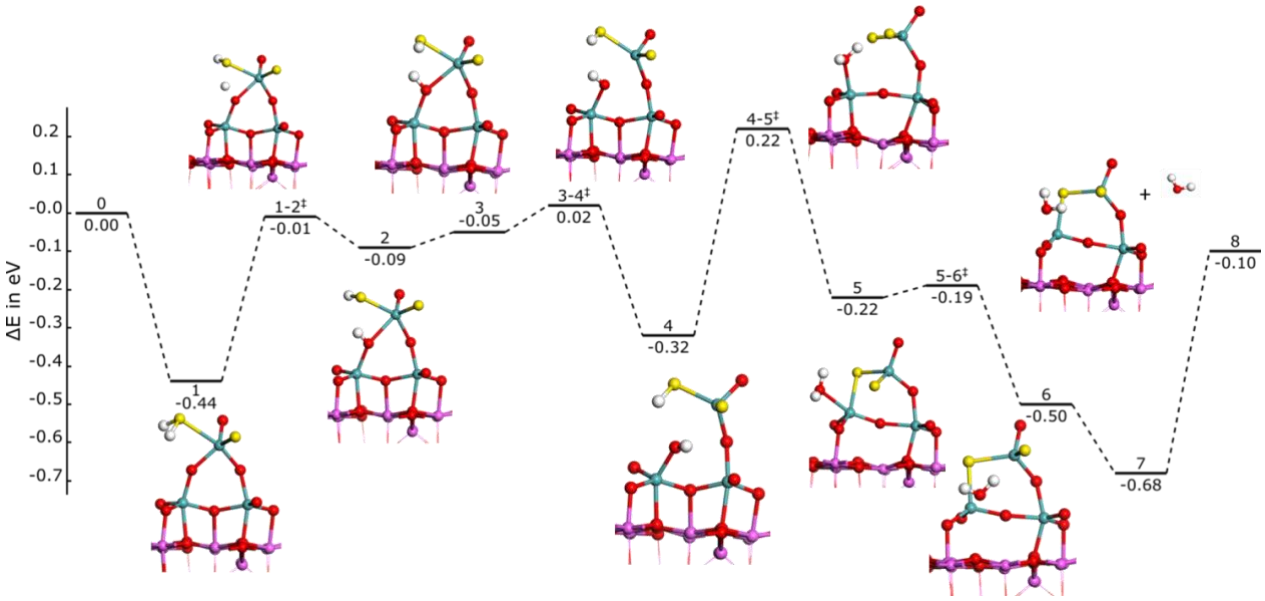

Figure B-18: Energetics of O/S exchange for bridging oxygen of cyclic trimer using H_2S ($Mo_3O_8S + H_2S \rightarrow Mo_3O_7S_2 + H_2O$) at 0K.

Bridging Oxygen: Thermodynamically, the second oxygen replacement occurs at the bridging site. During kinetics, similar steps are followed. The second proton transfer is the rate-limiting step and requires about 0.66 eV activation energy. The Bridging and terminal oxygen have similar kinetic limitations; therefore, they could be replaced simultaneously for the cyclic trimer.

Interfacial-bidentate oxygen site

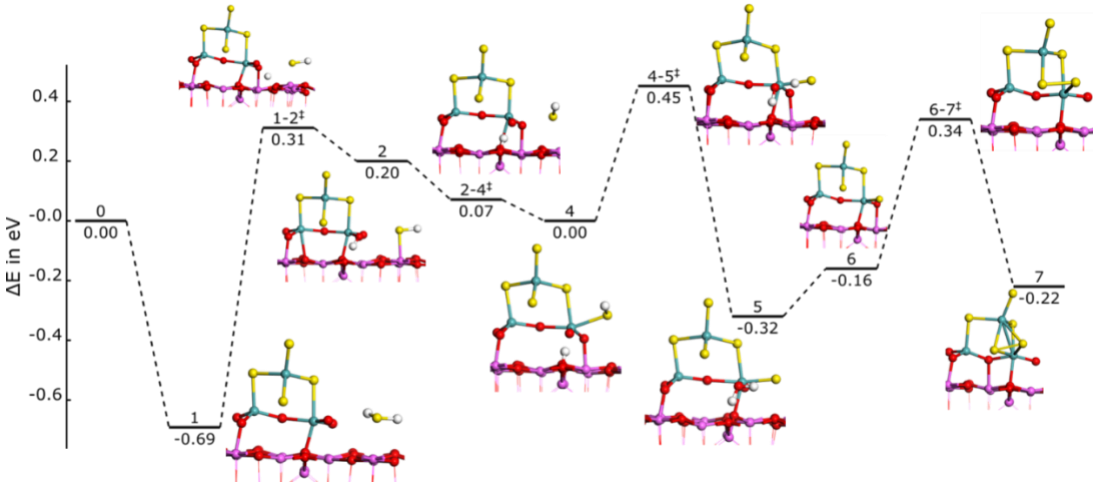

Figure B-19: Energetics of O/S exchange for interfacial-bidentate oxygen of cyclic trimer using H_2S ($MoO_5S_4 + H_2S \rightarrow MoO_4S_5 + H_2O$) at 0K.

Interfacial bidentate: As in the case of chain IB replacement, the adsorption of H_2S takes place on support. Dissociation of H_2S requires about 1 eV, and the rate-limiting step is the second proton transfer. The energy needed for activation is about 1.14 eV, which is significantly lower than the energy of the interfacial bidentate chain, approximately 1.42 eV. The desorption is relatively easy as the water remains on the cluster and does not move to the surface for the interfacial bidentate chain. Finally, a slight reconstruction of am oxysulfide cluster leads to a stabler conformer.

Interfacial tridentate oxygen sites

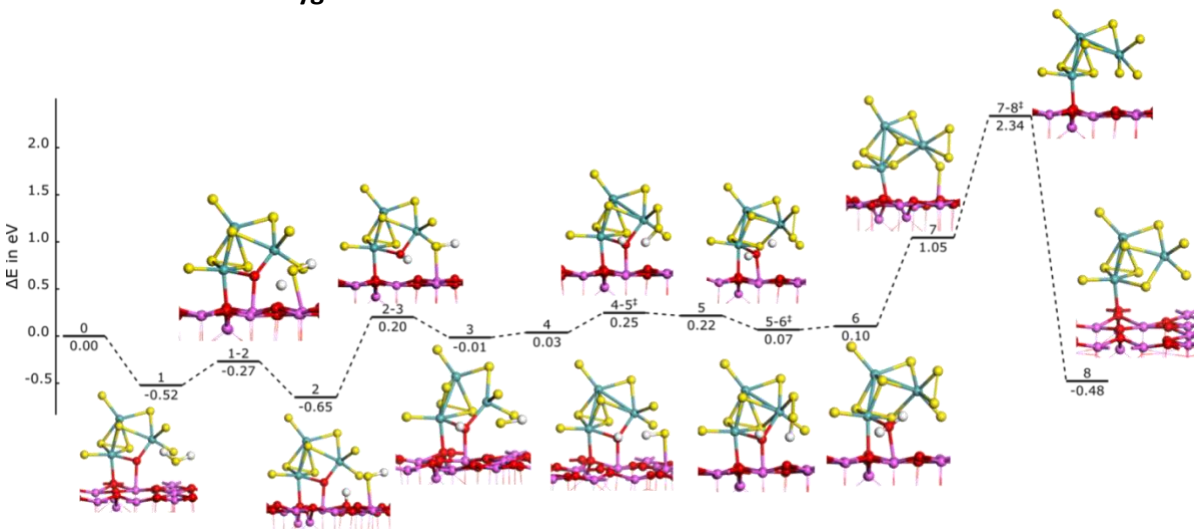

Figure B-20: Energetics of O/S exchange for interfacial tridentate oxygen of cyclic trimer using H_2S ($Mo_3OS_8 + H_2S \rightarrow Mo_3S_9 + H_2O$) at 0K.

Interfacial tridentate: These are the most challenging oxygen to be replaced. The activation of H_2S takes place on the surface. The earlier steps are not as expensive as water desorption and sulfur diffusion> This is similar to the case of the interfacial tridentate chain. The water desorption step is the second most costly step after sulfur diffusion. Water desorption requires 1.7 eV and reconstruction >2.5 eV, though entropy correction could change the order as in the interfacial tridentate chain.

B4.3 Energetic span analysis for the kinetics of cyclic-Mo_3O_9 O/S exchange

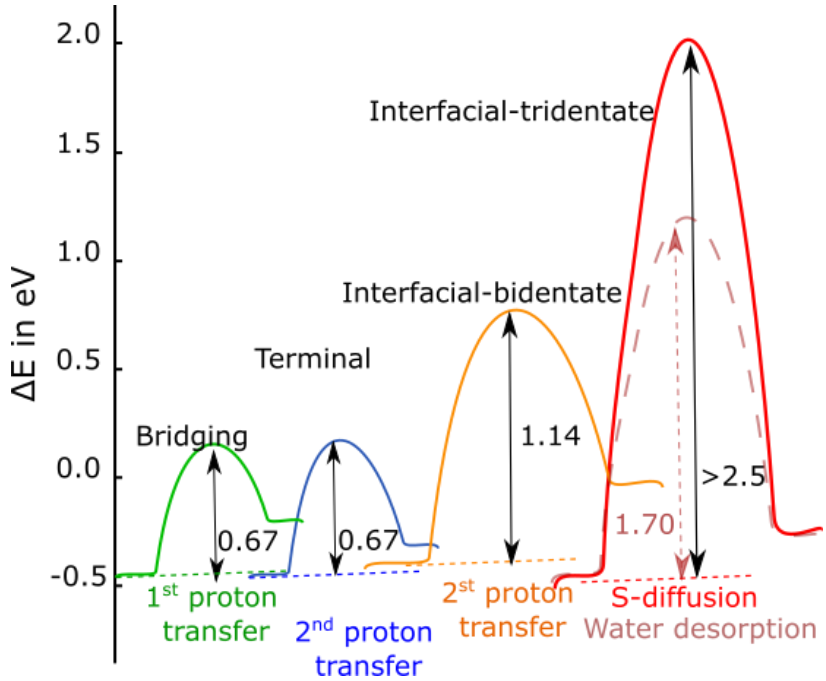

Figure B-21: Energetics span analysis of O/S exchange for various types of oxygen present in cyclic trimer at 0K.

The energetic span analysis has been represented in Figure B-21 with the respective rate-determining step. The O/S replacement trend remains similar between chain and triangular. Bridging is the most easily replaced, followed by the terminal. Interfacial bidentate and tridentate remain the most difficult to replace. The RDS for a similar class of oxygens is also the same.

B4.4 Electronic energy plots for removing oxygen from $Mo_3O_3S_6$(step-III)

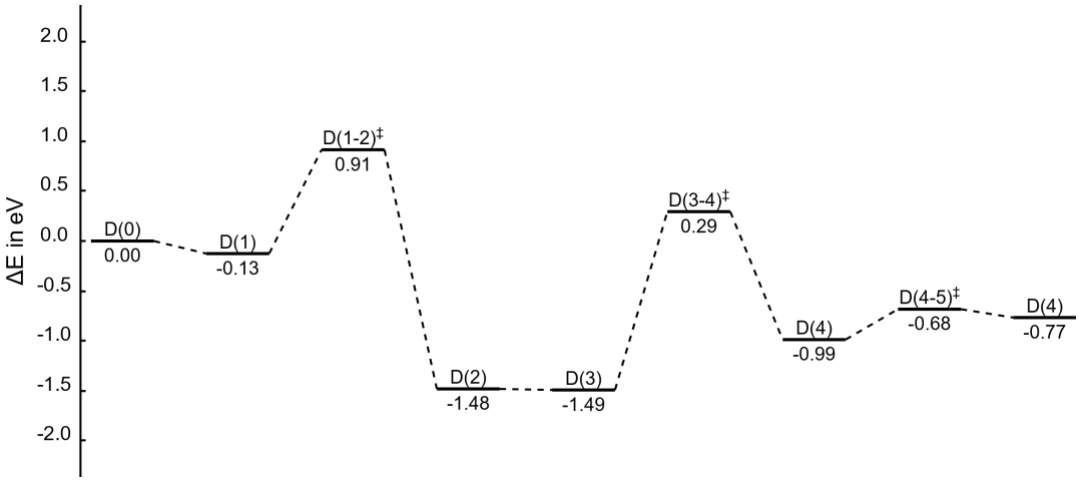

Figure B-22: ΔE plot for oxygen removal from $Mo_3O_3S_6$.

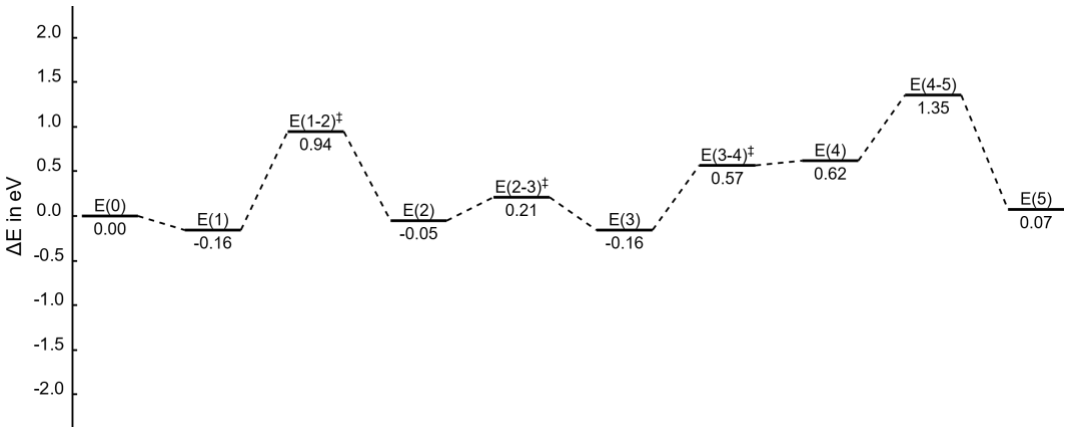

Figure B-23: ΔE plot for oxygen removal from $Mo_3O_2S_6$.

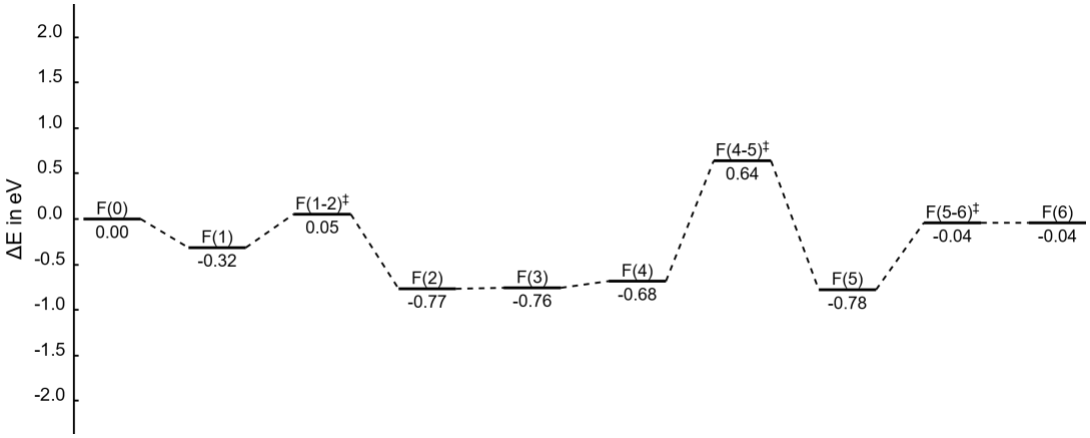

Figure B-24: ΔE plot for oxygen replacement of Mo_3OS_6.

B4.5 Electronic energy plots for removing sulfur from Mo_3S_9 (step-IV)

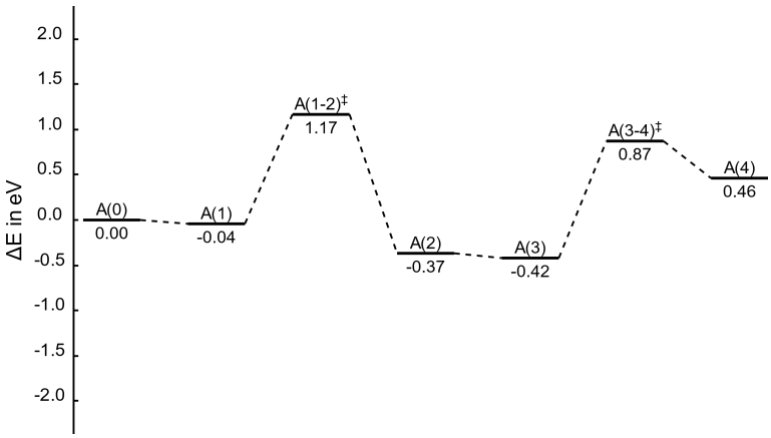

Figure B-25: ΔE plot for first sulfur removal from Mo_3S_9.

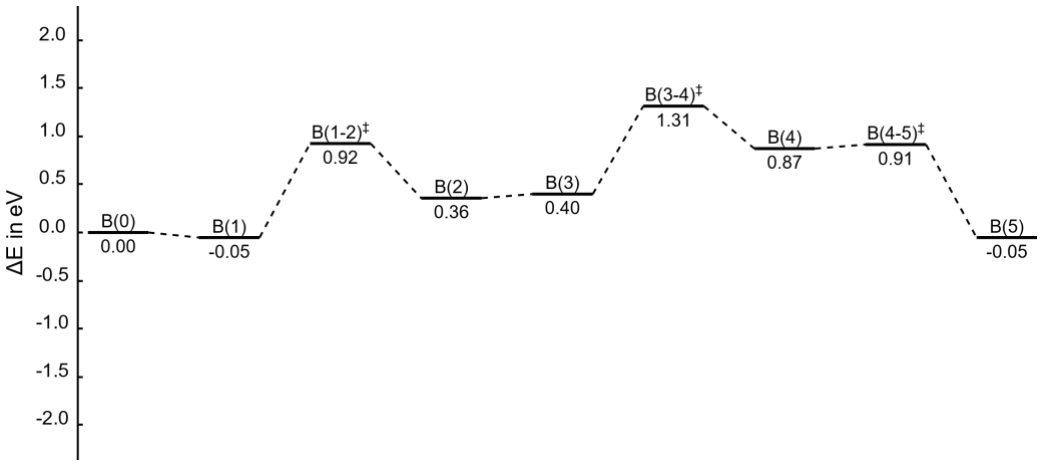

Figure B-26: ΔE plot for second sulfur removal from Mo_3S_8.

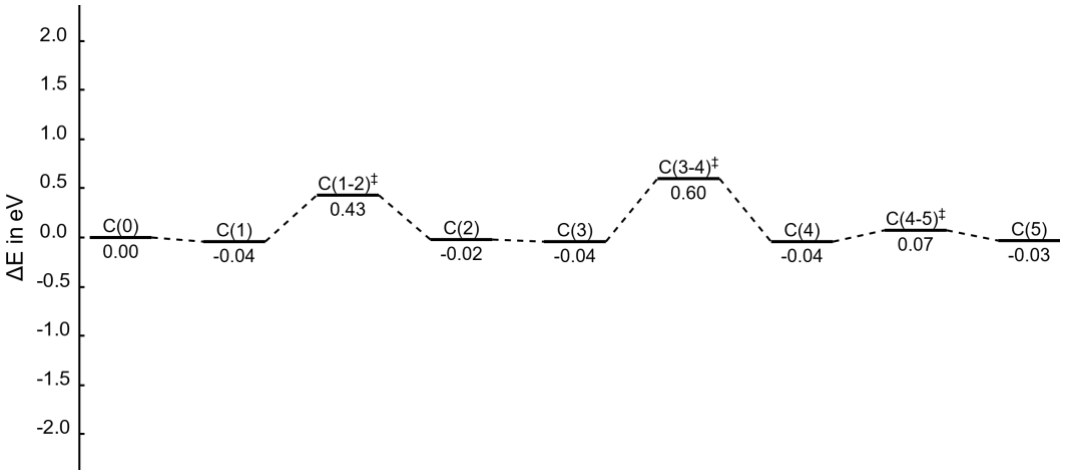

Figure B-27: ΔE plot for final sulfur removal to reach disulfide stage.

B5. O/S exchange on supported Mo_1O_3 (monomer)

B5.1 Terminal oxygen site

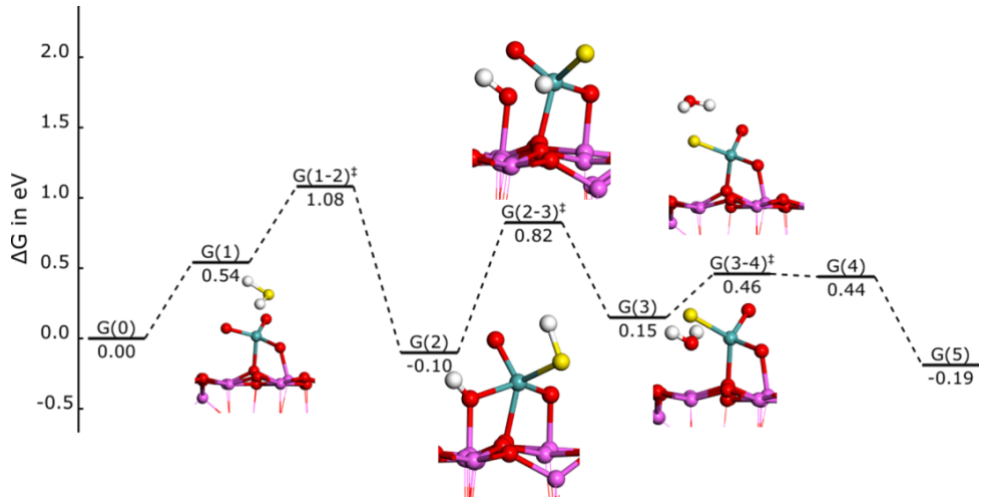

Figure B-28: Energetics of O/S exchange for terminal oxygen of monomer (MoO_3) using H_2S ($MoO_3 + H_2S \rightarrow MoO_2S + H_2O$) at 0K.

Sulfidation of Monomer: Gibbs free energy plot of O/S exchange for top-oxo of monomer (Figure B-28). The dissociation of H_2S is the rate-limiting step that costs 1.08 eV. The formation of water and the desorption of water are the other critical steps in this reaction mechanism. Overall, the process is exothermic and thermodynamically favorable. We assume that the second oxo would also be replaced similarly. We further investigated the interfacial oxygen in a monomer that has an activation energy of 1.35 eV (Figure B-28). This requires transferring of the second proton from sulfur to oxygen. Overall, the O/S exchange is more favorable for the monomer than the trimer due to the lower activation energy. Water desorption is the second most expensive step, as is the case for another interfacial oxygen.

B5.2 Interfacial oxygen site

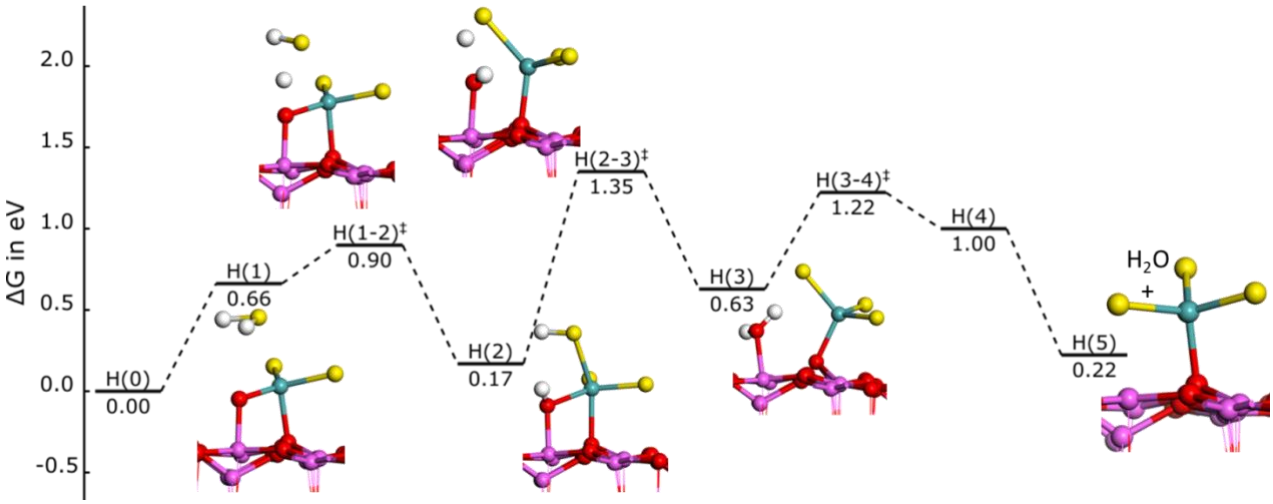

Figure B-29: Energetics of O/S exchange for interfacial oxygen of monomer using H_2S ($MoOS_2 + H_2S \rightarrow MoS_3 + H_2O$) at 0K.

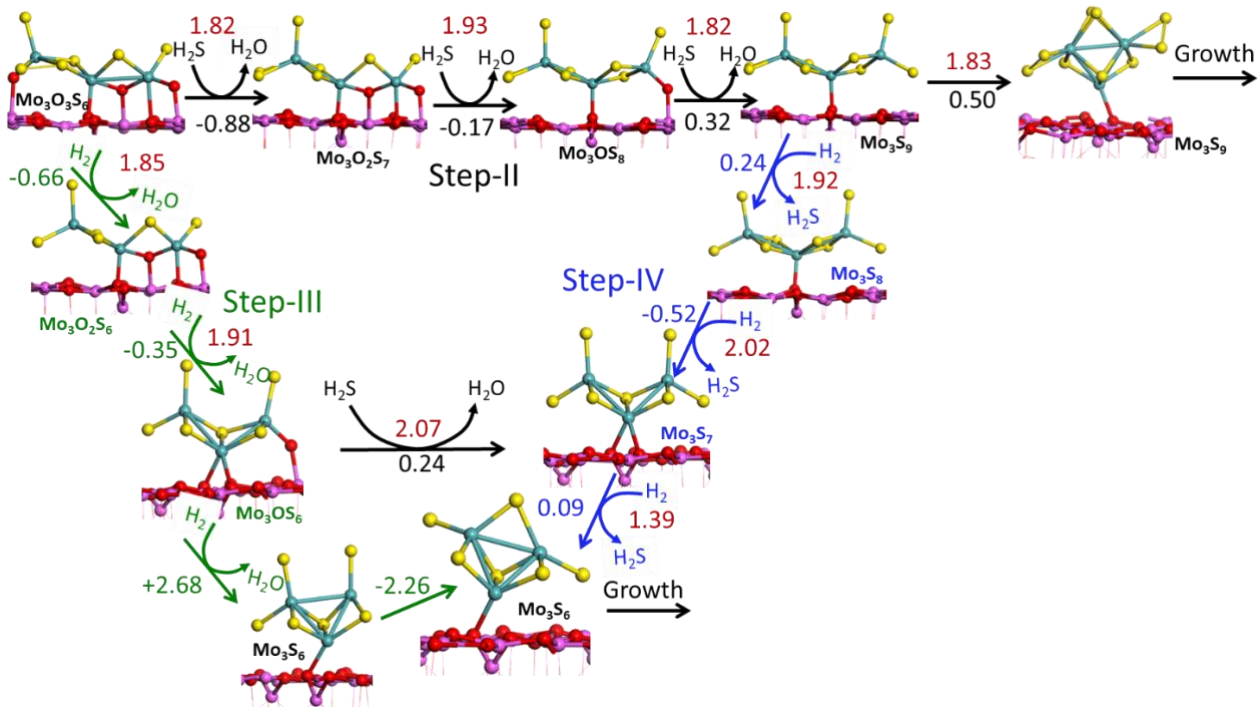

Figure B-30: Oxysulfides to trisulfides sulforeduction by H_2S (black arrows), trisulfides to disulfides transformation using H_2 (blue arrows), and direct reduction from oxysulfide to disulfides by H_2 (green arrows). The formalism for step-II, step-III, and step-IV and color coding is the same as in Figure **4-1**. Activation free enthalpies (red number) and reaction free enthalpy (black/blue/green numbers) are given in eV.

B6. Frequency analysis

Table B- 1: Transition state frequencies and their respective SH-OH, HH bond lengths with corresponding TS indicator.

TS Frequencies (cm^{-1})	SH bond (Å)	OH bond (Å)	OH bond (Å)	SH bond (Å)	HH bond (Å)	TS-indicator
761	1.61	1.25				br(1-2)
783	1.51	1.36				br(4-5)
572	1.62	1.23				t (1-2)
1468	2.23	1.28				int-bi(1-2)
963	1.49	1.46				Int-tri(1-2)
1511		1.33	1.43			Int-tri(2-3)

452	1.48	1.5			Int-tri(4-5)
645	1.73		1.75	1.07	A(1-2)
877	1.44		2.01		A(3-4)
1108	1.58		1.63	1.08	B(1-2)
1000	1.71		1.73		B(3-4)
691	1.70		1.71	0.91	C(1-2)
890	1.69		1.65		C(3-4)
635	1.97	1.63		0.80	D(1-2)
1036	1.99	1.67			D(3-4)
215	1.82	1.28		0.97	E(1-2)
1286	1.41	1.59			E(2-3)
902	1.52	1.404			F(1-2)
688	1.47	1.46			F(4-5)
1029	1.61	1.25			G(1-2)
1250	1.72	1.31			G(2-3)
1001	1.55	1.34			H(1-2)
1318	1.89	1.28			H(2-3)

Table B-2 Vibrational modes of various intermediates of oxides to oxysulfide reduction.

Vibrational modes	Mo_3O_9	$Mo_3O_6S_3$		$Mo_3O_3S_6$		Mo_3S_9	
		Path-1	Path-2	Path-1	Path-2	Path-1	Path-2
Alumina Modes	652, 636, 578, 561, 540, 539, 514, 495, 480, 475, 465, 452, 446, 435, 433, 410, 310, 291, 281, 265, 258, 246	637, 573, 560, 546, 532, 484, 478, 469, 455, 447, 434, 426, 420, 393, 389, 383, 361, 344, 336, 311, 299, 292, 265, 249	704, 680, 648, 617, 580, 572, 536, 533, 508 490, 481, 467, 448, 440, 425, 421, 400, 386, 368, 332, 318, 309	651, 574, 510, 497, 478, 471, 448, 442, 427, 412, 408, 400, 383, 367, 348, 305, 291, 282, 257,	667, 578, 547, 513, 480, 474, 467, 464, 451, 450, 435, 420, 409, 406, 289, 268, 262,	639, 584, 564, 490, 486, 473, 471, 448, 444, 439, 436, 404, 397, 392, 373, 364, 359, 353, 314, 293, 284, 257,	638, 573, 562, 480, 477, 465, 446, 442, 438, 436, 425, 399, 388, 382, 372, 366, 355, 315, 311, 303, 297, 283, 266, 256,
Mo-O_t	991, 989,	978	982, 970	--	970		
Mo-$O_{int\text{-}bi}$	894, 866, 835, 825,	868, 831, 822, 799	839, 831,	874, 806,	813		
Mo-O_{surf}	816	755	704, 680, 648	738	702,	684	680,
Mo-$O_{int\text{-}tri}$	715, 625	645	680, 648	692	687		
Mo-(O-Al)	578, 557, 544, 539, 514, 495, 480, 475, 466, 435, 352, 335,	552, 532, 530, 511, 497, 455, 444, 434, 426, 420, 393, 383, 361, 344, 314,	580, 536, 533, 517, 508, 421, 368, 318, 309,	577, 556, 539, 497, 336, 319 , 251	575, 554, 547, 336, 316,		
Mo-O-Mo	787, 715, 652, 636, 557, 422, 410, 398, 381, 368, 363, 352, 326, 291, 274, 281,	831, 799, 511, 497, 478, 447, 420, 389, 361, 344, 265, 249, 233, 200	730, 648, 617, 533, 490, 440, 425, 347, 332, 318	548,	553, 501		

	265, 258, 246, 227						
Mo-S_t		573	461,	564, 560,	568	567, 559, 520, 495 (w-int-Al)	564, 559, 504(w-int-Al)
Mo-S-Mo		511, 497, 469, 420, 333, 311, 265, 249,	519, 508, 478, 318,	471, 467, 459, 448, 383, 375, 368, 358, 356, 348, 333, 326, 245, 235, 217	494, 467, 464, 388, 377, 363, 353, 347, 322, 311, 238, 240, 238, 219	483, 473, 471, 436, 428, 413, 404, 397, 379, 373, 364, 359, 353, 341, 294, 247, 243, 226	491, 467, 450, 438, 399, 382, 378, 372, 366, 356, 355, 325, 315, 311, 303, 246, 236,
Mo-S_2				471, 467,	543	486	540

Table B-3: ΔE and ΔG of oxides, oxysulfides, and sulfides for their respective steps.

Step	ΔE (ΔG)									
	Mo_3O_9	$Mo_3O_7S_2$	$Mo_3O_4S_5$	$Mo_3O_2S_7$	Mo_3OS_6	Mo_3S_9	Mo_3S_8	Mo_3S_7	$Mo_3O_3S_6$	$Mo_3O_2S_6$
Adsorption of H_2S or H_2	-0.48 (0.55)	-0.34 (0.79)	-0.49 (0.43)	-0.67 (0.37)	-0.28 (1.01)	-0.04 (0.19)	-0.04 (0.44)	-0.03 (0.35)	-0.12 (0.50)	-0.14 (0.38)
H_2S / H_2 dissociation	0.59 (1.19)	0.13 (0.97)	1.42 (1.82)	0.94 (0.74)	0.33 (1.41)	1.17 (1.92)	0.95 (1.69)	0.46 (1.27)	1.03 (1.85)	1.08 (1.91)
Proton transfer	0.55 (1.14)	0.79 (1.62)	1.05 (1.70)	1.22 (1.66)	1.37 (2.07)	0.90 (1.74)	1.35 (2.02)	0.63 (1.39)	1.87 (1.61)	0.48 (1.05)
Water / H_2S desorption	0.23 (0.77)	0.67 (1.22)	0.52 (1.55)	1.50 (1.93)	0.37 (0.72)	0.90 (1.74)	0.92 (1.54)	0.1 (0.78)	0.88 (0.86)	0.87 (1.19)
Reconstruction				2.20 (1.70)						1.37 (1.15)

Appendix C - Complementary analysis on various aspects of MoS_3 polymorphs

C1. Structural analysis

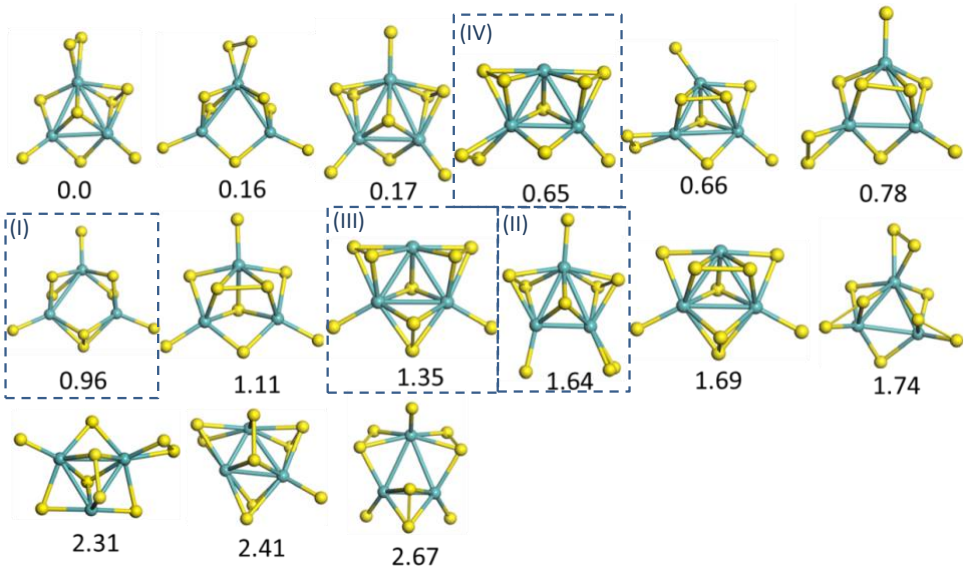

Figure C-1: Various explored 0D-Mo_3S_9 clusters and their relative energy (in eV) w.r.t most stable conformer.

The earlier structures (formal oxidation states of Mo is +4) proposed by Weber et al. and simulated by Jiao et al. are represented in the dashed squared frames with the original label by Weber et al. [40] To avoid the spurious interaction with its periodic images, we use a large cell 20 x 20 x 20. We checked the convergence in electronic energy by increasing the cell dimensions 5, 10, and 15 A in all three directions, and the respective change in electronic energy is ≤ 3 meV/Mo_3S_9.

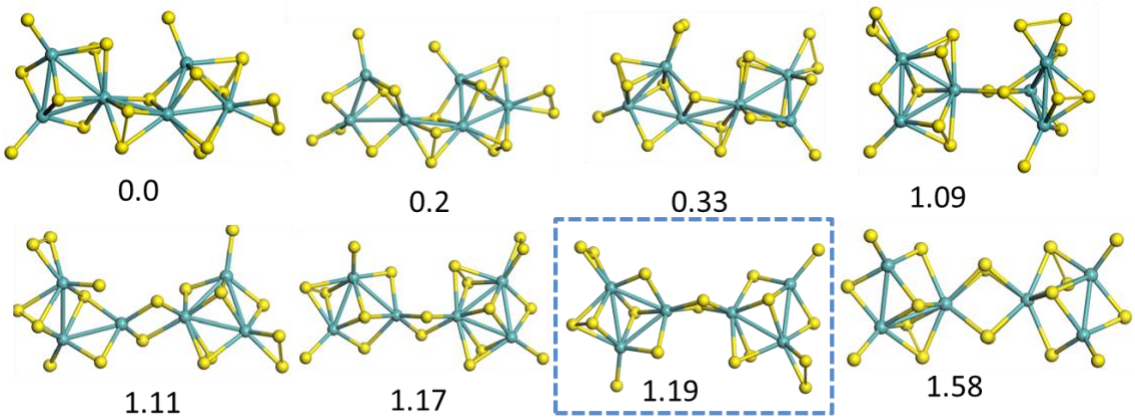

Figure C-2: Various explored 0D-Mo_6S_{18} clusters (triangular dimers) and their relative energy (in eV) w.r.t the most stable one. The conformer used for the initial configuration of AIMD is highlighted by a squared frame.

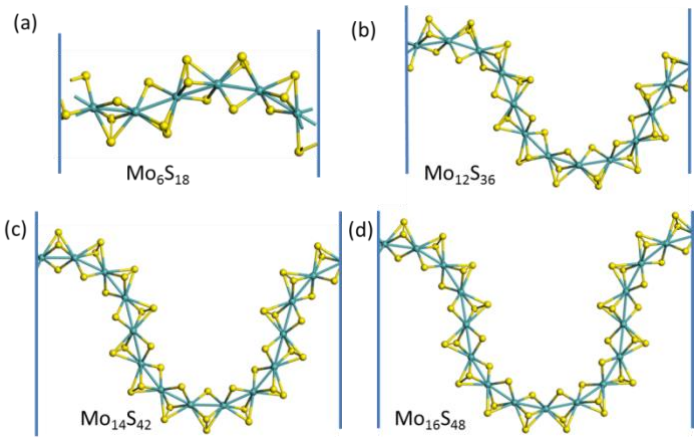

Figure C-3: Various 1D-periodic wave-like nano-structures with different number of Mo-atoms in unit cell. Corresponding structures with relative energy (w.r.t. per Mo_3S_9 of TO) (a)-2.45, (b) -2.69, (c)-2.71 and (d) -2.72 in eV.

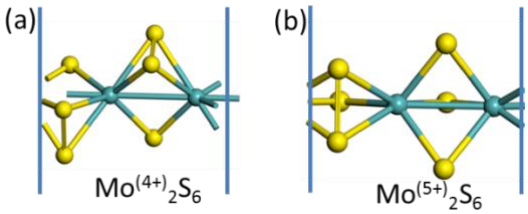

Figure C-4: Linear 1D-periodic structures: (a) O.S = +4, R.E. = -1.73 eV, and (b) O.S = +5, R.E. = -1.29 eV. Relative energy is w.r.t. per Mo_3S_9 (TO).

Table C-1: Electronic energy convergence with respect to cell size for various types of polymorphs, the currently used dimension of the cell is given in the first column for respective polymorphs.

Polymorphs	Increment along non periodic(Å)	$\Delta E/Mo_3S_9$ (meV)
TO-Monomer	**0**	**0**
(20, 20, 20)	**5**	**2.1**
	10	**2.7**
	15	**3.2**
TO-Hexamer	**0**	**0**
(26, 40, 23)	**5**	**1.5**
	10	**2.3**
	15	**2.3**
TO-Perioic	**0**	**0**
(23.16, 34.30, 21.29)	**5**	**1.3**
	10	**1.7**
	15	**3.1**
WL-Periodic	**0**	**0**
(23.67, 26.35, 37.95)	**5**	**0.5**
	10	**0.7**
	15	**1.6**

To treat the low dimentional system in VASP, a large vacuum is required to minimize the spurious interactions between neighboring cells. We observed, more than 12 Å distance between periodic images is sufficient to have a good balance between the computational cost

and accuracy. To check the effect of huge change in the vacuum on electronic energy, for most relevant polymorphs, we perform a systematic test by increasing the cell dimension along with the non-periodic directions with 5, 10, and 15 Å, respectively. During the electronic energy convergence check, we did not observe any strong change. The change in electronic energy is ≤3 meV/Mo_3S_9 in all the case has been tested. We also checked the dipole corrections to avoid polar interactions, if there are any. For MoS_3 case, we did not observe a significant change in electronic energy (< 2meV/Mo_3S_9) for Monomer, WL-P, TO-P.

Table C-2: Cell parameter for the various periodic structures along the direction of periodicity.

Polymorphs	Cell parameter (Å)
TO-P ($Mo_{18}S_{54}$)	**34.30**
WL-P($Mo_{12}S_{36}$)	**23.86**
WL-P($Mo_{14}S_{36}$)	**24.96**
WL-P($Mo_{16}S_{48}$)	**26.35**
L-P^{4+}(Mo_2S_6)	**5.79**
L-P^{5+}(Mo_2S_6)	**5.98**
NbS_3-ribbon (Mo_4S_{12})	**6.46**

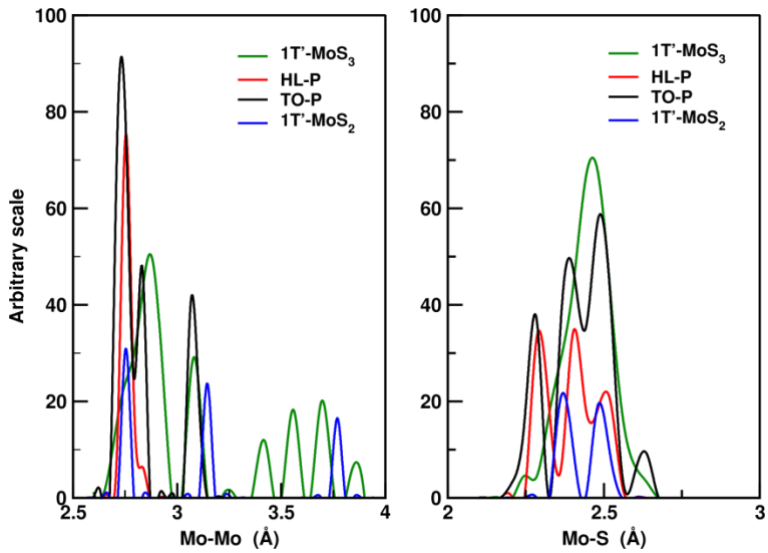

Figure C-5: Pair correlation function (PCF) for Mo-Mo and Mo-S bonding distribution for various types of MoS_3 polymorphs.

Note: The Mo-S PCF for TO-P reveals four distinct peaks corresponding to the various Mo-S bonds involving the different μ_i-S_j species represented in Figure **5-2**a. Table **5-1**, Table C-3 reports only two types of Mo-S bonds: one short (2.27 Å) present in μ_2-S and μ_1-S_2 species and one long bond by averaging over μ_2-S, μ_3-S, and μ_1-S, μ_2-S_2 (2.44 Å).

For HL-P, the PCF for Mo-S shows that three distinct peaks are identified in the HL-P (also valid for R and WL structures): one short Mo-S bond (2.31 Å) involving μ_2-S species and two long bonds fused in one single in Table **5-1**, Table C-3, involving μ_2-S_2 species (Figure **5-2**b).

Table C-3: Average bond lengths of Mo-Mo, Mo-S, S=S for different clusters and in parenthesis number of Mo-Mo bonds presents in the cluster as a function of size.

No of Mo atoms	$Mo\text{-}Mo_{long}$(Å)	$Mo\text{-}Mo_{short}$ (Å)	Mo-S (Å)	S-S (Å)
Triangular oligomer (TO)				
3	**2.96 (2)**	**2.72 (1)**	**2.35**	**2.05**
6	**2.95 (2)**	**2.81 (5)**	**2.37**	**2.04**
9	**3.04 (2)**	**2.79 (9)**	**2.36**	**2.04**
12	**3.06 (3)**	**2.78 (12)**	**2.38**	**2.04**
15	**3.10 (4)**	**2.78 (15)**	**2.40**	**2.04**
Open Ring (OR)				
3		**2.72 (2)**	**2.39**	**2.07**
6		**2.73 (5)**	**2.40**	**2.06**
9		**2.75 (8)**	**2.40**	**2.06**
12		**2.75 (11)**	**2.40**	**2.06**
15		**2.75 (14)**	**2.41**	**2.05**
Ring (R)				
6		**2.79 (6)**	**2.46**	**2.05**

12	**2.73(12)**	**2.41**	**2.05**
14	**2.74(14)**	**2.41**	**2.05**
16	**2.76(16)**	**2.40**	**2.05**

C2. Spectroscopic analysis

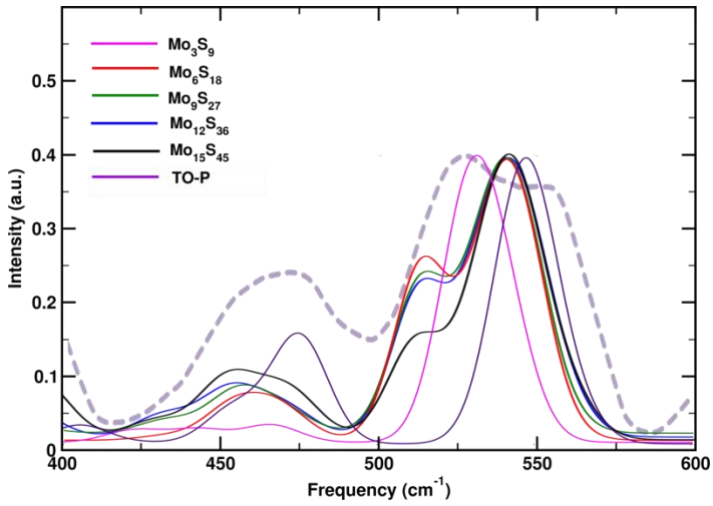

Figure C-6: DFPT simulated IR spectrum of various Mo_kS_{3k} TO (solid lines). Experimental IR spectrum (dashed line) from Ref.[40] All simulated spectra have been renormalized while keeping the highest intensity peak fixed.

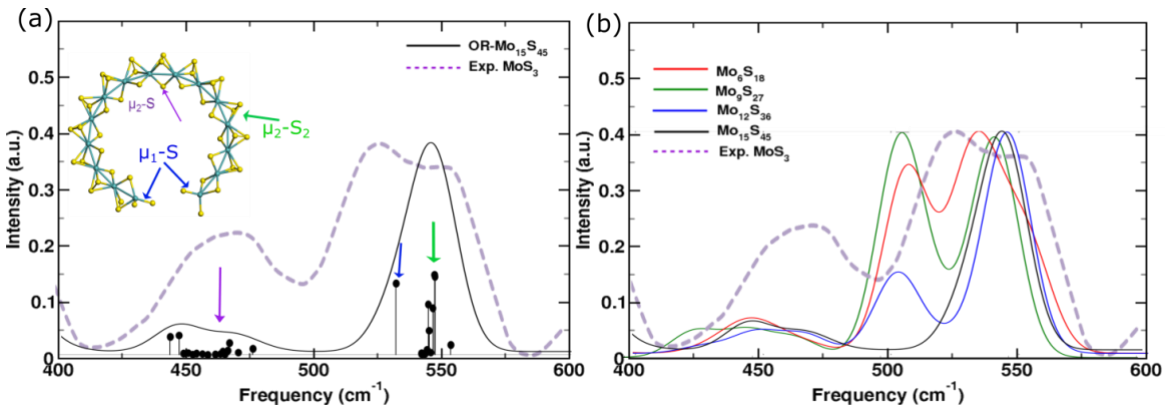

Figure C-7: DFPT simulated IR spectrum of open-ring (OR) models (solid lines): a) for $Mo_{15}S_{45}$, b) various Mo_kS_{3k}. All simulated spectra have been renormalized while keeping the highest intensity peak fixed. Experimental IR spectrum (dashed lines) from ref.[40]

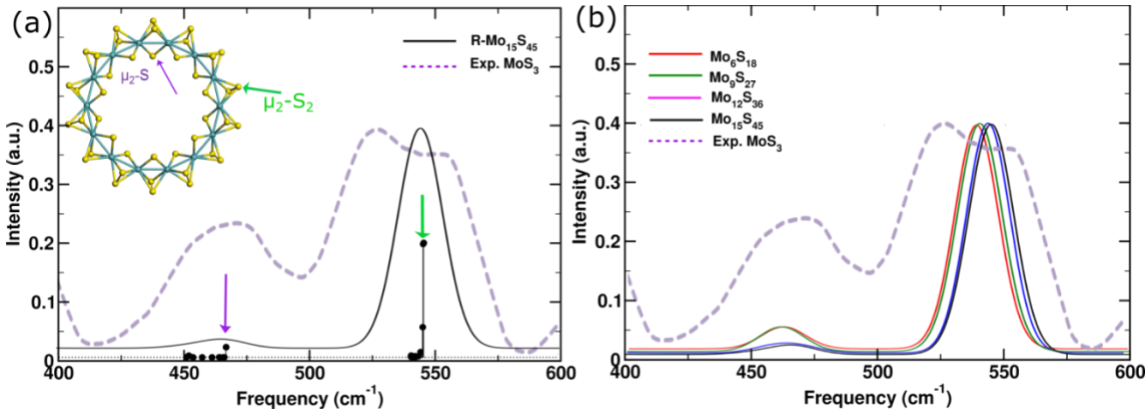

Figure C-8: DFPT simulated IR spectrum of ring (R) models (solid lines): a) $Mo_{14}S_{42}$, b) various Mo_kS_{3k} . All simulated spectra have been renormalized while keeping the highest intensity peak fixed. Experimental IR spectrum (dashed lines) from ref.[40]

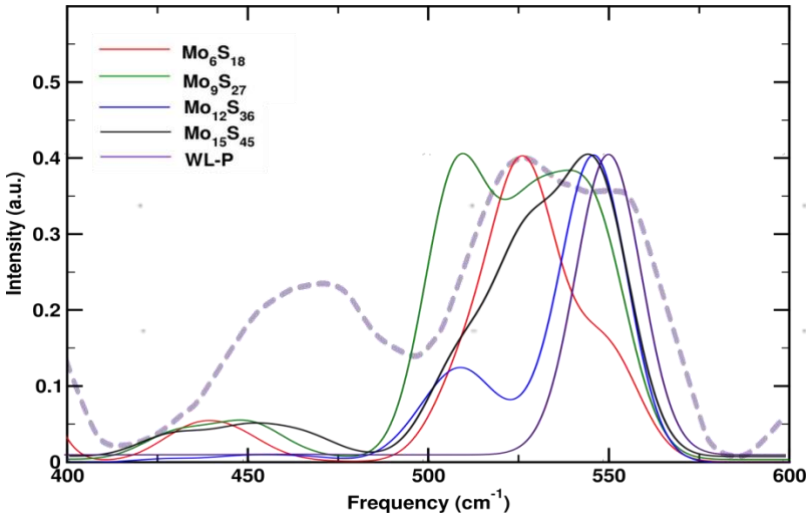

Figure C-9: DFPT simulated IR spectrum of various Mo_kS_{3k} Wave-like (WL) polymorphs (solid lines). Experimental IR spectrum (dashed line) from Ref.[40] All simulated spectra have been renormalized while keeping the highest intensity peak fixed.

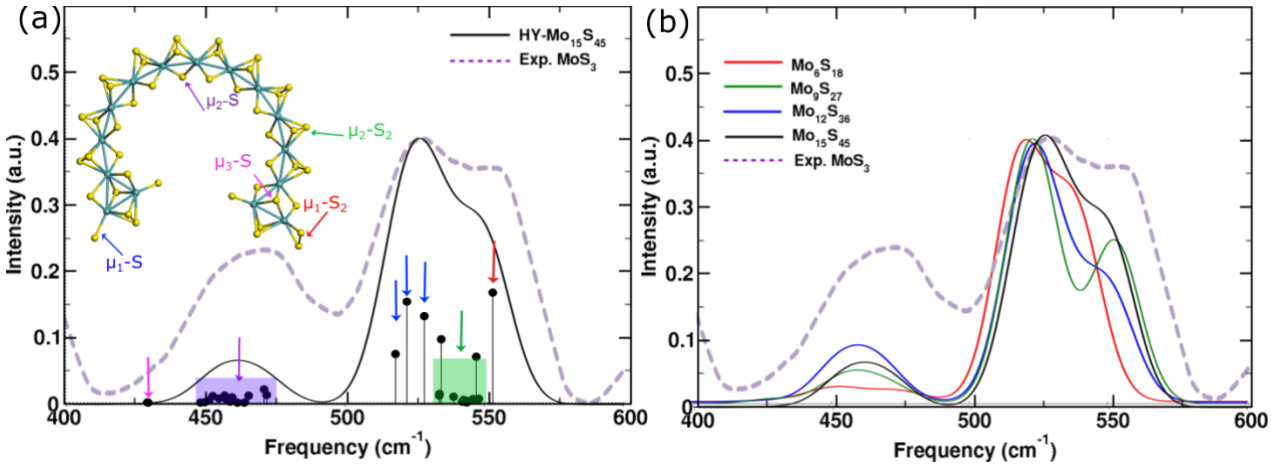

Figure C-10: DFPT simulated IR spectrum of hybrid (HY) models (solid lines): a) $Mo_{15}S_{45}$, b) various Mo_kS_{3k}. All simulated spectra have been renormalized while keeping the highest intensity peak fixed. Experimental IR spectrum (dashed lines) from ref.[40]

Table C-4: Calculated vibrational frequencies of the various μ_x-S_y species present in the different oligomeric models as a function of size.

No of Mo atoms	μ_2-S_2(cm^{-1})		μ_1-S_2 (cm^{-1})	μ_1-S (cm^{-1})	μ_2-S(cm^{-1})	μ_3-S(cm^{-1})
Triangular oligomer (TO)						
	μ_2-S_2 bridging two triangles	μ_2-S_2 in triangles				
3		539	542	527, 532	443, 466	422
6	539	549-555	573	507, 526,533	447-464	421, 429
9	535-537	545-557	539-544	512, 533	455-471	427-432
12	535-538	547-558	538-546	512, 533	447-453	426-432
15	537-538	555-558	538-545	512, 533	446-475	425-432
Open ring (OR)						
6	541-555			531, 507, 504	470-451	
9	541-547			523, 507, 502	443-469	
12	542-548			526, 509	443-468	
15	541-553			531, 508, 502	443-475	

No of Mo atoms	μ_2-S_2(cm^{-1})		μ_1-S_2 (cm^{-1})	μ_1-S (cm^{-1})	μ_2-S(cm^{-1})	μ_3-S(cm^{-1})
Hybrid (HY)						
	μ_2-S_2 in chain	μ_2-S_2 in triangles				
6	533-545	535	539-549	517,521	449 - 479	433
9	532-547	533,538	553	517,522,527	450 - 472	428,429
12	533-548	533,538	553	518,522,528	449 - 470	428,431
15	533-547	534,538	552	517,522,527	447 - 472	429,429
Ring (R)						
6	537-542				465-467	
12	541-544				454-467	
14	540-546				451-467	
16	541-547				449-466	
Wave Like (WL)						
15	542-553			527, 511, 508	467-435	
1T'-MoS_3						
12	534-554		558,561	503		416-468

Appendix D - Hydrodesulfurization of dibenzothiophene on CoMoS edge

Alexandre S. Dumon, Amit Sahu, Pascal Raybaud*

This appendix reproduces the text published in https://doi.org/10.1016/j.jcat.2021.01.030 and a part of a collaborative side project in which I have been involved with a post-doc A. Dumon. I contributed to this project by calculating many of the reported TSs for various pathways, thermal corrections, energy plots, and IRC analysis.

Appendix A - Abstract

Unraveling the mechanisms of hydrodesulfurization (HDS) of dibenzothiophene (DBT) and the corresponding active sites represents a scientific challenge to improve the intrinsic performances of Co-promoted MoS_2 (CoMoS) catalysts. By using density functional theory calculations, we compare two historical mechanisms for the C-S bond scission of DBT (direct desulfurization) : direct hydrogenolysis of DBT and β–elimination of α,β–dihydro-diobenzothiophene (α,β–DHDBT) on four relevant sites of the two CoMoS M- and S-edges. On the Co promoted M-edge, the α,β–DHDBT is formed through dihydrogenation which is kinetically competing with hydrogenolysis (both exhibiting activation free energies, $\Delta G^{\ddagger}$, smaller than +1.24 eV). On the S-edge, both dihydrogenation and hydrogenolysis exhibit higher $\Delta G^{\ddagger}$ (> + 1.78 eV). Interestingly, on the S-edge, the β–elimination (E2 type) on the α,β–DHDBT is found to be kinetically competing ($\Delta G^{\ddagger}$=+1.14 eV). The elimination of H_{β} atom involves a S_2 dimer close to the S-vacancy site where DHDBT is adsorbed. Since this leaving H_{β} atom is distinct from the one added at dihydrogenation step, this may explain why direct desulfurization of 4,6-alkyl substituted DBT compounds is hampered according to the elimination mechanism. We finally discuss the possible synergy between the two edges of CoMoS for HDS of DBT.

Keywords: hydrodesulfurization, dibenzothiophene, hydrogenolysis, β–elimination, CoMoS, edge sites, density functional theory

Appendix B - Introduction

Due to the ever-stronger environmental concerns, hydrotreatment and more particularly hydrodesulfurization (HDS) remain the unique catalytic processes able to reduce the sulfur contents in diesel and gasoline so that these fuels meet the 10 ppm regulations. In order to improve the eco-efficiency of these processes and optimize the use of metals, it is crucial to keep on developing improved HDS catalysts with higher intrinsic activity of the active phase. The active phase of HDS catalysts is made of Co or Ni promoted MoS_2 [1-3], and it was historically

identified as a so-called "mixed CoMoS phase" [4, 5]. Since these earlier findings, many experimental [2, 6-10] and theoretical [10-13] investigations have provided an ever deeper atomistic description of the potentially active sites located on the edges of the Co(Ni)MoS nano-crystallites. Nevertheless, challenging questions remain about the mechanism of transformation of sulfur containing polycyclic aromatic molecules such as derivatives of dibenzothiophene (DBT) on these edge-sites.

According to numerous experimental studies, the HDS refractory sulfur compounds are alkyl-substituted DBT, and more specifically the 4,6-dimethyldibenzothiophene (4,6-DMDBT) [14-17]. It is therefore crucial to better understand the HDS mechanism of this family of compounds in order to provide more efficient catalysts to achieve deep hydrodesulfurization at a lower energy process cost. For many years, this question has been addressed extensively by using kinetic studies combing both experimentation and modeling [18-25]. It is now largely accepted that the HDS of the family of DBT molecules undergoes via two-possible pathways: the hydrogenating (HYD) pathway, leading to cyclohexylbenzene (CHB) type compounds, while the second one, the direct desulfurization pathway (HYD), leads to biphenyl (BP) type compounds (**Fig. 1**) [21, 22, 25]. The probability of these two main pathways depend on the type of the DBT derivative and on the nature of the catalyst. For DBT, the HYD pathway is preferred on non-promoted MoS_2 active phase, while the DDS pathway is predominant on Co(Ni)MoS phases. For 4,6-DMDBT, the HYD pathway is preferred on MoS_2 and Co(Ni)MoS[25], and its overall desulfurization activity is significantly reduced with respect to DBT.

However, according to experimental kinetic studies the DDS pathway may follow two competing mechanisms (**Fig. 1**). The first and most direct one, called hydrogenolysis [26], assumes that the DDS pathway undergoes via two successive H additions. The first H addition occurs on the C_α position of DBT (carbon in position α to S atom, also numbered C_4 carbon in the chemical nomenclature) and leads to the C-S bond breaking with the formation of 2-phenyl-thiophenolate intermediate. The second H addition on the S atom would lead to 2-phenyl-thiophenol or intermediates [21]. The second possible DDS pathway suggests the formation of an α,β–dihydro-dibenzothiophene (DHDBT) intermediate by two H addition on the C_α and C_β positions of DBT (**Fig. 1**) [24, 25, 27]. The DHDBT would be the precursor for the C-S bond scission with concomitant β–elimination (E2 type). Moreover, this alternative mechanism also assumes that DDS and HYD pathways share the common DHDBT intermediate, that undergoes either the β–elimination, or subsequent hydrogenation steps. This concept of a common intermediate present at the crossing roads of DDS and HYD was earlier proposed by Singhal et al. [22]. However, it must be underlined that no direct experimental evidence of the formation of either DHDBT or 2-phenyl-thiophenol has been provided so far.

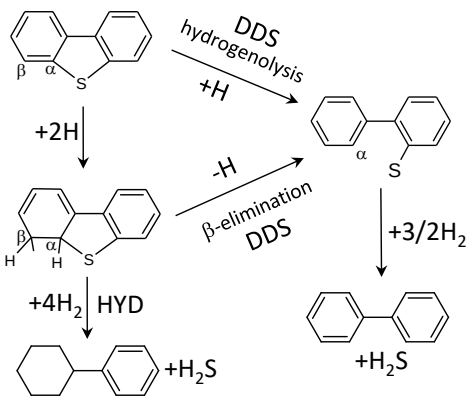

Fig. 1. Hydrodesulfurization of DBT through the DDS and HYD pathways involving either hydrogenolysis mechanism on DBT [28] or β–elimination mechanism of dihydrogenated DBT (DHDBT) [25]. Note: for sake of simplicity only the 2-phenyl-thiophenolate is represented but other intermediates such as 2-phenyl-thiophenol may form on the surface as discussed in the text.

At a molecular level, scanning tunneling microscopy (STM) combined with density functional theory (DFT) simulations have highlighted the various possible adsorption modes and energies of DBT derivatives on CoMoS supported on Au(111) surface [29-31]. These investigations reveal in particular how the underlying gold substrate may influence the spatial orientation of the DBT molecules adsorbed on the edge sites. DFT studies (including dispersion corrections) also showed that the adsorption energy and mode of 4,6-DMDBT on NiMoS depend closely on the nature of edge sites: in particular, 4,6-DMDBT is adsorbed perpendicularly with its S-atom located in a bridging position between two Ni sites of the S-edge, whereas it is absorbed in a nearly flat position on the Ni site of the promoted M-edge[32]. Since it is often referred that the HYD and DDS pathways might be controlled by the adsorption mode (either flat or perpendicular respectively)[27, 33], distinct activities are expected for the two edges. A similar proposal has been made by means of DFT simulation (without dispersion corrections) of DBT adsorption on non-promoted MoS_2[34]. However, as the present work will illustrate it, the link between the adsorption mode of DBT and the HYD/DDS pathways is not straightforward. Regarding the mechanistic aspects, Weber et al. investigated by DFT (without dispersion corrections) the hydrogenolysis mechanism of DBT on the Ni promoted M-edge site of a single NiMoS cluster[35], and shows that the first C-S bond breaking involves an activation energy of 1.37 eV. Surprisingly, this event is reported to occur during the DBT adsorption step on Ni site through a simultaneous H transfer from the same Ni site to the C_α atom of DBT. The possible formation of 2-phenyl-thiophenolate and 2-phenyl-thiophenol is also invoked in this study. By means of periodic DFT (without dispersion corrections), Paul et al. investigated the hydrogenolysis of DBT on the promoted S-edge of a CoMoS catalyst and found that the activation energy for the first S-C bond scission is about 1 eV: in this case, the H is transferred from a neighboring –SH group to the C_α atom of DBT[36]. More recently, the periodic DFT calculations of Saric et al. showed that the thiolate intermediates (including 2-phenyl-thiophenolate and methyl substituted 2-phenyl-

thiophenolate) are stabilized preferentially on coordinatively unsaturated sites (CUS) of a CoMoS catalyst (either corner or at the edge) with respect to brim sites[37]. In addition, by applying a simplified linear combination of atomic orbital scheme, activation energies for the first S-C bond scission on CUS were estimated at 1.2 eV, according to a hydrogenolysis mechanism. The same study shows that the activation energy is significantly higher on the brim S-edge site (~1.8 eV) which is partly due to the lower stability of the thiolate intermediate. Lastly, Ding et al. reported rather exhaustive DFT (with dispersion corrections) calculations of the hydrogenolysis mechanisms of DBT and 4,6-DMDBT on various edges of a large NiMoS cluster[38]. They reveal that on a mixed Ni-Mo site located on the M-edge, the C_α-S bond breaking during the hydrogenation involves a significant rotation of the phenyl group of DBT which is hindered in the case of 4,6-DMDBT. Hence, the activation energy increases from 1.40 eV for DBT to 1.74 eV for 4,6-DMDBT. Moreover, they reveal that their activation energies are greater on the Ni promoted S-edge (1.95 and 2.12 eV, respectively).

At this stage, none of the published theoretical studies have investigated if such DDS pathways can take place on the partially Co-promoted M-edge proposed. Numerous studies preferentially assumed that DBT desulfurization occurs exclusively on Co sites located on the S-edge. However, the partial location of Co on the M-edge has also been shown to be stable in HDS conditions by some of us[11, 39-42]. Thus, it is one goal of the present DFT work to explore if hydrogenolysis of DBT can take place on the partially Co-promoted edge and to determine the corresponding activation energies.

Moreover, it is important to address the alternative DDS pathway involving the hydrogenation of the C_α and C_β atoms of DBT followed by the β–elimination with S-C bond scission[24, 25]. To the best of our knowledge, none of the current theoretical studies has investigated the mechanism with a first hydrogenation in C_β position instead of C_α which may activate the elimination pathway as earlier proposed by Mijoin et al.[24]. This less straightforward pathway seems to be overlooked by many published studies without idenfying transition states (TS) and quantifying energy barriers. Thus, this will be the second challenge of this work to identify if the β–elimination pathway can take place on CoMoS sites.

At a molecular level, scanning tunneling microscopy (STM) combined with density functional theory (DFT) simulations have highlighted the various possible adsorption modes and energies of DBT derivatives on CoMoS supported on Au(111) surface [29-31]. These investigations reveal in particular how the underlying gold substrate may influence the spatial orientation of the DBT molecules adsorbed on the edge sites. DFT studies (including dispersion corrections) also showed that the adsorption energy and mode of 4,6-DMDBT on NiMoS depend closely on the nature of edge sites: in particular, 4,6-DMDBT is adsorbed perpendicularly with its S-atom located in a bridging position between two Ni sites of the S-edge, whereas it is absorbed in a nearly flat position on the Ni site of the promoted M-edge[32]. Since it is often referred that the HYD and DDS pathways might be controlled by the adsorption

mode (either flat or perpendicular respectively)[27, 33], distinct activities are expected for the two edges. A similar proposal has been made by means of DFT simulation (without dispersion corrections) of DBT adsorption on non-promoted MoS_2[34]. However, as the present work will illustrate it, the link between the adsorption mode of DBT and the HYD/DDS pathways is not straightforward. Regarding the mechanistic aspects, Weber et al. investigated by DFT (without dispersion corrections) the hydrogenolysis mechanism of DBT on the Ni promoted M-edge site of a single NiMoS cluster[35], and shows that the first C-S bond breaking involves an activation energy of 1.37 eV. Surprisingly, this event is reported to occur during the DBT adsorption step on Ni site through a simultaneous H transfer from the same Ni site to the C_α atom of DBT. The possible formation of 2-phenyl-thiophenolate and 2-phenyl-thiophenol is also invoked in this study. By means of periodic DFT (without dispersion corrections), Paul et al. investigated the hydrogenolysis of DBT on the promoted S-edge of a CoMoS catalyst and found that the activation energy for the first S-C bond scission is about 1 eV: in this case, the H is transferred from a neighboring –SH group to the C_α atom of DBT[36]. More recently, the periodic DFT calculations of Saric et al. showed that the thiolate intermediates (including 2-phenyl-thiophenolate and methyl substituted 2-phenyl-thiophenolate) are stabilized preferentially on coordinatively unsaturated sites (CUS) of a CoMoS catalyst (either corner or at the edge) with respect to brim sites[37]. In addition, by applying a simplified linear combination of atomic orbital scheme, activation energies for the first S-C bond scission on CUS were estimated at 1.2 eV, according to a hydrogenolysis mechanism. The same study shows that the activation energy is significantly higher on the brim S-edge site (~1.8 eV) which is partly due to the lower stability of the thiolate intermediate. Lastly, Ding et al. reported rather exhaustive DFT (with dispersion corrections) calculations of the hydrogenolysis mechanisms of DBT and 4,6-DMDBT on various edges of a large NiMoS cluster[38]. They reveal that on a mixed Ni-Mo site located on the M-edge, the C_α-S bond breaking during the hydrogenation involves a significant rotation of the phenyl group of DBT which is hindered in the case of 4,6-DMDBT. Hence, the activation energy increases from 1.40 eV for DBT to 1.74 eV for 4,6-DMDBT. Moreover, they reveal that their activation energies are greater on the Ni promoted S-edge (1.95 and 2.12 eV, respectively).

At this stage, none of the published theoretical studies have investigated if such DDS pathways can take place on the partially Co-promoted M-edge proposed. Numerous studies preferentially assumed that DBT desulfurization occurs exclusively on Co sites located on the S-edge. However, the partial location of Co on the M-edge has also been shown to be stable in HDS conditions by some of us[11, 39-42]. Thus, it is one goal of the present DFT work to explore if hydrogenolysis of DBT can take place on the partially Co-promoted edge and to determine the corresponding activation energies.

Moreover, it is important to address the alternative DDS pathway involving the hydrogenation of the C_α and C_β atoms of DBT followed by the β–elimination with S-C bond scission[24, 25]. To the best of our

knowledge, none of the current theoretical studies has investigated the mechanism with a first hydrogenation in C_β position instead of C_α which may activate the elimination pathway as earlier proposed by Mijoin et al.[24]. This less straightforward pathway seems to be overlooked by many published studies without idenfying transition states (TS) and quantifying energy barriers. Thus, this will be the second challenge of this work to identify if the β–elimination pathway can take place on CoMoS sites.

Appendix C - Computational methods

The total energies were calculated using the Density Functional Theory (DFT)[43, 44] calculations and were performed using the Vienna Ab Initio Simulation Program (VASP)[45, 46]. Within the generalized gradient approximation, the Perdew Burke and Ernzerhof (PBE) functional was used for the calculation of the exchange-correlation energies and the potentials[47]. The electron-ion interactions were described using the Projector Augmented Wave method (PAW)[48]. The density-dependent dispersion correction (dDsC) scheme was applied for including van der Waals interactions[49, 50]. In line with Ref. [32], dispersion corrections contribute strongly to adsorption energies of DBT by about 50%. We also noticed that the relative energy levels of intermediates involved in the reaction pathway are less impacted by values up to 0.1 eV (those of transition states being the least impacted, smaller than 0.01 eV).

The plane-wave cut-off expansion was set at 500 eV. Spin-polarization was included in order to take the magnetic properties of the M-edge induced by the presence of Co into account[51]. A Monkhorst-Pack mesh of 3x3x1 K-points was used for the 3D Brillouin zone integration.

In the same spirit as our previous DFT studies[39, 52], each edge was modeled by using five Mo layers, the top one being completed with the corresponding number of Co atoms represented in **Fig. 2** for the three edges stable in HDS conditions: the so-called M-edge and S-edge with Co atoms are substituting some of the Mo atoms on both edges. While the most stable S-edge is completely saturated by Co sites, the M-edge is partially promoted, presenting either Mo or Co sites: a configuration with …-Mo-Co-Mo-Co-… (called M-edge alternated) and a second one with …-Mo-Mo-Co-Co-… (called M-edge paired). Adsorption and reaction processes were performed on the top layer of the edges. While the bottom three layers were kept fixed in bulk positions during optimizations, the top two were relaxed.

The geometries were regarded as converged when the forces were smaller than 0.02 eV/Å. Transition states (TS) were determined using a combination of a path extrapolator[53] with the nudged elastic band (NEB), climbing image - NEB[54, 55], and dimer methods[56]. The status of the TS was confirmed by the presence of a single imaginary frequency associated to the corresponding reaction coordinate. In the specific case of the β–elimination mechanism (E2 type), which involves numerous bond breaking/formation events, we confirm the minimum energy path connecting the reactant, TS and product by undertaking an Intrinsic

Reaction Coordination (IRC) analysis [57, 58].

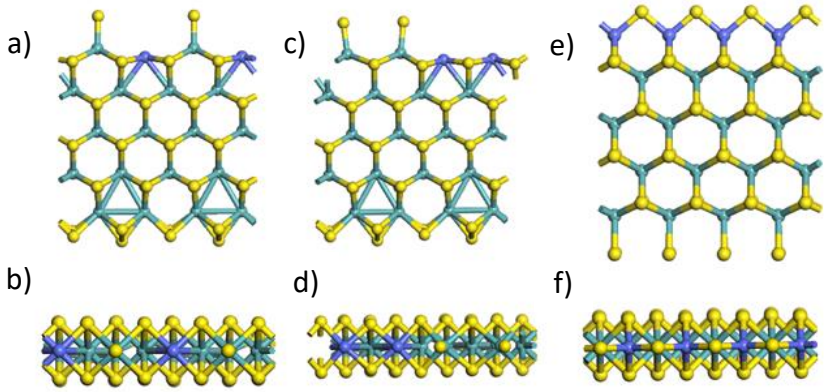

Fig. 2. Side and top views of the single slab stable in HDS conditions: M-edge with Co-Mo-Co-Mo site configuration (called "M-edge alternated" in the text) (a,b), with Co-Co-Mo-Mo site configuration (called "M-edge paired") (c,d) and of the reference S-edge with only cobalt sites (e,f). Color legend: blue balls: cobalt, green balls: molybdenum, yellow balls: sulfur.

All frequencies were calculated within the harmonic approximation. Some TS (respectively intermediates) exhibit two (respectively one) imaginary frequency with absolute values smaller than 30 cm^{-1}. The spurious imaginary frequencies (when they exist) are assumed to correspond to residual translational or rotational modes and was removed together with the 5 smaller frequencies in order to evaluate the free energies of adsorbed species considered as immobile adsorbate[59]. Alternative approaches such as replacing the spurious imaginary frequency by a normal mode of positive value[59] show minor impact on the reported thermodynamic trends. The Gibbs free energy, G, is expressed as a function of the enthalpy H and entropy S of the system:

$$G = H - TS \quad (1)$$

$$H = U_{elec} + U_{vib} + U_{trans} + U_{rot} + pV_m \quad (2)$$

$$S = S_{elec} + S_{vib} + S_{trans} + S_{rot} \quad (3)$$

where $U(S)_{elec}$, $U(S)_{vib}$, $U(S)_{trans}$, $U(S)_{rot}$ and V_m are respectively the electronic energy (entropy), vibrational energy (entropy) including "zero point energy", translational energy (entropy), rotational energy (entropy) and the molar volume. The molar volume term pV_m was considered for an ideal gas system and for condensed phase systems, H was assimilated to U. The electronic energy was obtained by DFT calculations, while other energy terms were calculated from statistical thermodynamics based on the vibrational frequencies previously calculated.

Appendix D - Results

D1. Adsorption configurations of DBT on 4 relevant edge sites

The most stable adsorption modes of DBT in presence of co-adsorbed H_2 on each edge is represented in **Fig. 3**, along with their

corresponding adsorption energies (including H_2 adsorption) according to the following equation:

$$G_{ads} = G(edge + H_2 + DBT) - G(edge) - G(H_2) - G(DBT) \quad (4)$$

where $G(slab + H_2 + DBT)$, $G(edge)$, $G(H_2)$ and $G(DBT)$ respectively corresponds to the free energy of the given edge with adsorbed H_2 and DBT, of the corresponding bare edge, the H_2 and DBT molecules. The bare edges are given as references in **Fig. 1**. For the S-edge, the adsorption energies value include the energy required to create the CUS: either through S-removal (**Fig. 3c**) or through S-diffusion (**Fig. 3d**), as discussed later.

Previous studies having shown that the H_2 dissociation on the three edges was weakly activated and endothermic[60, 61]. Considering DBT and H_2 adsorption, the resulting overall adsorption energies become exothermic due to the negative adsorption energy of DBT whatever the edge. However, when including entropic contributions, the free energies of adsorption become endergonic due to the significant loss of rotational and translational entropies of the DBT and H_2 molecules (**Fig. 3**) as already been reported in previous theoretical studies for similar sulfur or nitrogen containing organic molecules[32, 37].

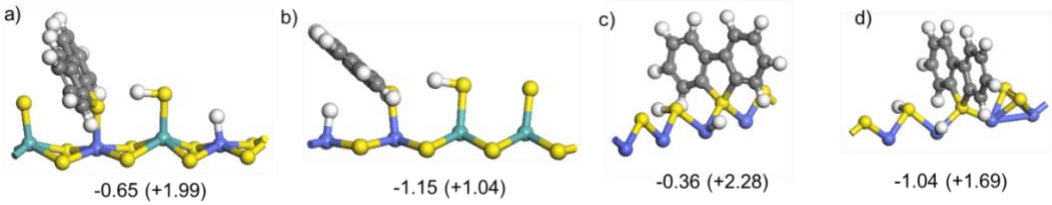

Fig. 3. DBT+H_2 most stable co-adsorption on M-edge alternated (a), M-edge paired (b), S-edge with S-removal (c), and S-edge with S-diffusion (d). The overall adsorption energies and free energies (in parenthesis) of DBT+H_2 are given in eV. These energies include the S-removal and S-diffusion energies for the S-edge. Color legend: blue balls: cobalt, green balls: molybdenum, yellow balls: sulfur, dark grey balls: carbon, light grey : hydrogen.

On the M-edge alternated, the DBT adsorbs in a slightly tilted η_1-mode through its S atom on top of the Co-promoter site located between one edge S and one –SH species, while the H_2 dissociates and adsorbs on the neighboring sulfur atom and the remaining Co-promoter (**Fig. 3a**) The DBT is slightly tilted toward the non H bearing surface S atom, while the –SH group is directly pointing towards the DBT molecule which features the formation of a hydrogen bond with the aromatic rings. It must be noticed that the symmetric configuration where DBT molecule is tilted toward the –SH species is not favorable because of the too close proximity of the H atom. As for the M-edge alternated, on the M-edge paired, the H_2 molecule is dissociated on one surface –S atom and one Co site, leading to Mo-SH and Co-H species (**Fig. 3b**). On the M-edge paired, the DBT molecule is even more tilted, and becomes in close interaction with the Co-H group with the formation of a second H-bond. This H-bond explains why the adsorption energy is more exothermic (less endergonic) on the M-edge paired than on the M-edge alternated.

On the S-edge, we compared the adsorption and reaction of DBT on two different models. The first one includes one S-vacancy (CUS) created by S-removal upon H_2/H_2S exchange (**Fig. 3c** and **Fig. 4a**), often reported in the literature[36, 37]. The second one assumes that CUS is created by edge diffusion of one S-atom from one bridging position to the next one inducing the formation of a S_2 dimer (S-S bond length ~2.03 Å) in the vicinity of the S-vacancy (**Fig. 3d** and **Fig. 4b**). The energy cost to create the S-vacancy by S-removal upon H_2/H_2S exchange is +1.66 eV (ΔG=+1.85 eV), whereas the diffusion of one S atom is less energy demanding +0.97 eV (ΔG=+1.03 eV). The corresponding activation energy for the S-diffusion is +1.61 eV (ΔG‡=+1.48 eV) which is also more favorable than the thermodynamic balance for S-removal. This edge state with the presence of a CUS should be considered a transient metastable state which comes back to the thermodynamic stable state at the end of the catalytic cycle. For this, the back diffusion of S-atom in the bridging position is expected to occur with a rather modest activation energy of +0.64 eV (ΔG‡=+0.45 eV). Hence, this back and forth diffusion of S-atom can be considered as a plausible scenario to generate transient CUS at edge.

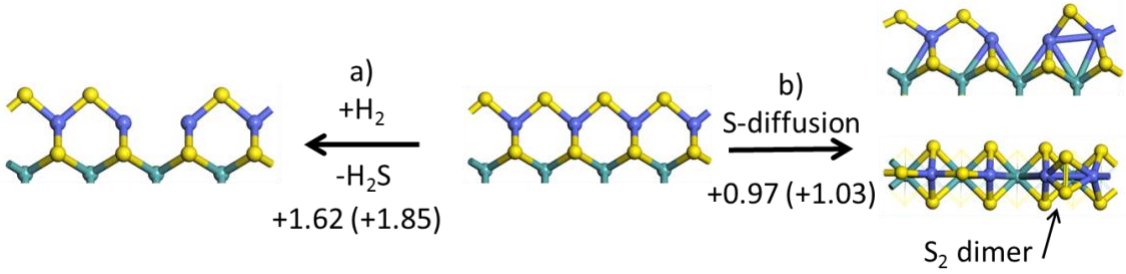

Fig. 4. Two possible processes creating two possible transient metastable states with one S-vacancy (CUS) from the most stable S-edge model: a) sulfur removal by H_2/H_2S exchange, b) sulfur edge-diffusion forming one S_2 dimer neighboring the vacancy. The reaction energies at 0K and free energies (in parenthesis) are given in eV.

For both S-edge models, the most favorable adsorption configuration of DBT is found in a bridging position between two Co atoms. DBT remains perpendicularly oriented to the edge and no close H-bond is formed. The DBT adsorption on the second S-edge model can be considered as a collaborative process: the DBT molecule approaching the surface, pushes one edge S-atom toward another neighboring S, creating a vacancy and the S_2 dimer. The H_2 molecule is dissociatively adsorbed on one surface – S atom and one Co site. If one include the energy cost for S-diffusion, the overall energy variation for the S-diffusion and adsorption of DBT and H_2 is (ΔE=-1.04 eV, ΔG=+1.69 eV) which is more favorable than on the S-edge after S-removal (ΔE=-0.36 eV, ΔG=+2.28 eV).

These four starting configurations will serve for investigating the DBT hydrodesulfurization pathways in the forthcoming sections. In the main text, we will report and discuss for sake of clarity the Gibbs free energy profiles obtained on the alternated M-edge and of the S-edge after S-diffusion only. The results for the

two other cases are reported in supplementary information where all energy profiles are given and discussed.

D2. Direct hydrogenolysis of DBT on the alternated M-edge

Following the DBT+H_2 adsorption described previously, the first step is the monohydrogenation of C_α by the neighbouring –SH species which exhibits an activation free energy of +1.16 eV. The corresponding TS A(1-2)‡ involves the H atom significantly elongated from the –SH group and the C_α atom that bends outward the cycle closer to the H (**Fig. 5)**. A(1-2)‡ can be characterized as a late-TS, resembling to the α-monohydrogenated DBT intermediate A(2), with an activation energy closer to the free energy variation of this elementary step (+1.02 eV).

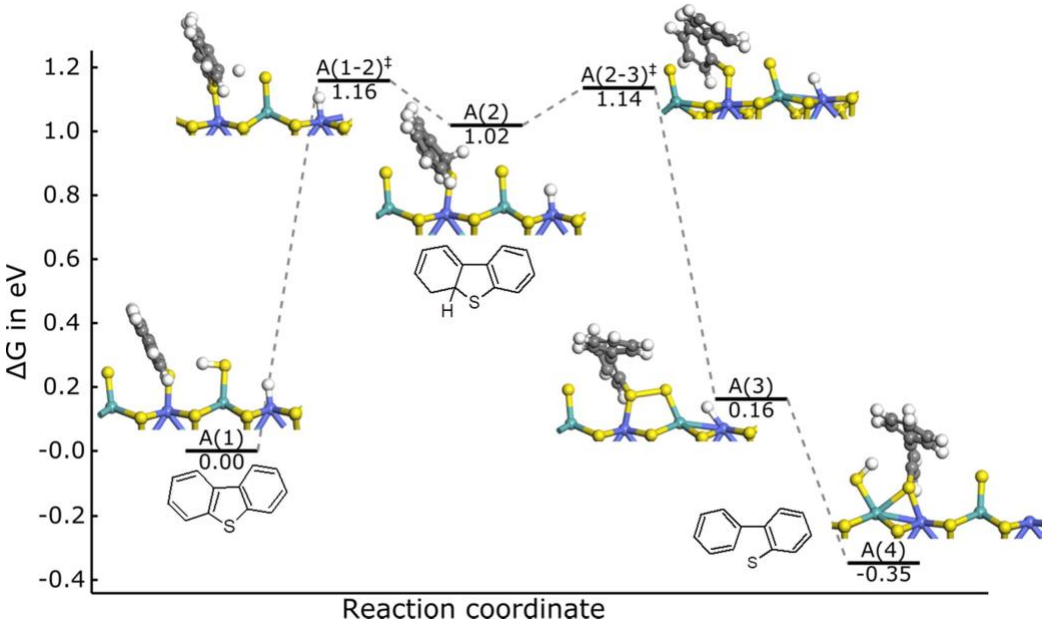

Fig.5. Free energy profile of the hydrogenolysis of the first C–S bond scission of DBT to biphenyl (BP) on M-edge alternated leading to the 2-phenyl-thiophenolate intermediate.

Once the C_α-H bond is formed, a weakly activated rotation of the phenyl group (TS A(2-3)‡ at +0.12 eV) leads to the first C-S bond breaking and the formation a 2-phenyl-thiophenolate intermediate A(3) stabilized by a S-S bond (2.27Å) formed between the S atom of the thiophenolate intermediate and the neighboring Mo-S species. The overall free energy variation for the C-S bond scission from adsorbed DBT+H_2 to thiophenolate is slightly endergonic (+0.16 eV). It becomes exergonic (-0.35 eV) after diffusion of H from Co site to Mo-S group and thiophenolate migration in a bridging Co-Mo position (A(4)).

According to the proposal made in Ref.[37], the stabilization level of 2-phenyl-thiophenolate might be a descriptor of the hydrogenolysis mechanism. However, it

must be noticed that the two TS, A(1-2)‡ and A(2-3)‡, as well as the α-monohydrogenated DBT intermediate, A(2), are located at significantly higher energies (~ +1 eV) than thiophenolate. This may be an indication that the thiophenolate stabilization is one necessary condition but probably not the sole descriptor for featuring if hydrogenolysis is kinetically possible or not. Analyzing the calculated reaction and activation energies for DBT and alkyl-DBT HDS on NiMoS sites reported by Ding et al., showed that it seems difficult identifying a direct correlation between the thiophenolate energy and the activation energy of hydrogenolysis for the various edge and corner sites [38]. Actually, the energy level of the TS is linked to various effects: the level of instability of α-monohydrogenated DBT intermediate, the steric hindrance of the rotational movement of the phenyl group during the C-S bond scission and the optimal position of the –SH groups involved in the H-transfer (see also further discussion). Hence, these three kinetic effects cannot be deciphered by a single descriptor based on the stability of the 2-phenyl-thiophenolate intermediate. In addition, depending on the DFT study, the existence of the α-monohydrogenated DBT intermediate as an intermediate is not always reported[36, 38] which is explained by its relative weak stability with respect to TS A(1-2)‡ and A(2-3)‡. The potential energy surface in the vicinity of TS A(1-2)‡, A(2) and A(2-3)‡ will thus intimately depend on the local nature of edge site (see also later for the S-edge).

From 2-phenyl-thiophenolate A(4), two possible pathways can be considered. The first one involves the formation of 2-phenyl-thiophenol intermediate leading to the second C-S bond scission, as described in details in **Fig. S2**. The second one involves a direct C-S bond scission of 2-phenyl-thiophenolate. For that purpose, a second H_2 molecule adsorption which leads to the thiophenolate co-adsorbed with two neighboring Mo-SH groups (**Fig. 6**). From this configuration, the second C_α hydrogenation by one SH can proceed in a similar way as the first one and the TS A(5-6)‡ exhibits a similar free activation energy of +1.35 eV. This second C-S bond breaking step leads to a physisorbed biphenyl (BP). Similar activation energies are found for the thiophenol pathway (**Fig. S2**) and will be discussed later for the second C-S scission on the S-edge (section 3.4). These values remain compatible with previously calculated activation energies of hydrogenolysis of alkane thiols on MoS_2, CoMoS and NiMoS edges [62-64]. The fact that the activation energy of the second C_α-S bond scission is similar or even slightly higher than the first one seems to be counter-intuitive since the conjugaison of S-lone pair electrons with those of the aromatic rings is expected to limit the first C-S bond cleavage. However, our TS analysis reveals that another effect may influence the relative activation energies of the two C_α-S bond scission: the optimal position of the Mo-SH group to attack the C_α atom during H-transfer. As illustrated in **Fig. S7**, the imaginary frequency of the reaction mode corresponding to the H-transfer (leading either to hydrogenolysis or to hydrogenation as detailed latter) is mainly correlated to the SH bond length. This trend indicates that the position and accessibility of –SH group is a key parameter for the activation step. In the case of the second bond C-S cleavage, the reorientation of the phenyl ring in 2-phenylthiophenol which becomes parallel to the edge hinders the optimal position of the second C_α atom with respect to the neighboring Mo-SH group. Hence, the C-S

bond breaking of 2-phenylthiophenol might not be as easy as usually observed for model thiols or thiophenol molecules.

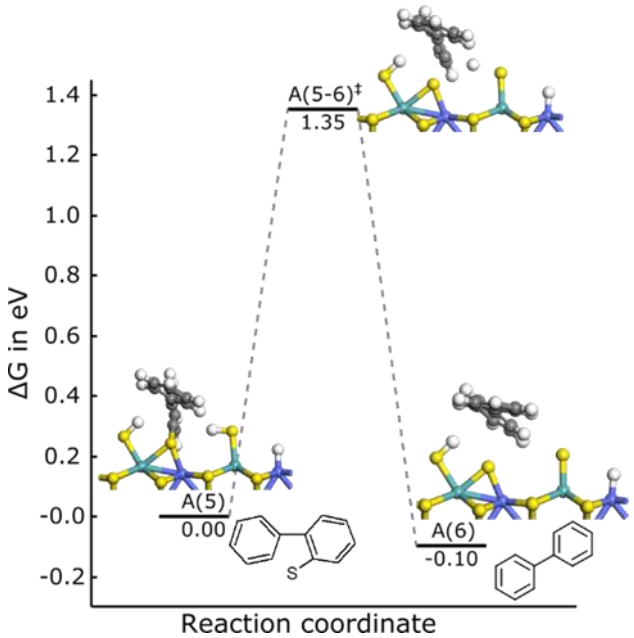

Fig. 6. Free energy profile of the second C-S bond scission on the M-edge alternated involving the 2-phenyl-thiophenolate and leading to biphenyl product.

After the BP molecule is desorbed, we reasonably assume that the remaining H atom reaches the S-H group, to form H_2S and desorb to recover the initial M-edge thermodynamically stable in typical HDS conditions (**Fig. S1**)[39]. The overall free energy variation for the BP+H_2S desorption is about +0.75 eV which is mainly due to the BP desorption energy involving mainly dispersion and H-bond interactions of BP on the edge.

According to the slightly different levels of theory of previous studies (cluster vs periodic systems, with or without dispersion corrections), the activation energies calculated for the two C_α-S bond scissions within the present work are either as competitive or even more competitive than those reported previously for different edge sites such as M-edge and S-edge of NiMoS[35, 38] and S-edge of CoMoS[36, 37]. This implies that the partially Co-promoted edge, with alternated Co-Mo-Co-Mo sites, is a relevant active edge for the hydrogenolysis pathway of DBT compounds.

Considering now the promoted M-edge with paired cobalt atoms, we start from the most stable configuration of **Fig. 3b** for DBT+H_2 adsorbed. However, on this edge configuration, we did not identify any relevant TS leading to the α monohydrogenation from the –SH group which may be explained by the too far position of the hydrogenating –SH species from the aromatic rings of DBT. Indeed, **Figs. 3b** and **3a** reveal that the tilting angles of DBT are not the same for

the promoted M-edge paired and unpaired which impact the accessibility of –SH. By contrast, the Co-H group which is located in closer interaction with the aromatic will be involved in these hydrogenation steps. We tried to hydrogenate in α position from the Co-H but the monohydrogenated intermediate is not stable and the H atom relaxes back to the Co site, while the S-C bond cleavage was not found as possible due to steric hindrance during the rotational movement of the phenyl group. The alternative possibility of the hydrogenation in β position will be discussed in the forthcoming sections.

D3. Dihydrogenation pathways leading to dihydrogenated DBT (DHDBT)

Case of the M-edge sites

As explained in introduction, we investigate here the alternative DDS pathway as proposed in the literature[24, 25] which consists in the preliminary formation of the DHDBT intermediate with C_α and C_β hydrogenation occurring on the same phenyl ring. If we restart our investigation right after the first monohydrogenation C_α-H step, the second monohydrogenation of the molecule may occur by transferring the second H atom on C_β However, our attempts to achieve this second hydrogen transfer either failed or involved energy costs greater than the modest activation energy (+0.12 eV) found for the first C-S bond breaking during the rotation of the phenyl ring of α-monohydrogenated DBT (as described before). Thus, once α-monohydrogenated DBT is formed by C_α hydrogenation, its further C_β hydrogenation seems to be unfavored with respect to the easier C_α-S bond breaking. To some extent, this result may also explain why many theoretical studies did not explore this pathway so far and preferentially follows the hydrogenolysis step. Alternatively, the hydrogenation pathway must be initiated by the hydrogenation of DBT in the C_β position as initially suggested by Mijoin et al.[24]. Starting from DBT+H_2 adsorption, the free energy profile corresponding to the two C_β followed by C_α monohydrogenation steps is reported in **Fig. 7**.

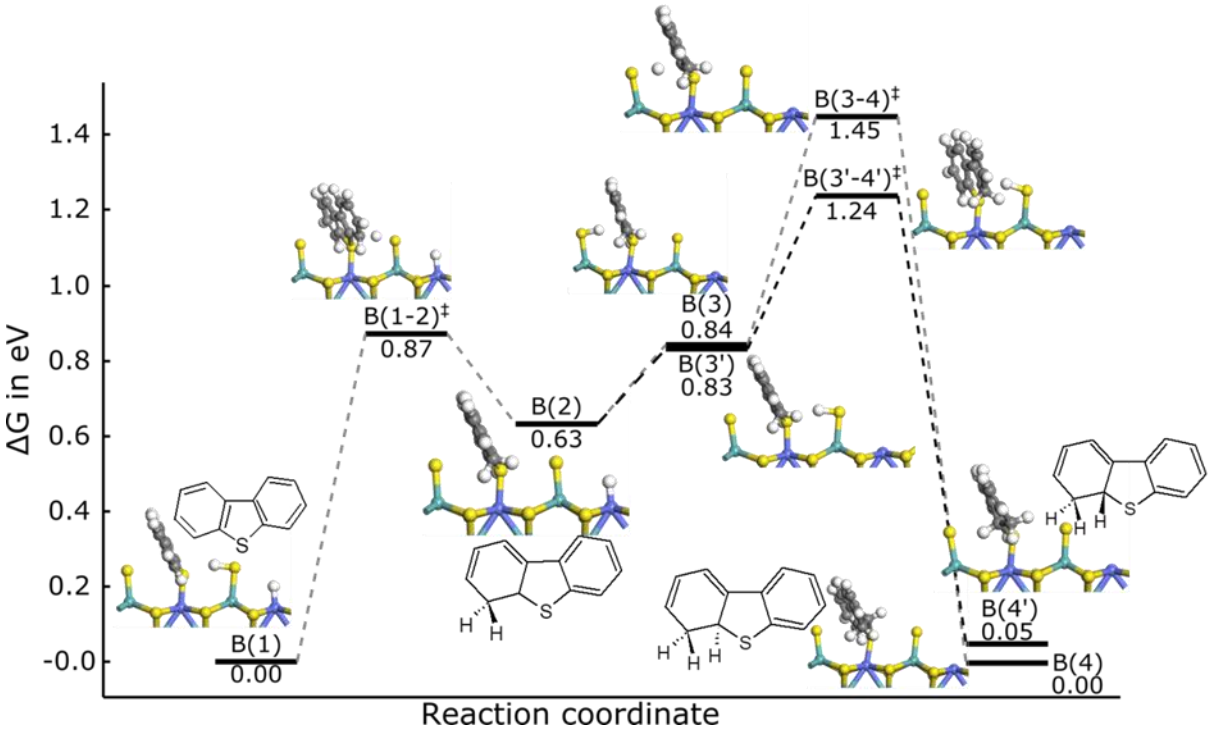

Fig. 7. Free energy profile of the Cβ followed by Cα hydrogenation steps of DBT leading to the β,α-dihydrogenated DHDBT intermediate. B(3-4)‡ corresponds to anti-pathway, B(3'-4')‡ to syn-pathway.

The activation free energy of the first monohydrogenation in C_β (through H transfer coming from a -SH group) is rather modest (+0.87 eV for B(1-2)‡) and is significantly lower than the one found for the previous hydrogenation of C_α. This value is also lower than any previous activation energies reported in the literature for the hydrogenolysis pathway so far; often greater than 1.3 eV[35, 37, 38], except results in [36] where dispersion corrections were not considered. The β-monohydrogenated DBT intermediate B(2) is thermodynamically more stable than α-monohydrogenated DBT A(2) by about -0.39 eV which is coherent with the kinetic trend, considering the late-TS character of both B(1-2)‡. The preferential hydrogenation in β than in α can be explained by the destabilization of α-hydrogenated intermediate or related TS, induced by the loss of conjugation involving the S lone pair electrons.

After this first monohydrogenation, the remaining H atom can diffuse to two possible Mo-S sites from which the second monohydrogenation in α position may occur through anti-B(3-4)‡ or syn- B(3'-4')‡ transfer and lead to two similar DHDBT conformers B(4) or B(4'), respectively in **Fig. 7**. In both cases, the reaction energies are exergonic (of -0.78 and -0.84 eV respectively), while both activation energies are pretty mild (+0.62 eV and +0.41 eV). Thus, the attack in α is stereospecific due to the different relative position of the tilted monohydrogenated-DBT and Mo-SH group. As observed for the hydrogenolysis mechanism, the frequency of the reaction mode is also strongly governed by the –SH stretching depending on the relative position of the –SH group and targeted carbons, C_α or C_β (**Fig. S7**).

Considering the first two hydrogenation steps, and applying an energetic span concept[65], the overall activation free energy corresponding to the formation of the dihydrogenated DHDBT intermediate is about +1.24 eV, which makes this pathway as competitive as other hydrogenation steps simulated either in the present study or in previously published works[35-38].

Although the existence of the DHDBT intermediate has been questioned in the experimental literature[21, 66], the present results reveal that it cannot be ruled out from a thermodynamic and kinetic point of view. From a thermodynamic point of view, the free energy level of DHDBT is also acceptable since it is only +0.49 eV higher than the iso-stoichiometric 2-phenyl-thiophenol intermediate which may be formed during hydrogenolysis.

Considering the promoted M-edge with paired cobalt atoms, the mechanism and energy profile reported in **Fig. S4** show that the both hydrogenation steps involve preferentially H transfer from Co-H site (and not from Mo-SH) with a moderate overall activation energy (+1.29 eV). Since it was not possible to identify a hydrogenolysis pathway on this type of edge (as mentionned in the previous section), we think that the dihydrogenation pathways is suspected to occur with a non negligible probability, knowing that the M-edge with such paired Co sites may co-exist according to previous DFT [39] and experimental studies [67].

Case of the S-edge sites

Since the dihydrogenation steps occur in a similar way on both types of S-edge sites illustrated in **Figs. 3c** and **3d**, we focus in the main text on the one corresponding to the S-vacancy obtained by S-diffusion (**Fig. 4b**) which is thermodynamically and kinetically favored with respect to the one where S-vacancy is obtained by S-removal (**Fig. 4a**).

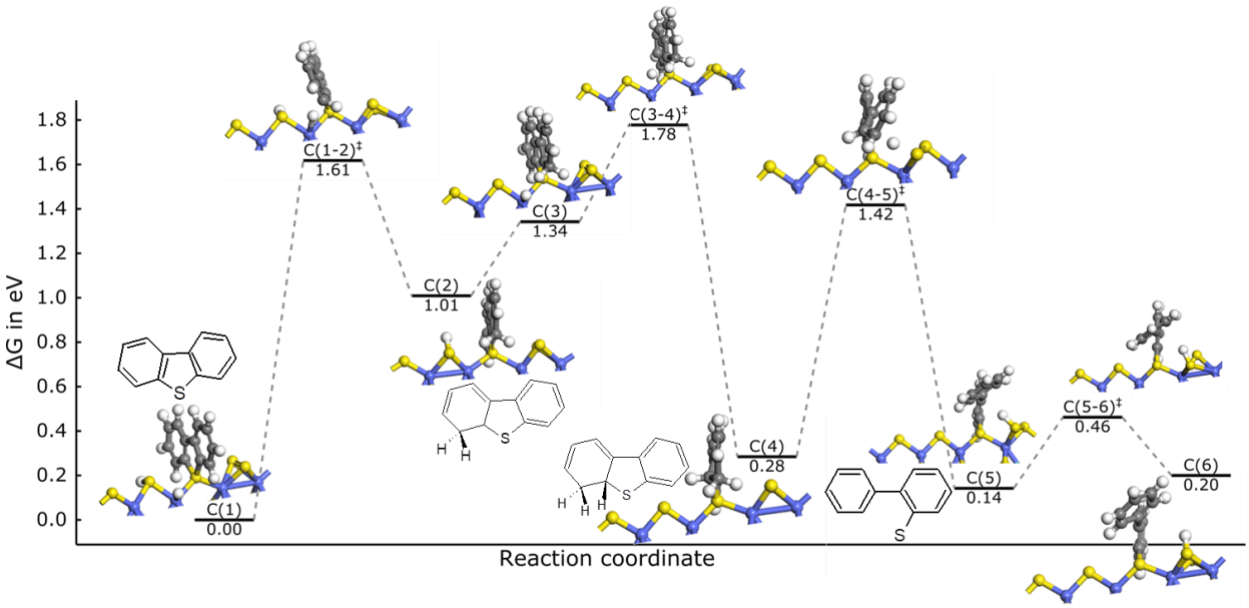

Fig. 8. Free energy profile of the DDS of DBT through β–dehydrogenation mechanism on the S-edge with preliminary S-diffusion leading to the formation of one S-vacancy and one neighboring S_2 dimer.

From the H_2 molecule dissociated on one S-atom and on one Co-atom, the Co-H species preferentially hydrogenates the two C atoms in α and β positions because of the unfavored orientation and distances of H from –SH group and the two C atoms : ~3.5 Å from the S-H to the α and β positions, compared to ~3 Å from the Co-H to the α and β positions. So, the first C_α monohydrogenation occurs through the Co-H species with an activation free energy of +1.61 eV (C(1-2)‡) and the second H also transferred through Co-H with an overall activation free energy +0.77 eV (including H diffusion step from –SH to Co-H and then C(3-4)‡). If we apply for the dihydrogenation steps the energetic span concept, we identify an overall activation free energy of +1.78 eV, which is higher than all activation free energies found on the M-edge. Since, a similar trend is reported for the S-edge site with S-vacancy after S-removal (**Fig. S6**), this indicates that the S-edge is less active for hydrogenation steps than M-edge.

D4. S-C bond scission of DHDBT according to β-elimination (E_2) mechanism

Interestingly, on the promoted S-edge with S-vacancy and neighboring S_2 dimer, the β-elimination with simultaneous C-S bond breaking can proceed with a reasonable activation free energy of +1.14 eV for TS C(4-5)‡ in **Fig. 8**. This mechanism involves three chemical events as described in the insets of **Fig. 9**: transfer of H in β position to the edge S atom, C-S bond scission, phenyl ring rotation and weakening of the neighboring S_2 dimer.

In order to confirm the validity of this complex mechanism and more particularly the connection between the reactant C(4), TS C(4-5)‡, and product C(4), we undertook a dedicated IRC analysis. This analysis clearly shows the key role of the S_2 dimer which captures the H_β-atom transferred from the C_β atom of DHDBT C(4) with the reactive mode frequency of 925 cm^{-1}. Interestingly, this mode also fits the correlation between frequency and SH bond length previously discussed for the hydrogenation steps (**Fig. S7**). In the starting conformation of DHDBT, the H_β involved in the transfer is located in anti-position to H_α which is the most favorable position to reach one S of the dimer.

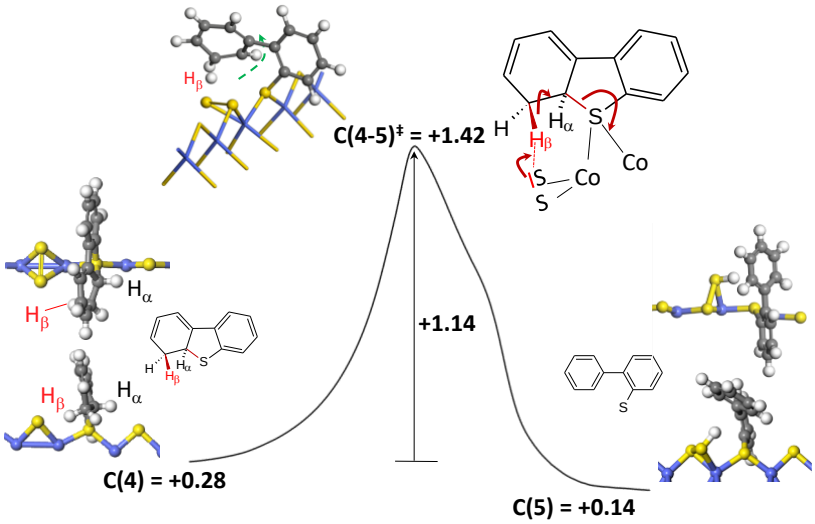

Fig. 9. Intrinsic Reaction Coordinate (IRC) path connecting reactant, TS and product of the β–elimination (E2) mechanism with S-C bond scission involving the S_2 dimer of the S-edge. The black line illustrates the energy evolution along the minimum energy path crossing the saddle point C(4-5)‡. The H_β atom involved in the transfer is written in red, while the H_α is written in black. The broken S-C bond is drawn in red. The green dashed arrow highlights the rotational movement of the phenyl group. The red arrows represent the formal electronic transfer involved. All energies are in eV.

At TS C(4-5)‡ the rotation of the phenyl group occurs simultaneously with the C_α-S bond scission, which allows the H_α and the second H_β atoms to move towards the plane of the phenyl group. In this case, there is no steric nor geometrical constraints for this movement. In the product, the S_2 dimer is not fully dissociated and an intermediate C(4) SSH species is formed. Hence, as earlier proposed by Bataille et al.[25], this mechanism is a true elimination of E2 type: the protonic H_β atom is captured by the S anionic base of the S_2 dimer, while the anionic S atom of DHDBT acts formally as the nucleofuge species stabilized by the Co cationic center and induced the C_α-S bond scission. The apparent leaving group is the phenyl which rotates away from the S atom of DHDBT. The reader may also visualize the complete IRC path on the movie provided in supplementary materials.

An important corollary related to the nature of H_β atom involved in the elimination mechanism must be added: this leaving H_β atom is located in anti-position of the two H_β and H_α atoms transferred during the dihydrogenation step presented before. Since the H_β added during hydrogenation and the leaving one during elimination are not the same, this implies that for 4,6-alkyl substituted DBT compounds, the H_β position involved in elimination is occupied by an alkyl group. Hence, the DDS pathway will be hampered since the elimination mechanism proposed here becomes impossible. This explanation was also one originally suggested by Bataille et al. to justify the lower reactivity of 4,6-DMDBT.[25]

Interestingly, the role of S_2 dimer in the reactivity of unsupported MoS_2 phase has been previously discussed in the experimental work of Afanasiev.[68] Moreover, scanning tunneling microscopy

(STM) combined with DFT calculations have shown that S_2 dimers exist in some sulfiding conditions on the Mo-edge of MoS_2.[69, 70] We thus propose here that S_2 dimer could be transiently formed through the back and forth edge diffusion of S-atom as described in section 3.1 in order to promote the reactivity of CoMoS edges. On the fully Ni promoted S-edge, Ding et al.[38] simulated the hydrogenolysis mechanism of DBT involving such S_2 dimers, stable in HDS conditions.[11, 39] Once H_2 molecule adsorbs dissociatively, the S_2 dimer dissociates into two –SH groups, one of which H is transferred to DBT[38].

To achieve a more consistent comparison for the CoMoS case, we simulate this similar hydrogenolysis mechanism of the first C-S cleavage involving H-transfer from one of the two neighboring –SH groups on the Co promoted S-edge (D(1) in **Fig. S8**). The free energy of activation for D(1-2)‡ is found at +1.83 eV which is close to value reported for NiMoS [38]. D(1-2)‡ leads to thiophenolate D(2) without formation of mono-hydrogenated DBT intermediate (as observed on M-edge). In addition, the H-transfer to C_α from Co-H species (as previously explored for the C_β hydrogenation) also reveals that the direct C-S bond cleavage leads to thiophenolate with a similar free energy of activation of +1.85 eV (TS E(1-2)‡ in **Fig. S8**). This analysis confirms that the β–elimination mechanism is kinetically possible once the α,β–DHDBT is formed.

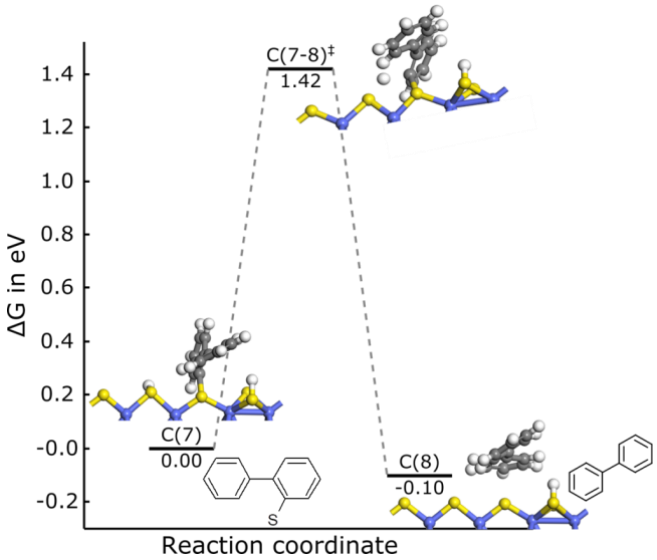

Fig. 10. Free energy profile of the second C-S bond scission on the S-edge with preliminary S-diffusion leading to the formation of one S-vacancy and one neighboring S_2 dimer.

Finally, the second C-S bond scission occurs through a direct hydrogenolysis mechanism involving an –SH species with an activation free energy of +1.42 eV (C(7-8)‡ in **Fig. 10**), and produces biphenyl (BP). This value is very similar to the one obtained on the M-edge. Again, the frequency of the reaction mode is closely related to the –SH bond stretching (**Fig. S7**). Contrasting with the M-edge, the

activation energy of the second C-S bond scission is now smaller than the first C-S bond scission (either through hydrogenolysis or through a dihydrogenation-elimination mechanism) which is in line with the chemical intuition. Since the activation free energies of the second C-S bond scission are similar on M-edge and S-edge, this trend results from the different activation free energies of the first C-S bond scission on S-edge and M-edge which may have significant implications on the design of the CoMoS active phase (as discussed in the next section).

Appendix E - Conclusions and perspectives

By means of DFT calculations including dispersion corrections, we investigated the HDS mechanisms of DBT and determined the corresponding free energy profiles considering four relevant adsorption configurations of DBT on 4 relevant types of CoMoS active sites:

- M-edge with alternated Co-Mo-Co-Mo sites exhibiting Co sites and neighboring Mo-S sites
- M-edge with paired Co-Co-Mo-Mo sites exhibiting Co sites and neighboring Co and Mo-S sites
- S-edge with one S-removal exhibiting one S-vacancy on Co-site
- S-edge with S-diffusion leading to S-vacancy on Co-site and S_2 dimer

Depending on the nature of edge, the hydrogenation steps involve either the Mo–S and Mo–SH species, or the Co-H species adsorbed in close vicinity of the DBT adsorption Co site. A synthetic view of the most relevant free energy profiles is illustrated in **Fig. 11**.

On the M-edge with alternated Co-Mo-Co-Mo sites, we identified two competing mechanisms for the direct hydrogenolysis of the C-S bonds of DBT involving either the 2-phenyl-thiophenolate or the 2-phenyl-thiophenol intermediate. Both mechanisms are activated by the formation of the α-monohydrogenated intermediate through Mo-SH species. In the case of 2-phenyl-thiophenolate, the free energy of activation is +1.16 eV. Once the α-monohydrogenated intermediate is formed, the S-C bond scission immediately follows with a low activation energy, avoiding the formation of the α,β–dihydrogenated DHDBT intermediate.

The α,β–DHDBT dehydrogenated intermediate is preferentially formed when the first monohydrogenation occurs on the Cβ atom of DBT followed by the second monohydrogenation on the Cα atom (through Mo-SH). This result is consistent with the earlier proposal by Mijoin et al.[24]. In this case, it is important to notice that the DHDBT formation involves a competitive activation free energies (+1.24 eV) revealing that this pathway cannot be excluded with respect to the hydrogenolysis mechanism on the same edge site.

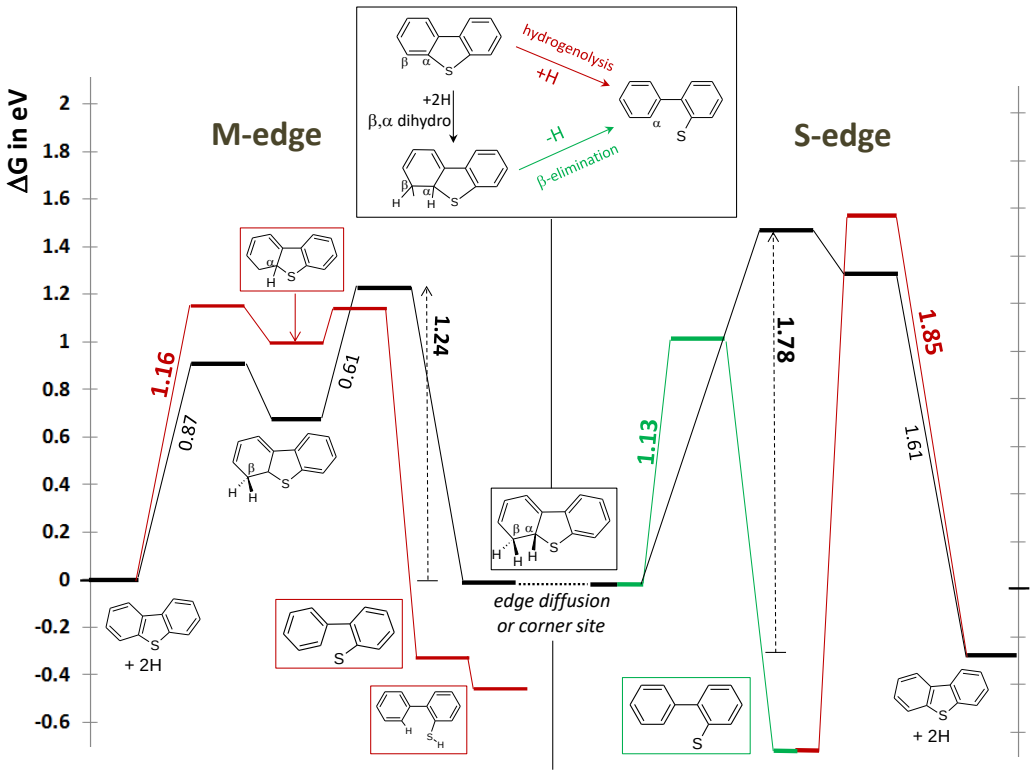

Fig. 11. Synthetic free energy profiles for the first C-S bond scission involving the hydrogenolysis pathway and β,α-dihydrogenation steps on the partially Co-promoted M-edge (alternated), followed by β–elimination on the Co-promoted S-edge (assuming edge diffusion or corner site). Note: the energy level of the S-edge is corrected by the energy required for S-diffusion to be consistent with the energy level of M-edge. Hydrogenolysis.

On the M-edge with paired Co-Co-Mo-Mo sites, we identified a unique mechanism where the first monohydrogenation occurs on the C_β atom of DBT and the second one leads to the α,β–DHDBT intermediate. The activation energies are slightly higher than those obtained on the M-edge with alternated Co-Mo-Co-Mo sites, which may be explained by the fact that the hydrogenating site is a Co-H species instead of a Mo-SH.

For the two S-edge models considered here, the most favorable pathway involves the formation of the α,β–DHDBT intermediate through the preliminary hydrogenation of the C_β atom of DBT. The overall activation energies are higher than those found on the M-edge (+1.78 eV for the S-edge involving one S-vacancy site and one S_2 dimer) which indicates that the hydrogenation pathway is kinetically less favored on the S-edge than on the M-edge. The hydrogenolysis pathway is slightly less favored with an activation energy of +1.85 eV which is significantly higher than on the M-edge. Hence, the partially Co-promoted M-edge is very active for DBT hydrogenolysis and dihydrogenation since their activation energies are competing with previous results reported so far in the literature [35-38].

Interestingly, we showed the possible existence of β–elimination mechanism involving α,β–DHDBT with simultaneous S-

C scission, corresponding to elimination of E2 type as earlier proposed by Bataille et al.[25]. The corresponding activation free energy of +1.13 eV reveals that this mechanism is strongly competing with the hydrogenolysis pathway calculated on the M-edge sites (present work) or on other sites reported in the literature[35, 37, 38]. For that, the transient local architecture of the active sites must combine one S-vacancy (CUS) together with one neighboring S_2 dimer which is directly involved as active center for the β–⍰ elimination. This architecture results from the back and forth diffusion process of S-atom on the edge which involves free energy barriers compatible with the whole HDS mechanism. The back and forth S-diffusion is also more favorable than the S-removal process. From an experimental point of view, we hope that future progress of operando spectroscopies will help to identify the presence of such transient S_2 species during HDS and their role on the β-elimination pathway.

At this stage, it was not possible to identify a TS for the β–elimination mechanism on the M-edge. Due to the rather complex intrinsic nature of the TS involving several intricated bond cleavage and formation as observed on the S-edge, progress on theoretical approach based on biased ab initio molecular dynamics will help to solve this open question.[71] In the present state, we propose that a possible optimal scenario for the hydrodesulfurization of DBT should actually combine both edges as illustrated in **Fig. 11**. The M-edge initiates the formation of the α,β–DHDBT intermediate at moderate activation energy. Then, DHDBT should diffuse from the M-edge to the S-edge. Although more investigation is required in the future on this event, diffusion seems possible considering the very close energy levels of DHDBT on both edges. Then, β–elimination mechanism with C-S bond scission occurs on the S-edge. Since previous studies [10, 37, 38, 70] suggested the specific role of corner sites, a DHDBT molecule formed on such a corner site could also benefit from a synergy effect between the close vicinity of the two edges. However, such a scenario requires specific design of the active phase where partial promotion of the M-edge and full promotion of the S-edge are simultaneously present on the CoMoS nano-crystallites. Standard CoMoS catalysts may not provide such an optimal configuration which requires to carefully tune CoMoS morphology, Co/Mo ratio and edge distribution of Co atom during the synthesis or activation steps, as proposed for other HDS reaction.[9]

Finally, during the β–elimination mechanism identified here, the leaving H_β atom is distinct from the H_β atom added at hydrogenation steps. This may explain for one part, the strong decrease of the DDS pathway of 4,6-alkyl substituted DBT compounds where only one H_β atom is available. In addition, we suggest to investigate the impact of akyl substituents on the rotational movement of the phenyl-group at transition states and on the corresponding activation energies identified in the present work, as a function of the edge sites. This would also enable to analyse the origin of the DDS/HYD pathways as a function of the reactant and of the active phase features. In order to better discriminate more clearly between these mechanisms, it would be also welcome to establish a microkinetic model based on the present DFT data.

Aknowledgements

The authors would like to thank T. Bučko (Comenius University in Bratislava) and J. Rey (IFP Energies nouvelles – Ecole Normale Supérieure de Lyon) for fruitfull discussions and advice on IRC analysis.

Fundings

Calculations were performed using HPC resources (Jean Zay and Occigen) from GENCI-CINES (Grant A0020806134) and ENER 440 from IFP Energies nouvelles. This work is part of the "RatiOnAl Design for CATalysis" (ROAD4CAT) industrial chair, project IDEXLYON funded by the French National Research Agency (ANR-16-IDEX-0005) and the Commissariat-General for Investment (CGI) within the framework of Investissements d'Avenir program ("Investment for the future").

References

[1] R. Prins, Handbook of Heterogeneous Catalysis, Wiley-VHC Verlagsgesellschaft, Weinheim, 1997.

[2] H. Toulhoat, P. Raybaud, Catalysis by Transition Metal Sulfides. From molecular theory to industrial applications., Technip Edition, Paris (France), 2013.

[3] H. Topsøe, B.S. Clausen, F.E. Massoth, Hydrotreating Catalysis - Science and Technology, Springer-Verlag, Berlin/Heidelberg, 1996.

[4] H. Topsøe, B.S. Clausen, R. Candia, C. Wivel, S. Mørup, J. Catal. 68 (1981) 433.

[5] I. Alstrup, I. Chorkendorff, R. Candia, B.S. Clausen, H. Topsoe, J. Catal. 77 (1982) 397.

[6] B.S. Clausen, H. Topsøe, Hyperfine Interact. 47 (1989) 203.

[7] S.M.A.M. Bouwens, J.A.R.v. Veen, D.C. Koningsberger, V.H.J.d. Beer, R. Prins, J. Phys. Chem. 95 (1991) 123.

[8] J.V. Lauritsen, M.V. Bollinger, E. Lægsgaard, K.W. Jacobsen, J.K. Nørskov, B.S. Clausen, H. Topsøe, F. Besenbacher, J. Catal. 221 (2004) 510.

[9] B. Baubet, M. Girleanu, A.-S. Gay, A.-L. Taleb, M. Moreaud, F. Wahl, V. Delattre, E. Devers, A. Hugon, O. Ersen, P. Afanasiev, P. Raybaud, ACS Catal. 6 (2016) 1081.

[10] S. Kasztelan, H. Toulhoat, J. Grimblot, J.P. Bonnelle, Appl. Catal. 13 (1984) 127.

[11] H. Schweiger, P. Raybaud, H. Toulhoat, J. Catal. 212 (2002) 33.

[12] L.S. Byskov, J.K. Nørskov, B.S. Clausen, H. Topsøe, J. Catal. 187 (1999) 109.

[13] P. Raybaud, Appl. Catal. A: Gen. 322 (2007) 76.

[14] X.L. Ma, K.Y. Sakanishi, I. Mochida, Ind. Eng. Chem. Res. 33 (1994) 218.

[15] U.T. Turaga, C.S. Song, Catal. Today 86 (2003) 129.

[16] D.D. Whitehurst, T. Isoda, I. Mochida, Advances in Catalysis, Vol 42 42 (1998) 345.

[17] B.C. Gates, H. Topsøe, Polyhedron 16 (1997) 3213.

[18] M. Daage, R.R. Chianelli, J. Catal. 149 (1994) 414.

[19] E.O. Orozco, M. Vrinat, Appl. Catal. A: General 170 (1998) 195.

[20] V. Vanrysselberghe, R. Le Gall, G.F. Froment, Ind. Eng. Chem. Res. 37 (1998) 1235.

[21] M. Egorova, R. Prins, J. Catal. 225 (2004) 417.

[22] G.H. Singhal, R.L. Espino, J.E. Sobel, G.A. Huff, J. Catal. 67 (1981) 457.

[23] V. Lamure-Meille, E. Schulz, M. Lemaire, M. Vrinat, Applied Catalysis A: General 131 (1995) 143.

[24] J. Mijoin, G. Perot, F. Bataille, J.L. Lemberton, M. Breysse, S. Kasztelan, Catal. Lett. 71 (2001) 139.

[25] F. Bataille, J.L. Lemberton, P. Michaud, G. Perot, M. Vrinat, M. Lemaire, E. Schulz, M. Breysse, S. Kasztelan, J. Catal. 191 (2000) 409.

[26] D.H. Broderick, B.C. Gates, AIChE J. 27 (1981) 663.

[27] V. Meille, E. Schulz, M. Lemaire, M. Vrinat, J. Catal. 170 (1997) 29.

[28] M. Egorova, R. Prins, J. Catal. 241 (2006) 162.

[29] A.K. Tuxen, H.G. Füchtbauer, B. Temel, B. Hinnemann, H. Topsøe, K.G. Knudsen, F. Besenbacher, J.V. Lauritsen, J. Catal. 295 (2012) 146.

[30] J.V. Lauritsen, F. Besenbacher, J. Catal. 328 (2015) 49.

[31] S.S. Gronborg, M. Saric, P.G. Moses, J. Rossmeisl, J.V. Lauritsen, J. Catal. 344 (2016) 121.

[32] S. Humbert, G. Izzet, P. Raybaud, J. Catal. 333 (2016) 78.

[33] D.H. Broderick, A.V. Sapre, B.C. Gates, H. Kwart, G.C.A. Schuit, J. Catal. 73 (1982) 45.

[34] S. Cristol, J.F. Paul, E. Payen, D. Bougeard, F. Hutschka, S. Clemendot, J. Catal. 224 (2004) 138.

[35] T. Weber, J.A.R. Van Veen, Catal. Today 130 (2008) 170.

[36] J.-F. Paul, S. Cristol, E. Payen, Catal. Today 130 (2008) 139.

[37] M. Saric, J. Rossmeisl, P.G. Moses, J. Catal. 358 (2018) 131.

[38] S.J. Ding, Y.S. Zhou, Q. Wei, S.J. Jiang, W.W. Zhou, Catal. Today 305 (2018) 28.

[39] E. Krebs, B. Silvi, P. Raybaud, Catal. Today 130 (2008) 160.

[40] A.D. Gandubert, E. Krebs, C. Legens, D. Costa, D. Guillaume, P. Raybaud, Catal. Today 130 (2008) 149.

[41] A. Travert, C. Dujardin, F. Maugé, E. Veilly, S. Cristol, J.-F. Paul, E. Payen, J. Phys. Chem. B 110 (2006) 1261.

[42] F. Caron, M. Rivallan, S. Humbert, A. Daudin, S. Bordiga, P. Raybaud, J. Catal. 361 (2018) 62.

[43] P. Hohenberg, W. Kohn, Phys. Rev. B 136 (1964) 864.

[44] W. Kohn, L.J. Sham, Phys. Rev. A 140 (1965) 1133.

[45] G. Kresse, J. Furthmüller, Comput. Mater. Sci. 6 (1996) 15.

[46] G. Kresse, J. Furthmüller, Phys. Rev. B 54 (1996) 11169.

[47] J.P. Perdew, K. Burke, M. Ernzerhof, Phys. Rev. Lett. 77 (1996) 3865.

[48] G. Kresse, D. Joubert, Phys. Rev. B 59 (1999) 1758.

[49] S.N. Steinmann, C. Corminboeuf, J. Chem. Phys. 134 (2011).

[50] S.N. Steinmann, C. Corminboeuf, J. Chem. Theory Comput. 7 (2011) 3567.

[51] M. Saab, P. Raybaud, J. Phys. Chem. C 120 (2016) 10691.

[52] E. Krebs, B. Silvi, A. Daudin, P. Raybaud, J. Catal. 260 (2008) 276.

[53] P. Fleurat-Lessard, Opt'n path software, http://pfleurat.free.fr/ReactionPath.php, in.

[54] G. Henkelman, H. Jonsson, J. Chem. Phys. 113 (2000) 9978.

[55] G. Henkelman, B.P. Uberuaga, H. Jonsson, J. Chem. Phys. 113 (2000) 9901.

[56] G. Henkelman, H. Jónsson, J. Chem. Phys. 111 (1999) 7010.

[57] K. Fukui, The Journal of Physical Chemistry 74 (1970) 4161.

[58] K. Fukui, Acc. Chem. Res. 14 (1981) 363.

[59] B.A. De Moor, M.-F. Reyniers, G.B. Marin, Phys. Chem. Chem. Phys. 11 (2009) 2939.

[60] A. Travert, H. Nakamura, R.A. van Santen, S. Cristol, J.F. Paul, E. Payen, J. Am. Chem. Soc. 124 (2002) 7084.

[61] A.B. Anderson, Z.Y. Alsaigh, W.K. Hall, J. Phys. Chem. 92 (1988) 803.

[62] T. Todorova, R. Prins, T. Weber, J. Catal. 236 (2005) 190.

[63] T. Todorova, R. Prins, T. Weber, J. Catal. 246 (2007) 109.

[64] C. Dupont, R. Lemeur, A. Daudin, P. Raybaud, J. Catal. 279 (2011) 276.

[65] S. Kozuch, S. Shaik, Acc. Chem. Res. 44 (2011) 101.

[66] Y. Sun, R. Prins, J. Catal. 267 (2009) 193.

[67] Y. Okamoto, M. Kawano, T. Kawabata, T. Kubota, I. Hiromitsu, J. Phys. Chem. B 109 (2005) 288.

[68] P. Afanasiev, J. Catal. 269 (2010) 269.

[69] M.V. Bollinger, J.V. Lauritsen, K.W. Jacobsen, J.K. Norskov, S. Helveg, F. Besenbacher, Phys. Rev. Lett. 87 (2001).

[70] H. Schweiger, P. Raybaud, G. Kresse, H. Toulhoat, J. Catal. 207 (2002) 76.

[71] J. Rey, C. Bignaud, P. Raybaud, T. Bučko, C. Chizallet, Angewandte Chemie International Edition 59 (2020) 18938.